
Nucleosynthesis in neutrino-driven winds

Nucleosynthese in neutrinogetriebenen Winden

Vom Fachbereich Physik zur Erlangung des Grades eines Doktors der Naturwissenschaften (Dr. rer. nat.) genehmigte Dissertation von M.Sc. Lutz Huther aus Dieburg

21. Januar 2014 — Darmstadt — D 17



TECHNISCHE
UNIVERSITÄT
DARMSTADT

Fachbereich Physik
Institut für Kernphysik
Theoretische nukleare Astrophysik

Nucleosynthesis in neutrino-driven winds
Nucleosynthese in neutrinogetriebenen Winden

Vom Fachbereich Physik genehmigte Dissertation von M.Sc. Lutz Huther aus Dieburg

1. Gutachten: Prof. Dr. Gabriel Martínez-Pinedo
2. Gutachten: Prof. Dr. Karlheinz Langanke

Tag der Einreichung: 16.10.2013

Tag der Prüfung: 02.12.2013

Erscheinungsjahr: 2014

Darmstadt – D 17 – 21. Januar 2014

Lutz Huther

lhuther@online.de

Schorlemmerstr. 28
64291 Darmstadt

Tel.:(+49) 06151/ 1360244
Mobil: (+49) 0163/ 2164463

Persönliche Daten

Geburtsdatum	14.06.1985
Geburtsort	Dieburg
Nationalität	Deutsch
Familienstand	ledig

Erfahrung

2011–2013	Doktorand Stipendium im Rahmen des Helmholtz International Center for FAIR (HIC for FAIR)
2010–2012	Doktorand Anstellung im Rahmen des Sonderforschungsbereiches 634 “Kernstruktur, nukleare Astrophysik und fundamentale Experimente bei kleinen Impulsüberträgen am supraleitenden Darmstädter Elektronenbeschleuniger S-DALINAC”

Bildung

2008–2010	MSc in Physik, TU Darmstadt, Darmstadt, Deutschland “(n,γ)-Reaktionen mit Hilfe eines paritätsabhängigen statistischen Modells“
2004–2008	BSc in Physik, TU Darmstadt, Darmstadt, Deutschland “Photonenkorrelationen bei der Spontanen Parametrischen Konversion”
2001–2004	Alfred-Delp-Schule, Dieburg, Deutschland Gymnasiale Oberstufe und Erlangung der allgemeinen Hochschulreife
1995–2001	Schule auf der Aue, Münster b. Dieburg, Deutschland Förderstufe sowie gymnasialer Zweig
1991-1995	John F. Kennedy Schule, Münster b. Dieburg, Deutschland Grundschule

Sprachkenntnisse

Deutsch	Muttersprache
Englisch	Fließend
Französisch	Grundkenntnisse
Latein	Grundkenntnisse



Erklärung zur Dissertation

Hiermit versichere ich, die vorliegende Dissertation ohne Hilfe Dritter nur mit den angegebenen Quellen und Hilfsmitteln angefertigt zu haben. Alle Stellen, die aus Quellen entnommen wurden, sind als solche kenntlich gemacht. Diese Arbeit hat in gleicher oder ähnlicher Form noch keiner Prüfungsbehörde vorgelegen.

Darmstadt, den 15.10.2013

(M.Sc. Lutz Huther)



Zusammenfassung

Das Ziel dieser Arbeit ist die Untersuchung, ob und in welcher Form neutrinoinduzierte Spallationsreaktionen an Kernen Einflüsse auf die Nukleosynthese hat. Die Spallation beschreibt in diesem Kontext einen Prozess, bei dem ein angeregter Atomkern seine Anregungsenergie durch die Emission von leichten Teilchen (Protonen, Neutronen und α -Teilchen) sowie durch γ -Strahlung verliert. Für die Nukleosynthese sind hierbei nur Kernreaktionen relevant, dessen Eingangskanal sich von dem Ausgangskanal unterscheidet. Diese Spallationsreaktionen wurden in verschiedenen astrophysikalischen Szenarien untersucht; zu diesen Szenarien zählen der νp -Prozess, der r-Prozess und der ν -Prozess, welche mit einer Kernkollaps-Supernova assoziiert werden. Welche Prozesse stattfinden ist jedoch stark davon abhängig, wie sich die astrophysikalischen Parameter, wie beispielsweise Temperatur und Dichte als Funktion der Zeit, verhalten. Daher erscheint es logisch, dass unsere Nukleosynthese sehr stark davon abhängt, was aktuelle Simulationen der Kernkollaps-Supernova prognostizieren.

Schwere Kerne werden in einer Kernkollaps-Supernova hauptsächlich in dem neutrinogetriebenen Wind erzeugt. In dieser Phase wird Materie aufgrund von Neutrino-Wechselwirkungen von der Oberfläche des Proto-Neutronensterns emittiert. Durch die sehr hohen Neutrinoströme die der Proto-Neutronenstern erzeugt, wird das Verhältnis von Protonen zu Baryonen über Neutrinoreaktionen bestimmt. Diese sogenannte Elektronenabundanz sowie die Entropie der Materie beeinflussen maßgebend, welcher astrophysikalische Prozess stattfindet. Die für die Nukleosynthese relevanten astrophysikalischen Parameter sind stark von der verwendeten Mikrophysik in dem Proto-Neutronenstern abhängig.

Wenn Elektronenabundanz erreicht werden, die kleiner als 0.5 sind – d.h. es sind mehr Neutronen als Protonen vorhanden – und eine hohe Entropie von mindestens $150k_B$ erreicht wird, kann ein r-Prozess in dem neutrinogetriebenen Wind stattfinden [1]. Falls die Elektronenabundanz über 0.5 liegt, kann der νp -Prozess stattfinden.

In den äußeren Brennschalen des Sterns führt die Propagation des Schocks durch die Materie zu einem Erhitzen, welches zusätzliche Brennprozesse ermöglicht. Die Materie in den äußeren Brennschalen wird auch Wechselwirkungen mit den Neutrinos des Proto-Neutronensterns haben, welches wiederum die Nukleosynthese durch neutrinoinduzierte Spallationsreaktionen beeinflusst [2, 3].

Zur Untersuchung des Einflusses von neutrinoinduzierten Spallationsprozessen an Kernen auf die Nukleosynthese wurden die neutrinoinduzierten Spallationsprozesse in einem zwei-Schritt Verfahren berechnet. In einem ersten Schritt wurde die Anregung des Kerns beschrieben; der zweite Schritt bestand in der Bestimmung der Zerfallswahrscheinlichkeiten für jede Anregungsenergie. Die Anregung des Atomkerns wurde in dieser Arbeit sowohl über den neutralen Strom, als auch über den geladenen Strom berechnet. Die Anregungsspektren berechneten sich über eine sphärische RPA mit Woods-Saxon Einteilchenenergien, wobei Anregungen bis zu $J=4$ berücksichtigt wurden. Das Woods-Saxon Potential wurde so angepasst, dass es die Separationsenergien für die betrachteten Prozesse reproduziert; innerhalb der RPA wurde eine Landau-Migdal Wechselwirkung benutzt. Für die Neutrinoenergien, die in einer Kernkollaps-Supernova erreicht werden, liegt die Anregung in der Region der Riesenresonanzen, welche typischerweise über der Schwelle für die Aussendung eines Teilchens ist. Daher ist es notwendig Spallationsprozesse explizit zu berücksichtigen und die partiellen Wirkungsquerschnitte für diese Reaktionen zu bestimmen.

Die Spallation eines Teilchens wurde in dieser Arbeit mit Hilfe des Programms MOD-SMOKER berechnet. Dieses Programm wird weitläufig in der Astrophysik eingesetzt [4, 5, 6, 7]. Für die niederenergetische Beschreibung der Zerfallswahrscheinlichkeiten ist es ideal, da es die ersten 20 angeregten Zustände explizit berücksichtigt, solange diese experimentell mit Drehimpuls und Parität bekannt sind. Jedoch erlaubt MOD-SMOKER nur 1-Teilchen Spallation. In Regionen der Nuklidkarte, in denen die Teilchenemissionsschwelle bei sehr niedrigen Energien zu finden ist, wurde daher ein anderes Programm benötigt, welches die Aussendung von mehreren Teilchen erlaubt. Dieses Programm ist ABLA07, welches explizit für die Aussendung mehrerer Teilchen und die Beschreibung von Spaltungsprozessen entwickelt wurde. Weiterhin haben wir uns davon überzeugt, dass die Zerfallswahrscheinlichkeiten im Übergang zwischen beiden Modellen konsistent beschrieben wurden.

Welche Zerfallskanäle für jeden Kern vorhanden sind, hängt sehr stark von dem Energiespektrum der Neutrinos aus dem Proto-Neutronenstern ab. Wir haben die Zerfallswahrscheinlichkeiten für jeden Kern bis zur einer maximalen Aussendung von vier Teilchen berechnet.

Anschließend wurden die partiellen Wirkungsquerschnitte mit einem Neutrinoenergiespektrum in Form einer Fermi-Dirac Verteilung berechnet. Diese Verteilung besitzt zwei Parameter, die Neutrinotemperatur T_ν und das chemische Potential μ_ν , die an das Neutrinospektrum von Kernkollaps-Supernova Simulationen angepasst werden können. Heutzutage existieren zwar bessere Verteilungsfunktionen, für die Vergleichbarkeit mit früheren Arbeiten haben wir allerdings die hier erwähnte Methode beibehalten. Es sei angemerkt, dass die Bestimmung unserer partiellen Wirkungsquerschnitte für eine andere Verteilung jedoch jederzeit möglich ist.

Sobald die neutrinoinduzierten Spallationsreaktionen an Kernen berechnet wurden, konnten wir diese in ein nukleares Netzwerk einbauen um die Nukleosynthese in verschiedenen Szenarien zu berechnen. Das benutzte Netzwerk wurde bis

zu dieser Zeit nur für r-Prozess Rechnungen mit Kernspaltung genutzt [8, 9]; um eine gute Beschreibung in der Nähe des Proto-Neutronensterns zu erhalten haben wir zusätzlich die schwachen Wechselwirkungsraten von [10] berücksichtigt.

Die Untersuchung des neutrinogetriebenen Windes basiert auf astrophysikalischen Daten, die von Simulationen der Kernkollaps-Supernova [11, 12] herrühren. Bis Mitte 2012 zeigten diese Simulationen, dass die im Wind ausgesandte Materie eine Elektronenhäufigkeit größer als 0.5 besitzt. Demnach wird die ausgesandte Materie schwere Elemente über den νp -Prozess herstellen. Unsere Berechnungen der gesamten Nukleosynthese von der Materie im neutrinogetriebenen Wind zeigen, dass die Berücksichtigung von neutrinoinduzierten Spallationsreaktionen die Nukleosynthese nur so minimal ändert, dass es in der finalen Häufigkeitsverteilung nicht erkennbar ist. Ein Grund dafür ist, dass die entstandene Materie protonenreich ist. Daher ist die Wahrscheinlichkeit für die Aussendung eines Neutrons wegen der hohen Separationsenergie sehr gering. Es sei angemerkt, dass Neutronen jedoch aufgrund ihrer Fähigkeit lange Halbwertszeiten von β^+ -Zerfällen überbrücken zu können, in explosiven Szenarien wie dem protonenreichen neutrinogetriebenen Wind die einzige Möglichkeit sind, schwerere Elemente zu erzeugen. Der zweite Grund liegt in der Häufigkeit der schweren Elemente. Diese ist sehr viel geringer als zum Beispiel die Häufigkeit eines freien Protons. Änderungen in den Häufigkeiten durch die neu berechneten Spallationsreaktionen konnten jedoch für die leichten Elemente ${}^7\text{Li}$ und ${}^{11}\text{B}$ festgestellt werden.

In dieser Arbeit haben wir uns weiterhin die Frage gestellt, ob die elementare Häufigkeitsverteilung aus diesen Kernkollaps-Supernova Modellen die Häufigkeitsverteilung metallarmer Sterne wie HD 122563 erklären kann. Dafür haben wir den gesamten neutrinogetriebenen Wind zweier Langzeit-Supernova-Modelle mit unterschiedlichen Anfangsmassen untersucht [11]. Das schwerere Modell mit einer Anfangsmasse von 18 Sonnenmassen konnte der elementaren Häufigkeit bis zu einer Kernladungszahl von $Z=44$ folgen. Elemente mit einer größeren Kernladungszahl, die in dem metallarmen Stern HD 122563 ebenfalls beobachtet werden können, müssen daher in einem anderen Szenario synthetisiert werden.

Mitte des Jahres 2012 zeigten aktuelle Simulationen, dass, wenn in dem Proto-Neutronenstern Neutrinoeinfangreaktionen an Nukleonen konsistent mit der zugrundeliegenden Zustandsgleichung berechnet werden, das emittierte Material anfangs Elektronenhäufigkeiten besitzt, die kleiner als 0.5 sind. Das später emittierte Material ist wieder protonenreich ($Y_e > 0.5$). Die Nukleosynthese wird hauptsächlich von der anfänglichen neutronenreichen Materie bestimmt, da der Massenfluss von dem Proto-Neutronenstern sehr schnell abnimmt. Jedoch werden immer noch hauptsächlich die Elemente produziert, die auch im νp -Prozess produziert werden. Dazu gehören die protonenreichen stabilen Elemente in der Massenregion um $A=70-90$, zum Beispiel ${}^{78}\text{Kr}$, ${}^{84}\text{Sr}$ und ${}^{92}\text{Mo}$.

Die größten Änderungen durch die berechneten Spallationsreaktionen können wieder bei den leichten Kernen beobachtet werden, jedoch sind diesmal auch kleine Änderungen in der finalen Häufigkeit des gesamten Windes bei den neutronenreichen Isotopen zu beobachten. Diese Änderungen sind in der elementaren Häufigkeitsverteilung nicht zu beobachten, da über die Häufigkeiten der einzelnen Isotope summiert wurde. Vergleicht man die erhaltene elementare Häufigkeitsverteilung mit der beobachteten Häufigkeitsverteilung von HD 122563, ist eine Übereinstimmung bis zu einer Kernladungszahl von $Z = 42$ erkennbar.

Ein weiterer astrophysikalischer Prozess, den wir mit Hilfe unserer neuen Spallationsreaktionen untersucht haben, ist der r-Prozess im neutrinogetriebenen Wind. Obwohl wir mehrmals in dieser Arbeit darauf hingewiesen haben, dass der r-Prozess in aktuellen Kernkollaps-Supernova Simulationen nicht stattfinden kann, deuten galaktische Evolutionsmodelle darauf hin, dass der r-Prozess in Kernkollaps-Supernovae stattfinden muss. Dies könnte ein Indikator dafür sein, dass noch nicht alle relevanten Prozesse in den Simulationsmodellen berücksichtigt werden. Um den r-Prozess zu studieren, haben wir einen Datensatz genommen, der beim "α-rich freezeout" eine Elektronenhäufigkeit von 0.469 besitzt. Die mittleren Energien und Luminositäten der Neutrinos sind von der Simulation übernommen [13], jedoch musste die Entropie um einen Faktor 2 erhöht werden, um einen effektiven r-Prozess zu erhalten. Da keine Informationen über die mittleren Energien und Luminositäten der μ - und τ -Neutrinos in [13] angegeben wurden, konnte durch Variation dieser Werte in einem physikalisch sinnvollen Bereich der Einfluss von neutrinoinduzierten Spallationsreaktionen über den neutralen Strom studiert werden, da aufgrund der größeren mittleren Energien der neutrale Strom hauptsächlich von den μ - und τ -Neutrinos beeinflusst wird. Wir konnten beobachten, dass Spallationsreaktionen über den geladenen Strom die Produktion von schweren Elementen reduziert. Wenn Spallationsreaktionen über den neutralen Strom berücksichtigt werden, ist die Produktion von schweren Kernen sehr stark beeinträchtigt. Der Grund für diese Beeinträchtigung sind Neutrinoeinfangreaktionen an ${}^4\text{He}$, die ${}^3\text{H}$ erzeugen. Durch vielfache α -Einfangreaktionen wird so die Anzahl an schweren Kernen erhöht, während gleichermaßen die Anzahl an freien Neutronen reduziert wird.

Zusätzlich haben wir das Szenario der "hot convective bubble" untersucht. Auch in diesem Szenario wird die Materie aufgrund von Wechselwirkungen mit Neutrinos emittiert, jedoch ist die Materie nicht so nahe an der Oberfläche des Proto-Neutronensterns. Da die Emission des Material sehr früh geschieht, ist die Elektronenhäufigkeit nur schwach protonenreich (zwischen 0.5 und 0.54). Unsere Studien zur Nukleosynthese ergaben, dass die Berücksichtigung von Spallationsreaktionen die finale Häufigkeit kaum ändert.

Als letztes Szenario haben wir die Nukleosynthese in den äußeren Brennschalen des Sterns untersucht, wenn der Schock der Kernkollaps-Supernova durch den Stern läuft. Die Neutrinoflüsse sind bedingt durch den geometrischen

Faktor $1/r^2$ natürlich viel kleiner als im neutrinogetriebenen Wind. In vorigen Arbeiten wurde schon gezeigt [2, 3], dass die Berücksichtigung von Neutrinoreaktionen die finalen Häufigkeiten von Elementen mit ungerader Ladungszahl beeinträchtigen kann. Ein Grund dafür ist, dass Elemente mit gerader Ladungszahl häufiger sind. Wenn das Verhältnis der Häufigkeiten zwischen Mutterkern, mit gerader Ladungszahl, und Tochterkern ungefähr den Faktor 10^3 beträgt, dann ist eine Produktion über den ν -Prozess möglich [2, 3]. Insbesondere die Isotope ${}^7\text{Li}$ und ${}^{11}\text{B}$ können über diesen Prozess synthetisiert werden.

In dieser Arbeit haben wir ein phänomenologisches Modell benutzt, um das Erhitzen durch den Schock sowie die einhergehende Expansion zu erklären. Weiterhin waren unsere mittleren Neutrinoenergien sehr groß, insbesondere für μ - und τ -Neutrinos. Um unsere Ergebnisse mit vorigen Ergebnissen zu vergleichen, haben wir diese Daten beibehalten. Durch die hohen Energien waren die dominierenden Prozesse immer Spallationsreaktionen über den neutralen Strom. Jedoch konnten wir auch beobachten, dass Reaktionen über den geladenen Strom nicht vernachlässigt werden können.

Es stellt sich natürlich die Frage, wieso in dem Szenario des ν -Prozesses ein Effekt durch die Berücksichtigung von neutrinoinduzierter Spallation beobachtet werden kann, jedoch nicht im neutrinogetriebenen Wind. Der Hauptgrund dafür ist, dass das Isotop mit welchem das Neutrino reagiert in dem ν -Prozess schon vorhanden ist, während es in dem neutrinogetriebenen Wind zuerst erzeugt werden muss. Dies reduziert das Zeitfenster, in dem Neutrinos mit dem Isotop wechselwirken können. Weiterhin ist auch die Emissionsgeschwindigkeit der Materie im neutrinogetriebenen Wind viel größer. Diese Effekte reduzieren die Neutrino fluenz soweit, dass diese vergleichbar oder sogar kleiner ist als für den ν -Prozess. Zusätzlich ist die absolute Häufigkeit der schweren Elemente im neutrinogetriebenen Wind viel geringer als die Häufigkeiten der Elemente in den äußeren Schalen.

Zusammenfassend lässt sich sagen, dass die Berücksichtigung von neutrinoinduzierten Spallationsprozessen keinen Einfluss auf die Nukleosynthese hat, jedoch für die Synthese einiger Elemente (${}^7\text{Li}$, ${}^9\text{Be}$, ${}^{11}\text{B}$, und auch ${}^{138}\text{La}$, ${}^{180}\text{Ta}$) relevant ist. Falls ein r-Prozess in dem neutrinogetriebenen Wind stattfindet, können neutrinoinduzierte Spallationsprozesse einen wichtigen Einfluss haben, insbesondere gilt das für die Neutrino prozesse an ${}^4\text{He}$. Im protonenreichen neutrinogetriebenen Wind konnten wir keine Änderungen in der Nukleosynthese von schweren Elementen erkennen; jedoch konnten Änderungen in den leichten Kernen beobachtet werden. Für die Nukleosynthese des gesamten Sterns spielen diese Änderungen jedoch keine Rolle.



Danksagung

Mein größter Dank geht an meine Betreuer Gabriel Martínez-Pinedo und Karlheinz Langanke für die Möglichkeit, bei ihnen und mit ihrer Unterstützung diese Doktorarbeit schreiben zu können. Ihr tiefes und detailliertes Wissen der Physik hat mich jedes Mal aufs Neue fasziniert.

Insbesondere bin ich sehr dankbar für die zahlreichen Gespräche und anregenden Diskussionen, die, besonders zum Ende diese Doktorarbeit, in eigentlich arbeitsfreien Zeiten stattgefunden haben. Es war mir eine sehr große Hilfe, dass ich zu fast jeder Uhrzeit/Zeitzone meine beiden Betreuer erreichen konnte und unverzüglich Rückmeldungen erhielt. Vielen Dank dafür!

Meiner Arbeitsgruppe möchte ich danken, in der immer eine angenehme Arbeitsatmosphäre herrschte. Die Vielzahl an geteilten Kuchenstücken hat dazu sicherlich beigetragen. Auch die rituellen Kart-Verabschiedungsrennen haben mir viel Spaß gemacht. Ein großer Dank geht natürlich auch an meine ehemalige Arbeitsgruppe der GSI, insbesondere an Klaas Vantournhout und Dennis Weber.

Ein besonderer Dank geht an Joel Mendoza-Temis, mit dem ich alleine ein Großraumbüro und häufig unmögliche Arbeitszeiten teilte. Seine offene und freundliche Art hat mich immer wieder überrascht und in weniger motivierten Phasen des Arbeitens aufgebaut. Auch Andreas Lohs war ein guter Begleiter meiner Promotionszeit, besonders die regelmäßigen Gänge zum Supermarkt und die damit verknüpften Diskussionen, die sowohl physikalische als auch nichtphysikalische Themen beinhalteten, haben mich unterstützt. Tobias Fischer möchte ich danken, dass er mir bei dem Verständnis von Supernova-Modellen und den dabei ablaufenden physikalischen Prozessen immer sein Wissen zur Verfügung gestellt hat.

Ferner gebührt Hans-Peter Loens mein Dank, der mir die Funktionsweise des MOD-SMOKER Codes sehr anschaulich beigebracht sowie zu jeder Zeit ein offenes Ohr für mich hatte.

Bei meinen Freunden möchte ich mich für die gemeinsame Zeit bedanken, bei der sie für die nötige Ablenkung von der Arbeit gesorgt haben. Natürlich möchte ich auch meiner Familie, insbesondere meinem Bruder, danken, dass sie Verständnis für meinen Mangel an Freizeit aufbringen konnten. Der gesamten Familie Willmann möchte ich für aufmunternde Worte und Gesten über die letzten Jahre hinweg danken.

Den Dank an meine Freundin Michaela Willmann kann ich gar nicht in Worte fassen. Ich möchte mich bei ihr dafür bedanken, dass sie mich in jeglicher Form unterstützt hat, diese Arbeit fertig zu stellen. Ihr Verständnis für meine unsagbar langen Arbeitszeiten, auch an Wochenenden, die dazu führten, dass ich kaum zuhause war, sind mir unbegreiflich. Natürlich bin ich auch dankbar, dass sie meine zeitweise schlechte Laune, wenn Dinge nicht so liefen wie geplant, immer wieder aufmuntern konnte. Dass wir diese Zeit zusammen durchgestanden haben zeigt mir, dass wir alles gemeinsam schaffen können.



Contents

Zusammenfassung	5
------------------------	----------

Danksagung	9
-------------------	----------

I Introduction **13**

1 Introduction **15**

1.1 Life of a star	16
1.2 Neutrinos and nucleosynthesis	22
1.2.1 Nucleosynthesis in neutrino-driven winds	23
1.2.2 Neutrino-nucleosynthesis	26

II Theory **29**

2 Nuclear theory **31**

2.1 Weak interactions	31
2.2 Nuclear reactions	35
2.3 Nuclear structure	36
2.3.1 Independent particle model	37
2.3.2 Random Phase Approximation	38
2.3.3 Residual interaction	41
2.3.4 Partial occupancy	42
2.3.5 Sum rules	42
2.3.6 Reduction of transition operators	45
2.3.7 Model space considerations	45
2.4 Description of the decay	46
2.4.1 Statistical model considerations	46
2.4.2 Combined model	47
2.4.3 Transmission coefficients	48
2.4.4 Level density description	49
2.4.5 Applicability of the statistical model	51
2.4.6 Multi-particle spallation	52
2.4.7 The unified nuclear model	56

III Results **59**

3 Neutrino-induced spallation rates **61**

3.1 Consistency	61
3.2 Neutrino scattering rates	69
3.2.1 Partial neutrino scattering rates	71
3.2.2 Average neutrino particle emission	72
3.3 Charged-current rates	73

4 Nucleosynthesis results with new rates **75**

4.1 Heavy element production in neutrino-driven winds	76
4.2 Integrated nucleosynthesis in neutrino-driven winds	84
4.2.1 Light element production in the neutrino-driven wind	92



4.3	r-process nucleosynthesis under strong neutrino fluxes	94
4.3.1	Neutrino reactions on α -particles	97
4.4	Nucleosynthesis in the hot convective bubble	98
4.5	Neutrino nucleosynthesis	102
4.5.1	Nucleosynthesis effects	104
4.6	Neutrino processes and neutrino fluence	112
IV	Summary & Outlook	113
4.7	Summary	115
4.8	Outlook	118
V	Appendix	119
4.9	Nuclear astrophysics	121
4.9.1	Nuclear reaction networks	121
4.9.2	Implementation of the neutrino rates in the network	123
4.10	Nuclear physics	125
4.10.1	Angular momentum coupling and spherical harmonics	126
	Bibliography	129

Part I.

Introduction



1 Introduction

The origin of nuclear astrophysics is related with the fundamental question of how the sun produces energy. It was not clear how the sun could withstand against gravity and furthermore is able to emit thermal energy visible to us as light. Soon the realization has been made, that nuclear reactions can produce the enormous amount of energy, it was however not understood which processes govern this energy gain. It was the pioneering work of Bethe and Critchfield [14] to understand that a reaction sequence of proton captures resulting to helium is the main energy source of our sun. This reaction sequence is known as the pp-chain.

Based on this elemental question, a whole field arose working on topics ranging from the Big Bang over the formation of stars, up to the structure of a neutron star – just to mention a few. In these astrophysical scenarios matter is brought to extreme conditions that even current technology is not able to reproduce such as very high densities, temperatures or magnetic fields. However the key question in nuclear astrophysics might have always been to understand the production of the elemental abundance that can be observed in our solar system and is therefore also called solar system abundance.

It is currently accepted that these elements will have to be produced in stars by nuclear reactions and have to be expelled into the interstellar medium to produce such an uniform abundance distribution as it can be observed in our solar system. We furthermore have to assume that the isotopic abundance pattern shown for example in figure 1.1 is a superposition of many single nucleosynthesis events in different astrophysical scenarios. Elements produced in a star's life, will most likely be expelled at the end of the stars life and the expelled matter will serve as the basic constituents for the new formation of stars. With each death of a star, the created elements will constitute the initial composition of a new star, leading to a mixing of all different astrophysical processes that have been occurring in previous generations of stars, creating an abundance pattern as it is observed in figure 1.1. The first authors able to explain the different features

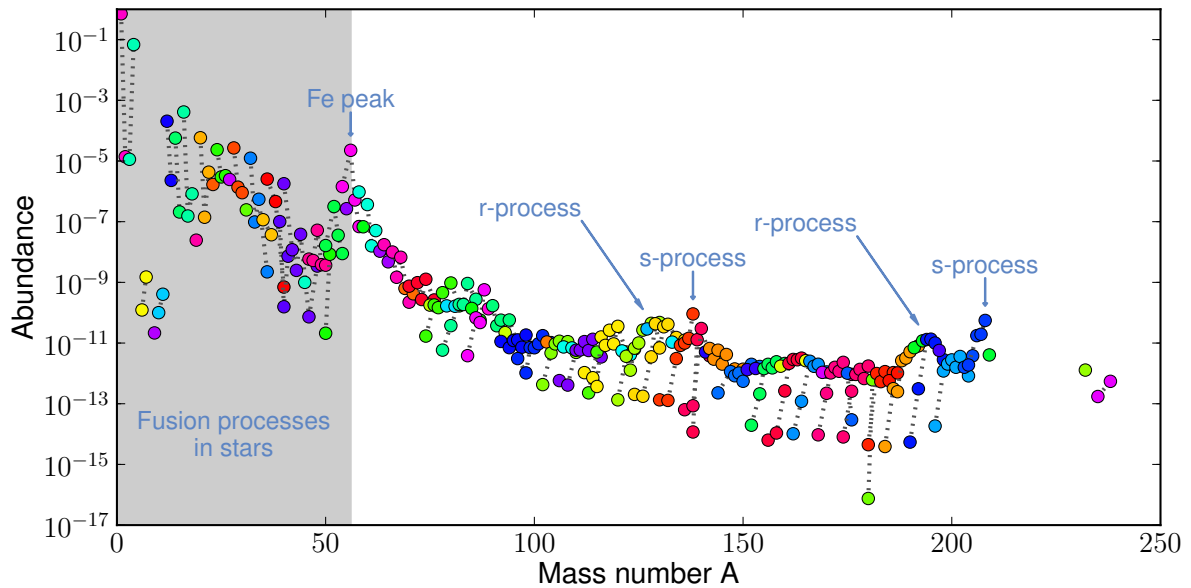


Figure 1.1.: The solar photospheric and meteoritic isotopic abundances given as described in [15]. In general only elemental abundances can be obtained from photospheric measurements, it is therefore assumed that the terrestrial isotopic compositions can be scaled to the obtained elemental abundances, except in the cases for the noble gases and hydrogen. The abundance pattern can be differentiated roughly in two parts. The first part contains nuclei where the majority is produced within stellar burning processes. The most abundant nuclei in this first part are protons and then alpha-nuclei. Within this context alpha-nuclei are nuclei that have an even and equal number of protons and neutrons, thus can be created by increasingly adding α -particles to the nuclei. The only exception to this trend is ${}^8\text{Be}$ which ground state energy is above the combined energy of two α -particles and will subsequently decay into its initial constituents. The second part, which is the abundance pattern of isotopes beyond the iron peak, looks completely different. While the previous ones are produced by fusion reactions, these elements are almost exclusively created by neutron capture processes. It requires at least two different astrophysical scenarios for the description of the abundance pattern that are called s - and r -process.

of the solar system abundances were Burbidge, Burbidge, Fowler and Hoyle [16] and at the same time Cameron [17]. In their seminal papers they laid the foundation of the modern theory of nuclear astrophysics.

For a rough explanation of the different processes creating the elements of the solar system, we will now sketch very briefly how a star will – due to nuclear fusion processes – withstand against gravitational collapse and during its life create the elements up to the iron peak shown in figure 1.1. After that, we will focus shortly on how the star will end its life in a massive explosion, expelling a majority of its mass back into the interstellar medium. In the next part we then want to come back and describe the scenarios and processes required to produce the elements heavier than $A = 56$.

1.1 Life of a star

Under the assumption that the first stars were only formed with the elements created in the Big Bang, these stars initially consisted in large part of hydrogen, about 25% of helium and very few light elements up to mass number $A = 7$. The process of star formation itself is an interesting topic, in which a molecular cloud will collapse, due to the fact that the thermal energy of the gas cloud cannot withstand against its own gravitational potential energy. Since this thesis is concerned with the nucleosynthesis in stars, we will assume that the formation of the star has already occurred.

It can be observed just as in the case of our sun that stars emit a substantial amount of energy due to radiation. This energy loss has somehow to be compensated to obtain an equilibrium between energy loss and gain. This energy has to be produced within the star. The most efficient possibility of generating this energy is due to nuclear reactions. The first process that will be initiated by a star consisting solely of the Big Bang elements, is the fusion of four protons to one α -particle via the pp-chain under a net energy gain of 26.7 MeV radiated away in photons and neutrinos – just as it occurs in our sun [18, 19]. For completeness we should mention that stars, containing of matter that already underwent one or several stellar life-cycles and feature masses slightly heavier than our sun, are able to produce elements over the so called *CNO cycle*. Within this CNO cycle carbon, nitrogen and oxygen act as a catalyst for the creation of α -particles from free protons. Due to the stronger temperature dependence, the CNO cycle is for higher mass stars the dominant ${}^4\text{He}$ -creation source, because the temperature in the center of the star increases with increasing mass.

A star will spend most of its time in this phase of central *hydrogen burning*, however with ongoing time, the helium density in the center of the star will gradually increase up to a point where helium is more dominant than hydrogen. The pp-chain will not be able to operate efficiently and to produce enough energy. To withstand against gravity the nuclear burning region thus moves to a shell around the inert helium core where the proton abundance is still sufficient, continuously increasing the helium core due to hydrogen shell burning. The central density increases the pressure in the helium core leading to a temperature increase until helium nuclei can fuse to ${}^{12}\text{C}$ and ${}^{16}\text{O}$ – also called helium burning – via the *triple- α* reaction ($\langle\alpha\alpha\alpha\rangle$). With increasing time, the star will have too much carbon and oxygen in the center and the helium core burning will evolve to a helium shell burning. After these burning stages, the further fate of the star is very sensitive to its initial mass. Typically, stars with masses smaller than $8 M_{\odot}$ ¹ are not able to reach densities and temperatures high enough to start the following burning stages and will therefore end their life as a white dwarf. The final mass of the white dwarf will be typically around $0.5 M_{\odot}$, but can have a maximal mass reaching up to $1.4 M_{\odot}$. The remaining matter has been ejected due to thermal pulses during helium shell burning [20].

Stars with an initial mass higher than $11 M_{\odot}$ reach densities and temperatures that are high enough that they will experience further burning stages. These *advanced burning stages* occur in the same manner as the burning stages mentioned above. Within each of these advanced burning stages will the core, consisting mainly of the nuclear ashes of the preceding burning stage, increase its central density and pressure, due to gravitational contraction, to stabilize the star. At one point the conditions are high enough that the Coulomb barrier will be overcome releasing an additional source of energy, stalling the contraction of the star. With ongoing time the ashes will become dominant in the center of the star leading to a shell burning. The various burning stages are called carbon-, neon-, oxygen- and silicon-burning [19]. These different burning processes can roughly explain the creation of elements up to the iron group peak marked in figure 1.1. The steep decline from hydrogen up to iron is related to the increasing Coulomb barrier accompanying charged particle reactions. Note that this increase in Coulomb energy already modifies silicon-burning in such a way that it is not anymore a fusion reaction of identical nuclei as in the burning stages before, instead photo-disintegration plays a essential role in creating the charged reaction partners for silicon. Due to its strong binding the dominating charged reaction partners are basically α -particles, leading to a chain of capture processes until the iron group nuclei are reached. Again, with increasing burned material in the center of the star Si burning will evolve to a shell burning around an iron group core. Note that from beginning of silicon-core-burning the importance of weak interaction processes increases, because electron and positron captures will occur creating free neutrinos. The density however is not large enough that neutrinos will be trapped and therefore act as an energy dissipation source.

¹ $1 M_{\odot} = (1.98855 \pm 0.00025) \times 10^{30} \text{ kg}$ is the standard unit of mass in astronomy, which equals the mass of our sun.

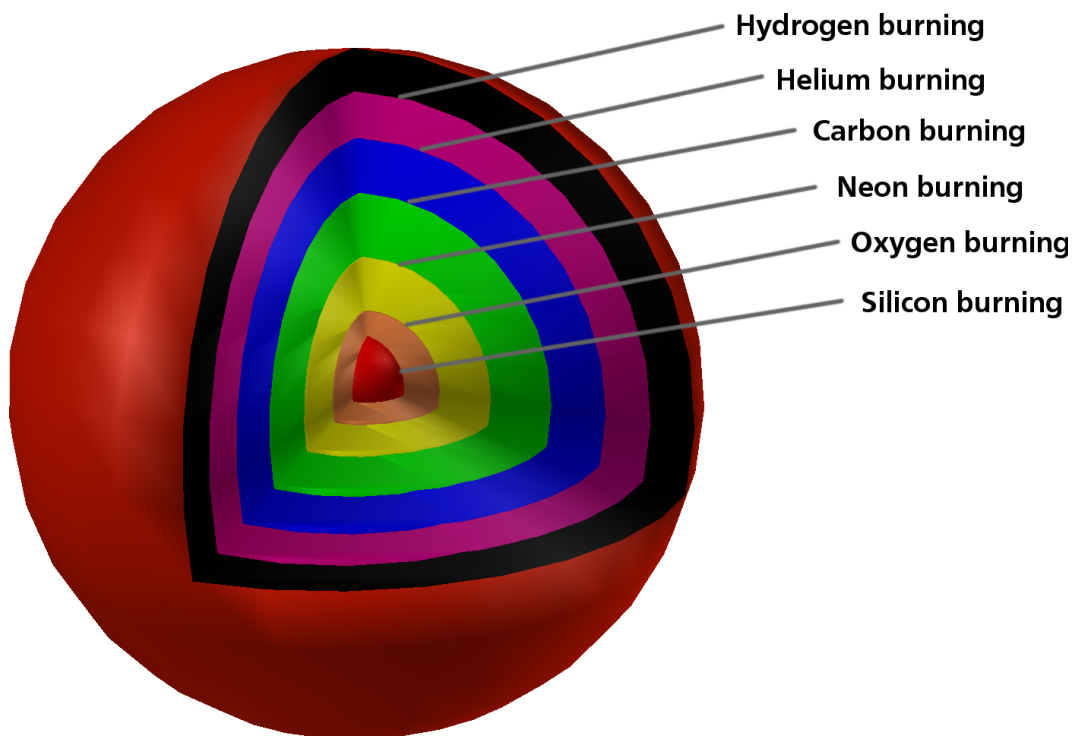


Figure 1.2.: A massive star at the end of its life. All stellar burning processes still occur in shells around the core. Thus the star has an onion like structure. In the core it is not possible to gain energy due to fusion or capture processes on the iron-peak nuclei, since the binding energy per nucleon has its maximum at $A = 56$. Due to the continuous mass increase of the iron core, the star will reach its final fate in a core-collapse supernova.

Core-collapse supernova

At the end of its life, a massive star will have an onion like structure – as it is shown in figure 1.2 – and different burning processes will still occur in shells around the core of the star that continuously gains mass due to silicon shell burning. The synthesis of heavier elements due to fusion processes is no longer possible for nuclei above the iron peak, since these processes will no longer release energy, instead energy has to be absorbed that these reactions actually happen. Fusion will be additionally hindered by the fact that the Coulomb barriers are already substantially high. The core of such a massive star is quite dense, electron degeneracy pressure is a large contribution in resisting against gravitational pressure. With increasing mass of the iron core – around the Chandrasekhar mass limit of about 1.44 solar masses – electron degeneracy pressure is not able to further stabilize the core and it will collapse. For a detailed description of the onset of gravitational collapse, weak interactions play a tremendous role, because they control the evolution of the electron number due to electron captures on iron group nuclei. Furthermore, neutrinos produced by weak interactions will transport a significant fraction of energy out of the star. Since their cross section is very small, very little scattering/capturing processes will occur on their way outwards [19]. Due to the fact that electrons are taken away by electron captures, the electron degeneracy pressure will decrease, leading to a speedup of the collapse. This is the onset of what is known as a *core-collapse supernova*, expelling most of the star's material into the interstellar medium. With the increasing densities originating from the gravitational infall, neutrino interactions with matter become more and more important, up to the point when neutrinos have such a short mean free path that they are basically trapped. The finite compressibility of nuclear matter stops the collapse quite abrupt at densities above nuclear saturation densities, leading to an outwards moving shock wave, that dissociates on its way the material into free protons and neutrons. The point in time with maximal density is usually called *bounce* and marks the onset of explosion. In all current models the shock is not energetic enough to explode the star directly, because energy losses due to dissociation of the iron core matter are too strong, resulting in a stalled shock at radii around several hundreds of km [21].

In the center of the former star a compact object is starting to form. This nascent remnant will either evolve to a neutron star or further contract and form a black hole and will from now on be referred to as the *proto-neutron star* (PNS). The PNS contains a large number of degenerate electrons and neutrinos. The latter ones have such short mean free path due to the very high densities that their average time of escaping from the PNS is of the order of several hundred milliseconds, increasing up to seconds for neutrinos from the center of the star [21]. Within this time period they traverse outwards while being downscattered in energy until they reach densities where they are able to stream out

freely. Due to the escape of neutrinos, electron captures will drive the matter in a neutron rich regime. Later cooling of the now neutron rich PNS proceeds by neutrino pair production and diffusive loss of neutrinos [21]. The cooling of the PNS is a very interesting and fascinating topic, because neutrinos will interact with the material above the neutron star. The interaction includes absorption of ν_e and $\bar{\nu}_e$, neutrino-electron scattering and neutrino-antineutrino annihilation [22]. Due to the fact that $\nu_{\mu,\tau}$ and $\bar{\nu}_{\mu,\tau}$ can only interact over neutral-current neutrino scattering the neutrino spectra are expected to have the following neutrino-energy hierarchy : $\langle E_{\nu_{\mu,\tau},\bar{\nu}_{\mu,\tau}} \rangle > \langle E_{\bar{\nu}_e} \rangle > \langle E_{\nu_e} \rangle$, where $\langle E_{\nu_x} \rangle$ gives the average neutrino energy of the neutrino spectrum with flavor x . The net effect of the neutrino interactions will be that energy from the neutrinos will be transferred to the material on top of the PNS, which is thereby heated. Consequently, the material will be ejected from the surface of the PNS. This mass outflow is what is known as the *neutrino-driven wind* [23] and we will study the nucleosynthesis of this environment in detail within this thesis.

It is still subject to debate how the core-collapse supernova reignites the aforementioned stalled shock and the star finally explodes. Currently one scenario seems favorable which is that neutrinos, originating from the PNS, will help reigniting the shock. During a core-collapse supernova event, neutrinos carry away most of the energy set free due to the gravitational collapse, only a small portion of this energy (approximately 1%) is sufficient to reignite the shock [24]. To reignite the shock, the neutrinos have to deposit some of their energy in the region behind the stalled shock by means of neutrino scattering/capturing processes. A constant energy deposition can then help reigniting the shock and eventually lead to successful explosions. As mentioned before, to this day not all core-collapse supernovae models explode without artificially increasing the energy deposition behind the stalled shock, pointing to some missing input physics in the simulations.

Due to the high temperatures that can be reached while the shock is propagating through the outer layers of the star, nuclear reactions will occur in time scales much shorter than the dynamical timescale and therefore give rise to explosive nucleosynthesis scenarios [20]. The dynamical timescale is defined as

$$\tau_{dyn} = \frac{1}{\sqrt{G\rho}}, \quad (1.1)$$

where R is the star's radius, G the gravitational constant, M gives the mass of the star and ρ is the local matter density [25, 26].

The creation of elements beyond iron

For understanding the abundance pattern above $A = 56$ as it is for example shown in figure 1.1, one might first notice that the pattern appears almost flat in comparison to the isotopic pattern of the elements up to iron. Elements below iron are related to fusion processes in stars – as mentioned above – therefore they have to overcome the Coulomb barrier, giving rise to the decrease of abundance with increasing mass number. Around iron ($A = 56$) a strong peak can be observed, which is also denoted as *iron peak*. The reason why this isotopic region shows such a strong peak arises basically due to the fact, that at $A = 56$ the binding energy per nucleon shows a maximum. The production of heavier elements is required to occur in other nucleosynthesis processes.

By general considerations one can observe, that the almost flat behavior above the iron peak has to be created with processes that do not feel the Coulomb potential and can therefore only be neutron capture reactions. Furthermore the abundance pattern shows two distinct peaks around each neutron shell closure. These abundance patterns can be related with two distinct scenarios with different neutron densities. Based on the height of the abundance peaks one is also able to note that both processes contribute almost equally to the total production of elements beyond the iron peak.²

The first process – exhibiting a low neutron density – is called *s-process*. Due to its low neutron densities the typical time for a neutron capture is of the order of several month [28] which is the key argument why the *s-process* will operate on nuclei very close to stability, because the typical β^- -decay half-life will be smaller. It is noteworthy to mention that the *s-process* requires seed nuclei to operate. Therefore it is not possible that the first generation of stars will have produced *s-process* elements. Currently it is believed that the *s-process* operates in low mass stars ($1 M_{\odot} < M < 3 M_{\odot}$) and massive stars ($M > 8 M_{\odot}$) while their He burning phase [29].

The second process is known as the *r-process*. Contrary to the *s-process* it is believed that the neutron density is very large, resulting in several neutron captures before a β^- -decay will happen. This will drive the reaction path to the neutron rich side of the nuclear chart, far off the valley of stability, making this process an ideal candidate for nuclear structure theorist since almost no experimental information could be gained so far. The *r-process* does not require seed nuclei that are created beforehand. The production of the elements over the *r-process* is thus independent of the initial heavy element content of the star and can in general start from nuclear statistical equilibrium (NSE) or bare protons

² By a closer look one is able to realize that a minor selection of nuclei cannot be created by neutron capture processes because these nuclei are neutron deficient. These nuclei are usually called *p-nuclei*, because it is believed that they are produced by the *p-process*, that photodisintegrates previously produced neutron rich or stable elements [27].

and neutrons. The r-process has been studied extensively from a theoretical point of view and there are several different scenarios for obtaining a similar r-process pattern as the solar ones³, although the precise abundance pattern is strongly dependent on the theoretical input physics, with all uncertainties inherited from the underlying assumptions.

The astrophysical site of the r-process is up to this date a subject of debate. It has to be assigned with explosive scenarios in which neutron densities can be reached that are high enough to have a full r-process. Within this context a full r-process denotes an astrophysical process that is able to explain in large part the remaining elemental abundances, which cannot be explained by the s-process above $A = 56$. Key ingredients for such a full r-process are the ratio of electrons to baryons (electron fraction Y_e), the expansion timescale and the entropy of the system.

To the end of the last century it was believed that the r-process will occur in the neutrino-driven wind phase of a core-collapse supernova. Current core-collapse supernova simulations with accurate neutrino transport show that the scenario is not extreme enough to reach such a full r-process. A full r-process will especially have to explain the formation of the heavy elements beyond lead that cannot be reached by the s-process and are used within cosmochronometry, such as $^{235,238}\text{U}$ and ^{232}Th . A more detailed explanation why a full r-process will not occur within current supernova simulations will be given in subsection 1.2.1. Nevertheless, the neutrino-driven wind is a fascinating scenario for nucleosynthesis studies, since it describes an astrophysical site, where material is subject to strong neutrino fluxes of all flavors. We will discuss this too in more detail in section 1.2.1.

Another feasible model that satisfies the needs for an efficient r-process is the neutron-star merger scenario, in which two remnants of core-collapse supernova in a binary system slowly approach each other until they collide and form a dense massive object, eventually resulting in a black hole. Within this collision phase an accretion disc is formed, expelling very neutron rich material. Simulations of such neutron-star mergers scenarios show – within the model uncertainty – that the results are able to reproduce the solar r-process pattern [30]. As we will see in the next subsection, the neutron-star merger scenario has also drawbacks that need to be clarified.

Metal poor stars and the r-process

To gain additional insight about the r-process and its possible astrophysical site, abundances obtained from metal-poor stars might shed light on this issue. Metal-poor stars are stars which have a very small enrichment in metals⁴ observable in the atmosphere. During the life of a star, metals are produced due to the aforementioned burning processes. Based on the assumption that no metals have been produced within the Big Bang and that these metals can only be produced in stars, the metallicity can be used as an indirect indicator of age. For historical reasons iron is commonly utilized as a reference of metallicity/age. Thus, by the observation of an element in various metal-poor stars with different metallicities, the elemental abundance of a nucleus can be studied as a function of time. If one quantifies the abundance of a typical r-process nucleus, such as europium, one is actually able to observe the elemental production of the r-process over time.⁵ By comparison of this quantity with galactic chemical evolution models and a reasonable assumption on the average rate of neutron star mergers in a galaxy, one realizes that r-process elements created in neutron-star mergers can account for the current amount of r-process material produced in a galaxy. However, for early times the neutron star merger scenario fails to reproduce the observed r-process abundance pattern [31]. This relates to the fact that before having a neutron-star merger scenario, the two remnants have to be produced beforehand in core-collapse supernovae and then start merging each other, which requires time. However, observations show that metal-poor stars with a metallicity of $[\text{Fe}/\text{H}] \approx -3$ show already a large production of r-process elements. The existence of these heavy elements in the observed stars show that the preceding star will already have produced elements assigned to the r-process [32]. This fact can hence not be explained with a neutron-star merger scenario. Thus, currently both models cannot consistently provide the full requirements for an astrophysical r-process site.⁶

With the observation of metal-poor stars we are also able to observe the robustness of the r-process. By comparing the abundance yields with the solar r-process pattern, the authors of [35] could show that for metal-poor stars with a strong enrichment in r-process nuclei, the heavy r-process elements ($Z > 50$) have the same behavior as the solar r-process pattern (see the left plot of figure 1.3). This fact tells us that no matter where and how the r-process occurs, its nucleosynthetic outcome is somewhat universal. An interesting fact is that this universality seems to be distorted for the light r-process elements, where discrepancies can be observed from the good agreement above $Z > 55$. Even more interesting is the fact that also stars exist, having a large disagreement between the light r-process and the heavy

³ The solar r-process pattern is obtained by subtracting the s-process yields (plus additional p-process corrections) of state-of-the-art s-process simulations from the total isotopic abundances measured from solar photospheric abundance determinations. These r-process abundances therefore are only as good as the precision of the s-process simulations.

⁴ Note that we use the astronomers definition of metals, meaning everything that is not hydrogen or helium is a metal.

⁵ We assumed for this argumentation that whenever we produce europium in the r-process, we will have what we defined beforehand as a full r-process.

⁶ This argumentation only includes the core-collapse supernova models that do not include magnetic fields. The inclusion of magnetic fields in core-collapse supernovae can have influence on the explosion process and the nucleosynthesis [33, 34].

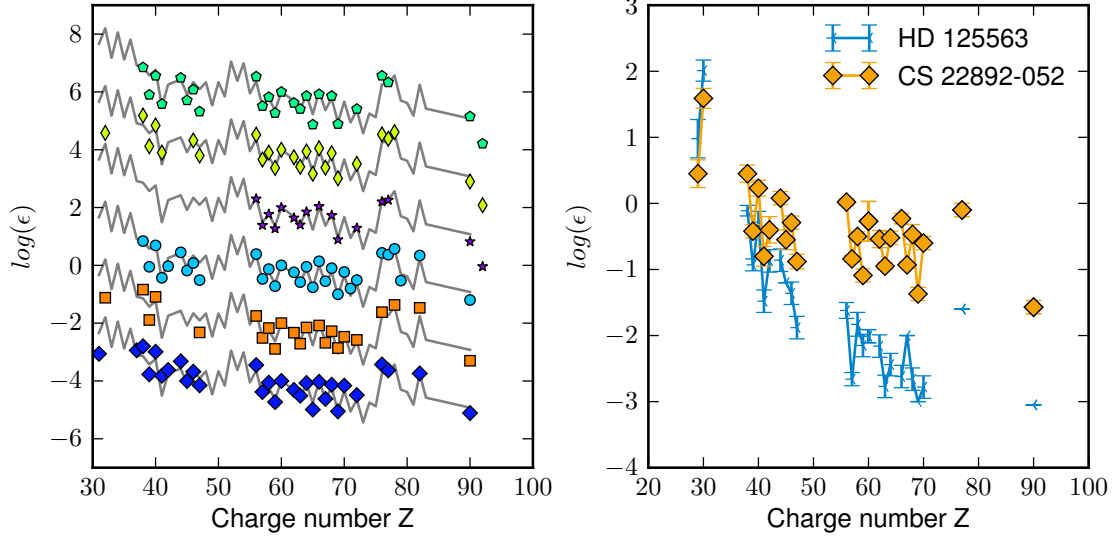


Figure 1.3.: Plotted here are the abundance pattern of the r-process rich metal-poor star CS 22892-052 and the r-process poor star HD 125563. $\log(\epsilon)$ gives the abundance relative to hydrogen. By comparing both abundance patterns, it appears as if the elements assigned to the classical r-process are produced in two different processes. HD 125563 shows a depletion of r-process nuclei with $Z > 50$, but nevertheless is enriched in the light r-process elements.

r-process nuclei such as HD 122563, which has only a small amount of heavy r-process elements. The right plot of figure 1.3 shows the two metal-poor stars CS 22892-052 and HD 122563 that have a completely different elemental pattern⁷. The authors of [35] concluded that the elements assigned to the “classical” r-process have to be produced in two different astrophysical scenarios. This assumption can be supported by observations of metal-poor stars with small abundance in heavy r-process elements such as HD 122563 [36]. It is easy to observe that the abundance pattern of this metal-poor star is completely different to the r-process rich metal-poor star CS 22892-052 [37]. This behavior can well be explained under the assumption that these light r-process elements are created by a different process [38, 1]. Whether this process is now a completely different process or a sequence of interrupted r-processes that create the nucleosynthetic outcome within this mass region is not known so far. The authors of [1, 39] suggested that these light r-process elements might be produced in a core-collapse supernova. Later nucleosynthesis studies, where the electron fraction was taken as a free parameter [40], showed that the astrophysical site can reproduce the abundance pattern of HD 122563.

The assumption of creating the light r-process nuclei in supernovae might however be validated by observations of metal-poor stars. Therefore we have to note that as an indicator for the r-process usually europium is chosen, due to the fact that it is almost exclusively produced by the r-process. By taking a large set of metal-poor star data, given in [35, 41] and references therein, we observe a behavior as shown in figure 1.4 a. With decreasing metallicity of the metal-poor stars a larger spread of the europium ratio $[\text{Eu}/\text{Fe}]$ is observable. This behavior can be explained with a chemically unmixed galaxy and individual nucleosynthesis events that will show such a natural scatter. With increasing time or decreasing metallicity ($[\text{Fe}/\text{H}]$), this spread is decreased, since the galaxy becomes more homogeneous. Since we only want to select metal-poor stars with a small yield of heavy r-process nuclei, but with a high abundance of light r-process nuclei, we require that $[\text{Eu}/\text{Sr}] < 0$. Note that this requirement is completely arbitrary. It just considers the fact that metal-poor stars of the type like HD 122563 have little heavy r-process contribution and substantial amount of light r-process contribution. By applying this additional requirement, the amount of observed metal-poor stars is reduced tremendously, as can be observed in figure 1.4 b .

If the light r-process elements are created in core-collapse supernovae, we should observe a correlation between these light r-process elements with respect to iron, since most of the iron is produced during a core-collapse supernova. We have to note further that some additional creation mechanisms of these elements in the range of $28 < Z < 50$ will bias our analysis with decreasing metallicity. The main source comes from the fact that a substantial part of the total yield of these elements are also produced within the s-process. Since the s-process is a secondary process, it requires already ashes of a dead star in its composition, the s-process cannot occur in the first generation of stars. With decreasing metallicity, the s-process contribution will increase, distorting our correlation. Another fact that has to be considered is

⁷ We adopt the standard spectroscopic notation where $\log \epsilon(A) \equiv \log_{10}(N_A/N_H) + 12$ and $[A/B] \equiv \log_{10}(N_A/N_H) - \log_{10}(N_{A\odot}/N_{H\odot})$. N_x gives the number density of element x. Number densities denoted with an additional index \odot relate to the solar system number density.

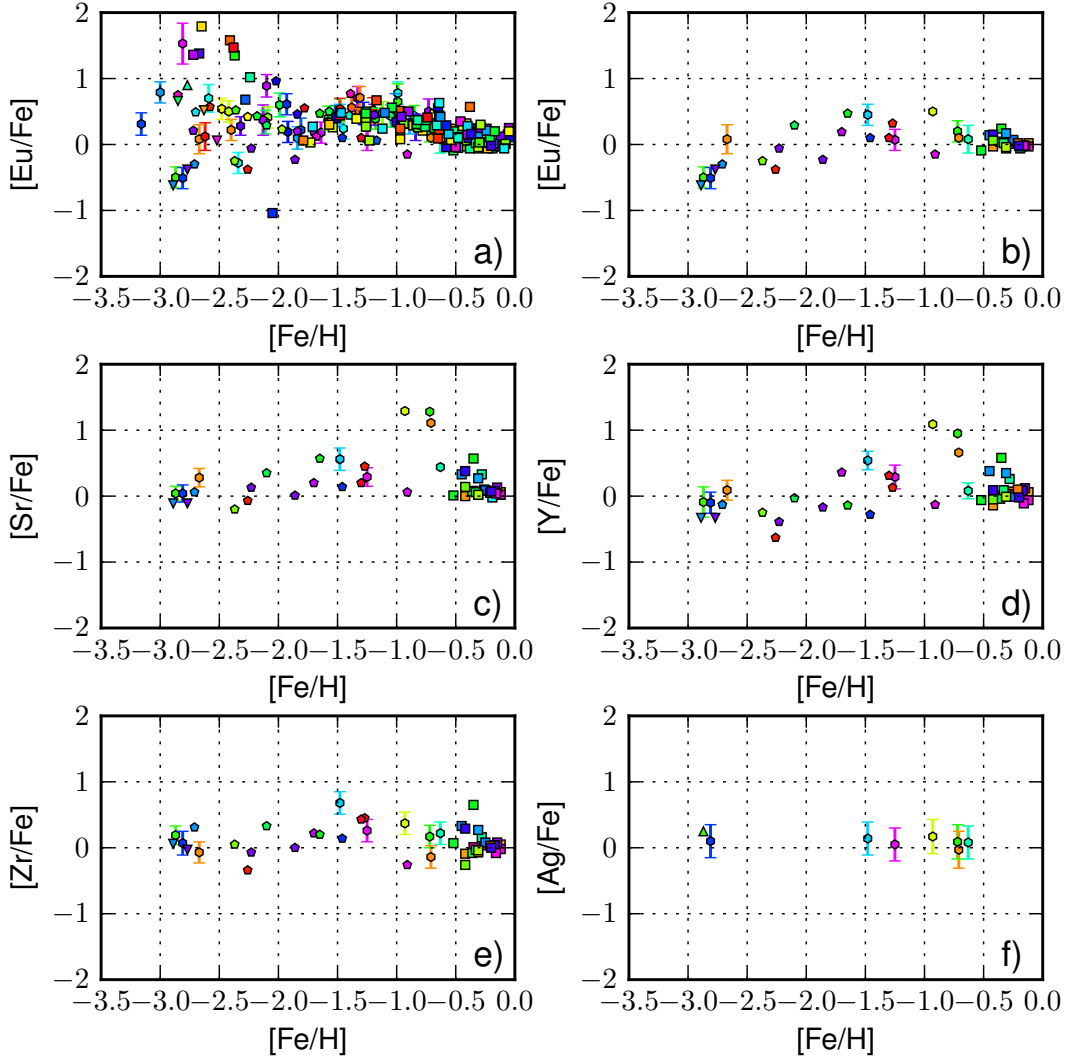


Figure 1.4.: Relative abundance ratios of observed metal-poor stars. a) $[\text{Eu}/\text{Fe}]$ plotted over metallicity $[\text{Fe}/\text{H}]$. b) Under the additional constraint that $[\text{Eu}/\text{Sr}] < 0$ we obtain a smaller subset of metal-poor stars. The $[\text{Eu}/\text{Fe}]$ relative abundances show maybe a reduced staggering, a strong correlation is however not observable. c-f) Relative abundances for the elements Sr, Y, Zr and Ag. Up to a metallicity of -1.5 a correlation can be observed, although better statistics would be desirable. The scattering of data increases with increasing metallicity. This might however arise due to the production of these light r-elements in the s-process. Therefore information on silver is required, because it is assumed that almost no silver is created in the s-process. Overall our constraint results in a very good correlation, however it might be misleading based on the very few data points that we have.

that type Ia supernovae also produce iron. These processes also require time, since first a white dwarf has to be produced. These additional processes force us to concentrate our attention on very old metal-poor stars, to keep the influences from different sources small. The results can be seen in figures 1.4 c-f for the elements Sr, Y, Zr and Ag. Observations on silver are especially important because they can give us an estimation of how far the production of elements will occur in core-collapse supernovae.

We can observe that – based on the data that we could gather – a correlation exists for the light r-process nuclei up to probably silver, although in the case of silver the data is very sparse and more data would be desirable. In the cases of Sr, Y and Zr we can observe that below a metallicity of -1.5 a linearity might be observable. Beyond $[\text{Fe}/\text{H}] = -1.5$ possible influences from s-process nucleosynthesis might be observable.

It is one goal of this thesis to explore what the nucleosynthetic outcome of current state-of-the-art supernova simulations within its neutrino-driven wind is, with a special focus on the inclusion of previously neglected neutrino reactions that can alter the nucleosynthetic outcome.

1.2 Neutrinos and nucleosynthesis

This thesis deals with the impact of neutrino interactions on the nucleosynthesis. To be more precise it is concerned with neutrino induced excitations of nuclei above the particle threshold. Within this work we calculated the neutrino scattering and capture spallation reactions up to four particle emission. Therefore we utilized a two step approach, creating the neutrino excitation cross section with the help of a *Random Phase Approximation* (RPA). The subsequent decay is determined on basis of the compound hypothesis and calculated within the statistical model. We calculated these rates for all nuclei over the whole nuclear chart.

The cross sections of neutrino interactions, for the energies reached in core collapse supernovae, are very small (several 10^{-42} cm²) and in usual astrophysical environments, such as stellar burning, the influences of neutrino interactions play only a role as a source for energy dissipation. However in some cases neutrinos can change the nucleosynthetic path. These cases can be classified by two key quantities namely the neutrino flux and the exposure time. The different astrophysical scenarios are combined within the schematic plot given in figure 1.5, where all scenarios are included in which neutrino-nucleus reactions might have an influence on the final nucleosynthetic outcome.

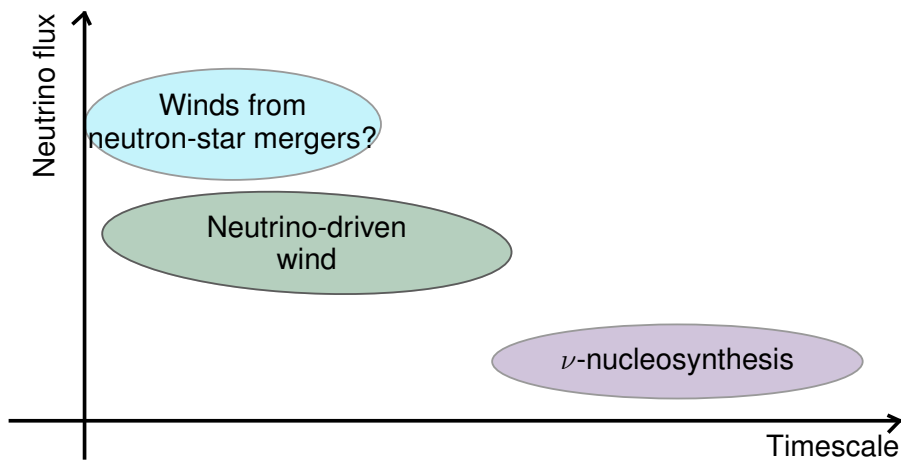


Figure 1.5.: Schematic plot of different astrophysical scenarios, in which the inclusion of neutrino-nucleus cross section will have influence on the nucleosynthesis. While for example in the neutrino-driven wind a large neutrino flux is present for only a small period of time, in the ν -process matter will be irradiated to a much smaller neutrino flux, however for a longer timescale.

With the neutrino-driven wind we are studying a scenario where matter is exposed to very high neutrino fluxes at high velocities. These high neutrino fluxes will be present for very short times only, because when matter is ejected from the PNS surface, the fluxes will decrease with r^{-2} , effectively shutting of all neutrino interactions very soon after emission from the PNS. We will study the neutrino-driven wind for the first time including a full set of neutrino-induced spallation rates calculated within this thesis. It is the first time that neutrino induced spallation rates are used up to full four-particle emission. We will study the nucleosynthetic outcome of state-of-the-art supernova models, and discuss current improvements due to newly improved microscopic nuclear input.

Matter can also be subject to smaller neutrino fluxes over a longer time. A process where this is realized is known as the ν -process. The ν -process occurs during the core-collapse and the subsequent explosion in the outer shells of the star. Neutrinos emitted from the proto-neutron star interact in this process with the matter in the outer shells, that might be created due to burning processes, s-process nucleosynthesis or might be in the initial composition of the star while its formation. The neutrino fluxes will be decreased in comparison to the neutrino-driven wind, due to the fact that matter is at larger radii. However, for ν -nucleosynthesis this reduction is compensated with the fact that the matter expansion occurs slower than from the neutrino-driven wind. Therefore neutrino induced spallation processes will change the nuclear composition. Furthermore is this process enhanced by the shock propagation through the corresponding shells, that are accompanied with an increase in temperature. Many odd-Z elements from Li to Cu are produced partly in this astrophysical scenario [2].

Both mentioned processes occur within the same astrophysical environment of a core-collapse supernova. Exactly this is the main argument why we will focus in this work on this astrophysical region. Note however that other exciting regions come in reach for a reliable study of neutrino induced effects on the nucleosynthesis within the next decade. The prime candidate for these studies will be neutrino-driven wind scenarios of neutron-star mergers. Within this scenario

the electron fraction will be low (between 0.1 and 0.2 [42]) reaching conditions extreme enough for the production of heavy elements via the r-process.

Until today, the computational requirements for neutron-star merger scenarios in full general relativity and including detailed neutrino transport models are too demanding for reliable simulations. However, first studies with post-processed multi-angle neutrino transport show important facts [42]. The first fact is that neutrino-driven winds are also formed in the neutron-star merging scenario. The second fact is that the neutrino induced mass outflow is of the order of $10^{-4} M_{\odot}$, which is comparable to the mass outflow within normal neutrino-driven winds of core collapse supernovae. The luminosities reach very high values up to 10^{53} ergs/s, with a cooling time of 1 s. Since the simulations of [42] are the first models on neutrino-driven winds in neutron-star merger scenarios and have not been confirmed by other simulations, we will concentrate on the influence of neutrino nucleus-processes within the neutrino-driven wind and ν -nucleosynthesis, keeping in mind that a new possible site for heavy element production under strong neutrino fluxes might come in reach in the near future.

Within our studies on the nucleosynthesis in various sites of the core-collapse supernova, we will explain within each of these scenarios how our newly calculated rates will influence the nucleosynthesis. Therefore we would like to examine in the next sections how the nucleosynthesis will occur within the aforementioned astrophysical scenarios, and how neutrino interactions will influence the nucleosynthesis. We would like to start with a short discussion about the neutrino-driven wind scenario where mass outflows in the order of $10^{-3} M_{\odot}$ are expected [43].

After our discussion of the neutrino-driven wind we will review briefly the underlying ideas of ν -nucleosynthesis and how we will simulate the astrophysical requirements.

1.2.1 Nucleosynthesis in neutrino-driven winds

When a successful explosion in a core-collapse supernovae occurs, the shock will on its way outwards heat matter and therefore increase nuclear reactions, resulting in explosive burning scenarios, such as explosive Si- and O/Ne burning [20]. The latter one is believed to be a possible site for the production of p-process nuclei in the mass range of $110 < A < 150$.

For the inner ejecta the rise in temperature is high enough that material will be dissociated into free protons and neutrons. Additionally this material is close enough to the PNS, that it will be subject to very strong neutrino fluxes, arising from the cooling of the PNS. Due to neutrino-induced heating, part of this material will be ejected from the PNS forming what is known as the neutrino-driven wind. Material that is ejected from the region above the PNS will then expand adiabatically.⁸ Once the temperature is low enough, protons and neutrons will recombine and start to form nuclei. The nucleosynthesis in this scenario depends strongly on outflow parameters, such as the expansion timescale, the electron fraction Y_e and the entropy. These initial values have to be given by hydrodynamical simulations with detailed neutrino transport.

As long as matter consists solely of free protons and neutrons and is close to the PNS, the weak interaction processes will dictate the evolution of the electron fraction Y_e . As the material cools due to expansion, electron and positron captures become negligible due to a strong temperature dependence. The change in the electron fraction is therefore mainly governed by neutrino reactions

$$\dot{Y}_e = \lambda_{\nu_e n} Y_n - \lambda_{\bar{\nu}_e p} Y_p, \quad (1.2)$$

where $\lambda_{\nu_e n}$ is the rate for capturing an electron neutrino on a neutron and $\lambda_{\bar{\nu}_e p}$ describes the rate for capturing an anti-neutrino on a proton. Assuming the composition stays the same and the neutrino fluxes do not change, we will obtain an equilibrium value for the electron fraction by demanding that the right hand side of the upper equation is zero. This results to the equilibrium value of

$$Y_e = \frac{\lambda_{\nu_e n}}{\lambda_{\bar{\nu}_e p} + \lambda_{\nu_e n}}, \quad (1.3)$$

where the abundances can be expressed as $Y_e = Y_p$ and $Y_n = 1 - Y_p$, since still no nuclei are present.

If the temperature continues to decrease, eventually α -particles start to form. Furthermore the electron fraction is now $Y_e = Y_p + X_{\alpha}/2$ and mass conservation tells us $Y_n + Y_p + X_{\alpha} = 1$. The change in Y_e can under these assumptions be formulated to [44]

$$\dot{Y}_e = \lambda_{\nu_e n} + (\lambda_{\bar{\nu}_e p} - \lambda_{\nu_e n}) \frac{X_{\alpha}}{2} - (\lambda_{\bar{\nu}_e p} + \lambda_{\nu_e n}) Y_e, \quad (1.4)$$

⁸ This adiabatic expansion might be interrupted due to collision with the matter ejected with the shock, forming the so called reverse shock.

where X_α is the mass fraction of α -particles, as defined in 4.9.1. For the derivation of this equation, it is assumed that neutrino reactions on ${}^4\text{He}$ are neglected. The equilibrium value for the electron fraction changes accordingly to

$$Y_e = \frac{\lambda_{\nu_e n}}{\lambda_{\bar{\nu}_e p} + \lambda_{\nu_e n}} + \frac{\lambda_{\nu_e p} - \lambda_{\nu_e n} X_\alpha}{\lambda_{\bar{\nu}_e p} + \lambda_{\nu_e n} 2}. \quad (1.5)$$

This so called *alpha-effect*[45] drives the material towards electron fractions of $Y_e \approx 0.5$, preventing the system to reach either very low ($Y_e \ll 0.5$) or very high ($Y_e > 0.5$) values for the electron fraction. In neutron rich cases this effect makes it more difficult to reach r-process conditions.

Based on the assumption that the cross section for (anti-)neutrino capture on free (protons) neutrons can be simply given by $\sigma = \sigma_0 E_e^2$, where the energy of the outgoing (positron) electron is related to the incoming neutrino simply via $E_e = (E_\nu \pm \Delta)^2$,⁹ the rates based on the (anti-)neutrino luminosities ($L_{\bar{\nu}_e}$) L_{ν_e} and average neutrino energies are then given by

$$\begin{aligned} \lambda_{\nu_e n} &= \frac{L_{\nu_e}}{4\pi r^2} \sigma_0 \left(\epsilon + 2\Delta + \frac{\Delta^2}{\langle E_{\nu_e} \rangle} \right), \\ \lambda_{\bar{\nu}_e p} &= \frac{L_{\bar{\nu}_e}}{4\pi r^2} \sigma_0 \left(\epsilon - 2\Delta + \frac{\Delta^2}{\langle E_{\bar{\nu}_e} \rangle} \right). \end{aligned} \quad (1.6)$$

ϵ is hereby defined by $\langle E_\nu^2 \rangle / \langle E_\nu \rangle$. Under the assumption that both luminosities are equal, one is able to derive that the material that is ejected from the PNS will become proton rich if $\epsilon_{\bar{\nu}_e} - \epsilon_{\nu_e} < 4\Delta$, otherwise the material will be neutron rich ($Y_e < 0.5$). This is a good approximation to estimate whether the neutrino-driven wind will be proton or neutron rich. Again we would like to point out that the detailed values for the composition and the hydrodynamical evolution in the region around the PNS, where densities are still very high and blocking plays a substantial role in shaping the neutrino spectra are best obtained by solving the hydrodynamical equations including detailed neutrino Boltzmann transport covering all necessary interaction processes. Once densities become small enough and weak interactions freeze out, the electron fraction stays almost constant.

Regardless of the exact value for the electron fraction, with ongoing expansion from the PNS of the material the temperature will continue to drop. As said above, α -particles will be the first nuclei that will form. From this point on, the nucleosynthesis is very sensitive to the exact value of the electron fraction. As temperature keeps decreasing ${}^{12}\text{C}$ will be created by three-body reactions. Additional captures of α -particles on ${}^{12}\text{C}$ will lead to elements up to ${}^{56}\text{Ni}$. The exact amount of elements produced above helium is strongly dependent on the expansion timescale and the entropy of the ejecta. Due to its strong density dependence of three body reactions, the formation of ${}^{12}\text{C}$ freezes out very soon, furthermore higher entropies implicate a higher photon density leading to a larger photodissociation rate, reducing the ${}^{12}\text{C}$ formation. With the usual expansion timescales of a few milliseconds, α -particles are still available in a substantial amount when three body reactions freeze out, leading to a so called *α -rich freeze-out*. If remaining free protons or neutrons are available, the created nuclei above helium act as seed for the formation of heavier elements, via continuous particle captures.

Parametric studies showed that in the case of r-process nucleosynthesis the neutron-to-seed ratio $n/seed$ scales with s^3/τ , where the entropy s is given in k_B /baryon and τ is the expansion timescale [46] in milliseconds. The argumentation for this scaling is the same as given above, with increasing entropy photodissociation will destroy seed nuclei and shorter expansion timescales reduce the efficiency of the ${}^{12}\text{C}$ formation. To obtain a full r-process, the dynamical timescale has to be of the order of a few milliseconds, the entropy is required to be above 150 k_B /baryon and the electron fraction has to be below 0.5. Up to today it appears that the required entropies are difficult to obtain in current core-collapse supernova models. Furthermore the question arises how well known the neutrino spectra are, because they will determine the value of the electron fraction. The dependence of the electron fraction within the neutrino-driven wind is schematically shown in figure 1.6.

Note that within the neutrino-driven wind, neutrino-nucleus interactions were not considered so far. Within this thesis we will be able to study the influence of neutrino-nucleus spallation processes in the nucleosynthesis of the neutrino-driven wind.

In the next section we would like to focus on proton rich ejecta in the neutrino-driven wind, in which the νp -process occurs. However we want to stress once more, that the spallation rates obtained within this thesis will be applicable to all nuclei that are subject to a substantial neutrino flux. With a different value of the electron fraction, the reaction path might be changing and different elements will be produced, however, the nuclei in the neutrino-driven wind will also interact with the neutrinos coming from the PNS.

⁹ Here Δ is the mass difference between neutrons and protons, σ_0 is given by $2.569 \times 10^{-44} \text{ cm}^2$.

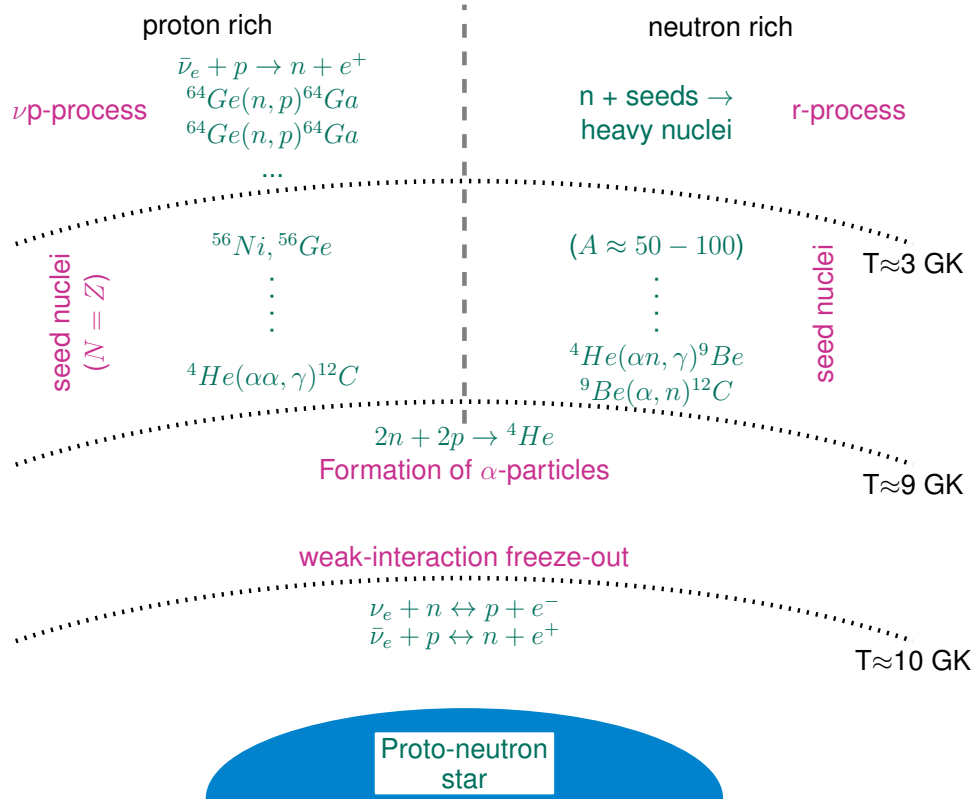


Figure 1.6.: Different nucleosynthesis processes that can occur within the neutrino-driven wind. The figure shows the dominant reactions while the matter is expanding from the PNS. Rather than showing radii, which will be model dependent, the different reactions are mentioned when they are relevant for the shown temperature. The left side shows the plausible scenario in the case of proton rich ejecta, accordingly the right hand side represents the case of very neutron rich ejecta.

The νp -process

The neutrino-driven wind is a scenario in which only primary processes can occur, because all heavy seed nuclei that might have been created due to stellar burning processes will be destroyed due to the extreme conditions in the wind. Currently ejecta in the neutrino-driven wind have entropies ranging between $10 - 80 k_B$ per baryon, short expansion timescales and Y_e values above 0.5 over the whole period of deleptonization up to in extreme cases 0.63 [11].¹⁰ On its expansion outwards, free protons and neutrons will assemble first to α -particles and then to ^{12}C . Since matter is proton rich, all free neutrons from the proto-neutron star surface will be used up for the production of α -particles, leaving only free protons behind. Once ^{12}C is formed, it acts as seed nucleus for the formation of heavier elements. This can be achieved by a sequence of (p, γ) , (α, γ) and (α, p) reactions that will drive matter mainly into $N = Z$ nuclei up to ^{64}Ge . It is noteworthy to mention that proton-rich ejecta in the neutrino-driven wind are believed to be a source of the production of elements such as ^{45}Sc , ^{49}Ti and ^{64}Zn [47].

Without taking into account the influence of neutrino interactions on protons and neutrons, the creation of elements heavier than $A > 64$ is effectively hindered. The reason for this occurrence is that captures on ^{64}Ge lead to ^{65}As in the case of proton captures, and ^{68}Se for α capture reactions. Both created nuclei are unstable against particle-decay and will emit the incoming particle almost instantaneously, making the possibility for a particle capture on these compound nucleus very unlikely. Furthermore for these reactions to occur, the Coulomb potential has to be overcome. Especially the

¹⁰ As we will discuss later during this thesis, this statement has changed due to an improved microphysics treatment in the PNS. With these improvements it can occur that initial material can be slightly neutron rich. However later ejecta will still become proton rich.

α -channel is very small, due to the fact that the Coulomb barrier is twice as large than if the projectile would be a proton. The only possibility to overcome ${}^{64}\text{Ge}$ is therefore β^+ -decay, that has a half-life of 64 s, which is very long compared to the usual expansion timescales. Therefore most material will be stuck at ${}^{64}\text{Ge}$.

With the inclusion of neutrino interactions on free protons and neutrons, bottleneck reactions as on ${}^{64}\text{Ge}$ can be overcome, simply due to the fact that anti-neutrino captures on free protons will convert free protons into free neutrons. These free neutrons do not feel the Coulomb repulsion and are therefore easily captured by heavy nuclei, such as ${}^{64}\text{Ge}$. The capture process will mimic a β -decay by a (n, p) reaction¹¹, allowing matter to reach higher values of A on the proton rich side by subsequent (p, γ) reactions. This is how the νp -process operates that produces neutron-deficient nuclei above ${}^{64}\text{Ge}$ [48]. Within their paper the authors of [48] argue that all core-collapse supernovae will eject material created with this new nucleosynthesis process in the neutrino-driven wind phase due to the fact that matter will be subject to strong neutrino fluxes as long as the composition is proton rich. The detailed evolution of the material produced within this new process is very sensitive to parameters of the astrophysical environment. Key aspects are for example the initial electron fraction, neutrino luminosities, average energies, and of course also the temperature and radius and how they evolve with time [43]. It turned out that an efficient νp -process can be obtained if the electron fraction is very large, because then the amount of free protons is still high after α -rich freeze-out so that the creation of free neutrons can work efficient. It seems furthermore logical that by the increase of the neutrino luminosity the νp -process will work more efficiently. An example for the effect on the nucleosynthetic outcome of the νp -process can be found in figure 1.7. Depending on the effectivity of the νp -process, this scenario can serve as a possible production site of the light p-process nuclei such as Sr, Mo and Y that are hard to reproduce within the classical p-process picture of photodissociation within explosive O/Ne burning.

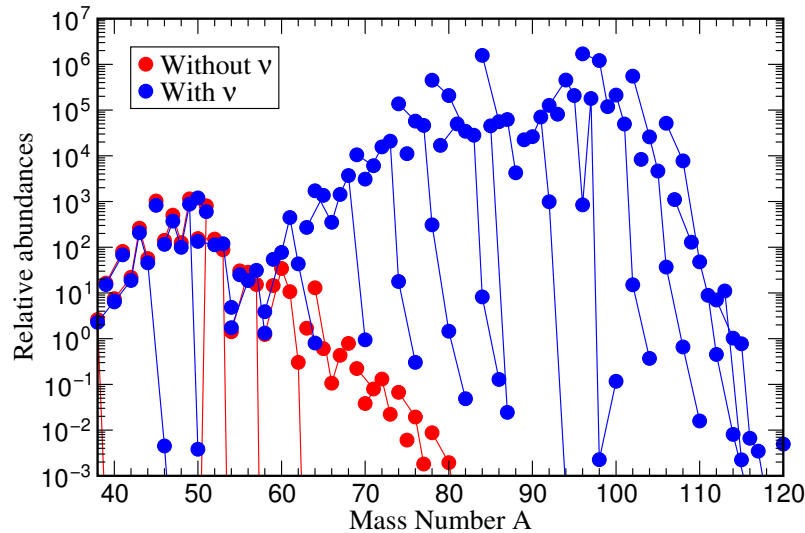


Figure 1.7.: Relative abundances (mass fraction of a given isotope normalized to the solar mass fraction of the element) for the same astrophysical trajectory. The red dots show the results of a nucleosynthesis study without taking into account the interactions on free protons and neutrons. It can be observed that very little matter is produced above $A = 64$ due to the reasons mentioned in the text. The blue dots on the other hand show the relative abundance for the same trajectory with the inclusion of (anti-)neutrino captures on (protons) neutrons. One is able to observe a huge increase due to the fact that bottle-neck reactions are overcome by charged-current neutrino interactions.

1.2.2 Neutrino-nucleosynthesis

During a core-collapse supernova a vast amount of neutrinos is emitted from the formation and cooling of the neutron star. The luminosities are so high that the neutrino fluxes are still substantial in the outer shells, leading to neutrino-nucleus scattering reactions with the evaporation of light particles such as protons, neutrons and α -particles. The dominant contribution to these neutrino scattering evaporation reactions is covered by μ and τ flavor neutrinos, due to their higher average energies [2]. This also tells us that the ν -process is very sensitive to the average neutrino energies, making the ν -process more effective with increasing neutrino average energies.

¹¹ Due to the very low proton separation energies, the created nucleus is in most cases above the proton emission threshold and will dominantly emit a proton instead of emitting a γ -particle.

The nucleosynthesis is furthermore increased due to the passage of the shock through the various shells under consideration, resulting to a speedup of temperature leading to an increase of nuclear burning processes. Matter will then be expanded outwards by the shock-wave, resulting in a drop in temperature and density. The radial expansion will also decrease the neutrino fluxes.

From the nucleosynthesis point of view the ν -nucleosynthesis scenario is strongly dependent on the initial composition, since matter will not be dissociated and recombined again while the expansion process. The temperatures furthermore will be in most cases too small to reach nuclear statistical equilibrium, forcing us to use the initial composition as it is given by stellar evolution models. Therefore our nucleosynthesis will be sensitive to the initial composition, especially the metallicity. The main nucleosynthetic outcome will be the production of ${}^7\text{Li}$, ${}^{11}\text{B}$ and ${}^{19}\text{F}$ that are almost exclusively produced in ν -nucleosynthesis events [20]. Further a contribution of the production of odd-Z nuclei up to copper is also observable.



Part II.

Theory



2 Nuclear theory

In this chapter we will give the basic formalism that has been used to determine the nuclear neutrino spallation rates. Therefore we would like to discuss how the neutrino-nucleus capture and scattering cross sections are obtained. Since neutrino-nucleus interactions are weak interaction processes, they can be well described by the Glashow-Salam-Weinberg theory [49]. Due to the rather low energies in these semileptonic processes, we can simplify this theory to a current-current interaction. We will first describe this current-current interaction. In a second step we define how we will calculate cross sections between two nuclear levels with definite angular momentum and parity for neutral-current neutrino scattering as well as for charged-current capture processes.

In the following step we will show how the nuclear excitation states are obtained with the help of the phenomenological Random Phase Approximation that is able to give a fast and reliable description of the nuclear excitation spectra over the whole nuclear chart.

Furthermore we will discuss the description of the decay from the former excited states. We will do this in a two-fold way. For low excitation energies we apply a statistical model that includes the excited states explicitly. If the excitation energies are above the two particle emission threshold, a Monte-Carlo ablation model is utilized, based in the Weisskopf-Ewing picture [50], that allows for multi-particle spallation.

We now want to start with a short introduction of semileptonic weak interactions.

2.1 Weak interactions

Contrary to the strong interaction, the weak interaction operates between all elementary particles (electrons, neutrinos, quarks). Within the standard model it is well described by the Glashow-Salam-Weinberg theory that unifies the electromagnetic and weak interaction [49]. The standard model describes the weak interaction by the exchange of W^\pm and Z^0 bosons between the up and down quark isodoublet, when one only considers the case of weak interactions on nuclei. The masses of these exchange bosons are in the order of 80 – 90 GeV.

Weak interaction processes in stars can be classified as pure leptonic, such as muon decay, and as semileptonic processes that describe all interactions of leptons with hadrons. The latter case is the one that we are interested in within this thesis. Since for our applications the momenta of the particles involved in this case are much smaller than the rest masses of the W^\pm and Z^0 bosons, we are able to treat these processes as an effective current-current interaction of the $V - A$ type. The $V - A$ structure of the interaction is borne out of experiment [51]. This effective current-current interaction is then only a point-like interaction. Due to this effective treatment, the coupling constants may be different from the ones that have been obtained at the quark level and might furthermore be dependent on the momentum transfer. The interaction can be described by the current-current Hamiltonian

$$\mathcal{H}_{int} = \frac{G}{\sqrt{2}} \int d\vec{x} \mathcal{J}^\mu(\vec{x}) \hat{j}_\mu(\vec{x}), \quad (2.1)$$

where the leptonic current $\hat{j}_\mu(\vec{x})$ and the hadronic current $\mathcal{J}^\mu(\vec{x})$ are left to define. The coupling constant is given for charged-current processes by $G = G_F \cdot V_{ud}$ and for neutral-current processes by $G = G_F$, where G_F denotes the Fermi coupling constant and V_{ud} gives the up-down component of the Cabbibo-Kobayashi-Makasawa matrix [52].

Let us now discuss the structure of the leptonic current very briefly, because it can be obtained from the standard electroweak model. The leptonic current for the charged-current case takes the form

$$\hat{j}_{CC}^\mu(\vec{x}) = \bar{\Psi}_l \gamma^\mu (1 - \gamma_5) \tau_\pm \Psi_l. \quad (2.2)$$

Hereby the leptonic currents appearing in this current are defined by the doublet

$$\Psi_l = \begin{pmatrix} \psi_e(\vec{x}) \\ \psi_{\nu_e}(\vec{x}) \end{pmatrix}, \quad (2.3)$$

for all three leptonic flavors known so far (e, μ, τ). Furthermore we included the isospin lowering and raising operator $\tau_\pm = \frac{1}{2}(\tau_1 \pm i\tau_2)$. In the case of neutral-current interactions the leptonic current is given by

$$\hat{j}_{NC}^\mu(\vec{x}) = \bar{\Psi}_l \gamma^\mu (1 - \gamma_5) \frac{1}{2} \tau_3 \Psi_l + 2 \sin^2 \theta_W \bar{\Psi}_l \gamma^\mu \frac{1}{2} (1 + \tau_3) \Psi_l, \quad (2.4)$$

where the last term is the electromagnetic interaction. Depending on the type of reaction that we want to model, we will use one of the leptonic currents stated above. For the description of semileptonic processes, we can now turn towards the more complicated hadronic current, since nucleons by itself have substructure and internal degrees of freedom. It is convenient to describe protons and neutrons as different projections of the same particle which is called nucleon. To differentiate between the two possible states of the nucleon, we add another quantum number that obeys SU(2) symmetry just like the spin of fermions. In analogy to this formulation, we call this quantum number *isospin*. Thus protons and neutrons are simply nucleons with different projections of the isospin state $T = 1/2$. One usually defines protons with an isospin projection $m_T = +1/2$ and neutrons have $m_T = -1/2$. The hadronic part can then be written in direct analogy to 2.3 as the isodoublet

$$\psi_H = \begin{pmatrix} \psi_p(\vec{x}) \\ \psi_n(\vec{x}) \end{pmatrix}. \quad (2.5)$$

Since the nucleons within the nucleus will also interact via the strong interaction additionally to the weak interactions, we will compose the hadronic current starting from basic arguments of Lorentz covariance and isospin invariance. The effective hadronic current can be decomposed into isoscalar and isovector components, both will contain vector and axial-vector components. In light of those statements, we can look at the decomposed currents in isospin space and discuss their influences in various processes that can be described in semileptonic current-current theory. For each isovector state and its m_T -projection we can write the current in the form of

$$[\mathcal{J}]_{T,m_T}^\mu = \left[\beta_V^{(T)} \mathcal{J}_V^\mu + \beta_A^{(T)} \mathcal{J}_A^\mu \right]_{T,m_T}. \quad (2.6)$$

The vector (axial-vector) part is denoted by \mathcal{J}_V^μ (\mathcal{J}_A^μ). The total hadronic current will always consist of the sum over all allowed isovector states and m -projections. The factors in front of the currents are not depending on the m -projection, which is also called *isovector triplet hypothesis* [53].

With the above framework we are now already able to conclude that for example electron scattering via the exchange of a photon only has contributions that do not change charge. Furthermore we know from quantum electrodynamics that the current has only vectorial contributions. Thus

$$\mathcal{J}_{e.m.}^\mu = \left[\mathcal{J}_V^\mu \right]_{0,0} + \left[\mathcal{J}_V^\mu \right]_{1,0}. \quad (2.7)$$

For reactions that will change the charge of the nucleus, such as the capture of a (anti-)neutrino, we will have vectorial and axial-vectorial parts while changing the isospin

$$\mathcal{J}_{CC}^\mu = \left[\mathcal{J}_A^\mu \right]_{1,m_T} + \left[\mathcal{J}_V^\mu \right]_{1,m_T} \quad m_T = \pm 1. \quad (2.8)$$

Note that we applied within our work the *conserved-vector current* (CVC) hypothesis [54]. CVC states that the isovector part of the electromagnetic current can be identified as part of the isovector component in the charge changing process. The hadronic current, which is however most relevant for our work, is the hadronic neutral-current. Obviously these processes will not have a charge changing character. Thus the general description has to be

$$\mathcal{J}_{NC}^\mu = -2 \sin^2 \theta_W \left[\mathcal{J}_V^\mu \right]_{0,0} + (1 - 2 \sin^2 \theta_W) \left[\mathcal{J}_V^\mu \right]_{1,0} + \left[\mathcal{J}_A^\mu \right]_{1,0}. \quad (2.9)$$

In equations 2.7, 2.8 and 2.9 we already applied the coupling constants $\beta_V^{(T)}, \beta_A^{(T)}$ as they are given by the standard model [53].

The nuclear transitions that will be induced by these weak current operators involve initial and final states with definite eigenstates of angular momentum, parity and isospin. We define the lepton four-momentum transfer by $q^\mu = p_{\text{final}}^\mu - p_{\text{initial}}^\mu = (q_0, \vec{q})$. This allows us to do a multipole expansion of the leptonic current operators. We obtain

$$\hat{\mathcal{M}}_{J,m_J} \equiv \hat{M}_{J,m_J}^V + \hat{M}_{J,m_J}^A = \int d\vec{x} j_J(q\vec{x}) Y_J^{m_J} \hat{\mathcal{J}}_0(\vec{x}) \quad J \geq 0, \quad (2.10a)$$

$$\hat{\mathcal{L}}_{J,m_J} \equiv \hat{L}_{J,m_J}^V + \hat{L}_{J,m_J}^A = \frac{i}{q} \int d\vec{x} \vec{\nabla} [j_J(q\vec{x}) Y_J^{m_J}(\Omega_x)] \cdot \hat{\mathcal{J}}(\vec{x}) \quad J \geq 0, \quad (2.10b)$$

$$\hat{\mathcal{T}}_{J,m_J}^{el} \equiv \hat{T}_{J,m_J}^{V,el} + \hat{T}_{J,m_J}^{A,el} = \frac{i}{q} \int d\vec{x} (\vec{\nabla} \times (j_{\mathcal{J}}(q\vec{x}) \mathcal{Y}_{J,J,1}^{m_J})) \cdot \hat{\mathcal{J}}(\vec{x}) \quad J \geq 1, \quad (2.10c)$$

$$\hat{\mathcal{T}}_{J,m_J}^{mag} \equiv \hat{T}_{J,m_J}^{V,mag} + \hat{T}_{J,m_J}^{A,mag} = \int d\vec{x} j_{\mathcal{J}}(q\vec{x}) \mathcal{Y}_{J,J,1}^{m_J} \cdot \hat{\mathcal{J}}(\vec{x}) \quad J \geq 1, \quad (2.10d)$$

with $\mathcal{J}^\mu = (\mathcal{J}_0, \vec{\mathcal{J}})$. These irreducible tensors are called in the order given above Coulomb, longitudinal, transverse electric, and transverse magnetic multipole projections. Each multipole operator has contributions of both parities, since the weak hadronic current has both vector and axial-vector contributions. The multipoles $\hat{M}^V, \hat{L}^V \hat{T}^{V,el}, \hat{T}^{A,mag}$ all have parity $(-1)^J$, the others have opposite parity. The multipole expansion preserves good angular momentum and the integrals are projections on partial waves of the hadronic current.

As mentioned in appendix (4.10.1), in the upper equations we require the vector spherical harmonics that are defined by

$$\mathcal{Y}_{J,l,1}^{m_J} = \sum_{\mu\lambda} \langle l, 1, J | \mu\lambda m_J \rangle Y_J^\mu \vec{e}_\lambda, \quad (2.11)$$

with Y_J^μ being the usual spherical harmonics with angular momentum l and projection μ . The unit vector given above is defined with the complete orthogonal set of spherical basis vectors as

$$\vec{e}_0 = \vec{q}/q, \quad \text{and} \quad \vec{e}_{\pm 1} = \mp \frac{1}{\sqrt{2}} (\vec{e}_x \pm \vec{e}_y). \quad (2.12)$$

Due to CVC we are able to rewrite one vector multipole by another. Conventionally one choses

$$\hat{L}_{J,m_J}^V(q) = -\frac{\omega}{q} \hat{M}_{J,m_J}^V. \quad (2.13)$$

Before we can move on and describe how the semileptonic cross sections will be calculated, we first have to settle how we describe the nuclear current in our nuclear model. The multipole operators defined within equation 2.10 are in general A-body nuclear operators. However, since we are interested in low energy scales for the nuclear system, these weak interactions will perturb the nuclear system only slightly, so that it is a good approximation to assume only one-body components, since they will be the dominant one to the transitions we are interested in. We follow the arguments of [53, 55] and assume that the nuclear current density in the origin can be simply formulated in second quantization as

$$\hat{J}^\mu(0) = \sum_{\alpha,\alpha'} \langle \alpha' | \mathcal{J}^\mu | \alpha \rangle a_{\alpha'}^\dagger a_\alpha, \quad (2.14)$$

where the $|\alpha\rangle$ and $|\alpha'\rangle$ are assumed to be a complete set of single-particle states. As stated by the authors of [55], by choice of an one-body density we effectively neglect two-body meson exchange currents and other many body effects. For an inclusion of two body operators within the nuclear current the reader is referred e.g. to [56].

We furthermore make use of what is known as *impulse approximation*, where the nucleon that is undergoing the weak interaction can be treated as a free nucleon satisfying the Dirac equation. We should expect that modifications occur due to their confinement in a specific region. However following the arguments of [55] the modifications due to this simplification should be generally small and therefore negligible. The reason for that is that the total mass of the nucleus is considerably larger than the binding of the nucleons to the nucleus.

For a single free nucleon we are thus able, by utilizing Lorentz covariance, conservation of parity, invariance under time-reversal and isospin invariance, to formulate the vector and axial-vector parts of the hadronic current as

$$\langle \vec{k}', \lambda', 1/2, m_{\tau'} | [\mathcal{J}_V^\mu]_{T,m_T} | \vec{k}, \lambda, 1/2, m_\tau \rangle = \bar{u}(\vec{k}', \lambda') \left[F_1^{(T)} \gamma^\mu + F_2^{(T)} \frac{i}{2M} \sigma^{\mu\nu} q_\nu + F_3^{(T)} q^\mu \right] u(\vec{k}, \lambda) \langle 1/2 m_{\tau'} | \mathcal{J}_T^{m_T} | 1/2 m_\tau \rangle, \quad (2.15a)$$

$$\langle \vec{k}', \lambda', 1/2, m_{\tau'} | [\mathcal{J}_A^\mu]_{T,m_T} | \vec{k}, \lambda, 1/2, m_\tau \rangle = \bar{u}(\vec{k}', \lambda') \left[F_A^{(T)} \gamma^\mu \gamma_5 + F_T^{(T)} \frac{i}{2M} \sigma^{\mu\nu} q_\nu \gamma_5 + F_P^{(T)} q^\nu \gamma_5 \right] u(\vec{k}, \lambda) \langle 1/2 m_{\tau'} | \mathcal{J}_T^{m_T} | 1/2 m_\tau \rangle. \quad (2.15b)$$

The plane wave single-nucleon states are labeled with the three momentum \vec{k} (\vec{k}'), helicity λ (λ') isospin of 1/2 and m -projection value of the isospin m_τ ($m_{\tau'}$).

One is able to observe that the isospin dependence of the nuclear current, both for the vector and the axial-vector, is completely settled by the factor

$$\mathcal{J}_T^{m_T} = \frac{1}{2} \times \begin{cases} 1 & T=0 \quad m_T=0 \\ \tau_0 = \tau_3 & T=1 \quad m_T=0 \\ \tau_{\pm 1} = \mp \frac{1}{\sqrt{2}} (\tau_1 \pm \tau_2) & T=1 \quad m_T = \pm 1. \end{cases} \quad (2.16)$$

The factors in equation 2.15 labeled $F_i^{(T)}$ are the so called *single nucleon form factors*. They all are functions of the four-momentum transfer q_μ^2 . We assume within this work that there are no second class currents available, which results to the fact that $F_s^{(T)}$. This statement bases on the work of [57] and follows from the requirement that the hadronic current obeys the same properties under transformation of \mathcal{P} , \mathcal{C} and \mathcal{T}^1 as the strong interaction. The form factors $F_1^{(T)}$ and $F_2^{(T)}$ can directly be obtained from electron-scattering experiments. The form factors have the following values:

$$F_{1,2}^{(T)}(q_\mu^2) = F_{1,2}^{(T)}(0)/(1 + (q_\mu^2/M_{V,A})^2) \quad (2.17)$$

with

$$F_1^{(0,1)}(q_\mu^2) = 1 \quad \text{and} \quad F_1^{(T)}(q_\mu^2) + 2M_N F_2^2(q_\mu^2) = \mu^{(T)}(q_\mu^2). \quad (2.18)$$

$\mu^0(0) = (\mu^p(0) - 1) + \mu^n(0) = -0.1202$ and $\mu^1(0) = 3.706$ are the single nucleon isoscalar and isovector magnetic moments. The axial-vector form factor at zero momentum transfer is determined via the neutron decay to $F_A^{1,2}(0) = -1.2701$. The form factor F_p^1 is called *induced pseudo scalar coupling*.

Under the assumption, that the strong force between nucleons can be described with the mediation of pions [55], and by applying the famous Goldberger-Treiman relation [58, 59] as well as pion-pole dominance, we can determine F_p^1 as

$$F_p^1(q_\mu^2) = \frac{2M_N F_A^1(0)}{(q_\mu^2 + m_\pi^2)}. \quad (2.19)$$

According to [53, 55] the induced pseudo scalar term cannot enter for neutrinos and ultra relativistic leptons. For all form factors given in equation 2.15, we assume the *dipole approximation*, stating that the momentum transfer dependence is given as

$$F_i^{(T)}(q_\mu^2) = F_i^{(T)}(0) \left(\frac{1}{1 + \left(\frac{q_\mu^2}{M_{V,A}^2} \right)} \right)^2, \text{ where} \quad \begin{array}{l} M_V = 843 \text{ MeV} \\ M_A = 1032 \text{ MeV,} \end{array} \quad (2.20)$$

for all form factors except the induced pseudo-scalar. The four-momentum transfer is hereby given simply by $q_\mu^2 = \omega^2 - q^2$.

The matrix elements of the multipole operators between nuclear many-body states labeled as $|J_i, m_{J_i}; T_i, M_{T_i}\rangle$, can be complicated configurations of protons and neutrons. By applying the Wigner-Eckart theorem on angular momentum, we are able to reduce the matrix element of an arbitrary multipole operator $\mathcal{X}_{J,m_J;T,M_T}^{\hat{}}$ as

$$\langle J_1, m_{J_1}; T_1, M_{T_1} | \mathcal{X}_{J,m_J;T,M_T}^{\hat{}} | J_2, m_{J_2}; T_2, M_{T_2} \rangle = (-1)^{J_1 - M_{J_1}} \begin{pmatrix} J_1 & J & J_2 \\ -M_{J_1} & M_J & M_{J_2} \end{pmatrix} (-1)^{T_1 - M_{T_1}} \begin{pmatrix} T_1 & T & T_2 \\ -M_{T_1} & M_T & M_{T_2} \end{pmatrix} \langle J_1; T_1 || \mathcal{X}_{J;T}^{\hat{}} || J_2; T_2 \rangle, \quad (2.21)$$

where we followed the description of Edmonds [60]. The reduced matrix elements can be recognized due to the double bars (||) and tells us that this matrix element is reduced in angular momentum and isospin. Since we decided on formulating the multipole operators as one-body operators we are able to write

$$\langle J_1; T_1 || \mathcal{X}_{J;T}^{\hat{}} || J_2; T_2 \rangle = \sum_{\alpha\alpha'} \frac{\langle J_1; T_1 || [a_\alpha^\dagger \otimes \tilde{a}_\alpha]_{J,T} || J_2; T_2 \rangle}{\sqrt{(2J+1)(2T+1)}} \times \langle \alpha' || T_{J,T}(q) || \alpha \rangle, \quad (2.22)$$

where the sum runs over a complete set of single-particle wavefunctions $\alpha = \{n, l, j\}$. The tensor product involves single-particle creation operators. The creation and destruction operators are given by $a_\alpha^\dagger = a_{\alpha, m_{j_\alpha}, m_{t_\alpha}}^\dagger$ and $\tilde{a}_{\alpha, m_{j_\alpha}, m_{t_\alpha}} = (-1)^{j - m_{j_\alpha}} (-1)^{1/2 - m_{t_\alpha}} a_{\alpha, -m_{j_\alpha}, -m_{t_\alpha}}$. The phase space is chosen such that the operator transforms as a spherical tensor [60].

For our purposes we assume that the motion of the nucleus can be treated non-relativistically, which will be a reasonable assumption for the energies we are considering. That fact however allows us to do a non-relativistic reduction of the

¹ Here \mathcal{P} , \mathcal{C} and \mathcal{T} denote transformations under parity, charge and time reversal.

single-nucleon amplitudes up to the order of one inverse nucleon mass. In doing that one obtains the following nuclear density operators

$$\begin{aligned}
\hat{\rho}_V^i(\vec{x}) &= F_1^{(i)} \sum_{j=1}^A \tau_i(j) \delta(\vec{x} - \vec{x}_j) \\
\hat{J}_V^i(\vec{x}) &= \frac{F_1^{(i)}}{2iM} \sum_{j=1}^A \tau_i(j)^i \left[\delta(\vec{x} - \vec{x}_j) \vec{\nabla}_j - \vec{\nabla}_j \delta(\vec{x} - \vec{x}_j) \right] + \frac{F_1^{(i)} + 2MF_2^{(i)}}{2M} \vec{\nabla}_j \times \left(\sum_{j=1}^A \tau_i(j) \vec{\sigma} \left[\delta(\vec{x} - \vec{x}_j) \vec{\nabla}_j - \vec{\nabla}_j \delta(\vec{x} - \vec{x}_j) \right] \right) \\
\hat{J}_A^i(\vec{x}) &= F_A^{(i)} \sum_{j=1}^A \tau_i(j) \vec{\sigma}(j) \delta(\vec{x} - \vec{x}_j) \\
\hat{\rho}_A^i(\vec{x}) &= \frac{F_A^{(i)}}{2Mi} \sum_{j=1}^A \tau_i(j) \vec{\sigma}(j) \cdot \left[\delta(\vec{x} - \vec{x}_j) \vec{\nabla}_j - \vec{\nabla}_j \delta(\vec{x} - \vec{x}_j) \right] + \frac{m_{lep} F_P^{(i)}(j)}{2M} \vec{\nabla}_j \cdot \sum_{j=1}^A \tau_i(j) \vec{\sigma}(j) \delta(\vec{x} - \vec{x}_j).
\end{aligned} \tag{2.23}$$

Again V denotes the vectorial and A the axial-vectorial current, i gives the direction of the reaction in isospin space. M is the mass of the nucleon, m_{lep} is the mass of the absorbed/produced lepton for charged-current capture processes. In the extreme relativistic limit ($\beta = v/c \rightarrow 1$) this term only plays a role in reactions as muon capture and is consequently not relevant for us. The axial-vector coupling constant is denoted as F_A and the pseudo scalar is named F_P .

2.2 Nuclear reactions

In this section we would like to present how we can obtain – from the information we gained in the last section – the cross sections of each process relevant for the rates that we would like to calculate. The interaction matrix element, summed and averaged over initial and final nuclear angular momentum projections can be given as [61]

$$\begin{aligned}
& \frac{1}{2J_i + 1} \sum_{M_i} \sum_{M_f} |\langle f | \hat{\mathcal{H}}_{int} | i \rangle|^2 = \frac{G^2}{2} \frac{4\pi}{2J_i + 1} \\
& \times \left\{ \sum_{J=0} \left\{ (1 + \vec{e}_v \cdot \vec{\beta}) |\langle J_f || \hat{\mathcal{M}}_{J,T} || J_i \rangle|^2 + [1 - \vec{e}_v \cdot \vec{\beta} + 2(\vec{e}_v \cdot \vec{e}_q)(\vec{e}_q \cdot \vec{\beta})] |\langle J_f || \hat{\mathcal{L}}_{J,T} || J_i \rangle|^2 \right. \right. \\
& \left. \left. - 2 [\vec{e}_q \cdot (\vec{e}_v + \vec{\beta})] \text{Re} \langle J_f || \hat{\mathcal{L}}_{J,T} || j_i, T_i \rangle \langle J_f || \hat{\mathcal{M}}_{J,T} || j_i, T_i \rangle^* \right\} \right. \\
& \left. + \sum_{J=1}^{\infty} \left\{ [1 - (\vec{e}_v \cdot \vec{e}_q)(\vec{e}_q \cdot \vec{\beta})] [|\langle J_f || \hat{\mathcal{T}}_{J,T}^{el} || J_i \rangle|^2 + |\langle J_f || \hat{\mathcal{T}}_{J,T}^{mag} || J_i \rangle|^2] \right. \right. \\
& \left. \left. - 2 \cdot S \cdot [\vec{e}_q \cdot (\vec{e}_v - \vec{\beta})] \text{Re} \langle J_f || \hat{\mathcal{T}}_{J,T}^{el} || j_i, T_i \rangle \langle J_f || \hat{\mathcal{T}}_{J,T}^{mag} || j_i \rangle^* \right\} \right\}.
\end{aligned} \tag{2.24}$$

These matrix elements are universal, they can be applied for neutral- and charged-current neutrino captures as well as charged lepton capture. The initial total angular momentum projection is given as J_i , whereas the final value is J_f . \vec{q} is the three-vector momentum transfer ($\vec{q} = \vec{k} - \vec{v}$). Within this section we denote the initial momentum as \vec{v} and the final momentum as \vec{k} , regardless if the outgoing lepton is a neutrino or a lepton with mass. ϵ is the energy of the outgoing particle. We additionally introduced the unit vectors \vec{e}_v (\vec{e}_q) in the direction of the incoming neutrino momentum (momentum transfer).

Furthermore $\beta = |\vec{k}|/\epsilon$ is the momentum to energy ratio of the outgoing particle. In the case of β -decay both leptons are in the final state which results to $\vec{q} = \vec{v} + \vec{k}$. The factor S in front of the interference term is $+1$ in the case of neutrino capture/scattering and β^- -decay and -1 for antineutrino capture/scattering and β^+ -decay.

Obtaining the cross section for neutrino and antineutrino capture and scattering processes, it is now an easy task, where we simply have to apply Fermi's Golden Rule [62]. In the case of (in-)elastic neutrino scattering from a nuclear state $|J, T\rangle$ to the state $|J', T'\rangle$ the cross section will be given in the extreme relativistic threshold limit via

$$\left. \frac{d\sigma}{dq^2} \right|_{NC} = \left. \frac{2\pi}{2k\nu} \frac{d\sigma}{d\Omega} \right|_{NC} = \frac{G^2 k \epsilon}{2\pi^2} \frac{4\pi \cos(\theta/2)}{2J_i + 1} \left(\sum_{J=0}^{\infty} \sigma_{J,T}^{CL} + \sum_{J=1}^{\infty} \sigma_{J,T}^T \right), \tag{2.25}$$

where we have defined

$$\begin{aligned}\sigma_{J,T}^{CL} &\equiv \left| \langle J_f, T_f || \hat{\mathcal{M}}_{J,T} + \frac{q_0}{q} \hat{\mathcal{L}}_{J,T} || J_i, T_i \rangle \right|^2 \\ \sigma_{J,T}^T &\equiv \left(-\frac{q^\mu}{2q^2} + \tan^2 \left(\frac{\theta}{2} \right) \right) \left[|\langle J_f, T_f || \hat{\mathcal{T}}_{J,T}^{mag} || J_i, T_i \rangle|^2 + |\langle J_f, T_f || \hat{\mathcal{T}}_{J,T}^{el} || J_i, T_i \rangle|^2 \right] \\ &\mp \tan \left(\frac{\theta}{2} \right) \left(\frac{q_\mu^2}{q^2} + \tan^2 \left(\frac{\theta}{2} \right) \right) \left[2\text{Re} \langle J_f, T_f || \hat{\mathcal{T}}_{J,T}^{mag} || J_i, T_i \rangle \langle J_f, T_f || \hat{\mathcal{T}}_{J,T}^{el} || J_i, T_i \rangle^* \right].\end{aligned}\quad (2.26)$$

The plus/minus sign is for anti-/neutrino scattering processes. The superscripts *CL* are abbreviations for Coulomb plus longitudinal and *T* is for transverse.

The extreme relativistic limit is valid if $\beta = |\vec{k}|/\epsilon = k/\epsilon \rightarrow 1$, where \vec{k} and ϵ are the momentum and energy of the outgoing lepton. The quantities are assigned as in the equations above. In the case of neutral-current neutrino scattering we are always in the extreme relativistic limit, since the neutrinos have almost no mass² and therefore move with the speed of light. In the case of neutrino/antineutrino capture on nuclei that will interact over the charged-current, we have in the final state a lepton that has mass. Thus our used code explicitly calculates the cross section with the matrix elements from equation 2.24 via the Golden Rule. Under the suppression of target recoil, the cross section is then given by

$$\left. \frac{d\sigma}{d\Omega} \right|_{CC} = \frac{k\epsilon}{2\pi^2} F(Z \pm 1, \epsilon) \frac{1}{2J_i + 1} \sum_{M_i} \sum_{M_f} |\langle f | \hat{\mathcal{K}}_{int} | i \rangle|^2. \quad (2.27)$$

For simplicity we can assume that the mass of the outgoing lepton can be neglected, and we thus obtain the same limit for the cross section as above in the case of neutral-current reactions, except that the underlying currents will be different, as we discussed in the previous sections. However, the outgoing lepton (either an electron or a positron) will interact with the Coulomb potential. This is accounted by the factor $F(Z \pm 1, \epsilon)$ [63]. The charged-current neutrino capture process in the extreme relativistic limit is thus given by

$$\left. \frac{d\sigma}{dq^2} \right|_{CC} = \frac{2\pi}{2kv} \left. \frac{d\sigma}{d\Omega} \right|_{CC} = \frac{G^2 k\epsilon}{2\pi^2} \frac{4\pi \cos(\theta/2)}{2J_i + 1} F(Z \pm 1, \epsilon) \left(\sum_{J=0}^{\infty} \sigma_{J,T}^{CL} + \sum_{J=1}^{\infty} \sigma_{J,T}^T \right), \quad (2.28)$$

where $\sigma_{J,T}^{CL}$ and $\sigma_{J,T}^T$ are given as above. Note that here the coupling constant is $G = G_F V_{ud}$, as noted at the beginning of this section, whereas in the neutral-current cross section it is $G = G_F$.

2.3 Nuclear structure

After we have discussed how the neutrino cross section will be calculated, we want to describe how the nuclear states will be calculated within our work. These states are required for the determination of the excitation cross sections. Before we go on we should stress once more what the actual goal of this work will be. We want to obtain a model that is able to calculate charged and neutral-current spallation rates over the whole nuclear chart. The nuclear model we require therefore has to be able to calculate the nuclear excitation spectrum of each nucleus as accurate as possible within a reasonable calculation time. Our focus within the nuclear excitation spectrum is of course above particle threshold, where particle emission can occur, due to the fact that the average neutrino energies within this supernova environment are above 10 MeV, which shifts our focus in this region. In this region single-particle excitations play only a small role, whereas excitations in which several particles contribute dominate. These states are therefore called collective states or giant resonances. Thus we require a nuclear model that can give a good description of collective states. Especially coherent nuclear states where many nucleons participate are of interest for us.

The ideal solution for this problem would be large scale shell model calculations, since this model is able to correctly determine single-particle excitations and collective states. In these calculations, one starts with a model in which A non-interacting nucleons are contained in a potential. A harmonic oscillator potential is usually the choice to go, because analytical solutions exist that make computation easier. After obtaining the single-particle energies by solving the Schrödinger equation, the next step is diagonalizing a residual interaction which describes the interaction between the nucleons. This diagonalization is done in a basis consisting of all possible combinations how the A particles can be distributed in the Hilbert space created by the single-particle states. Depending on the number of nucleons and the number of single-particle states, the amount of basis configurations increases very rapidly, limiting this procedure to nuclei up

² Within the standard model of particle physics neutrinos are assumed to have no mass at all.

to $A = 60$, at most. There are possibilities of calculating nuclei near shell closures where the set of basis states can be restricted. However, calculations over the whole nuclear chart seem to be out of reach at least for the next decade.

Thus to describe the nuclear excitations – especially above particle threshold – we apply the *Random Phase Approximation* (RPA) which aims at a good description of the collective states that we are interested in. The starting point of this model is similar to the shell model case. The first step is the calculation of single-particle states with the Schrödinger equation under the assumption that the nucleons are not interacting with each other, instead they only feel an average potential created by all nuclei. This idea is referred to as the *independent particle model* (IPM). The ground state in the IPM is then given as the configuration where the system has minimal total energy. Therefore we start filling up the single-particle states with the lowest energy. When all A particles are put in, we have obtained the ground state of our IPM. The energy of the last filled single-particle state then defines our Fermi energy. Note that there also exist methods of obtaining the single-particle energies in a self consistent way, by applying Ritz variational principle and variation of the single-particle densities. These models are called Hartree-Fock models and give a good average description of the nucleus [64]. It however will not allow us to shift the energies of the single-particle states to the correct reaction Q -values, as we will describe later.

In a second step, a residual interaction is utilized for the description of excited states. The basis for finding the excited states can be approximated as a combination of all possible one-particle one-hole states. This description can be seen as a perturbative approach to the real physical excited states.

The exact physical solutions can always be expanded in a basis containing of a trial groundstate wavefunction and a combination of all n -particle n -hole excitations generated of this groundstate wavefunction. The exact physical groundstate – as well as excited states – can be correctly reproduced with a description like this [65]. However doing these n -particle n -hole excitations becomes more and more demanding with increasing n .

Under the assumption that higher particle-hole excitations have smaller contributions, a valid approximation will be to allow only for one-particle one-hole excitations. These one-particle one-hole states are configurations of the nuclear Hilbert space where one nucleon is taken from below the Fermi surface and put to an unoccupied single-particle state above the Fermi energy. This reduces the amount of basis states in such a way that the amount of calculations we have to face is still manageable over the whole nuclear chart. Before we now explain how the RPA works, we will make a few comments about the IPM that we're using.

2.3.1 Independent particle model

We would like to start with a short phenomenological description of how the average nucleon-nucleon potential will behave at certain regions in the nucleus. In the center of the nucleus, the forces from each directions should be the same, whereas at the edge of the nucleus the nucleons should feel an effective force binding the nucleons to the nucleus. At higher distances than the radius of the nucleus, the potential has to vanish. An analytical description that can cover all these phenomenological argumentations is the Fermi-function. It has additionally the advantage that it also measured resembles density distributions of nuclei [66]. The parametrization for the nuclear potential is called *Woods-Saxon* potential [67]

$$V(r) = -\frac{V_0}{1 + e^{\left(\frac{r-R}{a}\right)}}. \quad (2.29)$$

V_0 , R and a are parameters that have to be adjusted to each nucleus. This parametrization is not sufficient for a realistic description, because protons additionally feel the Coulomb force which neutrons do not. Another important issue that is not yet included is the spin-orbit coupling. It was the pioneering work of Mayer and Jensen [68, 69] to include a spin-orbit coupling to a central part as above for the description of the right shell closures. In contradiction to the atomic spin-orbit coupling this coupling has opposite sign and is very strong. One can show [70] that the spin-orbit contribution has its strongest value at the surface of the nucleus due to one-pion exchange forces. Thus the total Woods-Saxon potential can be written as

$$V(r) = -\frac{V_0}{1 + e^{\left(\frac{r-R}{a}\right)}} - V_{s.o.} R^2 \frac{1}{r} \frac{\partial}{\partial r} \left(\frac{1}{1 + e^{\left(\frac{r-R}{a}\right)}} \right) (\vec{L} \cdot \vec{S}) + \frac{1 + \tau_3}{2} V_C(r). \quad (2.30)$$

Within the description of the Woods-Saxon potential, we included six parameters that need to be determined. These are the nuclear radius R , the nuclear diffuseness a , the radius of the spin-orbit part R , the spin-orbit diffuseness a and the depth of the potentials V_0 and $V_{s.o.}$. Note that we already included the Coulomb potential V_C in above equation. As already can be observed from the used nomenclature, we assumed that the spin-orbit radius and the spin-orbit diffuseness have the same values as the ones used in the central part. The description of the spin-orbit part has its maximal value at the surface of the nucleus. Note that the Coulomb interaction is only acting on protons, as it should be.

It is noteworthy to mention, that for a small sample – especially for nuclei around shell closures – explicit values for the parameterizations can be found in the literature [71]. Due to the fact that we would like to calculate spallation rates from the proton drip-line to the neutron drip-line, we have to find a description that gives us the parameters based on simple models, that can be utilized over the whole nuclear chart.

For the determination of the nuclear radius, we applied one of the basic results from the liquid droplet model in which the nucleus is described as a drop [64]. In this model the nuclear radius can be calculated simply by

$$R = r_0 \cdot A^{1/3} \quad \text{with } r_0 = 1.22 \text{ fm.} \quad (2.31)$$

Bohr & Mottelson showed that the IPM results have no strong dependence on the used nuclear radius [67], thus this formula is precise enough for our purposes. The diffuseness is set to the constant value of 0.53 fm which has been the standard value of previous calculations within the same framework [72] for charged-current neutrino capture and muon capture processes. In the case of muon capture it has been pointed out that only for the case of high diffuseness values noticeable changes in the muon capture rate on neutron rich tin isotopes can be observed [73]. This fact however gives us the confidence that our results are not dramatically sensitive to the choice of the exact surface diffuseness.

We are now left with determining the last two parameters of the Woods-Saxon potential, namely the depth of the spin-orbit and the central part. For the spin-orbit depth we use the fixed value of 17.9 MeV, which reproduces the positions of the magic number in stable nuclei. It agrees furthermore quite well with the value given in [67]. The depth of the central potential has to be set in such a way that the single-particle Fermi levels are reproduced. This has to be done for neutrons and protons separately. Depending on the type of process we are studying, the neutron/proton single-particle orbits have to be assigned to the mother/daughter³. For example neutrino captures and β -decays change a neutron into a proton, thus the last neutron is related to the mother and the proton belongs to the daughter nucleus. A decent description for the energy difference of the last bound neutron can therefore be obtained by the neutron separation energy S_n of the mother nucleus with mass number A and charge number Z , whereas the proton separation energy S_p can be related to the daughter nucleus with mass number A and charge number $Z - 1$. Vice versa is the case for antineutrino and electron capture, where the proton separation energy of the mother with mass number A and charge number Z determines the energy difference of the last proton and the neutron separation energy of the daughter nucleus with mass number A and charge number $Z + 1$ determines the energy difference of the last bound neutron. For the description of neutral-current neutrino excitation mother and daughter present the same nucleus which simplifies the description. The last proton and neutron energy difference can thus be given by the proton and neutron separation energy of the nucleus under consideration. To obtain the neutron and proton separation energies we use experimental determined masses whenever possible [74], if no experimental data is available we use the FRDM theoretical model [75].

We should note here, that no analytical solutions exist for the solution of the Schrödinger equation with the Woods-Saxon potential as we described it in equation 2.30. To avoid numerical errors, we expanded our eigenvalues and eigenfunctions in solutions of the spherical harmonic oscillator, where analytical solutions are easy to obtain. To achieve convergence we utilize up to ten major oscillator shells. The drawback of this description is, that all single-particle states of the harmonic oscillator are bound state solutions, which is not the case for the Woods-Saxon potential. For the deep bound solutions of our potential we will have a decent description. However we will underestimate loosely bound or continuum solutions since the tail of the wavefunctions will extend far outside where bound solutions have a very steep decline. However in a later part we will show comparisons to results obtained in a model with correct continuum treatment and we can see that a good agreement is achieved.

The description above gives us the confidence that our model for obtaining the single-particle states is good enough to cover the basic physics that are important for the next step, which will be the RPA with its residual interaction. In the next subsection we will describe the basic theory of the RPA.

2.3.2 Random Phase Approximation

In this part we would like to show how one can derive the basic random phase approximation (RPA) equations starting from the Tamm-Dancoff method. The RPA is the essential part for modeling the nuclear excitation spectrum at energies above the particle threshold, since collectivity plays a mayor role in the description of the excitation spectrum and these collective states cannot be calculated in a simple IPM framework. However, we could argue that the IPM model is a valid way of describing the ground state. Starting with this ansatz we might argue that the collective states can be described as solutions to a residual interaction solved in a basis of IPM particle-hole excitations. The residual interaction can then be formulated as

$$V_R = \frac{1}{4} \sum_{\substack{k_1, k_2 \\ k_3, k_4}} \langle k_1 k_2 | \bar{v} | k_3 k_4 \rangle a_{k_1}^\dagger a_{k_2}^\dagger a_{k_3} a_{k_4}, \quad (2.32)$$

³ In this section the mother is defined by the initial nucleus on which the neutrino scattering/capture processes take place. The daughter is therefore the nucleus that will be created by the process. We will redefine this nomenclature in section 2.4 for the description of the decay probability.

where the k_i are an abbreviated form of all relevant quantum numbers. The exact diagonalization of this residual interaction in a basis consisting of all excitations up to full n-particle n-hole excitations is an impossible task. If we allow only 1-particle 1-hole excitations, we end up at the *Tamm-Dancoff approximation* (TDA). In the TDA, the ground state can be approximated as the ground state of the IPM

$$|GS_{TDA}\rangle \approx |IPM\rangle. \quad (2.33)$$

The excited states are given as linear combinations of the 1-particle 1-hole excitations

$$|\nu\rangle \approx \sum_{i,\alpha} X_{i\alpha}^\nu a_i^\dagger a_\alpha |IPM\rangle, \quad (2.34)$$

where i, j, k, \dots denotes particles above the Fermi surface and α, β, \dots are below the Fermi surface. Note that since we were requiring a Hilbert space in which all states have definite isospin and total angular momentum, we are able to couple each particle-hole pair to a definite spin J and isospin τ [64]. Using equation 2.34 as a variational ansatz, one obtains a secular equation that can be reformulated with the help of some basic commutation relations as

$$E_\nu^{TDA} X_{ai}^\nu = \sum_{j,\beta} \{ (\epsilon_i - \epsilon_\alpha) \delta_{ij} \delta_{\alpha\beta} + \bar{v}_{\alpha i, j\beta} \} X_{j\beta}^\nu. \quad (2.35)$$

The single-particle energy difference between particle and hole $\epsilon_i - \epsilon_\alpha$ comes from the IPM single-particle energies. The interaction \bar{v} is hereby described in two parts [64]

$$\bar{v}_{\alpha i, j\beta} = \langle \alpha i | \hat{v} | j\beta \rangle - \langle \alpha i | \hat{v} | \beta j \rangle. \quad (2.36)$$

The first part describes the so called *direct* term in which a particle-hole pair $|j\beta\rangle$ is destroyed and a new particle-hole pair $|\alpha i\rangle$ is created. In the second part, which is also called *exchange* term, the particle-hole pair $|j\beta\rangle$ scatters into $|\alpha i\rangle$. Both processes can be graphically represented as displayed in figure 2.1. The feature of the TDA as shown in equation 2.35 is that we built correlations into the excited states. The ground state however has no correlations build inside, which will definitely change our results.

To improve our model, we might think about allowing several particle-hole excitations, which however will increase the model space quite tremendously while the ground state will still remain untouched. A smarter alternative is to allow not only for the creation of particle-hole pairs, but also for the destruction of such a pair [64]. The creation operator can thus be formulated as

$$Q_\nu^\dagger = \sum_{i\alpha} X_{i\alpha}^\nu a_i^\dagger a_\alpha - \sum_{\alpha i} Y_{\alpha i}^\nu a_\alpha^\dagger a_i. \quad (2.37)$$

The first part of equation 2.37 equals the creation operator of the TDA. However the second part now allows for the destruction of a particle-hole pair. Note that the minus sign has been chosen for convenience. With these definition, we are able to define the creation of excited states as

$$|\nu\rangle = Q_\nu^\dagger |GS_{RPA}\rangle. \quad (2.38)$$

This redefines our ground state within the RPA. The RPA ground state should obey the following equation

$$Q_\nu |GS_{RPA}\rangle = 0. \quad (2.39)$$

The detailed structure of the ground state within the RPA is still unknown, which makes the definitions of the new creation/destruction operators a more philosophical improvement than one that can actually improve the model. Only

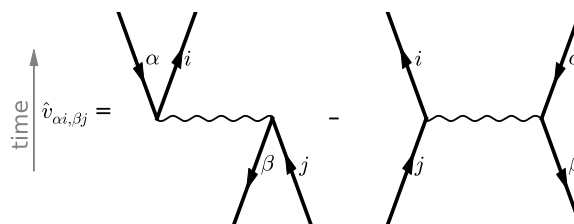


Figure 2.1.: Direct and exchange terms of the interaction $\bar{v}_{\alpha i, j\beta}$.

under the assumption that the used IPM ground state does not differ too much from the real RPA ground state, we can utilize the upper definitions for the determination of collective excited states. The approximation of replacing the exact ground state with the IPM ground state is called *quasi-boson approximation* [65]. The reason for this stems from the fact that if the particle-hole creation/destruction operators would satisfy the commutation rules for bosonic fields, this approximation would be an exact one. However, since we are dealing with fermionic particles, we are breaking Pauli principle with this approximation.

By applying the variational principle to both coefficients separately, we end up with two secular equations that can be written in the compact matrix form as

$$\begin{pmatrix} A & B \\ -B^* & -A^* \end{pmatrix} = E_v \begin{pmatrix} X^v \\ Y^v \end{pmatrix}. \quad (2.40)$$

The entry A is the same as in equation 2.35 for the case of the TDA

$$A_{i\alpha,j\beta} = (\epsilon_i - \epsilon_\alpha) \delta_{ij} \delta_{\alpha\beta} + \bar{v}_{\alpha i, j \beta}, \quad (2.41)$$

whereas B is given as

$$B_{i\alpha,j\beta} = \bar{v}_{ij,\alpha\beta}. \quad (2.42)$$

$\bar{v}_{ij,\alpha\beta}$ can again be sketched graphically as shown in figure 2.2. We can observe that these matrix entries basically describe virtual two-particle two-hole excitations [64]. Note that A is Hermitian while B is only symmetric, which implies that the total matrix in equation 2.40 is also not Hermitian. This results in eigenvectors that are not necessary orthogonal and real. However we can require orthogonality of the excited states [64] by

$$\langle v|v' \rangle = \delta_{vv'} = \sum_{i\alpha} (X_{i\alpha}^{v*} X_{i\alpha}^{v'} - Y_{i\alpha}^{v*} Y_{i\alpha}^{v'}). \quad (2.43)$$

From equation 2.40 we can easily see that by setting all Y^v to zero, we end up with the same equations as in the case of the TDA. Thus Y^v is a measure of correlations in the ground state.

A nice feature within the quasi-boson approximation is, that the absolute squares of the amplitudes $X_{i\alpha}^v, Y_{i\alpha}^v$ give directly the probability of finding the particle-hole ($a_i^\dagger a_\alpha |IPM\rangle$) or the hole-particle pair ($a_\alpha^\dagger a_i |IPM\rangle$) in the excited state $|v\rangle$. These probabilities can help us determining when the RPA with the quasi-boson approximation yields valid collective states. For a real collective state, many $X_{i\alpha}^v$ have to participate with almost the same order of magnitude, since in these cases the Pauli principle is minimally violated. Even more important is the fact that the amplitudes $Y_{i\alpha}^v$ are related with ground state correlations. If the $Y_{i\alpha}^v$ amplitudes are large, the ground state has already a strong mixture of hole-particle contributions. This however tells us that the quasi-boson approximation breaks down [64, 65].

Because we are treating protons and neutrons as individual particles, we have to incorporate this in our RPA equations. Depending on the type of reaction we are interested in, a neutron might have to be changed in a proton or vice versa. We do so by generating particle-hole pairs in such a way that they incorporate the isospin direction of the process. If the reaction is charge changing, e.g. a proton changes into a neutron, all particle states will be protons and all hole states neutrons. Our RPA therefore works in a mixed particle basis consisting of neutron/proton states and holes. If we consider neutral-current processes protons and neutrons will be considered separately.

For our rate calculations, we need to calculate transition matrix elements within the RPA. In our framework these transition elements are one body operators between the ground state of the mother nucleus and the daughter. Under the assumption of an Hermitian one-body transition operator \hat{T} the transition elements within the RPA can be given by [64]

$$\langle RPA|\mathcal{F}|v\rangle = \sum_{i\alpha} T_{i\alpha} X_{i\alpha}^v + T_{\alpha i} Y_{i\alpha}^v. \quad (2.44)$$

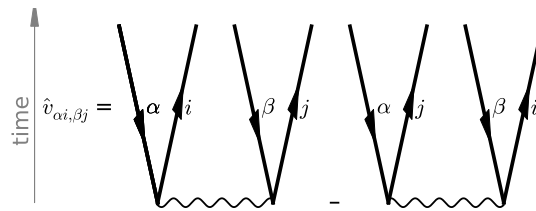


Figure 2.2.: Graphical representation of the matrix elements B.

$T_{i\alpha}$ can be determined as the overlap of operator $\hat{\mathcal{T}}$ with the single-particle states $\langle i|\hat{\mathcal{T}}|\alpha\rangle$.

Before we move on, we should stress out once more, that we are only interested in solutions of the RPA with definite angular momentum. Therefore our particle-hole creation/destruction operators (see eq. 2.37) have to carry good angular momentum

$$Q_v^\dagger(J, M) = \sum_{i,\alpha} X_{i\alpha}^v A_{i\alpha}^\dagger(J, M) - \sum_{i,\alpha} Y_{i\alpha}^v (-1)^{j_i+j_\alpha+M} A_{i\alpha}(J, M). \quad (2.45)$$

We applied basic angular momentum coupling of the single-particle states

$$A_{i\alpha}^\dagger(J, M) = \sum_{m_i m_\alpha} (-1)^{j_\alpha+m_\alpha} \langle j_i j_\alpha J | m_i m_\alpha M \rangle a_{j_i m_i}^\dagger a_{j_\alpha - m_\alpha}, \quad (2.46)$$

j_α and j_i are the total angular momenta of the single-particle states. If we apply equation 2.45 instead of equation 2.37, we always obtain good total angular momenta values J for all particle-hole pairs.

This nice feature allows us to split up the RPA equations for each J -value. Furthermore, by looking at the orbital angular momentum of the single-particle states l_α and l_i of the particle-hole pairs, we are able to assign the parity of the particle-hole state. If the sum of both orbital angular momenta has an even value, we have positive parity, otherwise we have negative parity.

2.3.3 Residual interaction

For obtaining results with our RPA, we still need a residual interaction that determines the matrix elements A and B . It is evident that for realistic nuclear structure results the residual interaction has to provide a consistent interplay between particles and holes. The best way would be to utilize a self-consistent RPA. Within such an approach one starts with a realistic effective nucleon-nucleon interaction within a Hartree-Fock calculation. After obtaining the self consistent single-particle energies, one automatically obtains the interaction between particles and holes. This interaction can then be utilized for the RPA to obtain collective states. The main advantage of such methods is that one obtains self consistent and stable solutions within the RPA, which is not necessarily the case when a phenomenological model is used. We will show such inconsistent solutions and how we will separate them in our work within part 3. The drawback of such a method is that it is computationally quite expensive, whereas phenomenological residual interactions with IPM single-particle energies are computationally cheap and give reasonable agreement to realistic calculations. Since we would like to describe neutrino-nucleus interactions over the whole nuclear landscape, we have to find a compromise between detailed description and computation time. Due to the fact that we are interested in how these rates influence the nucleosynthesis of e.g. supernova scenarios, the rates based on the simpler picture should be fine enough, since our neutrino reactions are mainly sensitive to resonances which are reasonably well described in such a model. If the obtained rates show large influences on the nucleosynthesis, we are still able to improve our model.

The phenomenological interaction that we applied is of the Landau-Migdal type. This model has been used in various applications for the description of collective excitations in nuclei. It is based on the interacting quasi-particle concept of Landaus theory of Fermi liquids [76] and first applied to collective phenomena by Migdal in 1967 [77]. The basic structure of the residual interaction originates from an expansion in momentum space. Since we are interested in excitations of the nucleus instead of its structure properties – such as saturation – the expansion can just be a constant. In coordinate space this results to the three dimensional δ -function. However, we still have to consider that the interaction is depending on spin and isospin. It can be parameterized in general as

$$V(\vec{r}_1, \vec{r}_2) = C_0 \delta^3(\vec{r}_1 - \vec{r}_2) (f + f' \vec{\tau}_1 \cdot \vec{\tau}_2 + g \vec{\sigma}_1 \cdot \vec{\sigma}_2 + g' \vec{\tau}_1 \cdot \vec{\tau}_2 \vec{\sigma}_1 \cdot \vec{\sigma}_2). \quad (2.47)$$

Following a proposal of Gunmar and Birbar [78] the interaction that we utilize will be density dependent. The following parametrization has been applied for both the parameters f and f'

$$f = f^{ex} + (f^{in} - f^{ex}) \frac{\rho(r)}{\rho_0}, \quad (2.48)$$

all other variables are assumed to be constant. Within the IPM or an Hartree-Fock model, we would be also able to determine the density within the model description. However as we already mentioned above, the density can be very good described through a Fermi-distribution

$$\rho(r) = \frac{\rho_0}{1 + \exp(\frac{r-R}{a})}, \quad (2.49)$$

where ρ_0 describes the density at $r = 0$. To maintain consistency the parameters for the nuclear radius R and diffuseness a are set to the same values as in our description for the Woods-Saxon potential. The additional parameters are set to the

C_0	$\frac{\text{MeV}}{f_m}$	f^{in}	f^{ext}	f'^{in}	f'^{ext}	g	g'
302		0.2	-2.45	0.90	1.5	0.55	0.80

Table 2.1.: Parameters for the effective interaction of the Landau-Migdal type.

values given by Rinker & Speth in 1978 [71]. For a better reproduction of the isobaric analog state in ^{48}Ca and ^{208}Pb the internal isospin coupling factor f'^{in} has been adjusted to reproduce the isobaric analog states in ^{48}Ca and ^{208}Pb [79]. The actual values can be found in table 2.1. Due to the fact that scattering rates have been shown to be quite insensitive to the detailed values used in the calculations, we keep this values constant for all of our calculations. Once again we would like to point out that we are interested in understanding how these rates change the nucleosynthetic outcome, therefore we accept uncertainties within these rates in the first place, keeping them in mind as a further point for improvements.

2.3.4 Partial occupancy

By looking at the RPA equations, one realizes that the RPA assumes that all single-particle orbits below the Fermi level are completely occupied in the ground state. This would reduce the amount of nuclei that we could address with our model. Since we are however interested in a full description from proton drip to neutron drip, we have to find a description that allows us to treat such open-shell nuclei. A realistic formulation can be obtained within the quasi-particle RPA model (QRPA). Within this model one starts from an IPM that includes mean-field contributions plus pairing, which are important for open shell nuclei. The more important part is however that the RPA is calculated for particle-hole, particle-particle and hole-hole contributions [64], instead of the simple particle-hole interactions alone. However, this complicates the residual interaction quite tremendously. To avoid this task, we apply an approximate scheme, which has been introduced in the case of ^{12}C [80]. This approximation scheme replaces the residual matrix element as

$$\langle j\beta|V_{res}|i\alpha\rangle \rightarrow n_i n_j \langle j\beta|V_{res}|i\alpha\rangle, \quad (2.50)$$

where n_i and n_j describe the partial occupancies of the two hole orbits. By this simple approach the matrix element is weighted according to which degree they contribute to the IPM ground state. The proton and neutron occupation numbers will be given by the IPM model for the single-particle orbits of the corresponding mother nucleus.

2.3.5 Sum rules

Sum rules allow a simple calculation of global properties. They are an useful tool for testing different approximations for describing collective phenomena. All sum rules base on a Hermitian single-particle operator \mathcal{F} [64]

$$S_k(f) = \sum_{\nu} (E_{\nu} - E_0)^k |\langle \nu | \mathcal{F} | 0 \rangle|^2. \quad (2.51)$$

This equation gives us the k -th moment of the excitation strength, obtained by the single-particle operator \mathcal{F} . The $|\nu\rangle$ states hereby represent the complete set of nuclear eigenstates of the exact Hamiltonian. S_1 is also called the energy weighted sum rule. It can be shown that the RPA fulfills the energy weighted sum rule exactly [64].

One of the most important sum rules is the *Thomas-Reiche-Kuhn* (TRK) sum rule, which helps us to determine the total cross sections for dipole excitations. The total cross section is obtained by summing over all final states ν and integrating over the energy

$$\sigma_{tot} = \int \sum_{\nu} \sigma_{\nu}(E) dE = \frac{4\pi^2 e^2}{\hbar c} \int \sum_{\nu} (E_{\nu} - E_0) |\langle \nu | \hat{D} | 0 \rangle|^2 \delta(E - E_{\nu} + E_0) dE. \quad (2.52)$$

\hat{D} is hereby the dipole operator as it can be found in many textbooks (e.g. [65, 64]). It reads as

$$\hat{D} = \sum_{i=1}^A \left(\frac{1}{2} - \tau_3^{(i)} \right) r_i Y_1, \quad (2.53)$$

where r_i gives the radius to particle i and Y_1 are the spherical harmonics of degree one. In equation 2.52 E_{ν} and E_0 are the energies of the excited state and of the ground state respectively. Under the assumption of a velocity independent two body Hamiltonian of the Wigner type [64] the total cross section can be given as

$$\sigma_{tot} = \frac{2\pi^2 e^2 \hbar N Z}{mc} \frac{NZ}{A}. \quad (2.54)$$

This is the famous Thomas-Reiche-Kuhn sum rule; for heavy nuclei the *giant dipole resonance* (GDR) exhausts up to 100% of the TKR sum rule. In these cases the GDR has a large overlap with what is known as the *Goldhaber-Teller state* [81] which is a coherent excitation of particle-hole pairs. This is one of the reasons why the RPA is an ideal model for the description of the GDR, because it is based on particle-hole excitations.

In the case of weak interactions, especially for charged-current processes, the *Ikeda sum rule* (ISR) plays an important role. It is defined as

$$ISR = S_+ - S_- = \sum_{\nu} |\langle \nu | \hat{\sigma} \tau_+ | 0 \rangle|^2 - \sum_{\nu} |\langle \nu | \hat{\sigma} \tau_- | 0 \rangle|^2. \quad (2.55)$$

Hereby $|0\rangle$ is the ground state and $|\nu\rangle$ an excited state. The operator between ground state and excited state is split up into an operator acting on spin and the isospin changing operator τ_{\pm} . The spin operator can be either unity or change the total angular momentum by one. In general the Ikeda sum rule can be formulated as

$$ISR = (2J + 1)(N - Z), \quad (2.56)$$

with J being the change in total angular momentum; N (Z) is the number of neutrons (protons). Note that J is within the Ikeda sum rule only allowed to have values of 0 and 1, because higher changes in J might create complicated couplings. The ISR basically arises from the conservation of isospin in nuclei. If we assume first that the spin operator is unity, we are able to show that with the help of $(\tau_{\mp})^{\dagger} = \tau_{\pm}$ and the completeness equation $\sum_{\nu} |\nu\rangle\langle \nu| = 1$ the Ikeda sum rules gives

$$\begin{aligned} ISR(J=0) &= S_-^F - S_+^F \\ &= \sum_{\nu} |\langle \nu | \tau_+ | 0 \rangle|^2 - \sum_{\nu} |\langle \nu | \tau_- | 0 \rangle|^2 \\ &= \sum_{\nu} \langle \nu | \tau_+ | 0 \rangle^* \langle \nu | \tau_+ | 0 \rangle - \sum_{\nu} \langle \nu | \tau_- | 0 \rangle^* \langle \nu | \tau_- | 0 \rangle \\ &= \sum_{\nu} \langle 0 | \tau_- | \nu \rangle \langle \nu | \tau_+ | 0 \rangle - \sum_{\nu} \langle 0 | \tau_+ | \nu \rangle \langle \nu | \tau_- | 0 \rangle \\ &= \langle 0 | \tau_- \tau_+ | 0 \rangle - \langle 0 | \tau_+ \tau_- | 0 \rangle = \\ &= \langle 0 | [\tau_-, \tau_+] | 0 \rangle = 2 \langle 0 | \tau_3 | 0 \rangle = N - Z. \end{aligned} \quad (2.57)$$

S_{\pm}^F is called Fermi β -strength, because the pure isospin operator is also called Fermi operator. That is the reason why the upper sum rule is also called *Fermis sum rule*. The RPA fulfills the ISR exactly. We would like to show this explicitly, again only for the case of Fermi transitions, since we then do not have to consider angular momentum coupling.

$$\begin{aligned} ISR(J=0)^{RPA} &= \sum_{\nu} |\langle \nu | \tau_+ | 0 \rangle|^2 - \sum_{\nu} |\langle \nu | \tau_- | 0 \rangle|^2 \\ &= \sum_{\nu} \left| \sum_{i\alpha} X_{i\alpha}^{\nu} T_{i\alpha}^{-} + Y_{i\alpha}^{\nu} T_{i\alpha}^{-} \right|^2 - \left| \sum_{i\alpha} X_{i\alpha}^{\nu} T_{i\alpha}^{+} + Y_{i\alpha}^{\nu} T_{i\alpha}^{+} \right|^2 \\ &= \sum_{\nu} \left[\sum_{i\alpha} \left(|X_{i\alpha}^{\nu}|^2 |T_{i\alpha}^{-}|^2 + |Y_{i\alpha}^{\nu}|^2 |T_{i\alpha}^{-}|^2 \right) + 2\Re \left\{ \sum_{\substack{i,\alpha \\ j,\beta}} X_{i\alpha}^{\nu*} T_{i\alpha}^{-*} Y_{j\beta}^{\nu} T_{j\beta}^{-} \right\} \right] \\ &\quad - \sum_{\nu} \left[\sum_{i\alpha} \left(|X_{i\alpha}^{\nu}|^2 |T_{i\alpha}^{+}|^2 + |Y_{i\alpha}^{\nu}|^2 |T_{i\alpha}^{+}|^2 \right) + 2\Re \left\{ \sum_{\substack{i,\alpha \\ j,\beta}} X_{i\alpha}^{\nu*} T_{i\alpha}^{+*} Y_{j\beta}^{\nu} T_{j\beta}^{+} \right\} \right]. \end{aligned} \quad (2.58)$$

Hereby we applied $T_{i\alpha}^{\pm} = \langle i | \tau_{\pm} | \alpha \rangle$. With the help of the orthogonality relation showed in eq. 2.43 we can simplify above result to

$$ISR(J=0)^{RPA} = \sum_{i\alpha} \left(|T_{i\alpha}^{-}|^2 - |T_{i\alpha}^{+}|^2 \right). \quad (2.59)$$

The first part of this equation turns neutrons into protons, because it contains the isospin lowering operator τ_- . By doing the summation of the squared transition elements over all protons, we obtain the occupation number of neutrons within the orbit α . Vice versa, we obtain the proton occupation via the second part

$$ISR(J=0)^{RPA} = \sum_{\alpha} (2j_{\alpha} + 1)n_{\alpha} - \sum_i (2j_i + 1)n_i. \quad (2.60)$$

The indices α and i describe neutrons and protons, respectively. n_i gives the occupation numbers of the orbits i . By evaluating the sum, we obtain the desired result:

$$ISR(J = 0)^{RPA} = N - Z. \quad (2.61)$$

There also exists a sum rule for the combination of operators consisting of spin and isospin operator. This operator is called Gamow-Teller operator. Subsequently this sum rule is also called *Gamow-Teller sum rule*. It reads as

$$ISR(J = 1) = S_-^{GT} - S_+^{GT} = 3(N - Z). \quad (2.62)$$

Until today there exist various discussions about the validity of the Gamow-Teller sum rule. First attempts of obtaining the total strength showed that only a fraction of the sum rule can be found experimentally. By detailed measurements and careful analysis of the obtained results, especially of strength in the continuum⁴, current experiments are able to almost fully reproduce the Gamow-Teller sum rule [82, 83]. However most theoretical models – including the RPA – have the problem of overestimating the Gamow-Teller strength at low energies [84].

From a theoretical point of view the question was, if this overestimation stems from nucleonic renormalizations or non-nucleonic renormalizations of the Gamow-Teller operator $\sigma\tau$ [85]. With non-nucleonic renormalization one usually assumes an in-medium renormalization of the axial-vector coupling constant g_A . However, today this fact seems to be unlikely because measurements of (p, p') , (γ, γ') and (e, e') in M1 transitions show a similar renormalization without being sensitive to g_A [86], particularly for M1 (e, e') cross sections this holds true as a consequence of the CVC theorem. Therefore nucleonic renormalization is the more plausible possibility. The question however is shifted towards finding the explanation why the strength is too strong at low excitation energies. There are many possibilities that might account for the overestimation of low lying strength. One possibility is that these models neglect subnuclear degrees of freedom.

Rho [87] showed that the Δ resonance is able to take strength away from low lying states and push it towards higher excitation energies. The details of these effects are crucial to the nucleon-delta interaction. Detailed studies showed that only a small amount can be explained within the assumption of nucleon- Δ interactions [88, 89]. Thus the most probable case is that the inclusion of several particle-hole excitations pushes strength to higher energies [90, 84].

However, all these models which describe the Gamow-Teller strength at low energies correctly are based on models beyond RPA. Therefore we need a way of reproducing the low energy part of the Gamow-Teller strength. As stated before, the RPA fulfills the Gamow-Teller sum rule exactly, therefore we have to break this sum rule by the inclusion of a *quenching* factor. In our work we will utilize a quenching factor of $(0.74)^2$ [72].

These sum rules are only strictly valid for self-consistent RPA models. However for a phenomenological RPA model including a good residual interaction the results will be not to far off.

We should note that the Fermi-transition can be applied for the improvement of the model space in the case of (anti-) neutrino captures. The strength of the Fermi transition is essentially concentrated in the so called *isobaric analog state* in the daughter nucleus. Its transition strength will be $|N - Z|$ and is consequently a $J^\pi = 0^+$ excitation. The energetic position of the isobaric analog state can be approximated at an excitation energy of the daughter nucleus [45] by

$$E_{IAS} \approx \Delta M_{Nuc} \mp \Delta M_{np} \pm \frac{6}{5} \frac{Z\alpha\hbar c}{R_{nuc}}. \quad (2.63)$$

The first term hereby describes the mass difference between parent and daughter nucleus in its ground states. Furthermore ΔM_{np} is the mass difference between a neutron and a proton, with the value of 1.2934 MeV. The last term approximates the difference of the Coulomb potential between mother and daughter. The nuclear radius R_{nuc} has been given by the authors of [45] as

$$R_{nuc} = 1.12A^{\frac{1}{3}} + 0.78, \quad (2.64)$$

given in units of fm. The upper signs of equation 2.63 describe the case of neutrino captures and β^- -decay with the additional constraint that $N > Z$, the latter ones describe antineutrino captures and β^+ -decay with $Z > N$. If the above mentioned conditions are not fulfilled, no Fermi transitions exist since these states are occupied. As mentioned previously, the position of the IAS can help us to constrain the model space. In the cases where an IAS exists, we will shift the single-particle energy such that the dominant $J = 0$ state will be at the position given by equation 2.63.

Note that the response of the multipole operators are strongly dependent on the momentum transfer q . Therefore only in the limit $q \rightarrow 0$ will the responses of 0^+ and 1^+ reduce to the Fermi and Gamow-Teller operators [55] discussed above. At finite q other operators will be present that appear in the nuclear response of the RPA. The resonances of these operators will be dominant at higher excitation energies, however they will also have interference with low lying states. The above discussed quenching of the Gamow-Teller strength is within our code applied for the whole 1^+ strength. This effectively means that we not only quench the pure Gamow-Teller operator, but also the higher order contributions, which in general should not be quenched. We however assume that the contributions of these other operators are quite small and we do not make a substantial error by quenching the whole 1^+ strength.

⁴ The continuum hereby describes the energy region above the first particle emission threshold.

2.3.6 Reduction of transition operators

For the calculation of the transition matrices, as in equations 2.24 and 2.25, we require to determine the single-particle matrix elements between particles and holes and multiply them with the amplitudes given by the RPA solutions. Furthermore we have to sum over all particle-hole pairs. Thus for all possible cases, our remaining task reduces to the determination of the elements in the transition matrix. Basically we have to calculate transition elements with a structure

$$\langle J_f M_f, T_f m_{T_f} | \hat{\mathcal{A}}_{J M, T M_T} | J_i M_i, T_i m_{T_i} \rangle. \quad (2.65)$$

Hereby J_x and M_x are the total angular momenta and its projection of the initial and final state. $\hat{\mathcal{A}}_{J M, T M_T}$ is an operator that carries angular momentum J and projection M as well as isospin with value T and projection m_T . T_x and m_{T_x} are the isospin and isospin projection values of the initial and final nucleus. We are able to reduce the transition matrix element by applying the Wigner-Eckart theorem [60] for spin and isospin as shown already in equation 2.21.

Since we are interested in evaluating the transition matrix elements between the parent ground state and all excited states in the daughter, the particle-hole elements can be written as

$$\langle 0 | \hat{\mathcal{A}}_J | [i\alpha]_J \rangle = \langle i | \hat{\mathcal{A}}_J | \alpha \rangle, \quad (2.66)$$

where we suppressed isospin, because – as stated above – the isospin part is easily calculated. The equality shown in equation 2.66 is only valid in the case of one-body currents and particle-hole states with definite angular momentum and isospin. In the upper equation $[i\alpha]_{J,T}$ refers to a particle-hole pair coupled to isospin T and angular momentum J . The operator $\hat{\mathcal{A}}$ will in general have parts acting on spatial coordinates, spin and isospin. It is helpful to write reduced single-particle elements within full detail as

$$\langle (l_i \ 1/2) j_i | \hat{\mathcal{A}}_J | (l_\alpha \ 1/2) j_\alpha \rangle. \quad (2.67)$$

The orbital angular momentum l couples with the spin of the particle/hole to total angular momentum j . We now like to shortly summarize some manipulations that can be applied for the determination of the nuclear transition matrix elements.

As we already stressed before, we work in a model in which our nuclear states have definite angular momentum as well as parity, which lets us classify the currents in terms of parity as well. The total parity of a nuclear matrix element is then given by the combination of angular momentum J , the multipole expanded nuclear current operators as defined in 2.14 and the parities of the single-particle wave functions of particle and hole. Therefore we need to look at the orbital angular momentum and not the total angular momentum, which is a simple task with the usual angular momentum coupling techniques [60]. By doing so, one realizes that the vector Coulomb, longitudinal and transverse electric have natural parity which means that $l_\alpha + l_i + J$ is even, the transverse magnetic has unnatural parity, meaning $l_\alpha + l_i + J$ will be odd. The situation is reversed for the case of the axial-vector terms.

2.3.7 Model space considerations

Maybe the crudest approximation that we do while calculating the nuclear excitation spectra is, that we assume for all nuclei a ground state for the RPA with a given spin and parity of $J^\pi = 0^+$. For odd-odd and odd-even systems we will therefore probably have not the right low energy behavior. However our reactions are dominated by giant resonances in the region around 10 – 15 MeV. Classical arguments about oscillations in finite quantum systems show that sum rules and energies are supposed to be smooth functions of the nucleon number. Experimental observed resonance strength and energies support this assumption [64]. Theoretical models as large scale shell model calculations furthermore support this assumption, too [91].

This gives us reason to believe that our model of the RPA is also good for the description of nuclei with an odd number of protons or neutrons. Once again note that the low energy strength of odd-odd and odd-even nuclei will probably not be described correctly.

To guarantee the convergence of our results, we included all single-particle levels in our calculation up to the 8. major oscillation shell.

2.4 Description of the decay

After the calculation of the nuclear excitation cross section with the help of the RPA, we have to determine all allowed decay probabilities for each excited state with its given quantum numbers. The decay will be described within a statistical approach. It is based on the assumption of Niels Bohr, that in capture processes a compound nucleus is formed that almost completely forgets from which constituents it was created [92]. In this approach the formation of a compound nucleus and its decay into the final product are formulated as two separate processes. The theory is based on the work of Hauser & Feshbach [93] and is subsequently also called *Hauser-Feshbach model*. We will shortly formulate how to calculate cross sections within the statistical model, although we are only interested in the decay. However, since we will inherit the nomenclature within the model for our decay probability calculations, it is an useful and only short detour.

2.4.1 Statistical model considerations

A neutron capture reaction with the latter emission of a proton can be described as



or shortly as

$${}^A_Z X^{\nu}(n, p) {}^A_{Z-1} Y^{\mu}. \quad (2.69)$$

The reaction takes place from the ν -th excited state of target ${}^A_Z X$ to the daughter⁵ in its μ -th state. It is clear that we cannot label the explicit state of the compound nucleus since the cross section is determined by all possible allowed combinations that can be reached in the compound nucleus. With a quite simple but tedious derivation, which we will not repeat here, we are able to determine the formula for the cross section within the statistical model. It is given for a reaction ${}^A_Z X^{\nu}(i, j) {}^A_{Z'} Y^{\mu}$ as

$$\sigma_{i,X}^{\nu\mu}(E_{iX}) = \frac{\pi\hbar^2}{2ME_{iX}} \frac{1}{(2J_X^{\nu} + 1)(2J_i + 1)} \sum_{J,\pi} (2J + 1) T_i(E, J, \pi; E_X^{\nu}, J_X^{\nu}, \pi_X^{\nu}) \frac{T_j(E, J, \pi; E_Y^{\mu}, J_Y^{\mu}, \pi_Y^{\mu}) W(E, J, \pi)}{T_{\text{Tot}}(E, J, \pi)}. \quad (2.70)$$

The cross section is calculated for a center-of-mass energy E_{iX} . M is the reduced mass of target and projectile. The state of the compound nucleus is given with energy E , spin J and parity π , subsequently energies, spins and parities with subscripts i or j belong to the corresponding target/daughter nucleus. $W(E, J, \pi)$ corresponds to the width fluctuation corrections that account for decays, that are not fully statistical, but some information remains that influences the available decay choices. The major effect of these width fluctuation corrections is the increase of elastic scattering, where the incoming particle will immediately be re-emitted before the equilibration of the nucleus. The total transmission coefficient T_{Tot} in equation 2.70 gives the transition into all possible bound and unbound states

$$T_{\text{Tot}} = \sum_x T(E, J, \pi; E_x, J_x, \pi_x). \quad (2.71)$$

The task of determining a cross section within the statistical model thus reduces to calculate the transmission coefficients T . We can rewrite equation 2.70 by neglecting the width fluctuation functions $W(E, J, \pi)$ that will not be necessary within our combined model as

$$\sigma_{i,X}^{\nu\mu}(E_{iX}) = \sum_{J,\pi} \sigma_{i,X}^{\text{Form}}(E_{iX}, J, \pi) \times P(E, J, \pi). \quad (2.72)$$

The formation of the compound nucleus for a specific compound spin J and parity π is described by

$$\sigma_{i,X}^{\text{Form}}(E_{iX}, J, \pi) = \frac{\pi\hbar^2}{2ME_{iX}} \frac{1}{(2J_X^{\nu} + 1)(2J_i + 1)} (2J + 1) T_i(E, J, \pi; E_X^{\nu}, J_X^{\nu}, \pi_X^{\nu}). \quad (2.73)$$

The decay probability, which is the quantity that we are interested in, is therefore given as

$$P(E, J, \pi) = \frac{T_j(E, J, \pi; E_Y^{\mu}, J_Y^{\mu}, \pi_Y^{\mu})}{T_{\text{Tot}}(E, J, \pi)}, \quad (2.74)$$

with the same definitions as before.

⁵ Note that we redefined the definitions in equation 2.68 for mother and daughter according to our needs in this section.

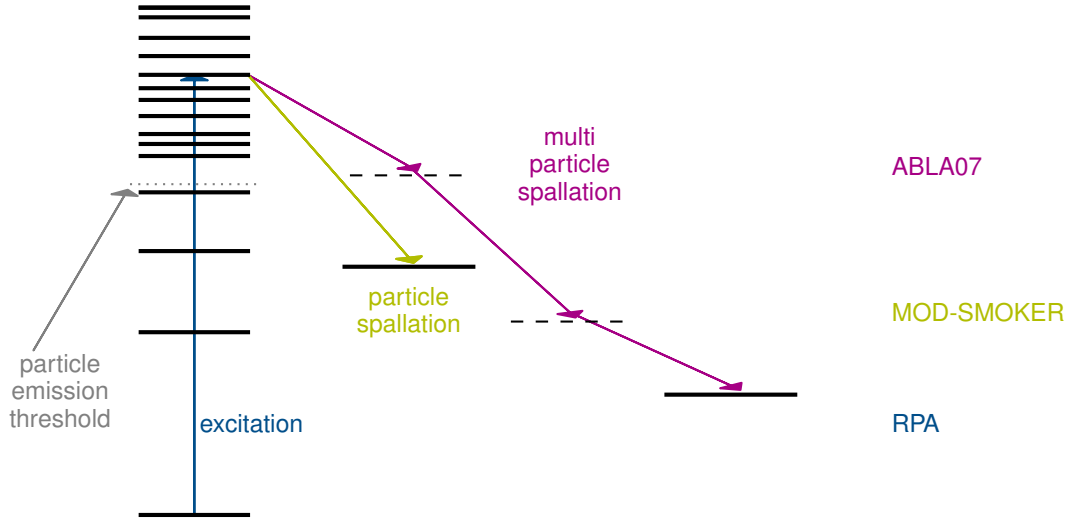


Figure 2.3.: Schematic plot of the utilized model. In the first step we describe the excitation spectra with the help of the RPA. If the excitation is above the lowest particle emission threshold, the nucleus will emit with a specific branching ratio a proton, neutron or an α -particle. These branchings are calculated under the usual compound picture assumption, where formation and deexcitation of the compound nucleus can be treated separately. If the excitation energy is high enough, we allow also for multi-particle emissions that will be calculated within the framework of ABLA07. On the right side of the plot the tools utilized for the different steps are mentioned.

2.4.2 Combined model

Instead of particle captures on nuclei, the formation of the compound nucleus will be described in our work by the excitation cross section given by the previously formulated RPA. In the case of neutral-current scattering processes, the compound nucleus will be the same as the target nucleus in the description above. For charged-current processes, neutrino captures will change the proton number as well as neutron number, while keeping the total mass number constant. Depending on the direction of the process, the energies in the compound will reach energies high enough that particle emission channels are dominant. We therefore require to allow for the evaporation of particles.

The model that we will follow is a combination of the excitation given by the RPA and the spallation, described within the statistical model. Therefore we require simply to change the formation cross section of 2.72 while keeping the description of the decay probability as defined above. Our cross section can be formulated in similar fashion as equation 2.68 as

$$\nu + {}^A_Z X \rightarrow {}^A_Z X^* + \nu' \rightarrow {}^{A-A_j}_{Z-Z_j} Y + j + \nu', \quad (2.75)$$

for the case of neutral-current processes. In the case of charged-current processes it will read as

$$\begin{aligned} \nu_e + {}^A_Z X &\rightarrow {}^A_{Z+1} Y^* + e^- \rightarrow {}^{A-A_j}_{Z-Z_j+1} Z + j + e^-, \\ \bar{\nu}_e + {}^A_Z X &\rightarrow {}^A_{Z-1} Y^* + e^+ \rightarrow {}^{A-A_j}_{Z-1-Z_j} Z + j + e^+, \end{aligned} \quad (2.76)$$

for neutrino/ antineutrino capture processes with the following description of particle evaporation.

Regardless of the exact semileptonic process under consideration, the cross section for a neutrino with incoming neutrino energy E_ν will be described as

$$\frac{d\sigma(E_\nu)}{dE} \sigma(E_\nu, E) = \sum_{J, \pi} \sigma^{RPA}(E_\nu, E, J, \pi) \times P(E, J, \pi), \quad (2.77)$$

where the decay probability is described as shown within equation 2.74.

The most important ingredients for statistical model calculations are the transmission coefficients T and the excited states or the level density, respectively. The reliability of our decay probability is determined by the accuracy with which these values can be evaluated. We now want to discuss how these values are determined.

2.4.3 Transmission coefficients

The transmission coefficient from an excited state in the compound nucleus (E, J, π) to a state $(E_Y^\mu, J_Y^\mu, \pi_Y^\mu)$ in the daughter nucleus under the emission of a particle j with intrinsic spin s_j is given by the summation over all quantum mechanical allowed partial waves as

$$T(E_Y^\mu, J_Y^\mu, \pi_Y^\mu) = \sum_{l=|J-s|}^{J+s} \sum_{s=|J_Y^\mu-s_j|}^{J_Y^\mu+s_j} T_{ls}(E_Y^\mu, J_Y^\mu, \pi_Y^\mu). \quad (2.78)$$

The angular momentum l and the channel spin s couple to J . The transition energy in the chosen channel is $E_{Y,j}^v = E - S_j - E_i^v$, where S_j is the channel separation energy⁶. For the calculation of the individual particle transmission coefficients we solve the Schrödinger equation with an optical potential for the particle-nucleus interaction. The optical potential that we chose for protons and neutrons has been determined by the authors in [94], based on a local density approximation in microscopic infinite nuclear matter. Corrections to the imaginary part have been included [95, 96]. In the case of α -particle emission we use a phenomenological Woods-Saxon potential [97]. The optical α -nucleus potential is one possible reason for uncertainties in the determination of our decay probabilities. Better – although not fully realistic – results might be obtained by the inclusion of double-folding potentials where data so far is still scarce and reliably parameterizations are still out of reach. In the case of deformed nuclei the deformed potential is averaged over all possible angles between the incoming particle and the orientation of the deformed nucleus resulting in an effective spherical potential of equal volume.

In addition to the emission of neutron, proton and α -particles it is necessary to include the dominant γ -transitions. These are of course E1 and M1 transitions. For the M1-photon transition a IPM approach has been used [98, 99]. The transmission coefficient within this picture is then proportional to E^3 . The E1 transitions are calculated on bases of the Giant Dipole Resonance with a Lorentzian shape. The E1 transition coefficient can be calculated as

$$T(E_\gamma) = \frac{8}{3} \frac{N}{A} \frac{Z}{\hbar c} \frac{e^2}{mc^2} \frac{1 + \chi}{3} \sum_{i=1}^2 \frac{i}{(E_\gamma^2 - E_{G,i}^2)^2 + \Gamma_{G,i}^2 E_\gamma^2} \frac{\Gamma_{G,i} E_\gamma^4}{E_\gamma^2}, \quad (2.79)$$

by the emission of a photon with energy E_γ in a nucleus ${}^A_Z N$. In equation 2.79 χ denotes the neutron-proton exchange contribution, its value is 0.2 [100]. The summation accounts for the split of the GDR in statically deformed nuclei along and perpendicular to the axis of rotational symmetry. The energies ($E_{G,i}$) and width ($\Gamma_{G,i}$) of the GDR are parameterized as given by the hydrodynamic droplet approach [101]. In the case of deformation the centroid energies (given in MeV) are related by

$$\begin{aligned} E_{G,1} + 2E_{G,2} &= 3E_G, \\ E_{G,2}/E_{G,1} &= 0.911\eta + 0.089, \end{aligned} \quad (2.80)$$

where η describes the ratio of the diameter along the nuclear symmetry axis to the diameter perpendicular to it [102].

Additionally we require for the determination of the transmission coefficients the information of excited states in the daughter nuclei. If available, the first 19 excited states are taken from the RIPL-3 database [103]. These levels are only used if it is believed that the level spectrum of the nucleus is fully known up to this energy. If the energy is above the last used level, a level density model is utilized.

A good example how the transition from discrete excited states to a level density description can be envisioned is by the total transmission coefficient $T_j^{Tot}(E, J, \pi)$, which is simply a summation over all energetically possible transmissions to excited states in the daughter nucleus. This transmission coefficient is relevant when comparing to experimental cross sections, since in general all target states will be populated and we therefore have to sum over all allowed final states of the reaction

$$T_j^{Tot}(E, J, \pi) = \sum_{\mu=0}^{\mu_{max}} T_j(E, J, \pi; E_Y^\mu, J_Y^\mu, \pi_Y^\mu) + \int_{E_{\mu_{max}}}^{E-S_j} T_j(E, J, \pi; E_Y, J_Y, \pi_Y) \rho(E_Y, J_Y, \pi_Y) dE_Y. \quad (2.81)$$

When no information about excited states in the daughter nucleus exists, the summation is changed in a global integration over the level density ρ .

⁶ The masses within the statistical model are the same as taken in the discussion of adjusting the RPA model space [74].

2.4.4 Level density description

Nuclear level densities are possibly the largest input for the statistical model, because it basically settles the position of the states where the transitions go to. For high excitation energies it is not useful to speak of single states anymore, because a lot of resonances contribute and a large overlap within the states exists. Instead of counting these levels individually, it is useful to describe these levels as a level density. It is given as⁷

$$\rho(E, J, \pi) = \frac{\# \text{ states with } J \text{ and } \pi \text{ within } E \text{ and } E + \Delta E}{\Delta E}. \quad (2.82)$$

The nuclear level density model that we apply in our work is the *back-shifted Fermi-gas* model (BSFG). This model is a phenomenological approach that – despite its simplicity – compares well with Monte-Carlo shell model [105] or combinatorial approaches [106]. The BSFG model can be factorized as

$$\rho(E, J, \pi) = \Pi(E, \pi)F(E, J)\rho(E), \quad (2.83)$$

where the first factor describes the projection on a specific parity, the second factor accounts for a spin distribution [4, 107]. $\rho(E)$ gives the total level density which reads as

$$\rho(E) = \frac{1}{\sqrt{2\pi\sigma}} \frac{\sqrt{\pi}}{12a^{1/4}} \frac{e^{(2\sqrt{a(E-\delta)})}}{(E-\delta)^{5/4}}. \quad (2.84)$$

The spin- and parity-distributions can be given as

$$\Pi(E, \pi) = \frac{1}{2}, \quad (2.85)$$

$$F(E, J) = \frac{2J+1}{2\sigma^2} e^{-\left(\frac{J(J+1)}{2\sigma^2}\right)}, \quad (2.86)$$

where we use the following abbreviation

$$\sigma^2 = \frac{\theta_{\text{rigid}}}{\hbar^2} \sqrt{\frac{(E-\delta)}{a}} \quad \text{with} \quad \theta_{\text{rigid}} = \frac{2}{5} m_u AR^2. \quad (2.87)$$

By the total level density formula of the BSFG, given in equation 2.84, one can already observe that this model diverges if the factor δ is larger than zero and the energy approaches values close to δ . We circumvent this non-physical behavior of the Fermi-gas model by combining it with the *Constant-Temperature model* [108]. The Constant-Temperature model assumes that the total level density increases as a simple exponential. It can be formulated as

$$\rho_{CT}(E) \propto \frac{e^{(E-\delta')/T}}{T}, \quad (2.88)$$

which resembles the low energy behavior of the level density obtained from excited states quite well [107]. For a smooth description from low to high excitation energies we apply a tangential fitting for the total level density and its first derivative, which will give us the values of δ' and T by the fitting routine.

In the upper definitions of spin and parity-projections, a few crucial points have to be noted before we move on. First of all, we assumed that parity and spin projections are disentangled from each other. For high excitation energies this will definitely be a fair description, since a lot of levels contribute – most of them broad resonances – at the energy that we are interested in (see [109, 106]). The parity distribution is simply given by a factor of 1/2 which will also be a valid assumption for high excitation energies. For low energies this description will break down. However, previous studies on parity in nuclear level densities have shown that deviations from this equipartition occurs in general at excitation energies below the particle separation threshold, which is exactly the energy range that is not relevant for our current purposes because the only open channel is the γ -channel, leading to a probability for emitting a γ to 100 %.

Equation 2.87 allows us to fix the total spin distribution by assigning the spin cutoff parameter σ based on models of a liquid drop nucleus. Since the spin projection is completely determined via the spin cutoff, the BSFG level density can therefore be determined with only two parameters, the level density parameter a and the back shift δ . The latter should account for the pairing gap of the nucleus and the spacing between the ground state and the first excited state. Usually,

⁷ Note that within this work we do not differentiate between a state and a level, although in general a difference exists. A state is usually defined with a specific projection of the angular momentum value. Thus the number of states can be related by the number of levels by $N_{\text{states}}(J) = (2J+1)N_{\text{levels}}(J)$. However when we talk about states, we only consider the level given at that energy with a specific spin [104].

the energy gap is the dominant contribution to the back-shift, only close to shell closures the ground space spacing is dominant [107]. These two parameters have to be adjusted to experimental data of the nuclear level density. Obtaining level densities experimentally however is a complicated task that basically consists of counting the number of levels at low excitation energies. For higher energies two possibilities exist to determine experimental information on the nuclear level density. Neutron resonance spacings can give us information on the inverse level density of s- and d-wave [103]. However most experimental resonance spacings have a substantial error which is complicated to reduce. Furthermore it can only be determined at the neutron separation energy.

In the last five years the so called *Oslo-method* proved to reliably obtaining nuclear level densities over the whole energy range up to the particle emission threshold. In this method either neutron pickup or inelastic scattering with ^3He is applied to record the full γ -spectrum as a function of incoming excitation energy [110]. Of course it will not be possible to determine the level density experimentally over the whole nuclear chart. However to guide theoretical descriptions, this method shows promising opportunities in the next few years for the improvement of reliable level density modeling.

In our work we utilize an energy dependent parametrization that correlates the level density parameter a with experimental shell corrections. The level density parameter can be given as

$$a(E, \delta, Z, N) = \tilde{a}(A) \left[1 + C(Z, N) \frac{f(E - \delta)}{E - \delta} \right], \quad (2.89)$$

where

$$\tilde{a} = \alpha A + \beta A^{2/3}. \quad (2.90)$$

The function f is given as

$$f(E) = 1 - e^{-\gamma E}, \quad (2.91)$$

which has two limits. In the case of small excitation energies the function f vanishes, resulting in a strong contribution of the corrections $C(Z, N)$. For high energies the function approaches zero, resulting in a damping of the corrections. The correction parameter C was earlier related to the shell correction S of the liquid droplet model. However its origin is in the correction for nuclei where the description differs from a macroscopic spherical description. Therefore a better choice than the shell corrections S is actually the microscopic correction E_{mic} , that includes corrections due to pairing, shell effects and the deformation of the nucleus.

For the shown parametrization the values α , β and γ have to be adjusted to the experimental information about level densities (that mostly arise from resonant s- and d- wave spacings) as well as the mass model that has been utilized, since the microscopic correction is of course not model independent. In our work we use the parameter set determined by the authors of [4], which have been adjusted to the FRDM mass model and the experimental masses given by the Audi compilation [74]⁸. Their values are $\alpha = 0.1337$, $\beta = -0.06571$ and $\gamma = 0.04884$.

Before we move on, we still have to explain how we calculate the back-shift for all nuclei under consideration in this work. The back-shift is correlated with the pairing energy in the nuclear droplet model, that can be given as $k \times 12/\sqrt{A}$, where k is +1 for even-even nuclei, -1 for odd-odd nuclei and $k = 0$ else.

The authors in [4] show that actually a more detailed description can be obtained with the help of the neutron and proton pairing gaps. The proton pairing gap is given by

$$\Delta_p(Z, N) = \frac{1}{2} (2B(Z, N) - B(Z - 1, N) - B(Z + 1, N)). \quad (2.92)$$

$B(Z, N)$ gives the binding energy of nucleus ${}^A_Z X$. The neutron pairing gap can be obtained in the same way. The back-shift δ for the BSFG model can then be extracted as

$$\delta(Z, N) = \frac{1}{2} (\Delta_p(Z, N) + \Delta_n(Z, N)). \quad (2.93)$$

⁸ Note that the fitting has been evaluated for the mass model in 1995. We are however using the updated database of 2003 which includes various changes of nuclei away from the valley of stability. We assume that the changes for our results will be negligible, although a reevaluated fitting procedure is desired.

2.4.5 Applicability of the statistical model

As already stated above, the statistical model allows for a description of the cross section as an “averaged” description. Therefore we have to assume that in the compound nucleus a high level density exists, such that for each spin and parity of the compound nucleus several levels/resonances are available [111]. For nuclei with an intrinsic high level density such as heavy or deformed nuclei this will definitively be the case, for light and semi- or doubly-magic nuclei this assumption might break down.

For the description of decay probabilities within the Hauser-Feshbach model the level density should be sufficient for a realistic description of the decay probabilities in the region of the valley of stability. This is of course due to the fact that the decay probabilities will start to be important when the excitation energy is above the first particle emission threshold, because then not only the γ -channel is open. For nuclei close to the valley of stability this is approximately at an energy of 7 – 8 MeV where the number of levels should be sufficient.

In nuclei far off the valley of stability, the particle separation energy will decrease very quickly. With the reduction of the separation energy the applicability of the statistical model will decrease because the level density in the compound might not be large enough. However for the description of the decay probabilities moving closer to a drip-line might actually be advantageous, because in a very neutron rich nucleus the decay probability of emitting a proton is energetically strongly disfavored. A good example therefore is the neutron separation energy for ^{150}Sn which is at an energy of solely 2.5 MeV, whereas the proton and α separation energy is given at an excitation energy of 19.6 MeV and 11.5 MeV respectively, according to the FRDM mass model [74]. We therefore note that for nuclei far off the valley of stability the decay probability for low excitation energies will be governed by only one particle emission channel. Thus there is only a competition between the γ -channel and the particle emission channel.

Typically, particle transmission coefficients are in general higher than the γ transmission coefficients [112], thus in the case of only one particle emission channel the decay probability should be well described.

2.4.6 Multi-particle spallation

In the last section we argued, that for neutron- and proton-rich nuclei the corresponding separation energies will decrease with increasing neutron and proton number. We mentioned that in the case of ^{150}Sn the neutron separation energy is at 2.5 MeV.

At already 3.5 MeV the two-neutron emission channel opens. If we assume that the typical excitation spectrum for supernova-neutrino induced excitations of our RPA is in the region of the giant dipole resonances, where the energy will be above ten MeV, we observe that the most probable channel will not always be an one particle decay, but multi-particle emission can play a tremendous role. Therefore we need to find a good description that allows us to follow all possible decay probabilities that can occur. In general we therefore require a model that allows us to calculate the decay probabilities for single and several particle emission in the whole energy range that can be reached by nuclear excitation of neutrino-nucleus scattering induced by neutrinos with a supernova spectrum.

In the case where only one particle will be emitted in the process, we utilize the MOD-SMOKER code. It is a code written for the calculation of astrophysical reaction rates within the statistical model [113]. In its common description it only allows for the emission of one particle in the outgoing channel. We therefore need a description of the decay channels for several particle spallation.

We will calculate them with the statistical deexcitation code ABLA07. It is a dynamical Monte-Carlo code that describes the thermalized system by simultaneous break-up, particle emission and fission [114]. Contrary to the description given by the SMOKER code, ABLA07 includes the emission of neutrons, light charged particles (p, d, t, \dots) up to $Z = 3$, γ rays and intermediate mass fragments of arbitrary size. The way of describing the various particle width is different from the way that we showed above in the case of the Hauser-Feshbach code MOD-SMOKER. Therefore we would like to show how the multi-particle spallation is calculated in the ABLA07 code.

ABLA07 is based on a simplified Hauser-Feshbach model that is called *Weisskopf-Ewing* theory [50]. This theory provides a description within the region where the levels of the final nucleus are given by a continuum (such as a pure level density description). Following from this request, one can note that this theory is adjusted to reactions at high excitation energies where the first excited states in nuclei do not contribute or only play a diminishable role. Thus a complete description with a nuclear level density over the whole energy range has no influence on the final result, while in the previously mentioned statistical model – especially at low energies – the excited states show a strong impact. In general, one is able to derive the Weisskopf-Ewing formula from the Hauser-Feshbach formula, as stated in 2.70; a detailed explanation can be found for example in [115]. We now would like to repeat the basic thoughts of obtaining the Weisskopf-Ewing formula from the Hauser-Feshbach model. Therefore we assume the same reaction as for the Hauser-Feshbach reaction ${}^A_Z X(i, j) \rightarrow {}^A_{Z'} Y$. The basic requirement for the Weisskopf-Ewing formula is that the energy of the compound nucleus is large enough that the level density is sufficiently high, such that the decay is dominated by a level density description. The fraction to discrete known states should be limited. At such high energies width fluctuations will be very small and can therefore be neglected. If we furthermore assume that the level density is parity independent and that the spin dependence is proportional to $(2J + 1)$ we can in contrary to equation 2.72 factorize the cross section as

$$\sigma_{i,X}(E_{iX}, J_X) = \sum_J \sigma_{i,X}^{CMP}(E_{iX}, J_X; E, J) \times P(E), \quad (2.94)$$

with E_{iX} being the energy of the incoming particle, J_X is the total angular momentum of particle X . The compound energy and spin is given by E, J . Note that only the formation cross section is sensitive to the compound spin and parity, the decay probability is completely independent from spin and parity. We should stress once more that the RPA will be responsible for the formation cross section and we focus here on the description of the decay.

To show how one can easily derive the Weisskopf-Ewing decay probability on basis of the upper assumptions, we describe the decay by combinatorics. Therefore we start with describing the decay probability from the compound nucleus into nucleus Y at an energy E_Y

$$P(E, E_Y) = \frac{\mathfrak{J}_{J_Y}(E, E_Y)}{\sum_x \int_0^{E_{max,x}} \mathfrak{J}_{J_x}(E, E_x) dE_x}, \quad (2.95)$$

where the integration in the denominator is carried out over the kinematic accessible region in the residual nucleus and summed over all open channels. $\mathfrak{J}_{J_Y}(E, E_Y)$ is a sum of the product of transmission coefficients and level densities for the desired channel with daughter nucleus Y . E denotes again the energy of the compound nucleus and E_Y is the energy of the daughter nucleus Y . The same holds true in the denominator for $\mathfrak{J}_{J_x}(E, E_x)$, where the sum is carried out for all allowed final-state spins J_x that satisfy angular momentum conservation.

For this derivation, that we like to present here, we only consider spinless particles where the transmission coefficients T_l^Y can solely be considered by orbital angular momentum l . Note that the result will not depend on this restriction, as we will see later. The term \mathfrak{J} can be given as

$$\mathfrak{J}_{J_Y}(E, E_Y) = \sum_{J_Y=J_{Y_{min}}}^{\infty} \sum_{l=|J-J_Y|}^{J+J_Y} \frac{T_j^l(\epsilon_Y) \rho_j(E_Y, J_Y)}{\rho(E, J)}, \quad (2.96)$$

where ϵ is the kinetic energy of the emitted particle, the residual nucleus is left with an excitation energy E_Y . $J_{Y_{min}}$ will be either 0 or 1/2 depending whether the number of nucleons in the nucleus is even or odd. A similar expression can be obtained for the denominator of equation 2.95. The level density ρ_j denotes the level density in the residual nucleus, while ρ is the level density of the compound. By factorizing the level density as $(2J+1)\rho'$ ⁹ and interchanging the two sums with the help of a generalized delta function $\Delta(j_1, j_2, j_3)$, returning 1 if the three angular momenta satisfy the vector relationship $\vec{j}_3 = \vec{j}_1 + \vec{j}_2$ and 0 otherwise, we obtain

$$\mathfrak{J}_{J_Y}(E, E_Y) = \rho'(E_Y) \sum_{l, J_Y} T_Y^l(\epsilon_Y) (2J_Y + 1) \Delta(J, l, J_Y). \quad (2.97)$$

The angular momentum conservation is provided with the help of the Δ function. With help of the identity

$$\sum_{J_Y} (2J_Y + 1) \Delta(J, l, J_Y) = (2J + 1)(2l + 1), \quad (2.98)$$

the value \mathfrak{J} becomes

$$\mathfrak{J}_{J_Y}(E, E_Y) = \frac{(2J_Y + 1) \rho'_Y(E_Y)}{(2J + 1) \rho'(E)} \sum_{l=0}^{\infty} (2l + 1) T_j^l(\epsilon_Y). \quad (2.99)$$

To obtain the final Weisskopf-Ewing form for the decay probability we furthermore note that the reaction cross section is given as in the case of the Hauser-Feshbach approach by

$$\sigma_Y^{reac}(\epsilon_j) = \frac{\pi \hbar^2}{2ME_{iX}} \sum_{l=0}^{\infty} (2l + 1) T_j^l(E_Y). \quad (2.100)$$

Solving for $T_Y^l(E_Y)$ and inserting into $\mathfrak{J}_{J_Y}(E, E_Y)$, we are able to write equation 2.95 as

$$P(E, E_Y) = \frac{k_Y^2 \sigma_Y^{reac}(\epsilon_j) \rho'_Y(E_Y)}{\sum_x \int_0^{E_{max,x}} dE_x k_x^2 \sigma_x^{reac}(\epsilon_x) \rho'_j(E_x)}. \quad (2.101)$$

k_x gives the wave number of the observed channel $k_x = \sqrt{2M_x \epsilon_x} / \hbar$. For the total decay probability we have to integrate above equation over all energetically allowed final energies. It has to be carried out up to the compound energy minus the separation energy of the channel plus additional barriers for charged particles – such as the Coulomb potential – that will be labeled by B [116]

$$P(E) = \frac{\int_0^{E-E_j-B_j} k_j^2 \sigma_Y^{reac}(\epsilon_j) \rho'_Y(E_Y) dE_Y}{\sum_x \int_0^{E_{max,x}} k_x^2 \sigma_x^{reac}(\epsilon_x) \rho'_j(E_x) dE_x}. \quad (2.102)$$

Equation 2.102 is the decay probability given in the Weisskopf-Ewing approach. The derivation that we showed can be carried out for nonzero spin, which however is more tedious but showing the same result. The quantities σ^{reac} are usually referred to as inverse cross sections, since they correspond to the absorption of the emitted particle. Within the Weisskopf-Ewing approach it is assumed that the cross section for absorption is not sensitive in which nuclear state the particle is absorbed [117]. For sufficient high energies the inverse cross section can thus be given by the area of the nucleus as πR^2 , under the assumption that the radius R of the nucleus is considerably larger than the radius of the projectile. Within this work we calculate the inverse cross sections with energy dependent cross sections based on the ingoing wave boundary condition model [118].

With the inclusion of the correct prefactors, it is very easy to convert the integrand in the upper equation to a decay width, resulting that equation 2.102 can also be formulated to $P(E) = \Gamma_j(E) / \sum_k \Gamma_k(E)$. The total decay width of emitting

⁹ $\rho' = \rho / (2J + 1)$ denotes the remaining part of the original level density.

a particle j with kinetic energy ϵ_j from a nucleus with excitation energy E leaving a nucleus Y at an excitation energy $E_{Y\mu}$ will be calculated in the abrasion-ablation code by

$$\Gamma_j(E) = \frac{2j_j + 1}{2\pi\rho(E)} \frac{2m_j}{\pi\hbar^2} \int_0^{E_j - S_j - B_j} \sigma^{reac}(\epsilon_j) \rho_Y(E_{Y\mu}) (\epsilon_j - B_j) dE_{Y\mu}. \quad (2.103)$$

Within this formula j_j denotes the spin of the emitted particle, ρ and ρ_Y are the level densities in the initial (compound) and daughter nucleus. Again the width requires the knowledge of the cross sections σ^{reac} for the inverse process. For the calculation of these reverse cross sections, several effects have been introduced to improve the simply geometrical cross section πR^2 . In the case of charged particle emissions the Coulomb repulsion and its quantum mechanical tunneling play a substantial role. Therefore additional barriers are introduced that try to incorporate the effects from the Coulomb potential and the nuclear potential. The nuclear potential is empirically treated as shown in [116], whereas for the Coulomb potential a charged sphere is assumed, just as in the case of our single-particle model for the proton part of the Woods-Saxon. The inverse cross section gives

$$\sigma^{reac} = \pi R^2 \left(1 - \frac{B_j}{\epsilon_j}\right), \text{ with } R = r_0(A_j^{\frac{1}{3}} + A_Y^{\frac{1}{3}}) + \sqrt{\frac{(A_Y + A_j)\hbar^2}{2MA_Y\epsilon_j}}. \quad (2.104)$$

M is the reduced mass of daughter and ejectile. The radius is approximated by two touching spheres plus corrections for low energy scattering. The corrections arise due to the fact that for low kinetic energies the wavelength of the absorbing particle will be comparable to the size of the nuclear potential – which in this case is assumed to be a square well – and is therefore a strong influence for the low energy capture cross section. The center-of-mass energy is given simply by

$$E_{Yi} = \frac{A_Y}{A_Y + A_j} \epsilon_j. \quad (2.105)$$

However we can observe that tunneling is not included in the above description of the cross section. At energies below or slightly above the Coulomb barrier, tunneling through the barrier will play a major role.

The potential is calculated as a sum of the nuclear potential plus the charge of a charged sphere, $V(r) = V_n(r) + V_C(r)$. The nuclear potential is parametrized as suggested by Bass [116]. At energies up to the Coulomb barrier tunneling through the barrier is a very important process that needs to be considered. Within the dynamical code ABLA07 the decay width is calculated with the classical cross section given in equation 2.104 resulting to a width Γ_{class} . This classical width is then multiplied by a function $f(E_Y, A_Y, A_j, V)$ that tries to mimic the change of the inverse cross section due to the inclusion of tunneling, $\Gamma_{ABLA} = f(E_Y, A_Y, A_j, V)\Gamma_{class}$. The tunneling function can be approximated by

$$f(E_Y, A_Y, A_j, V) = 10^{\left(\frac{x^{(-4.3/\ln(10))}}{2500}\right)} \quad x = \left(\frac{T}{(\hbar\omega)^2} \frac{1}{M^{(1/4)}}\right). \quad (2.106)$$

Within this formula x is the ratio of the nuclear temperature T of the daughter nucleus A_Y to the potential barrier energy V (given by $\hbar\omega$) times the inverse reduced mass M to the power of $1/4$.

The energy $\hbar\omega$ can be obtained by the second derivative of the Bass potential. The temperature T of the daughter nucleus is given by $\sqrt{a/E_Y^H}$ for the case of the Back-shifted Fermi-gas model, or by T_{CT} from the constant temperature model.

This parametrization has been obtained by numerical integration of equation 2.103, once with the use of the classical cross section 2.104 and once with the inclusion of tunneling through the barrier following the approach given by Avishai [119]. The ratio of the latter width and the classical width led to the function $f(E_Y, A_Y, A_j, V)$. It is of course obvious that specifically for low incoming energies the cross section is tremendously sensitive to the tunneling description.

Within our two-step approach the neutrino scattering determines the excitation energy of the compound nucleus. Therefore the compound energy (and its angular momentum value) will be dictated by the RPA. Within ABLA07 the kinetic energy of emitted particles is also required for the decay probabilities that we are interested in, because it determines the excitation spectrum of the residual nucleus. This energy will be determined from a Maxwell-Boltzmann type distribution at the corresponding temperature. Charged particle effects such as Coulomb barriers have of course to be included. The kinetic energy has been randomly picked from the energetically allowed region of the Maxwell energy distribution. The ideal way for obtaining a random number for an exponential decreasing function such as $e^{-E/T}$, can simply be given by

$$E = -T \ln(PRN), \quad (2.107)$$

PRN is hereby a pseudo-random number within the interval $[0, 1]$. For obtaining the pseudo-random numbers within our calculations we applied an algorithm that is known as the *Mersenne-Twister* [120], generating pseudo-random numbers in a very fast manner.

In the next step we would like to get an insight about the energy spectra of the emitted particles in the Weisskopf-Ewing approach. For this we can start from equation 2.94 in combination with equation 2.102 and differentiate for ϵ_j . We obtain

$$\frac{\partial \sigma_{iX}}{\partial \epsilon_j} \propto \epsilon_j \sigma_Y^{reac}(\epsilon_j) \rho_Y'(E_Y), \quad (2.108)$$

where the values which are not sensitive on ϵ_j are neglected and we furthermore utilized that $k_j^2 = 2M\epsilon_j/\hbar^2$. By simple thermodynamical relations [121] we are able to obtain the level density for the residual nucleus as [122]

$$\rho_Y(E - S_j - B_j) = \rho_Y(0) \exp\left(2\sqrt{a(E - S_j - B_j)}\right) \exp\left(-\frac{\epsilon_j}{k_B T}\right). \quad (2.109)$$

a denotes the usual level density parameter and T gives the nuclear temperature of the residual nucleus. The interesting fact which can be observed is that the energy spectrum with these approximations can be written as

$$\frac{\partial \sigma_{iX}}{\partial \epsilon_j} \propto \epsilon_j \sigma(\epsilon_j) \exp\left(-\frac{\epsilon_j}{k_B T}\right). \quad (2.110)$$

Additionally we are able to replace the cross section by $1/v = 1/\sqrt{\epsilon_j}$, trying to cover the low energy behavior of particle capture processes. For charged particle captures the cross section is modified by an additional factor $((\epsilon_j - B_j)/\epsilon_j)$ arising from equation 2.104, while the final kinetic energy of the emitted charged particle is higher by the value of the Coulomb barrier [123, 124]. In general the energy distribution has to be split up into two parts

$$\frac{\partial \sigma_{iX}}{\partial \epsilon_j} = \begin{cases} \sqrt{\epsilon_j} \cdot e^{-\frac{\epsilon_j}{T}}, & \text{if the emitted particle is a neutron,} \\ \frac{\epsilon_j^{(3/2)}}{\epsilon_j + B} \cdot e^{-\frac{\epsilon_j}{T}}, & \text{if the particles are charged.} \end{cases} \quad (2.111)$$

An exact formulation for the creation of energy spectra of these types with pseudo-random numbers cannot be given. However an approximation written as

$$\epsilon_j = \begin{cases} 2T \sqrt{\ln(PRN) \cdot \ln(PRN)} & \text{for neutrons,} \\ 3T (-\ln(PRN) \cdot \ln(PRN) \cdot \ln(PRN))^{1/3} & \text{for charged particles,} \end{cases} \quad (2.112)$$

can give very similar results, as has been shown in [114]. Note that each PRN implies a new generated pseudo-random number. To span the whole range of allowed kinetic energy values, for each compound energy and spin 1000 iterations have been carried out. The decay probabilities for each channel have been summed and then renormalized. The amount of 1000 iterations might look very small to span the whole range of allowed nuclear excitations. However the computing time tremendously increases when increasing the amount of iterations for a specific compound energy.

ABLA07 includes the possibility for emission of γ radiation. This is not common in evaporation codes because – as we already noted above – if particle emission is allowed this channel will dominate. However at energies slightly above the channel opening, the γ channel can become competitive to particle emission for heavy compound nuclei. Since we do not consider parity explicitly, the gamma width can be described via the giant dipole resonance to

$$\Gamma_\gamma(E) = \sum_{|I=J-1|}^{J+1} \int_0^E \epsilon_\gamma^3 k(\epsilon_\gamma) \frac{\rho(E - \epsilon_\gamma, I)}{\rho(E, I)} d\epsilon_\gamma. \quad (2.113)$$

E gives the excitation energy of the compound/mother nucleus and $k(\epsilon_\gamma)$ is the radiative strength function for an electric dipole transition [125].

The standard model for the decay probability within the Weisskopf-Ewing approach does not consider changes in the angular momentum due to particle emission. To overcome this, a formalism has been applied that determines the distribution of angular momentum during the emission from an excited nucleus with finite angular momentum. We will not repeat the whole derivation of estimating the orbital momentum distribution, just note that the code evaluates the most probable value of the orbital angular momentum l_{orb} from a collinear alignment of the total angular momenta of compound and daughter nucleus. The orbital momentum distribution is then approximated by a Gaussian with a mean value l_{orb} . The actual value is chosen by randomly picking the angular momentum value from the Gaussian.

Of course one can observe that numerous input is required. As the main input parameter we have to mention the level density, which is given by a Fermi-gas plus Constant-Temperature model, as in the case of MOD-SMOKER. However the detailed parametrization is different, although a similar behavior of the total level density will be obtained. For a more detailed description of the different input parameters and the description of the fission width within the dynamical code ABLA07, the reader is referred to [114].

2.4.7 The unified nuclear model

At this point, where we have discussed the initial components of our nuclear model, we simply need to combine them. In figure 2.3 we show schematically how our model is set up. The first step considers the initial nucleus on which the neutrinos will scatter inelastically. As mentioned above our nuclear model should give a good description of the resonances in the region of the giant dipole resonance as well as a decent description of low lying states. The RPA method hereby is the optimal tool for our task, given the amount of nuclei that we have to consider. With the help of the description above, we are able to obtain the cross section for population of an excited state, both for charge-conserving and charge changing reactions. Once the nucleus is excited by neutrino-scattering/-capture processes, additional particle emissions are considered. These particle emissions are described either by MOD-SMOKER, for one particle emission, or ABLA07 if more than one particle will be emitted. The total rate for emitting one neutron can then be given via

$$\sigma_{1n}(E_\nu) = \sum_i \sigma_{RPA}(E_\nu, E_i) \cdot p_{1n}(E_i). \quad (2.114)$$

This expression is also valid for capture and scattering processes. The initial energy of the neutrino is given as E_{ν_e} , the intermediate compound energy is given by E_i . At this compound energy the decay probability is determined. Of course we sum over all allowed intermediate compound energies. For different channels this formula can be easily generalized.

Above formula for the partial neutron emission cross section will be evaluated as a function of incoming neutrino energy. Within the stellar environment, we will never have one fixed energy, instead we have a distribution of neutrino energies. The optimal solution would be to use the discretized spectra of the neutrino distribution functions obtained within the simulations of the astrophysical environment, such as a core-collapse supernova and especially the neutrino-driven wind originating after the core has collapsed and the shock wave is already on its way outwards and fold the cross section with this distribution of neutrino energies. Computationally more feasible is the assumption, that the neutrino spectrum can be described by a standard Fermi-Dirac distribution

$$f(E, T, \mu) = N \left[1 + \exp\left(\frac{E - \mu_\nu}{T_\nu}\right) \right]^{-1}, \quad (2.115)$$

where E denotes the neutrino energy, T_ν is called neutrino temperature and μ_ν is the neutrino chemical potential. The factor N accounts for a proper normalization of the neutrino spectrum and can be evaluated to $0.5546/T_\nu^3$, if μ_ν equals zero. For the proper units, we require the neutrino temperature and the chemical potential to have units of MeV. For our purposes within the neutrino-driven wind it is usually sufficient to have a neutrino chemical potential of $\mu = 0$ MeV and only the neutrino temperature is required to be adjusted to fit the data. We should also note that a slightly better fit can be obtained by doing a so called α -fit, that reproduces the high energy part of the distribution function more consistently. Nevertheless the Fermi-Dirac distribution is and has been widely used. For comparison purposes therefore we will still use the Fermi-Dirac spectrum.

Thus for the nucleosynthesis in an astrophysical environment, we define the total cross section by simply folding with the neutrino distribution function. The one-neutron emission cross section then reads as

$$\sigma_{1n}^{\nu, \bar{\nu}}(T, \mu) = \int_0^\infty \sigma_{1n}(E_\nu) f(E_\nu, T, \mu) E_\nu^2 dE_\nu, \quad (2.116)$$

where we usually drop the second argument because, as argued above, the chemical potential is in the cases we are looking at always zero. The superscripts ν or $\bar{\nu}$ are used to specify whether a neutrino or antineutrino reaction is considered. The integration is carried out from zero to infinity. In general the cross section is increasing with incoming neutrino energies, however the distribution functions decrease faster than the neutrino cross section will rise, which will still give us a finite result. However, in our actual calculations we considered neutrino energies up to 180 MeV to have fully converged results, although very little strength in excited states above 50 MeV could be observed.

The commonly assumed values for the neutrino temperature have been varied over the years. The tendency seems to go towards lower temperatures the more the simulations advance. As a reference value we would like to quote the values coming from one core collapse simulation [12, 47, 126]. The neutrino temperatures are given as

$$\begin{aligned} T_{\nu_\mu} &\approx T_{\bar{\nu}_\mu} \approx T_{\nu_\tau} \approx T_{\bar{\nu}_\tau} \approx 4.5 \text{ MeV}, \\ T_{\bar{\nu}_e} &\approx 4.62 \text{ MeV}, \\ T_{\nu_e} &\approx 3.86 \text{ MeV}. \end{aligned} \quad (2.117)$$

These above values for the neutrino temperatures are related to the cooling of the proto-neutron star with a typical cooling lifetime of about 10-20 seconds. However in our nucleosynthesis studies we will always state the neutrino

temperatures for all flavors. Note that there is the aforementioned hierarchy within the neutrino temperatures and – as we will see – consequently for the mean neutrino energies, too.

If we calculate the mean energy of a Fermi-Dirac distribution, under the assumption that the neutrino chemical potential is zero and neutrinos are ultra relativistic, we obtain

$$\langle E \rangle = \int_0^\infty E_\nu f(E, T, \mu = 0) E_\nu^2 dE_\nu = N \int_0^\infty \frac{E_\nu^3}{1 + \exp(E_\nu/T_\nu)} dE_\nu. \quad (2.118)$$

The integral is actually analytical solvable by substitution of variables leading to the above mentioned relation between neutrino temperature and average neutrino energy

$$\langle E \rangle = 3.15 T_\nu. \quad (2.119)$$

This relation allows us to determine the total distribution function simply by knowing the mean neutrino energy. Once more we would like to stress that detailed knowledge of the neutrino spectra might change the results, because the Fermi-Dirac spectrum is a rather simple fit. However, within our results we will also discuss changes in the nucleosynthesis due to changes of the spectra which will be large enough to cover possible errors within the parametrization.



Part III.

Results



3 Neutrino-induced spallation rates

Before we will show the total final rates folded over neutrino temperature, as explained in 4.9.1, we will spend some time on the different inputs that are required for our description of the decay.

3.1 Consistency

Consistency of the decay

Since we are using two different models for the description of the decay probability, the reader might ask about the consistency of the obtained decay probabilities. Due to the fact that we use the statistical MOD-SMOKER code for the description of one-particle spallation and for several particle spallation we rely on the de-excitation code ABLA07, it might be possible that on the transition between both descriptions differences arise.

Therefore the most important fact is that for both models the same channel openings are used. These are given from the separation energies of the used mass model. As already mentioned before, the mass model that we utilized is the FRDM mass model [75], whenever possible we apply experimentally known nuclear masses [74]. In the case of ABLA07 initially a different mass model was used, however for consistency we also implemented the FRDM mass model within the ABLA07 code.

A first test for a consistent description of the decay probabilities with our combined statistical approach will be to compare the results of the low energy part of both models used in our description. If these probabilities show good agreement – especially in the region around the two-particle separation energy – we know that our approach is similar to applying the Weisskopf-Ewing model over the whole excitation spectrum, but with the advantages of a more suitable description for low energy cross sections including experimental known excited states as well as the inclusion of E1 and M1 transmissions for the γ -channel.

Before we move on and discuss the results of our calculated decay probabilities, we will spend some time on the most important parameters for the calculations of the decay probabilities that will have a strong influence on the calculated decay probabilities. A large influence will be given by the behavior of the level densities. In figure 3.1 we show the total level densities of both models in an energy regime up to 30 MeV for several nuclei, because – as discussed in section 2.4.3 – the transmission coefficients for the decay probabilities are at higher excitation energies calculated with the help of the level density.

This set of nuclei has been chosen for several reasons. The primary reason why we chose these nuclei are to observe the differences between even-even (^{56}Fe , ^{64}Ge), even-odd (^{121}Sn , ^{41}Ca), odd-even (^{107}Ag) and odd-odd (^{64}Cu) nuclei, because it has been shown that the low energy part of the level density is very sensitive to the back-shift introduced in subsection 2.4.4. Additionally some nuclei shown possess a proton-shell closure, that will reduce the level density. Considering these effects, the selected nuclei show a more or less similar behavior. In general the agreement between both models shows a trend to have a maximal diversity for the description of even-odd and odd-even nuclei. In these nuclei the difference can have values up to a factor of 2 – 3.

It is also evident that the description of the level density in the case of the de-excitation code ABLA07 depicts a jump at an energy below 10 MeV depending on the nucleus that arises from the fact of switching the description from a constant-temperature formulation to the Fermi gas description. This feature is avoided in the case of MOD-SMOKER due to a fitting routine, guaranteeing a smooth transition between both level density formulations. In comparison with “experimental” level densities¹, we can observe that both models do on average similarly well on reproducing the low energy behavior of the level density. The statistical model MOD-SMOKER however has the advantage that the level density is only used when no experimental data is known, which is not the case for ABLA07 that always uses a level density description.

Based on the arguments we mentioned above, we can show that for the purposes of this thesis the agreement within the level densities is good enough to have a consistent description of the decay within our approach. We also show that some advances arise due to the fact that we use the statistical code about excited states.

¹ This level density has not been taken from experiments to determine the nuclear level density, instead they have been derived following the basic definition of the level density. As mentioned above the level density is given as $\rho = \# \text{ of states} / \text{energy interval}$. Thus we simply created a level density by the experimental states known within the RIPL-3 database [103].

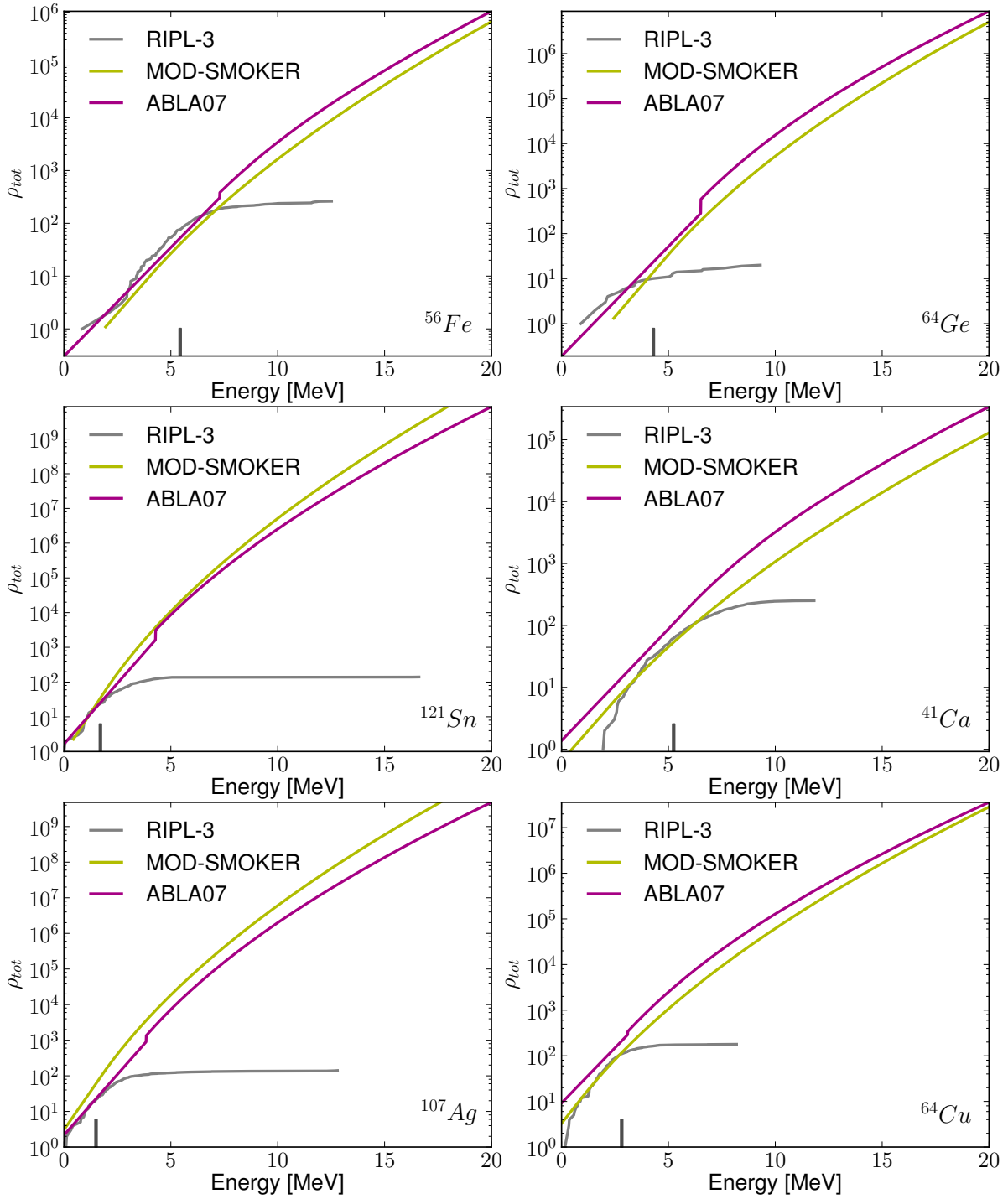


Figure 3.1.: Comparison between the level densities obtained by the statistical code MOD-SMOKER and the dynamical abrasion-ablation code ABLA07. We additionally included an experimentally derived level density that should be met with both theoretical curves from the model. The experimental level density shows a truncation at a few MeV depending on the nucleus. This feature arises from the fact that not all levels are experimentally measured or resolvable and therefore the level density will flatten. This flattening is unphysical and does not describe a physical level density anymore. To obtain a feeling up to which energy the experimental level density is reliable, the ticks on the x-scale have been added. At an energy higher than this value the nuclear database does not guarantee for a complete level scheme. For our plots these limits are a little bit conservative, but nevertheless they show good agreement with the theoretical approach.

After we ensured that the level densities give similar results, we will now turn towards the decay probabilities itself. We will show how the decay probability behaves as a function of energy, for both models utilized in the description of the decay. For a consistent description of the decay probability, the one-particle channel openings should be at the same position and have a similar probability. However, some changes are expected due to the detailed use of known excited states in the residual nuclei. Since we are using the same mass model, the separation energies have to be equal. Furthermore, due to the fact that experimental data is utilized whenever possible and that the underlying mass model is fitted to the known nuclear masses, the separation energies used in this work will be reliable.

The partial decay widths on the other hand are calculated with two different approaches. While the statistical model MOD-SMOKER calculates the width for particle emission by solving the Schrödinger equation with an appropriate optical potential, ABLA07 determines the width with the help of a geometrical cross section corrected by a function $f(E_\gamma, A_\gamma, A_j, V)$ that incorporates tunneling corrections. Although the latter description is computationally very fast, for low energies the width will be very sensitive to the correct description of tunneling effects through the barrier. Therefore the description of solving the Schrödinger equation with an optical equation seems to be more appropriate. In figure 3.3 the decay probabilities for the six exemplary nuclei have been plotted, that already have been utilized for the level density comparison. Note that for each excitation energy the decay probability should result to one – which is simply dictated by conservation of probability. In figure 3.3 one notes that the sum for high energies does not result to one, instead it is smaller than one. The reason for this occurrence is that decay channels below 0.1 % are not plotted for a better visibility.

The results from MOD-SMOKER only incorporate one-particle emission, thus even if the two-particle channel will open, MOD-SMOKER is not able to adjust for this. Therefore the comparison is in general only valid before the two-particle emission threshold opens, which is the energy when we switch from MOD-SMOKER to ABLA07.

One can observe that the channel openings for neutron emission energetically coincide for both models and a similar probability will be obtained. A beautiful example therefore is the case of ^{56}Fe , where the neutron separation energy is at an energy of 10.7 MeV. The trend is similar for the description given by ABLA07 and MOD-SMOKER, although in the energy region of 10 to 15 MeV ABLA07 shows some scatter. We could decrease this scatter by doing more iterations for each compound energy and spin. In the case of ^{64}Ge it is easy to observe that the proton emission channel within ABLA07 opens later than predicted by MOD-SMOKER. The reason for this occurrence is that the inverse process of proton captures on low energies requires the detailed description of tunneling through the barrier. The description within ABLA07 overestimates the Coulomb barrier such that the decay probability is pushed towards higher excitation energies. Note that this is an additional effect which has nothing to do with the mass model used. Furthermore this effect is sensitive on the charge number of the daughter nucleus, which determines the height of the potential. Thus with increasing charge number this effect will increase.

This shift of the decay probabilities for proton rich nuclei seems to be at first sight problematic, because the energy behavior will be different. However, since we utilize a two fold-model, the only possible mistake that we make is a possible overestimation of the one-proton emission region. Due to the fact that this strong shift can only be observed in very proton rich nuclei, where other decay channels than proton emissions are very unlikely, we will take away this additional decay probability only from the two proton emission channel.

We are able to see that once multi particle emission is energetically allowed, these processes will have strong influence. The decay probabilities coming from the MOD-SMOKER model give a completely wrong behavior, whereas the decay probabilities from ABLA07 give a consistent picture. We can see the above mentioned fact as a good indication why our two-model approach is the necessary way to obtain a good description. For low energies MOD-SMOKER will give the correct description of channel openings and Coulomb repulsion, while the multiple particle emission is covered by ABLA07. ABLA07 will then for very neutron/proton rich nuclei additionally suppress the other emission channels due to several neutron/proton emission.

In the case of ^{121}Sn , ^{107}Ag and ^{107}Cu the decay probabilities show a very good agreement. The only difference arises directly at the channel openings, where two additional processes influence the results. The first process that will influence the result is of course the γ -channel which is the only possible channel below the particle emission. Close to the particle

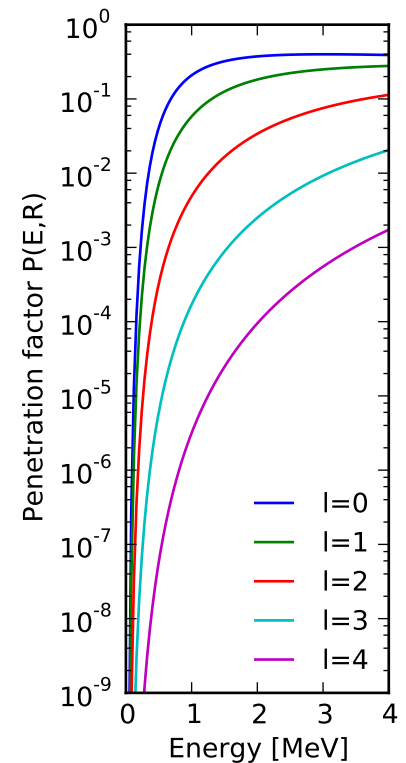


Figure 3.2.: The penetration factor as a function of excitation energy.

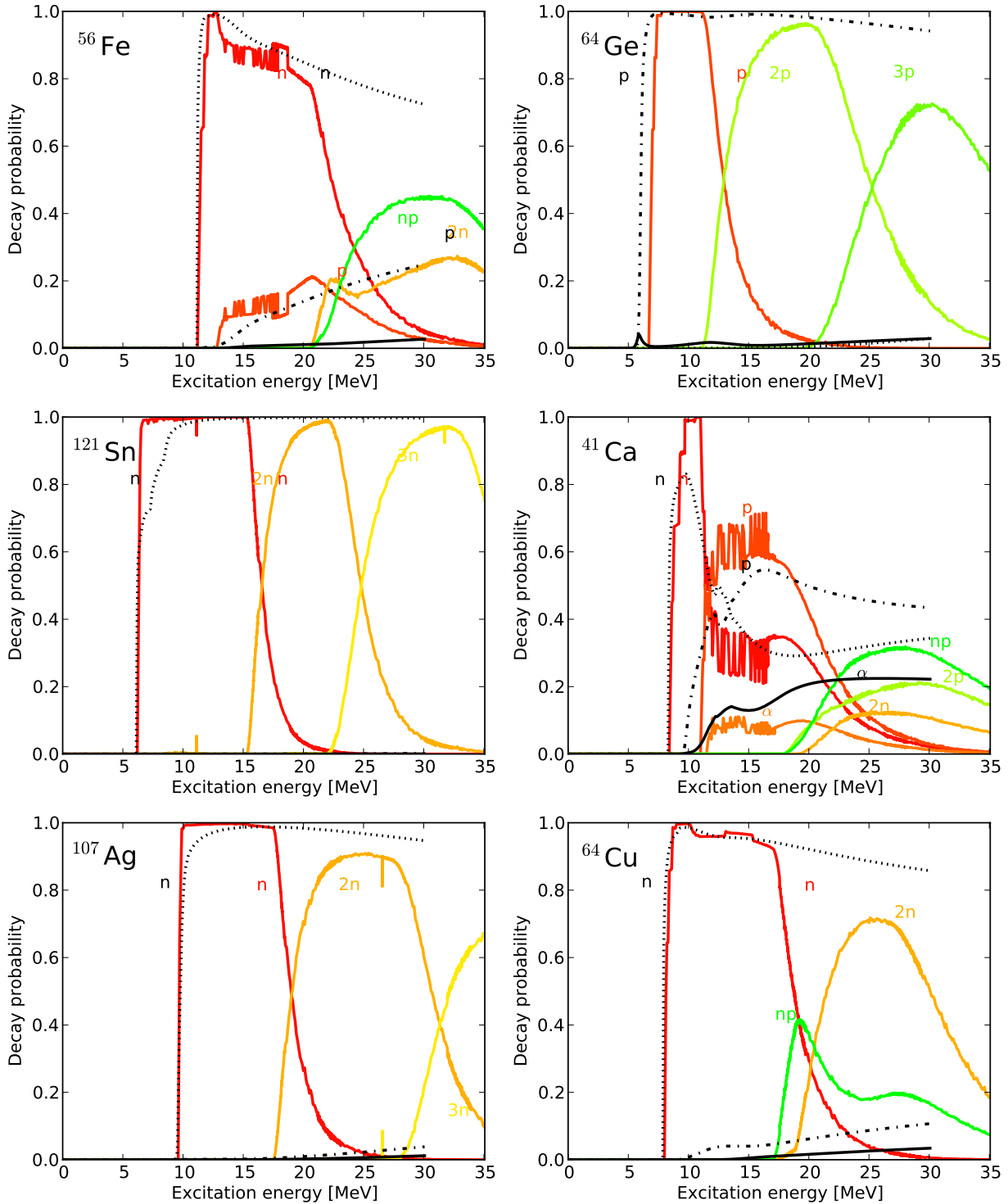


Figure 3.3.: The decay probabilities for the nuclei ^{56}Fe , ^{64}Ge , ^{121}Sn , ^{41}Ca , ^{107}Ag and ^{64}Cu . The decay probabilities displayed here are total decay probabilities, meaning that all compound spin states are weighted equally. We considered all angular momentum states from 0 to 4. A consistency between the detailed low energy (MOD-SMOKER) and the high energy description can be observed. MOD-SMOKER calculations are always plotted in black. Dotted black lines denote the neutron emission probability. Thick black lines give the emission probability of α -particles within the statistical model approach. Dash-dotted lines show the corresponding proton emission probabilities. The decay channels of ABLA07 are labeled for each plot to show the dominant emission channels.

emission threshold, the γ - and particle-width will still be comparable. This fact is however only valid very close to the emission threshold. However – as we saw above – contributions from the Coulomb barrier for charged particles can also increase the energy window where the γ -channel is comparable to particle emissions. The second and larger influence arises through the detailed use of angular momentum in MOD-SMOKER for the calculation of the transition width in comparison to the approximate treatment within ABLA07. MOD-SMOKER incorporates not only the penetration through the Coulomb barrier but also the effects of the centrifugal barrier whose energy is given by

$$V_l(r) = \frac{l(l+1)\hbar^2}{2Mr^2}, \quad (3.1)$$

where l is the orbital angular momentum between ejectile j and daughter Y^μ . This is usually accounted by the penetration factor $P_l(E, R)$, where R gives the nuclear radius. The width can be approximated via

$$\Gamma_l(E) = \frac{3\hbar}{R} \left(\sqrt{\frac{2E}{M}} \right) P_l(E, R) \Theta_l^2. \quad (3.2)$$

M is as before the reduced mass, while E gives the center-of-mass energy. The quantity Θ_l^2 is called reduced width of a nuclear state; its value is always $\Theta_l^2 \leq 1$. It represents the reduced width coming from an evaluation of the overlap integral between the compound nucleus and the products in the channel under consideration. It contains the nuclear structure information and is generally obtained from experiment or assumed to be one. The penetration factor $P_l(E, R)$ has to be obtained via

$$P_l(E, R) = \left| \frac{\chi(\infty)}{\chi(R)} \right|, \quad (3.3)$$

it involves the evaluation of the radial wave functions at distances $r \geq R$. The radial solution of the Schrödinger equation at these distances is given as a combination of the regular $F(r)$ and irregular wave functions $G(r)$

$$\chi(r) = AF_l(r) + BG_l(r), \quad (3.4)$$

with A and B being normalization constants [19]. For equation 3.3 this results to

$$P_l(E, R) = \frac{1}{F_l^2(E, R) + G_l^2(E, R)}. \quad (3.5)$$

The general behavior of the penetration factor can be seen in figure 3.2. It is easy to observe that for constant energy, the penetration factors with increasing orbital angular momentum l have smaller values and are therefore less probable. This can for example be observed within the different plots shown in figure 3.4, where we plotted the spin dependent decay probabilities that are used to obtain the total decay probabilities as they are shown within figure 3.3. Note that this argumentation is somewhat idealized and only strictly valid at very low energies above the channel openings. The reason for this occurrence is, that at higher energies than the channel opening, the decay can also occur to excited states where the change in orbital angular momentum is less, reducing the effect of the centrifugal barrier V_l . We can see that the emission of light particles in the MOD-SMOKER approach gets shifted to higher excitation energies. The reason for this is the correct inclusion of the orbital momentum in the used potential. To observe this behavior, the reader is referred to figure 3.4, where the decay probabilities of ^{121}Sn for $J=9/2$ are shifted to higher excitation energy due to the inclusion of the orbital momentum in the potential. For the other partial decay probabilities this cannot, or only very little, be observed since captures to excited states, with a larger spin difference, are more favorable.

Within this figure it is also obvious that this effect is not considered within the ABLA07 model, since the cross section assumes always s -wave scattering, which is in general the dominant cross section [114]. This does not mean that ABLA07 does not have a spin dependence. The spin dependence however is only not included within the capture cross section, for the level density description the spin dependence is utilized. That this spin dependence also has influence can be seen in the case of neutron emission of ^{41}Ca and of ^{56}Fe .

The last plot shown in figure 3.3 that we did not discuss so far is the case of ^{41}Ca . In this case several arguments have to be mentioned. The first point is that the total decay probability does not agree as good as in the other cases. For example, we can observe that the neutron branching height is different between both models. This however can be understood due to the fact that we only plot the total decay probability. For the partial channels of $J = 1/2$ up to $J = 7/2$ the decay probabilities for one-neutron emission show similar behavior, only the $J = 9/2$ channel has a very small neutron emission probability. The reason for this occurrence is that by emitting a neutron, we end up in the double magic nucleus ^{40}Ca , where the excited states are known with its detailed quantum numbers up to 5.2 MeV, corresponding to a compound energy of 13.6 MeV. The first possible s -wave emission from a $J = 9/2$ compound state is possible at an

energy of 4.4 MeV to the fifth excited state with $J = 5$, and as we already saw in the case of ^{121}Sn , partial waves with higher orbital angular momentum will be decreased and shifted towards higher excitation energy. For energies below the proton- and α -emission threshold, this results in a dominance of the γ -channel, which is not shown in the figures. Furthermore we can observe that the neutron decay probability within the ablation model shows also an increase at the channel opening, that has its origin from the spin dependent treatment of the level density.

In general one can observe that the decay probability of α -particles between both models is different. The reason for this occurrence is that α -emission becomes important with increasing excitation energy. As the energy increases, additional channels will open that will compete with pure α -decay. A good example for this is again the case of ^{41}Ca in figure 3.3, where the α -branching can be compared with the α -branching of ABLA07. The α -separation energy is at an excitation energy of 2.5 MeV which is up to 5.1 MeV the only open particle emission threshold. Nevertheless, the α -branching becomes relevant at energies above 10 MeV, because at lower energies the tunneling possibility is too small. In the energy range below 18 MeV both models utilized in this thesis show similar results, however when two-particle emissions are possible, both branchings seem to diverge.

It should be noted here again that the branching shown in this subsection are the sum of all branchings of angular momenta J up to four with the same weighting. This will of course not be true for the results of our neutrino scattering/capture cross sections, where $\Delta J = 4$ transmissions will be heavily fragmented. Instead $J = 0, 1$ will be the dominant decay channels.

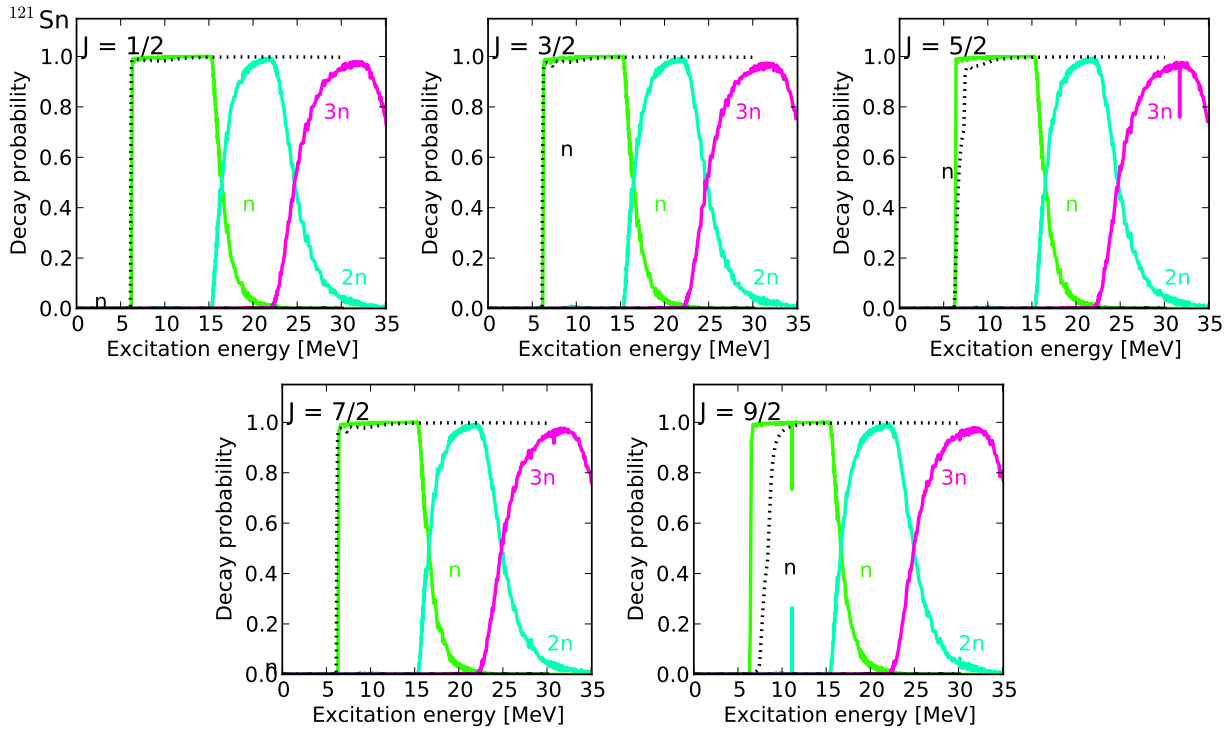


Figure 3.4.: Decay probabilities for the nucleus ^{121}Sn with different compound spins. One can observe that MOD-SMOKER has a spin dependence arising from the penetration factors $P_l(E, R)$ as described in the text. This effect is not considered within the ablation-model of ABLA07.

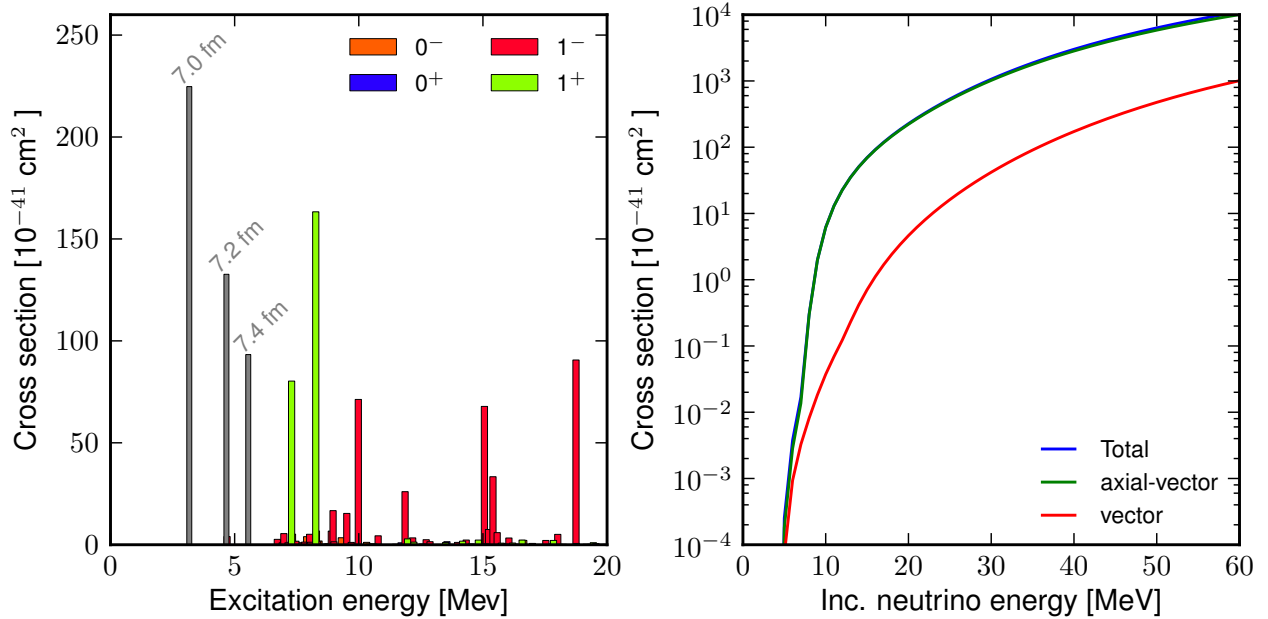


Figure 3.5.: Left: The excitation spectrum of (ν, ν') on ^{208}Pb obtained with our version of the RPA code, the multipoles are shown in different colors. The excitations shown in grey are spurious states which can be identified as center-of-mass motions. The spurious states are labeled with the radius used in the residual interaction. Right: The total cross section as a function of incoming neutrino energy. In addition the contribution of vector and axial-vector are plotted to justify the method of removing spurious states for our calculations.

Consistency of the RPA

To obtain the excitation cross section of neutral-current scattering and charged-current captures, the same framework has been already utilized in previous studies such as [127, 128, 80, 129, 63]. The RPA model has been proven to determine reliably the position and strength of the giant resonances [130], which are the important parameters for the determination of the neutrino-nucleus rates. Therefore the RPA is a good tool for the determination of the neutrino-nucleus cross sections in the supernova environment.

Thus our task is basically to reproduce with our model the results of previous calculations. We decided to reproduce the excitation spectrum of neutral-current neutrino scattering on ^{208}Pb with a neutrino temperature of 8 MeV and zero chemical potential.

With the inclusion of the single-particle states given in [71] for the single-particle states below the Fermi level, and the parametrization of the Woods-Saxon potential given above, we are able to almost reproduce the excitation spectrum given in [129]. To fully reproduce the excitation spectrum we had to set the radius used in the residual interaction to 6.8 fm instead the 7.22 fm that would result from equation 2.31. The excitation spectrum is also shown in figure 3.5. If one increases the radial parameter in the residual interaction, one can observe a strong excitation at small excitation energies appearing, that actually moves with increasing radius to higher excitation energies. Due to that radial dependency and the fact that this excitation is always a $J^\pi = 1^-$ excitation, it could be identified as the center-of-mass motion [131] that are possible to appear in models that are not self-consistent with their choice of the residual interaction and will mix with physical states [65]. These low lying strength is shown in equation 3.5 in grey, to present the dependence from the radius used for the residual interaction.

Due to this mixing the low lying states will gain more strength, which will alter the total strength. To remove these spurious states for our calculations we noted that these excitations are pure 1^- excitations. Therefore we are able to remove the spurious contribution by utilizing only the axial-vector component of the 1^- excitation.

The question that arises from this projection is, if we loose strength due to the fact that we neglect the complete vector part of the 1^- component. Luckily neutrino-nucleus reactions have dominance of axial-vector over vector-contributions [132] and we will therefore only have very small changes due to the projection on axial-vector. When applying this projection no changes have been found in the shown case of ^{208}Pb as in some other test cases. To show that vector contributions are less important than axial-vector, we plotted in figure 3.5 also the cross section split up in vector and axial-vector parts.

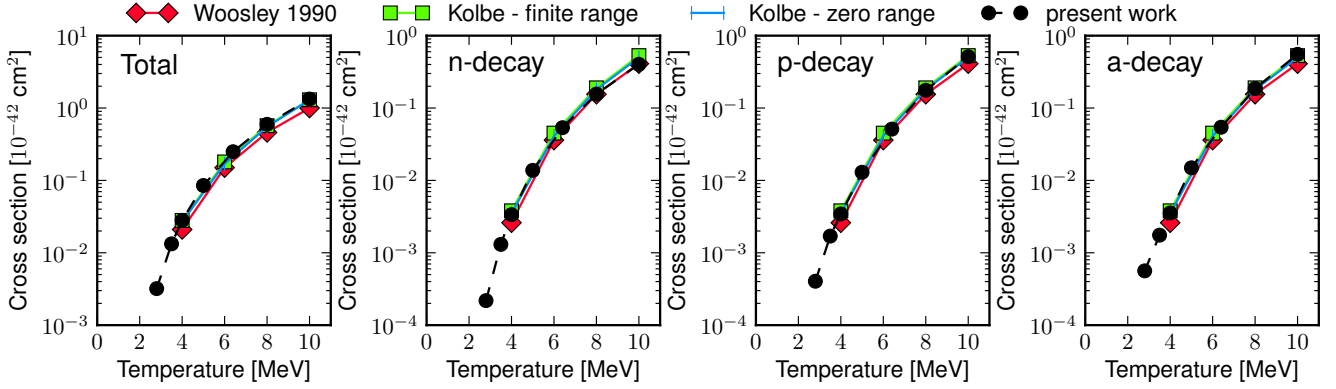


Figure 3.6.: The inelastic neutrino scattering rates folded over a Fermi-distribution. The figures show the folded cross section as a function of temperature for inelastic (anti-) neutrino scattering from ^{12}C . From left to right they show the total cross section, the partial cross section for emission of one neutron, one proton and an α -particle respectively. For comparison, previous studies have been included [2, 127].

After we are sure that the RPA and the decay branchings give a consistent and reliable description we would like to compare in this section the spallation rates with previously calculated spallation rates. Earlier work on this topic have either been done only on $N = Z$ nuclei including only up to one-particle emission [2] or the description of the decay has been implemented in a simplified fashion [63, 133]. For α -particles and ^{12}C models with an improved nuclear model and a realistic nucleon-nucleon interaction have been utilized to calculate the neutral- and charged-current neutrino-nucleus cross section including spallation of multiple particles [134, 135, 136].

As we discussed in section 1.2.1, while matter is ejected from the PNS surface, free protons and neutrons will start recombining to α -particles until either all neutrons or protons are used up, depending on the value of Y_e . The abundance of α -particles can then only be reduced by three-body reactions, or by very strong photo-disintegration. Thus within our studies, we are in an environment with a very strong α -abundance. It is therefore of key importance that we have a specifically good description of the spallation rate on ^4He . Furthermore the nuclear structure of ^4He is rather complicated, which cannot be incorporated within our RPA. Due to the importance of this nucleus and the better nuclear model and interaction used in the aforementioned model, we decided to use the results for neutral-current neutrino induced proton and neutron emission from the work of [135]², that utilizes a realistic nucleon-nucleon interaction. In comparison to previous work [2], that only employed a more-or-less phenomenological description, the cross section is increased by 15 % up to neutrino temperatures of 15 MeV, which has the advantage that changes due to the inclusion of these rates might be observed easier. The charged-current neutrino spallation rates are taken from [134].

All of the former mentioned models average over the neutral-current neutrino and antineutrino cross sections since the difference between both cross sections comes – as we have seen in the cross section for the considered process (eq. 2.26) – from the sign of the interference term. Since this difference is small an averaged cross section over neutrino and antineutrino seems reasonable. Within our thesis we decided not to average, due to the fact that ν_e and $\bar{\nu}_e$ will have different average energies within the astrophysical environments that we are studying. However for comparison we define the averaged cross section as

$$\bar{\sigma}_x(T) = \frac{1}{2} \left(\sigma_x^\nu(T) + \sigma_x^{\bar{\nu}}(T) \right). \quad (3.6)$$

As a first example we show in figure 3.6 the different spallation channels on ^{12}C , which include proton, neutron and α spallation. Within the description of the decay it is important to note, that ^{12}C is a self-conjugate nucleus and has therefore isospin $T = 0$. Due to isospin conservation, the $(\nu, \nu' \alpha)$ spallation cross section will be highly suppressed at low and medium energies. To correct for partial isospin mixing the mixing coefficient c has been introduced, that in general should be energy dependent. We will however follow the assumptions of [127] and set this coefficient to a constant value of $c = 0.01$. This results in the fact that there is a 1 % mixing of $T = 0$ states in the $T = 1$ states that will be excited by inelastic neutrino excitations. The mixing coefficient has been utilized for all isospin symmetric nuclei. We also would

² The authors of [135] study within their work the nucleosynthesis on ν -nucleosynthesis, where this reaction will also play a dominant role, as we will see later.

like to stress out that above work has been utilized with the help of a CRPA³ approach instead of the RPA that we are using, nevertheless the results show good agreement.

3.2 Neutrino scattering rates

After we have convinced ourselves that our results show reasonable agreement with previous calculations describing neutrino-scattering spallation reactions, we would first like to give here a global overview of the rates that we have calculated within this thesis. We would like to start by showing the scattering cross sections for neutrinos, keeping in mind that the antineutrino cross section presents the same features, because the only difference arises from the interference term.

We would like to note that the shown neutral-current neutrino rates in figure 3.7 are folded for a Fermi-Dirac neutrino spectrum with $T_\nu = 5$ MeV and zero chemical potential. The total cross section agrees with the usual observations that the cross section is increasing linearly as a function of mass number. In previous studies, at a neutrino temperature of 8 MeV, a proportionality factor of 0.7 could be found [2, 137, 138]. We could observe a similar trend with increasing mass number where the proportionality is given with 0.78 also at a neutrino temperature $T_\nu = 8$ MeV and zero chemical potential, similar to the values obtained in works before. Differences from this trend arise at shell closures, as can be seen in figure 3.7.

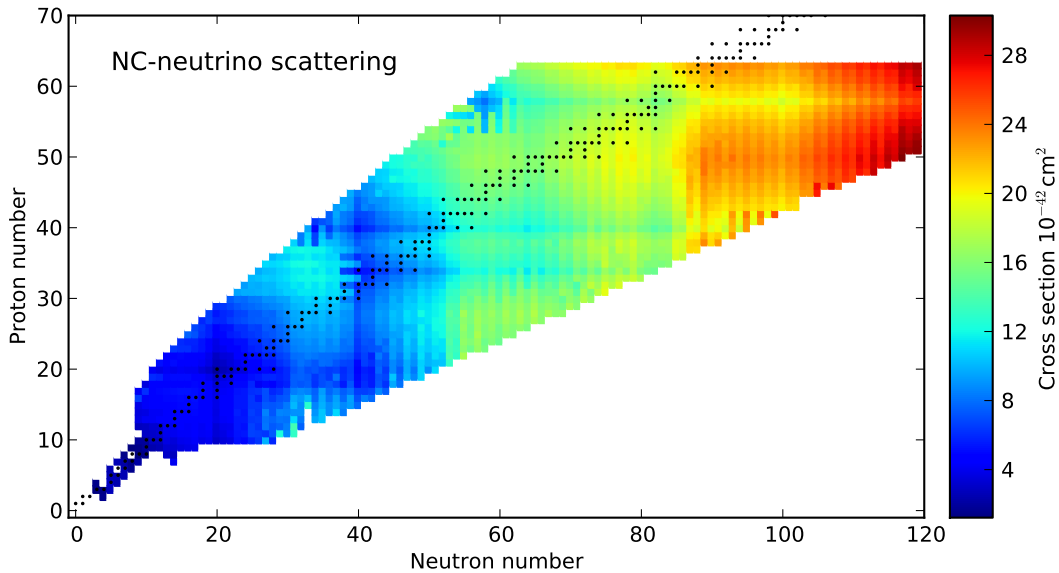


Figure 3.7.: The neutrino-nucleus cross section for each nucleus folded over a neutrino temperature $T_\nu = 5$ MeV and zero chemical neutrino potential. The cross section grows linear with increasing mass number.

The total cross section for neutrino-nucleus scattering is an interesting topic. Nevertheless, these processes do not contribute to the nucleosynthesis and we now focus on the particle-spallation cross sections. Again we would like to mention that we calculated up to four-particle emission, where these four particles can be any combination of neutrons, protons and α -particles. Only if spallation processes are included, the final nucleus will be different from the initial. This occurs if the compound nucleus is excited above the particle threshold. As already mentioned before, we assume our ground state to have $J^\pi = 0^+$.

The rate for one-neutron emission can be observed within figure 3.8. The rates are sensitive on the neutrino temperature of the astrophysical scenario. Again we show the spallation cross section for a neutrino temperature of 5 MeV and zero chemical potential. With a decrease of the neutrino temperature the cross sections will decrease, but furthermore the sensitivity of the cross sections on the particle emission threshold energy will increase. We will now discuss the results for a neutrino temperature of 5 MeV in detail.

It is interesting to see that a clear odd-even staggering is visible, arising from the staggering of the particle emission thresholds. The dominant spallation product of the stable nuclei is the emission of one neutron, as long as proton and neutron separation energies are almost equal. The reason for this occurrence is two fold. On the one hand, protons

³ CRPA is an improved model of the standard RPA model that we are using, in which continuum states are correctly described by plane wave solutions.

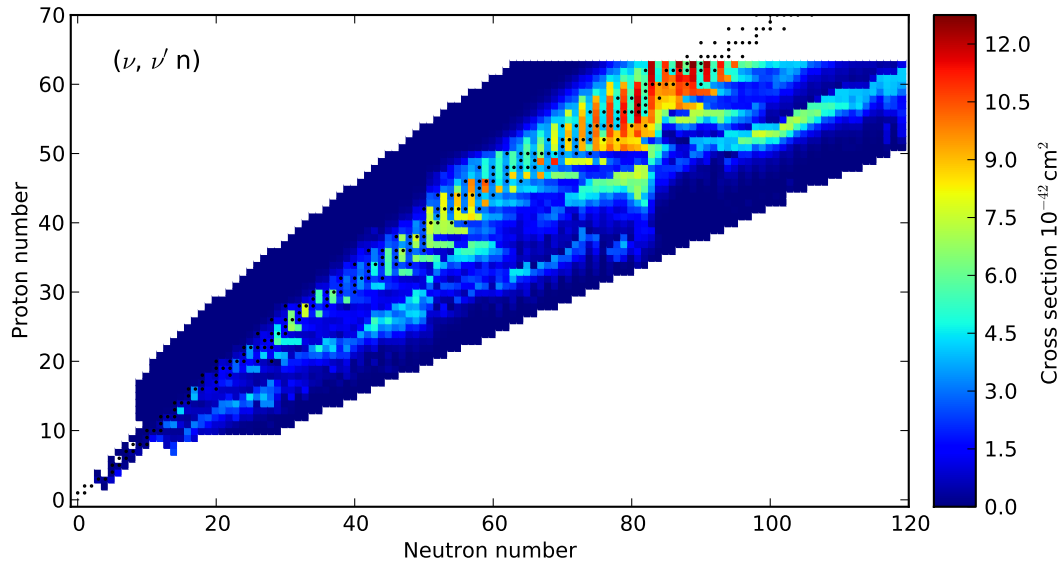


Figure 3.8.: The one-neutron emission cross section for neutrino scattering on the respectively nucleons. The black dots correspond to stable nuclei and should serve as a guideline. The cross section is folded as in equation 3.7 for a neutrino temperature of 5 MeV and zero chemical potential. Odd-even effects are quite pronounced, that arise due to the odd-even effect of the separation energies.

ejected out of the nucleus have to overcome an additional barrier due to the Coulomb interaction. On the other hand the Coulomb interaction has the effect, that stable nuclei with increasing mass number have more neutrons than protons, which increases the probability of emitting a neutron. This fact is also the reason why for $N=Z$ isotopes with increasing mass number the neutron separation energy keeps increasing. For example is the separation energy of ^{56}Ni for a neutron above 16 MeV while the proton separation energy is at 7 MeV. Furthermore we are able to observe that shell effects are not recognizable as clearly as before.

One-proton and α -emissions dominate at isospin symmetric nuclei, although the maximal rate is smaller than the ones for neutron emission. We will however not show a figure for these results here to save space.

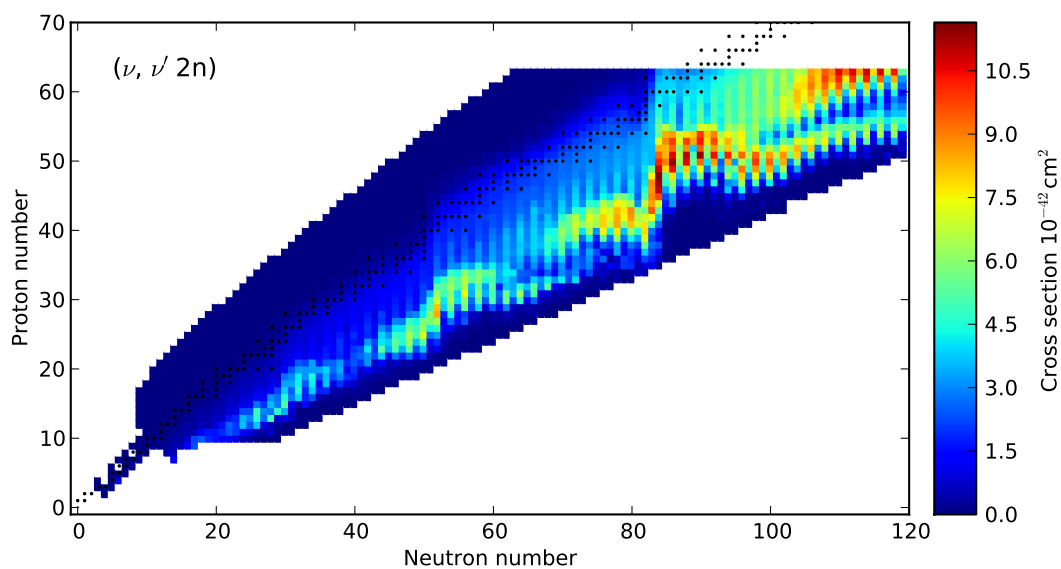


Figure 3.9.: The two-neutron emission rate for all nuclei considered here. The cross section has been folded over a neutrino spectrum with a neutrino temperature of 5 MeV and zero chemical potential.

On the neutron deficient side of the nuclear chart we expect an increase of the neutron separation energy, while the proton separation energy decreases. Consequently we will expect that the dominant spallation product will be governed by proton emissions, which is the reason why for the proton rich side very little neutron emissions are expected. On the neutron rich side of the nuclear chart, the argumentation is exactly the other way. With increasing neutron number it gets energetically harder to emit a proton and the neutron emission will be more likely. This is related to the fact that the neutron separation energies decrease the more neutrons are available. However in figure 3.8 we cannot observe an increase in the one-neutron emission rate for neutron richer nuclei, due to the fact that with increasing neutron number not only the one-neutron separation energy decreases, but also the energies for several particle emission will decrease, which allows for easier multi-particle emissions. For neutron rich nuclei this implies that the collective excitations to which we are sensitive, are above the multi-particle separation channel, and this will subsequently be the dominant decay channel. As an example we would like to show the two-neutron spallation rate in figure 3.9.

Within figure 3.9 we can observe that on the neutron rich side the two-proton emission rate contributes substantially over a large area. Even up to the stable nuclei the rate can have still a contribution of up to 5 %. Nevertheless, the dominant rate in the stable region is given by the one-neutron emission.

Another interesting feature can be found in the region with $N > 100$ and $Z > 50$ where the partial cross section with increasing mass number is suddenly decreased. Vice versa we are able to observe an increase in the partial rate of the one-neutron emission at this specific region, telling us that the major strength of our excitation is in the region of one-neutron excitation.

The two-neutron spallation rates show stronger shell closure effects than the one-neutron emission rates, especially at neutron shell closures. Very pronounced is the peak at $N = 82$. The arguments are related to the fact that for the emission of one neutron of an even-even nucleus a neutron pair has to be broken which requires additional energy. For the emission of two neutrons such a pair can be extracted directly.

3.2.1 Partial neutrino scattering rates

The figures shown above tell us that several-particle spallations are an important part for a correct description of neutrino-nucleus scattering cross sections for astrophysical scenarios.

In this subsection we want to show for some chosen cases the rate as a function of incoming neutrino energy, instead – as before – already folded over a Fermi-Dirac neutrino spectrum. This will give us the opportunity to observe not only the dominant cross sections but also give us clues about which reactions might be more important at other neutrino temperatures in the astrophysical scenario under consideration.

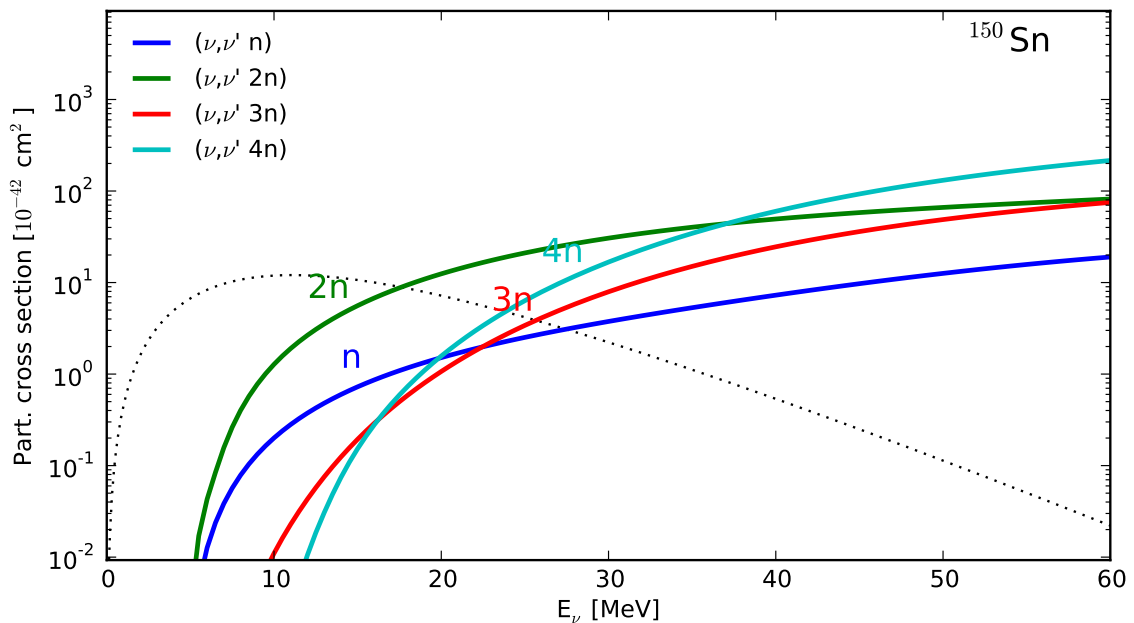


Figure 3.10.: The partial cross sections for neutrino-nucleus scattering with particle spallation on ^{150}Sn . The dotted line corresponds to a Fermi-Dirac spectrum with $T_\nu = 5$ MeV and zero neutrino chemical potential.

The first example that we would like to present is neutrino-nucleus scattering on ^{150}Sn , which is a very neutron-rich nucleus ($N/Z = 2$) and has subsequently a very low two-neutron separation energy. It seems therefore not surprising that the two-particle spallation rate is larger than the one-neutron spallation. One has to be careful not to be confused by the results shown in figure 3.10. The one-neutron separation energy is still below the two-neutron separation energy. The one-neutron separation energy opens at an energy of 2.56 MeV while the latter one already opens at an energy of 3.51 MeV. The reason why the two-neutron emission cross section is larger than the one-neutron emission relates to the fact that most of the excitation strength is above the two-neutron separation energy. It is interesting to see how the slopes of the channels behave different as a function of energy. In this case it would however require very high neutrino energies to obtain a dominance of the four-neutron emission channel.

Another example that we would like to show within this subsection is the rate on ^{52}Fe . The reason therefore is that it is a $N = Z$ nucleus such as ^{12}C . The second, and actually more important reason is, that it is believed to be a seed nucleus for the production of ^{51}V via the ν -process, that we will discuss later in more detail. The partial cross sections are given in figure 3.11. The dominant cross section is the spallation of one proton, followed by the emission of two protons. Neutron spallation is so small in this case that it is not displayed within this figure, which does not mean that no neutron emission will occur, it will however not be the dominant channel. However, the spallation of one neutron and one proton is then more favorable than the three proton channel. Once again, the reason why neutron capture processes are almost negligible is due to the fact that the neutron separation energy resides at an energy of 16.18 MeV, while the proton separation energy resides at 7.3 MeV. A similar behavior can also be found in heavier $N = Z$ nuclei, such as ^{56}Ni .

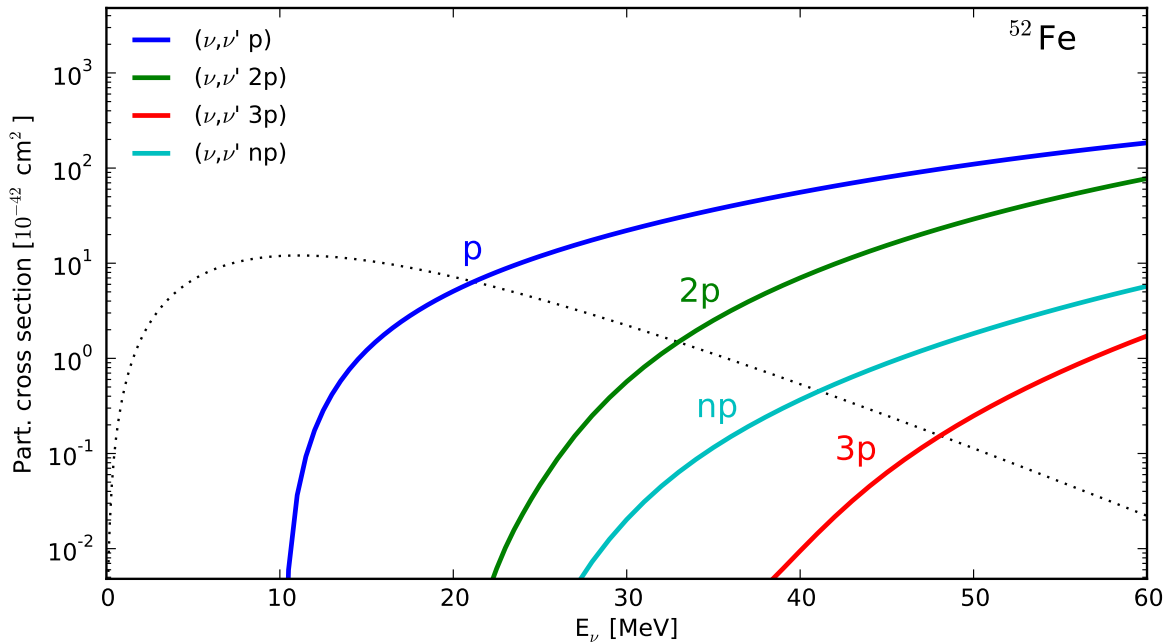


Figure 3.11.: The dominant partial cross sections for neutrino-nucleus scattering with particle spallation on ^{52}Fe . The most dominant partial cross section is the emission of one proton, followed by the emission of two protons. Again a Fermi-Dirac spectrum is shown additionally to guide the importance of the decay channels at a neutrino temperature $T_\nu = 5$ MeV and $\mu_\nu = 0$.

3.2.2 Average neutrino particle emission

In the case of very neutron and proton rich nuclei, it might actually happen that the collective excitations can easily reach above the five-particle emission thresholds. The dynamical ablation model ABLA07 is possible to account also for these many particle emissions. However, due to the increase of possible decay channels, only four-particle emissions have been included, which should be for the majority of nuclei more than sufficient. In the case where four-particle emissions are not enough, we are either in a very neutron rich or a very proton rich regime. We therefore know that either only neutrons or protons will be emitted. For these cases we modified ABLA07, such that it follows the emission of up to ten neutrons or protons. As an example for the capability of this code, we show in figure 3.12 the average proton/neutron emissions of a very neutron deficient/rich nucleus.

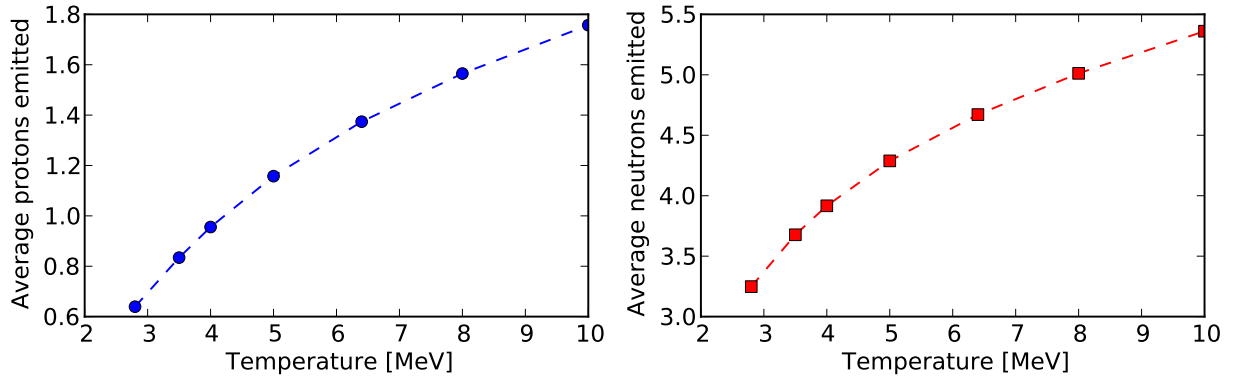


Figure 3.12.: Average emission of protons/ neutrons for very neutron deficient (left: ^{99}Sn) and neutron rich nuclei (right: ^{150}Sn). In the case of proton emission we are still in a regime where the standard description can account for the number of protons emitted. For ^{150}Sn the amount of neutrons emitted is larger than the initial model can handle.

3.3 Charged-current rates

Additional to neutrino scattering reactions we computed neutrino and antineutrino capture reactions by the charged-current. The total cross section for the charged-current reactions have been calculated within the same RPA approach for all nuclei within the work of [72]. However, within their work the decay of the created compound nucleus has not been considered. Furthermore we extended the calculation range closer to the drip-lines.

The rates for total neutrino/ antineutrino captures are similar to the ones given in previous work and we will not discuss the details here. However, it can be stated that the neutrino capture rates are in general larger than the corresponding neutral-current rates.

The total folded neutrino capture cross section increases with growing neutron number for an isotopic chain. Vice versa holds true in the case of antineutrino captures, where the rate grows with increasing proton number.

Charged-current neutrino-processes in general act supporting to β -decay processes. For β^- -decays electron neutrino captures behave similarly, except that the excitation energy of the compound nucleus is significantly larger than for β^- -

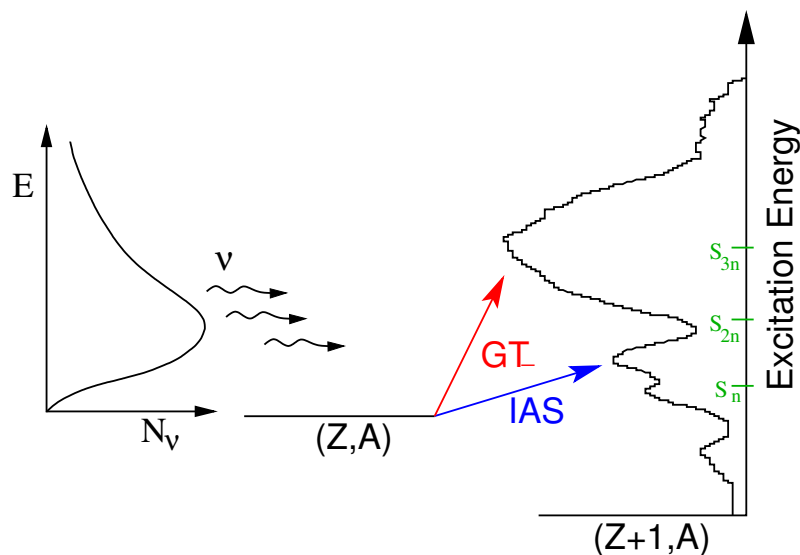


Figure 3.13.: A schematic sketch of the energy relations in neutrino captures on neutron rich matter. The dominant transitions, which are the Fermi (blue) and Gamow-Teller (red) transition, are also sketched. On the left hand side the neutrino spectra from the core-collapse supernova as a function of energy is shown. The particle emission thresholds are marked on the right ordinate – corresponding to the excitation energy in the compound. This image has been adapted from [139] with courtesy of G. Martínez-Pinedo.

decays, because the Q-value adds to the energy of the neutrino distribution (see figure 3.13 for a schematic plot). This additional energy increases the cross section for Fermi (IAS) and Gamow-Teller transitions. The higher energy in the compound nucleus is furthermore accompanied with a higher probability for particle spallation processes. Especially for neutron rich material the additional gain in energy due to the Q-value comes into play. Furthermore are the neutron separation energies for neutron rich matter very small. The combination of both facts increases the possibility of particle emission from the valley of stability. Vice versa is the fact for neutron deficient nuclei, where the ground state energy of the compound nucleus is above the ground state energy of the target nucleus. This leads to a reduction for the neutrino capture rates, because only the high energy part of the neutrino energy distribution is energetically allowed to capture a neutrino. Of course this also forbids/reduces the cross sections for Fermi and Gamow-Teller transitions. For antineutrino capture processes the arguments are the same, except that the roles are interchanged. Antineutrino capture processes will help increasing β^+ -rates. The spallation reactions with the largest cross sections, initiated by antineutrino capture processes, will therefore be of course one or several proton emissions, because the cross section for antineutrino captures is the strongest on the neutron deficient side of the nuclear chart.

In figure 3.14 we show exemplary the two-neutron emission rates for neutrino capture processes where the neutrino distribution function is assumed to be of Fermi-Dirac type with a neutrino temperature of 5 MeV and no chemical potential.

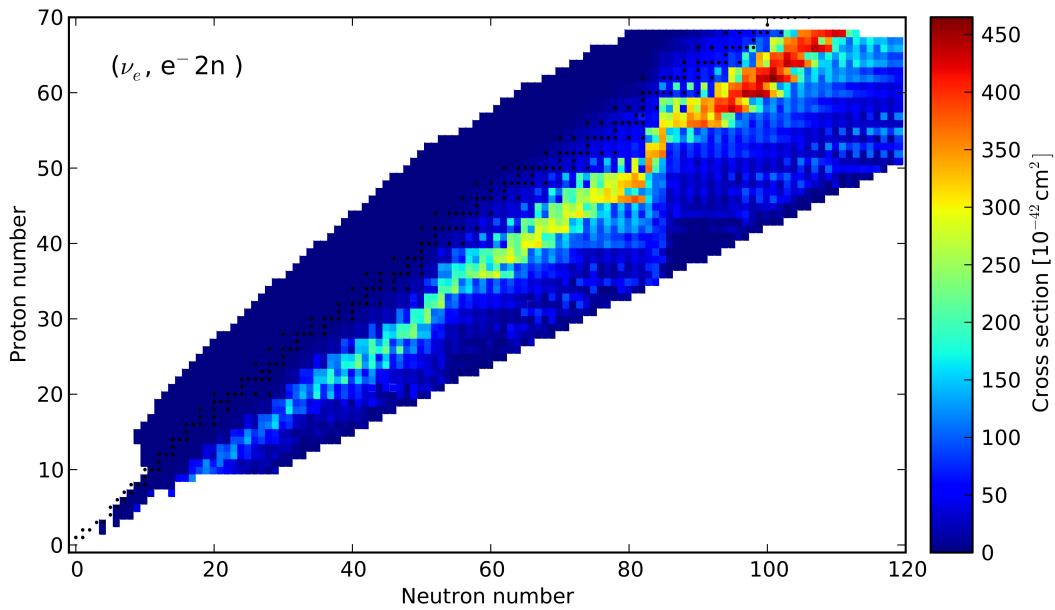


Figure 3.14.: The rate for neutrino capture with the subsequent emission of two neutrons. The maximum of the two-neutron is closer to the valley of stability.

4 Nucleosynthesis results with new rates

Since we have shown in the last section that the rates obtained within our work are described correct and give reasonable values all over the nuclear chart, we would like to present in this section how the inclusion of neutrino spallation reactions changes the final nucleosynthetic yields within various scenarios. These scenarios are always related to the core-collapse supernova environment. Furthermore we would also like to investigate the astrophysical scenarios with respect to the nucleosynthetic outcome.

First we would like to discuss the neutrino-driven wind, because it is the astrophysical site where it is expected that heavy elements are created. In the neutrino-driven wind exist two sites where neutrino interactions are of importance for the nucleosynthesis. The first is the decoupling region of the proto-neutron star, because at this point the electron fraction is determined, due to the shapes of the electron neutrino and antineutrino spectra. The second site is in the neutrino-driven wind, where the neutrinos can influence the nucleosynthesis directly.

In 2012 it was realized that a consistent treatment of charged-current neutrino processes with the underlying equation-of-state (EOS) will have influences on the spectra of electron neutrino and antineutrino [140]. This will change the electron fraction such that initial ejecta from the PNS will now be neutron-rich. However, we will first focus on simulations from before 2012, that are proton-rich during the whole period of deleptonisation. The reason why we spend time in understanding the nucleosynthesis in this environment, which is not consistently described with the underlying EoS, is, that the proton-rich wind is still an interesting astrophysical site that allows us to study the influence of our spallation cross sections as well.

After we have explored the nucleosynthesis in the proton-rich wind, we will then turn towards a neutrino-driven wind scenario where the new rates are included, and study the nucleosynthesis there. Our focus will be always directed to two aspects. First will we study the nucleosynthesis with respect to our included neutrino rates. Furthermore we will explore if the matter produced in the neutrino-driven wind can help explaining the abundance pattern of metal-poor stars as HD 122563.

Due to the fact that the neutrino-driven wind is still a possible site for the r-process, although the conditions of current models are not extreme enough, we will study r-process nucleosynthesis under strong neutrino fluxes including our new rates.

Furthermore will we study the ejecta of the hot convective bubble that are emitted before the neutrino-driven wind sets in, and discuss the relevance for the nucleosynthesis. It is believed that this astrophysical scenario helps explaining the production of rare isotopes like ^{45}Sc , ^{49}Ti and ^{64}Zn [47].

We however do not only focus on the nucleosynthesis that will go on in the neutrino-driven wind, we also would like to study the nucleosynthetic imprints that arise from the shock moving through the outer shells of the star. While the shock passes through the outer shells of the star, the temperature will increase, leading to what is known as *explosive nucleosynthesis*.

While these nuclear processes are ongoing, matter will be subject to neutrino fluxes arising from the surface of the PNS. Despite the facts that the outer shells are at large radii and that neutrino reactions are small, neutrino-induced particle evaporation can alter the nuclear composition. The neutrino processes that dominate are neutral-current processes of $\nu_{\mu,\tau}$ and $\bar{\nu}_{\mu,\tau}$ on nuclei, due to their larger neutrino temperatures. This is known as ν -process [2], it is believed that many elements with odd Z up to $Z = 31$ are partly produced in this process.

To differentiate between all these scenarios and their impact on the nucleosynthesis we will define a quantity that we will denote as *neutrino fluence*. It is given by

$$\mathcal{F}_i = \int F_i(t) dt \quad \text{where } i = \nu_e, \bar{\nu}_e, \nu_\mu, \bar{\nu}_\mu, \nu_\tau, \bar{\nu}_\tau, \quad (4.1)$$

which is simply obtained by the integration of the neutrino flux. The fluence is a measure of the exposure of matter to the different ν -flavor fluxes, which can give us comparable values for different astrophysical scenarios to compare how strong the neutrino exposure is. The neutrino flux is given by

$$F_i(t) = \frac{L_i(t)}{4\pi r^2(t) \langle E_i \rangle(t)}, \quad (4.2)$$

where the luminosities, average neutrino energies as well as the radius have to come from simulations or have to be provided elsewhere. The fluence is an useful quantity that can help us quantifying how important neutrino-interactions will be in different scenarios such as the neutrino-driven wind or the ν -process.

We will, when not mentioned differently – within this section – always represent network calculations where we included neutrino nucleus scattering and capture processes up to two-particle evaporation, because for the typical astrophysical parameters (especially the electron fraction) and mean energies in current core-collapse supernova models the

cross sections for more than two-particle evaporation are too small to influence the result and it increases the calculation time of the network calculation.

4.1 Heavy element production in neutrino-driven winds

The neutrino-driven wind is characterized by strong neutrino fluxes. These fluxes are initially so large that neutrino interactions will determine the final electron fraction close to the PNS. To obtain a consistent electron fraction from the data coming from the simulations of [11], we started our nucleosynthesis calculations in a region where the composition is dominated by free protons and neutrons and the electron fraction is governed by weak interactions on these two species. If however densities are too large, final state blocking effects will become relevant [141] which we do not consider in our nuclear network. Final state blocking effects may be important at high densities ($\sim 10^{12} \frac{\text{g}}{\text{cm}^3}$), however we always start at densities where these processes can be neglected. Therefore the initial starting temperature in our calculations of the neutrino-driven wind is generally in a temperature range between 1.5×10^{10} K and 1.0×10^{10} K, where densities are in the order of $\sim 10^{11} \frac{\text{g}}{\text{cm}^3}$.

The reason why the electron fraction has to be evaluated from a time where the composition consists only of free protons and neutrons is, that the electron fraction depends on the abundances of all species in the nuclear network. For each point in time the electron fraction in our nuclear network can be given as

$$Y_e = \sum_i Y_i Z_i, \quad (4.3)$$

where the sum runs over all nuclei in the network. Within above equation the abundance of isotope i is denoted by Y_i and the charge number is Z_i . Thus, when the temperature decreases and nuclei start to form, the electron fraction is dependent on the amount of nuclei in the network. Due to the complexity in core-collapse supernovae simulations these models only contain a small nuclear network with only a few nuclei, which will lead to the fact that once elements start to form the electron fraction can be different. At high temperatures, where matter basically consists of only free protons and neutrons the electron fraction of the simulation matches the electron fraction of our network. When we start at high temperature, we can thus have a precise matching of both electron fractions.

As said before, the nucleosynthetic yields are obtained based on the simulations of [11]. Within this work two different core-collapse supernovae have been followed over the whole period of deleptonization of the PNS. This brings us in the comfortable position that the dominant amount of matter has already been ejected from the PNS surface in the time that is covered within the simulation. Our task is reduced to follow the different mass elements as a function of radius, temperature and density. From the simulations, we additionally have insight on the average neutrino energies as well as the luminosities for all neutrino flavors included. If we run out of data from the simulation, we utilize an analytic expansion. It is also noteworthy that the neutrino luminosity and average energies are kept constant, once the time in our network calculation exceeds the data given by the simulation.

The expansion is of adiabatic character – which means constant entropy – as it is commonly assumed for neutrino-driven wind scenarios. The description we follow is very similar to that given in [43]. The basic assumption for obtaining a physical meaningful analytical description of neutrino-driven wind ejecta is a constant mass outflow rate

$$\dot{M} = 4\pi\rho r^2 \frac{dr}{dt} = \text{const.} \quad (4.4)$$

This corresponds to the assumption that matter reaches an asymptotic constant velocity. Under the further assumption that the density decreases like

$$\rho(t) = \rho_0 \left(\frac{\Delta + t_0}{\Delta + t} \right)^{-2}, \quad (4.5)$$

which arises from the analysis of current simulations (e.g. [13]). The time within this description is adjusted such, that the time is zero when matter starts being ejected from the PNS surface [142, 43]. The temperature will then behave like

$$T(t) = T_0 \left(\frac{t + \Delta}{t_0 + \Delta} \right)^{-\frac{2}{3}}. \quad (4.6)$$

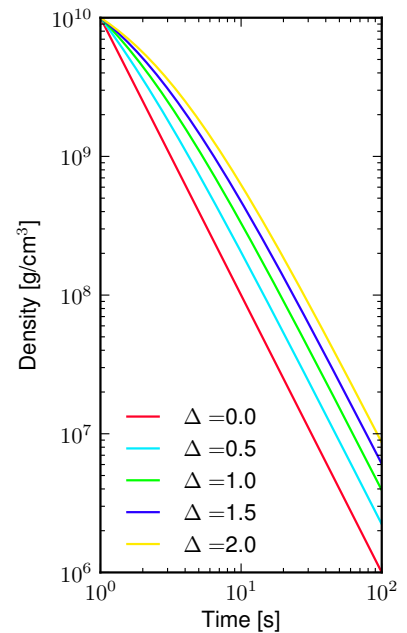


Figure 4.1.: The behavior of different Δ values for the density behavior as a function of time.

Under our assumption that the entropy is constant and we are in a radiation dominated regime ($s = T^3/\rho$), this result is easy to derive. Note however that for the behavior of temperature we do not use this analytic description, instead we obtain the temperature from an EoS [143]. The radial evolution can then be determined with the help of equation 4.4 to

$$r(t) = r_0 \left[1 - \frac{v_0(t_0 + \Delta)}{r_0} \left(1 + \left(\frac{t + \Delta}{t_0 + \Delta} \right)^3 \right) \right]^{1/3}, \quad (4.7)$$

the velocity expansion reads accordingly as

$$v(t) = u_0 \left[1 - \frac{v_0(t_0 + \Delta)}{r_0} \left(1 + \left(\frac{t + \Delta}{t_0 + \Delta} \right)^3 \right) \right]^{-2/3} \left(\frac{t + \Delta}{t_0 + \Delta} \right)^2. \quad (4.8)$$

t_0, r_0, v_0, ρ_0 and T_0 are time, radius, velocity, density and temperature at the end of the simulation. We are left with basically one free parameter given in the above description. This parameter is the Δ -factor. The Δ -factor accounts for the fact that simulations (e.g. [13]) show the behavior that the density behaves almost constant for a short period of time and then decreases with t^{-2} . To show the effects of this Δ -factor for the density evolution, we show in figure 4.1 the influence of the time evolution for an initial density of 10^{10} g/cm³ as a function of time, as determined by equation 4.5. To obtain the Δ -factor for each trajectory under consideration, we utilized a fitting procedure that gives us the optimal value of each trajectory within the neutrino-driven wind.

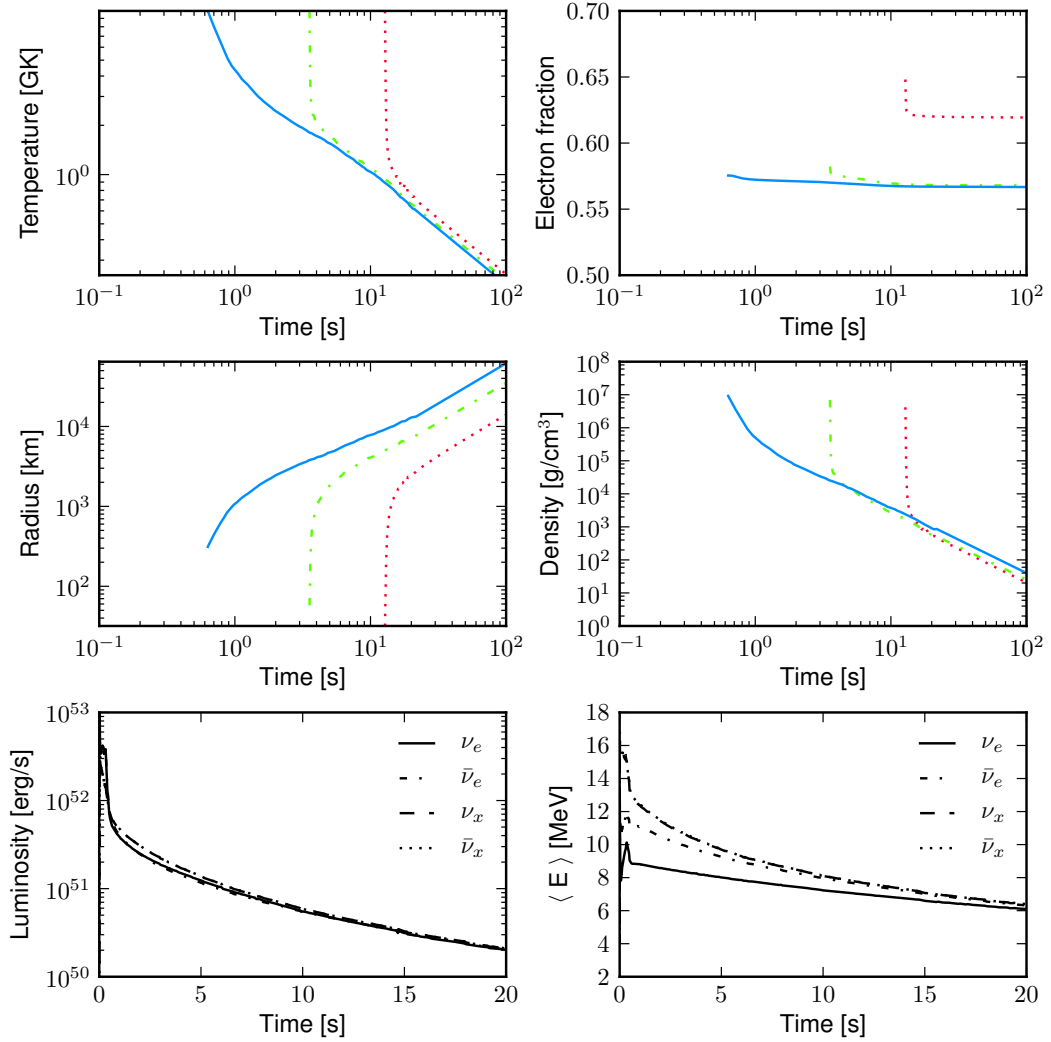


Figure 4.2.: The astrophysical relevant conditions for the trajectories chosen within this subsection. Blue corresponds to early ejecta, red are late ejecta and green gives intermediate ejecta. The electron fraction within this neutrino-driven wind shows always proton rich ejecta. The lower two figures show the luminosities and average energies from the simulation. The time is set such, that the time t is zero at core-bounce.

Due to the fact that the matter is expanding very fast from the PNS surface and the ejected mass is very small, the adaptive grid has to readjust between two timesteps of the simulation. Numerical issues, based on the adaptive grid of the simulations [144] made it not possible to obtain a consistent value for the velocity of the trajectories coming from [11]. The reason for this fact is basically that the velocity of the last ten timesteps has an average value very close to zero, due to the strong changes in the adaptive grid. To correct for this fact, the initial expansion velocity can be determined with the help of equation 4.7, where the initial expansion velocity v_0 can be determined by a least squares fit.

We would like to start discussing our nucleosynthesis results with three different trajectories from a core-collapse supernova with a progenitor mass of $18.0 M_{\odot}$. The three different trajectories basically correspond to early, intermediate and late ejecta. Depending on which time the mass element is ejected, it will be subject to different average neutrino energies and luminosities. We are therefore able to observe how changes within these important input parameters for our neutrino rates will be reflected on the nucleosynthesis of heavy elements. The astrophysical parameters as a function of time can be found in figure 4.2. Additionally to the temporal evolution of temperature, electron fraction, radius and density we show the average energy and luminosity over the whole simulation time. The time is set such that at core bounce the time is zero.

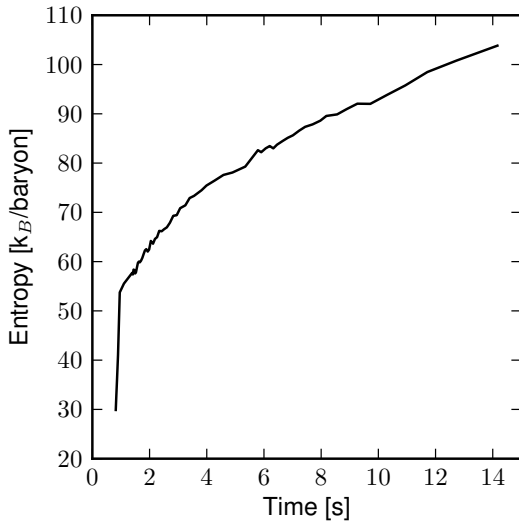


Figure 4.3.: The entropy of the ejecta in the NDW of the $18.0 M_{\odot}$ model.

As can be seen in figure 4.2, the electron fraction of the matter increases the later matter is ejected from the proto-neutron star. The reason is that the spectral difference between electron neutrinos and electron antineutrinos decreases with time. This can for example be observed in the behavior of the average energies as a function of time, where the values of the mean energies of electron neutrinos and electron antineutrinos approach the same final value, which according to our previous discussion increases the electron fraction. One is furthermore able to observe that the radius where matter reaches 1.5×10^{10} K decreases by observing later ejecta. This is related to the fact that the PNS cools and contracts due to the strong neutrino flux from the PNS. By observing the temperature and density behavior of the three trajectories shown in figure 4.2, we can see that the cooling timescale for temperature is similar for all ejecta. The behavior of density is different. Late ejecta show – after the first fast decrease in density – that the density is smaller than for early ejecta. If we estimate the entropy by $s \sim T^3/\rho$ for a radiation dominated environment, we would therefore expect that with increasing time the entropy of the ejecta will increase, which will also favor the nucleosynthesis. To show that this is actually true, we present in figure 4.3 the entropy of the ejected matter as a function of time. The time in figure 4.3 is only plotted up to a time of 15 s, which is exactly the

time, when the last trajectory reaches 1000 km.

The nucleosynthesis itself follows for each trajectory the general picture already outlined above. Protons and neutrons will recombine forming α -particles with an excess of free protons. With decreasing temperature α -nuclei will form up to ^{64}Ge where matter is stuck, as we explained before. The bottle-neck reaction can be overcome by antineutrino capture reactions on free protons. The detailed amount of how effective these capture processes will be, is very sensitive to values of the neutrino spectra and luminosities. The cooling of the PNS additionally leads to a convergence of the electron neutrino and electron antineutrino spectra which will force late ejecta to be more proton rich, favoring the νp -production. That is one of the reasons why we choose three trajectories with different ejection times. Note that hints for the shrinking of the PNS can also be observed with aid of the radial starting points for all the three trajectories shown in figure 4.2, which all start at an initial temperature of 15 GK.

The nucleosynthetic outcome for these three trajectories is shown in figure 4.4, where it is observable that the late ejecta show a strong production of heavy elements due to the very proton rich matter and the higher entropies [43]. To study the production of isotopes, it is helpful to define a *relative abundance* that is normalized to the isotopic abundance of our solar system

$$R_i = \frac{Y_i}{Y_{i,\odot}}, \quad (4.9)$$

where i runs over all stable nuclei.

The reason why the νp -process is more efficient in the late phases of the neutrino-driven wind can be explained due to the very high Y_e values and the entropy values around 100 that will be reached. The latter fact has the consequence, that photodissociation processes are more important due to the increased photon-to-baryon ratio [145]. Within figure 4.2 we see, that the electron fraction reaches values up to almost 0.65, meaning after α -rich freeze-out a substantial amount of free protons is still available, giving electron antineutrinos more possible reactants to convert into free neutrons.

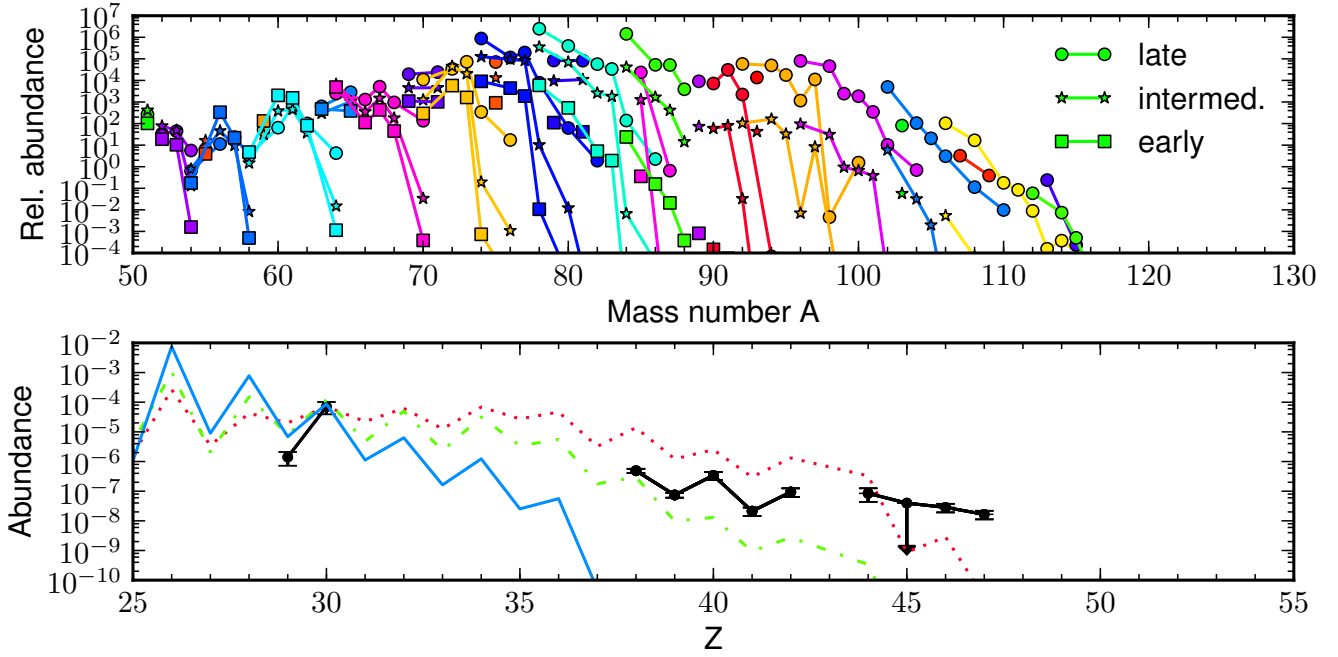


Figure 4.4.: Upper plot: The final abundance of the three chosen trajectories within the neutrino-driven wind. The production of late ejecta can be identified by squares, intermediate ejecta are marked with stars and early ejecta are given by circles accordingly. Lower Plot: Final elemental abundances. Blue corresponds to early ejecta, red are late ejecta and green gives an intermediate ejecta. For a reference we also showed the elemental abundances of the metal-poor star HD 122563 [36] scaled to the late ejecta case.

We can state that the nucleosynthesis results in the neutrino-driven wind are sensitive to the simulation data and the temporal evolution of these quantities. These are mainly the electron fraction, the neutrino luminosities as well as the entropy of the ejecta. We would like to note that the nucleosynthesis results obtained in this last segment agree with current parametric studies on the neutrino-driven wind [43].

Nevertheless the first topic that we would like to address here is how large the influence of our neutrino-nucleus rates are and if they have influence on the final nuclear composition, especially for heavy elements. Therefore we concentrated on the late time trajectory mentioned already above and suppressed different types of interactions. For example we neglected either all charged-current or all neutral-current processes, or we neglected all neutrino interactions at all, to

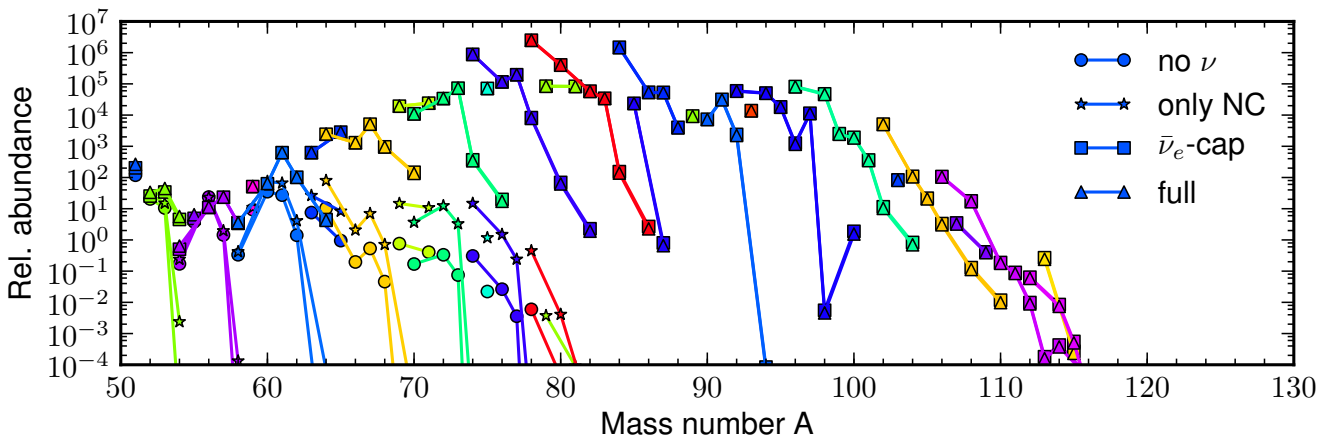


Figure 4.5.: The final abundances of the late ejecta trajectory. Differences can be obtained between the cases where no charged-current is considered. Note that the calculations where only charged-current rates are used and the case where all rates are used are hard to differentiate, because they basically lie on top of each other. The neutral-current shows therefore almost no influence for the creation of heavy elements when charged-current reactions come into play.

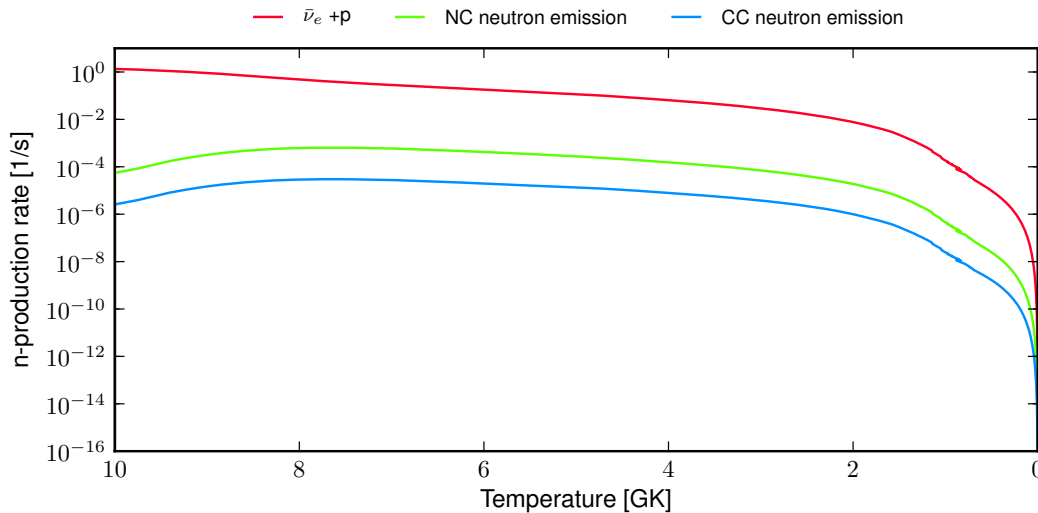


Figure 4.6.: All rates for neutron emission summed up and classified by its weak interaction channel. It is obvious that the dominant channel is still the antineutrino capture on free protons whereas the other channels only play a minor role. The dominant contribution for the neutral-current spallation rate is given by neutron spallation on ${}^4\text{He}$.

see the total importance of neutrino interactions. The results for the various calculations are presented in figure 4.5. The upper plot shows the relative isotopic abundance pattern, whereas the lower picture gives the elemental abundance pattern. From this figure it is obvious that the inclusion of neutrino scattering processes changes very little on the final nucleosynthetic yield of heavy elements, when also charged-current neutrinos are included, since charged-current reactions dominate. We observe that charged-current reactions are governed by antineutrino captures on free protons, capture reactions on heavier nuclei play only a very small role.

The reason why antineutrino captures on protons dominate, arises from the fact that although the total cross section for neutrino scattering processes grows with increasing mass number, the important quantity is the product of cross section with the isotopic abundance. However, the abundance of heavy elements is smaller than the increase in cross section could compensate for this fact. The abundance of heavy nuclei¹ is of the order 10^{-4} , whereas the proton abundance is around 10 % of the total mass. To obtain a similar neutron emission rate as for the νp -process, the cross section has to compensate for the decrease in abundance. Thus the neutrino cross section on heavy elements should be of the order of 10^3 higher than the capture process on free protons. To be comparable from the nucleosynthetic point of view with the classical νp -picture, not the total neutral-current neutrino nucleus cross section has to be that large, instead only the neutron spallation cross section has to fulfill this requirement.

This is however not met in our actual calculation, because we are in proton rich material where the neutron separation energy is very high, especially in comparison to the proton separation energies. To give an estimate how important the neutron evaporation channel of our heavy isotopes for this exemplary trajectory is, we calculated the production rate of emitted neutrons by spallation reactions over time, in comparison to the number of neutrons created by the antineutrino capture on free protons.

The result can be seen within figure 4.6. The dominant rate over the whole temperature range is the capture process on free protons, which follows by the arguments given above. Neutral-current spallation effects on ${}^4\text{He}$ play a dominant role for the production of free neutrons, due to the fact that it is very abundant in the ejecta. We see that the neutral-current neutron production is stronger than the charged-current neutron production, which arises due to the higher energies of μ and τ neutrinos. The neutrino interactions on α -particles play an important part in the neutrino-driven wind, due to the fact that matter ejected from the PNS – regardless of being proton rich or neutron rich – will undergo α -rich freeze-out [145]. We will go back to this issue when we discuss r-process nucleosynthesis in the neutrino-driven wind.

To study only the influence of our heavy element neutrino-nucleus spallation cross sections, we neglected the cross sections on α -particles. The results for these calculations are displayed in figure 4.7. Additionally to the rate, we also show the average mass number for the trajectory that we are studying. We notice that when the average mass number increases (the black dotted line in figure 4.7) the neutron emission rate increases, too. However, processes on heavy nuclei play only a minor role. We are also able to observe that the rate of neutron emission increases, once the formation of heavier nuclei becomes possible because the temperature is small enough. The continuous decrease of all rates arises

¹ Heavy nuclei are hereby again all nuclei with $A > 4$.

simply due to the geometrical factor r^{-2} of the neutrino flux, where r is the radius of the considered matter. For high astrophysical temperatures neutral-current neutrino spallation dominates over neutron evaporation by charged-current neutrino capture processes. The additional bumps observable for both spallation rates arise from the fact that when matter moves further away from the valley of stability, all neutron spallation rates will decrease very fast. To proof this statement we additionally added in figure 4.7 the difference between the average mass number in comparison with the average number of protons, which can be taken as a measure of where the centroid of the heavy nuclei contribution is located. The factor 0.5 multiplied with the average mass number is just a normalization factor. The total numbers are not that relevant, instead what is of more importance is that the pattern reflects very well the bump structure of the neutron spallation rates. When moving more to the proton rich side, $(\langle A \rangle / 2 - \langle Z \rangle)$ will reduce and neutrino-induced neutron spallation rates become less efficient. This picture completely agrees with the rates shown in figure 3.8 for the emission of one neutron. For neutron deficient nuclei – e.g. ^{56}Ni , which is the dominant nucleus in the proton rich neutron wind – the cross sections for neutron emission is very small.

It is interesting that within the temperature range of 5 to 1 GK the ratio between the antineutrino-capture rate and the neutron emission rate almost resembles the ratio between protons and heavy nuclei, which were the aforementioned 10^3 . This ratio of heavy elements to free protons and neutrons is sensitive to the entropy of the system and the expansion timescale from the PNS surface.

So far we can say that, for the conditions which we studied within the neutron-driven wind, the heavy element production neutrino-spallation reactions play only a negligible role. To support this statement we want to study some dependencies that might arise from the simulation that we chose. Hereby we would like to vary sensitive parameters that influence the spallation cross section, such as the neutrino temperature. Furthermore we compared with another astrophysical neutrino-driven wind model by a different group [126].

Since the neutrino temperature is an essential parameter, as we already saw in previous subsections, we now want to study the sensitivity of our neutrino spallation reactions by increasing the neutrino temperatures for μ and τ neutrino flavor. This will increase only the neutral-current spallation rates on heavy nuclei and keep the antineutrino capture rate constant. Remember that the neutrino temperatures are usually determined by the mean energy of the neutrino spectra via $T_\nu = \langle E_\nu \rangle / 3.15$. An increase by a factor of 2 would thus lead to an increase of the mean energies by also a factor of 2 (resulting to values above 30 MeV), which is not in agreement with any core-collapse supernova simulations.

We therefore see this increase of a factor 2 in the neutrino temperature as an increase which is larger than possible uncertainties in the neutrino cross sections as well as uncertainties for the utilized neutrino spectra determining the mean energies of the different neutrino flavors.

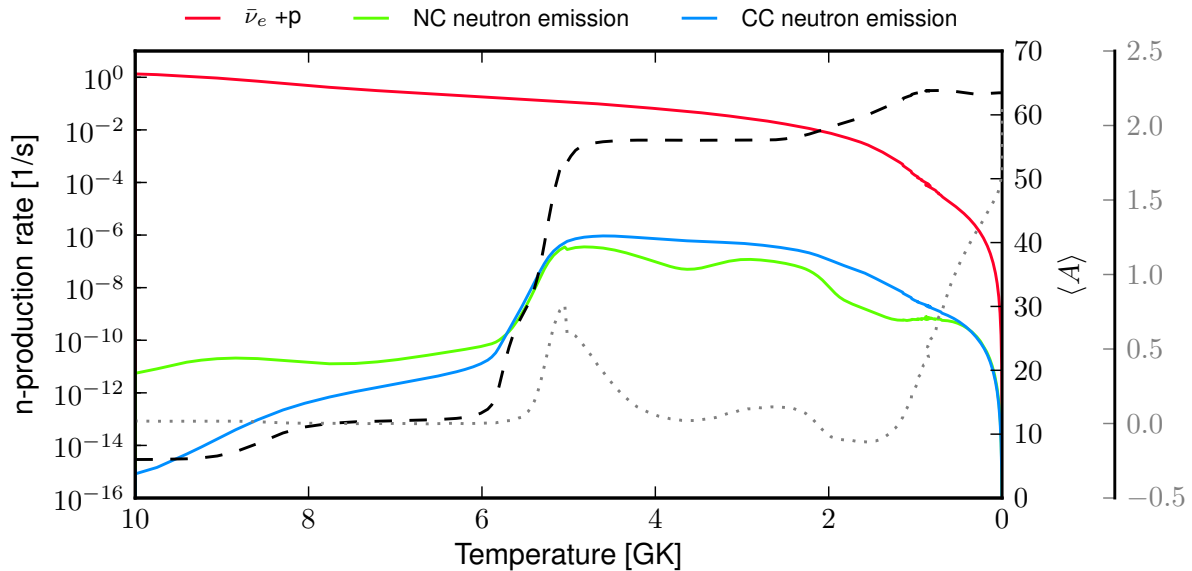


Figure 4.7.: All rates for neutron emission summed up and classified by its weak interaction channel. It is obvious that the dominant channel is still the antineutrino capture on free protons whereas the other channels only play a minor role. The black dotted line shown in the upper plot denotes the average mass number that can be obtained within the network. For an explanation of the wavy structure of the spallation rates we additionally plotted the difference between the average mass number and the average charge number (dashed line), which is a measure of the distance from isospin symmetry.

The results are similar to what is previously shown in figure 4.7, instead the neutral-current neutrino rates are now always larger than the charged-current reaction rates over the whole temperature range. Since the nucleosynthesis results do change only very little, we show within figure 4.8 only the neutron production rate, but additionally now with the temporal increased rate.

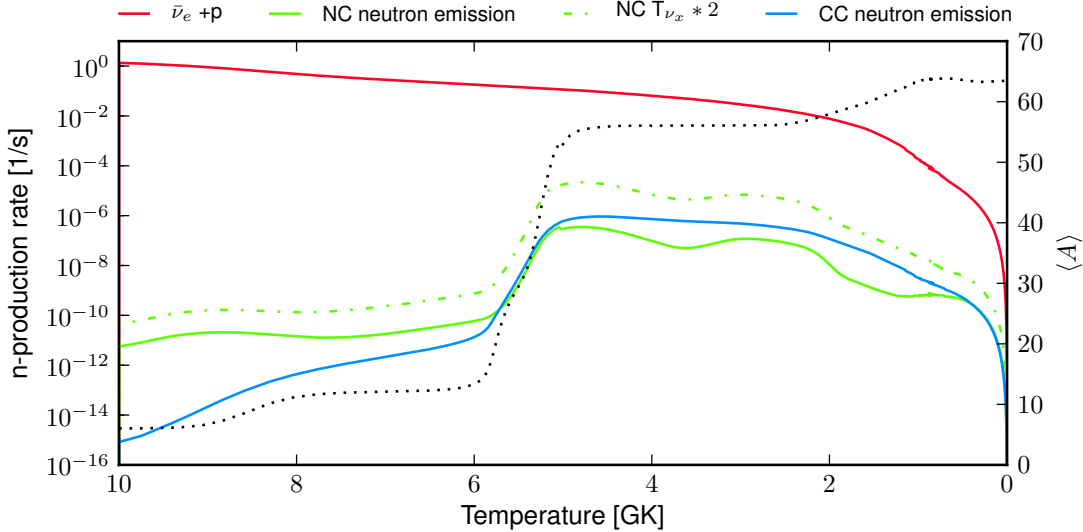


Figure 4.8.: The same as within figure 4.7, additionally we show the scattering rate increased by a factor 2 in neutrino temperature. Still the rate is not high enough, that neutrino spallation rates dominate.

To test if this result is model dependent, we calculated the nucleosynthetic outcome of a neutrino-driven wind scenario arising from a different core collapse supernova model [126], featuring a faster expansion, arising from higher luminosities and mean energies. The astrophysical parameters are given within figure 4.9. Within this figure we do not show the temporal evolution of the neutrino luminosities and average energies, because in this simulation we assumed that both quantities do not change over time. For the temporal evolution of the PNS this is however a very crude approximation, because we already saw in the previous model that the neutrino cooling of the PNS will reduce the neutrino flux. However, for the ejecta that we are studying in this work, the main reduction of the neutrino flux passing through the mass element under consideration will basically arise due to the radial expansion from the PNS which is very fast in this case. Therefore the decrease of all neutrino rates with time will be governed by the expansion, and the actual decrease of the neutrino flux by the cooling of the PNS is a second order effect. The values used within our simulation

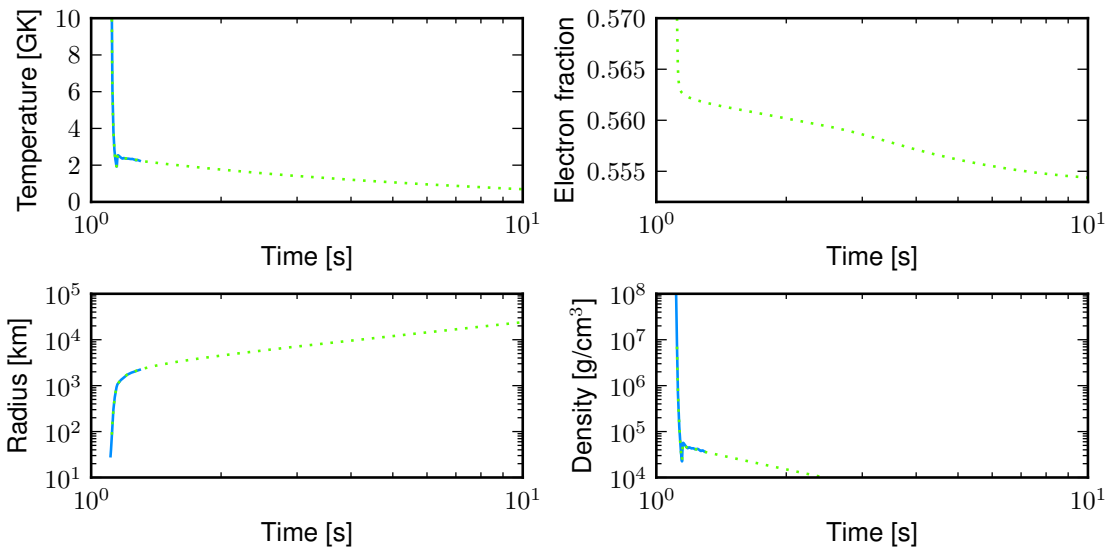


Figure 4.9.: The astrophysical parameters of the NDW simulations from [126]. For further details see the text.

are 17.9×10^{51} ergs/s and 17.7×10^{51} ergs/s for the electron neutrino and electron antineutrino luminosities. The luminosities for μ and τ neutrinos and antineutrinos all have the value of 24.5×10^{51} ergs/s. The mean energies are accordingly 12.15 MeV, 14.55 MeV and 15.4 MeV where the same order is applied as before. At the end we again follow an adiabatic expansion. Due to the simulation time of only 1.2 seconds we do not utilize a fitting routine, instead we only assume that our Δ is zero. Note that this Δ -parameter has a strong influence for the νp -process when the simulation is carried out for only a short period of time, since it can have influence on the expansion from the PNS. In terms of fluence a large Δ results in a longer exposure time, shifting this neutrino-driven wind scenario on the abscissa of figure 1.5 slightly to the right.

The chosen trajectory has an initial electron fraction of 0.57 and an entropy of $78 k_B/\text{nucleon}$. In comparison to the previously mentioned simulation data the expansion is faster, resulting in a less effective production of heavy elements over the triple- α rate.

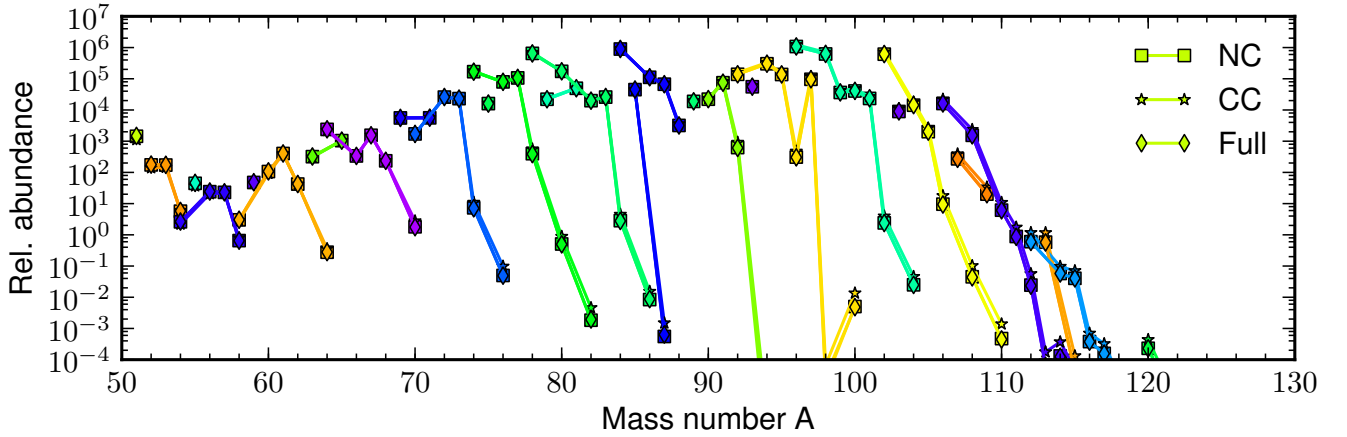


Figure 4.10.: The final nucleosynthetic yield for a trajectory of [126]. Note that the calculations where only charged-current rates are used and the case where all rates are used are hard to differentiate, because they basically lie on top of each other. The production of heavy elements is very effective due to the νp -process. Again we can observe that in comparison to the case where no neutrino interactions are considered a production of the NC neutrino spallation rates can be observed. If however charged-current rates are considered these changes are very small.

The results are shown in figure 4.10, where again a strong production via the νp -process can be seen up to mass number 130. The nucleosynthesis shows a stronger nucleosynthesis over the νp -process than in the previous model that we were studying. The reason why the production is stronger than for the previously shown case is due to the fact that the luminosities are substantially higher, which allows for a more effective production of free neutrons over antineutrino capture. Furthermore the average antineutrino energies are also higher.

Rather than showing the different channels separately – as we did in figure 4.5 – we show in figure 4.10 only the influence of our neutrino induced particle-spallation rates. Thus for all nucleosynthesis calculations shown in figure 4.10, we include the charged-current processes on free nucleons. The calculation where all neutrino interactions are utilized is labeled with “Full”. Furthermore we added two calculations labeled “CC”, where the neutral-current has been neglected, and “NC”, where the charged-current is disregarded. The changes that we can observe between the different calculations are rather small. Only for the neutron rich isotopes does the inclusion of neutral-current spallation cross section lead to a change in the final abundance. This small change is related to neutral-current spallation on He, which is higher due to the fact that the average energies of μ and τ neutrinos are higher than for the model that we discussed before. This increase explains the differences that can be seen for the inclusion of neutral-current neutrino processes.

In conclusion we can say that the inclusion of neutrino-nucleus interactions does only slightly change the final composition of the astrophysical trajectories of the neutrino-driven wind obtained within core-collapse supernova simulations with detailed neutrino Boltzmann-transport. The most important influence arises due to the inclusion of neutral-current neutrino-spallation processes of α particles, that change the final nucleosynthesis slightly.

The key point for the argumentation why the inclusion of heavy element neutrino-induced spallation rates produce very little change in the final nucleosynthetic yield arises from the fact, that neutron emissions from heavy elements are largely suppressed due to the proton richness of the ejecta. Furthermore our composition is dominated by α -particles and protons and only a small part is converted over the triple- α rate to heavy elements that act as targets for neutrino-nucleus evaporation processes. We could for example already observe that the evaporation of the isospin-symmetric nucleus ^{52}Fe

(see figure 3.11) is largely dominated by proton emissions instead of neutron emissions. The same holds true for the isospin symmetric nucleus ^{56}Ni , which will be the dominant nucleus in proton rich neutrino-driven winds.

More neutron deficient nuclei will only increase this tendency. The emission of protons by spallation reactions in proton rich ejecta does however not favor the creation of heavier elements, because we will only increase the amount of free protons, which is large anyhow and changes in the proton fraction will be very small.

4.2 Integrated nucleosynthesis in neutrino-driven winds

Although the microscopic description in the proto-neutron star is not treated consistently with the underlying equation of state – as we will discuss in 4.2 – we might pose the question what the nucleosynthetic outcome of proton rich winds will be. Due to the fact that we have a full description of neutrino nucleus processes, we are sure that all possible neutrino interactions important for the nucleosynthesis are considered in our network. Furthermore, the simulation data of [11] covers the whole period of deleptonisation, which allows us to study the total nucleosynthesis of the wind. This is especially important for the temporal behavior of neutrino luminosities and mean energies. We are therefore able to determine the final nuclear yields for the whole NDW phase, while exploring the impact of all possible neutrino-nucleus interactions that can alter the final nucleosynthetic outcome.

Even more interesting is the fact that within the work of [11] two core-collapse supernova simulations have been carried on for several tens of seconds, with different progenitor masses. This allows us not only to study the total nucleosynthetic outcome of the neutrino-driven wind within stars with different progenitor masses, but also to make statements about the dependence from the progenitor mass.

The two progenitor masses studied in [11] have an initial mass of 10.8 and 18.0 M_{\odot} [20]. In the above study on the impact of the new rates on neutrino-driven wind nucleosynthesis, we already presented three different trajectories of the 18.0 M_{\odot} model and the final nucleosynthetic outcome of these three trajectories. Of more relevance is however the question what the total nucleosynthetic outcome of the whole wind will be. We showed that due to the fact that the average energies for electron neutrino and antineutrino show almost the same energetic value, later ejecta will be more proton rich – as we discussed in 1.2.1 – leading to a more efficient νp -process. However with increasing time, the matter flux from the PNS surface will decrease, keeping the total heavy element production while the NDW uncertain. Within this work we have for the first time the possibility to determine the integrated nucleosynthesis of long-time core-collapse supernova simulations including all possible neutrino-nucleus rates that can have influence on the final nucleosynthetic outcome.

The total nucleosynthesis which is also called *integrated nucleosynthesis* – as suggested by [146] – can be calculated by weighting all trajectories from the simulation of the neutrino-driven wind by its mass content. The final integrated nucleosynthetic yield will thus be obtained by

$$X_i^{int} = \sum_m \frac{X_{i,m} M_m}{M_{wind}}. \quad (4.10)$$

The total mass of the neutrino-driven wind is split up into m different trajectories, the total mass of the wind will be simply $M_{wind} = \sum_m M_m$. It is helpful to define furthermore the *production factor*

$$P_i = \frac{M_{wind}}{M_{ej}} \frac{X_i^{int}}{X_{i,\odot}} = \sum_m \frac{X_{i,m} M_m}{X_{i,\odot} M_{ej}}, \quad (4.11)$$

where the final integrated nucleosynthetic yield is normalized to the solar system isotopic abundance, and rescaled by the ratio of mass ejected in the wind to the total mass ejected by the stellar explosion. The ejected mass is given as $M_{ej} = M_{star} - M_{NS}$, where M_{star} is the mass of the progenitor before explosion and M_{NS} is the mass of the neutron star. The relative abundance will give us directly the production of element i within the neutrino-driven wind. If this value is larger than one, we will have an overproduction of the corresponding elements in comparison to the solar system abundance.

As we already mentioned within the introduction, one major goal of this work is to determine the nucleosynthetic result of the neutrino-driven wind within state-of-the-art core-collapse supernova simulations and compare the integrated result with what is known from metal-poor stars to possibly link the production of the light r-process elements to core-collapse supernovae.

Parametric studies on the integrated nucleosynthesis in the neutrino-driven wind have been done by [146, 40]. In this work we are however for the first time able to take data from the simulation over the whole period of deleptonization of the PNS. We also obtain the electron fractions and luminosities within the simulations from detailed Boltzmann transport instead of a parametric study or approximate models. Furthermore we include all possible rates of relevance that will have influence on the nucleosynthesis.

Before we would like to show the results coming from our calculations, we would like to present in figure 4.11 the temperature and radial behavior of some of the studied trajectories. The left hand side shows temperature and radial evolution for the model with a progenitor mass of $10.8 M_{\odot}$ and the right hand side shows the corresponding parameters for the $18.0 M_{\odot}$ progenitor model. We are able to observe that the low mass model develops a reverse shock², which will

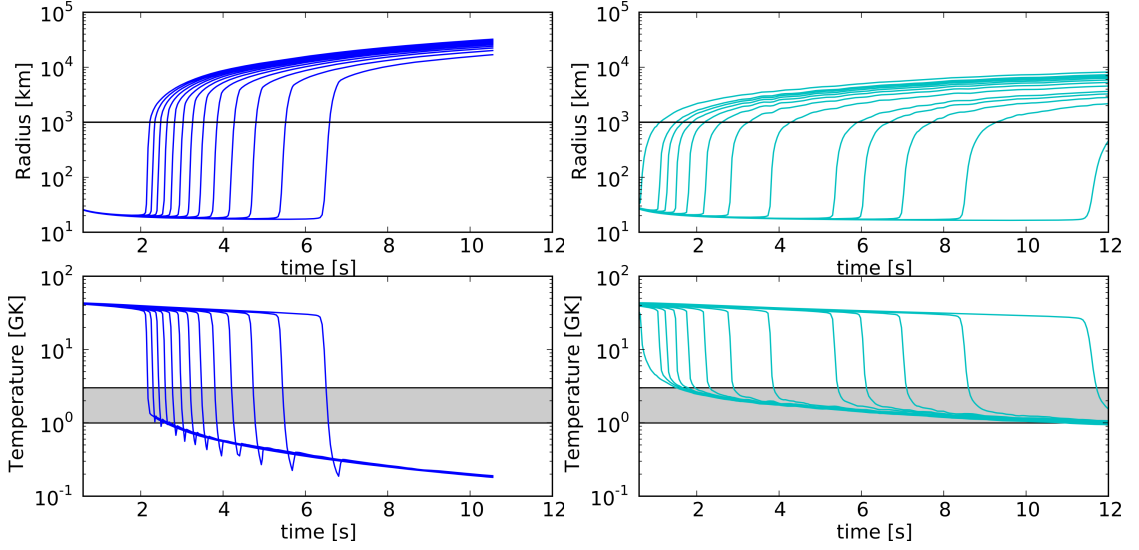


Figure 4.11.: Temperature and radial evolution of different trajectories of the NDW. The left hand side shows the evolution of the $10.8 M_{\odot}$ progenitor (blue) simulation whereas the right hand side represents a selection of the trajectories for the $18.0 M_{\odot}$ model (cyan). The marked area in the temperature plot represents the temperature range in which the νp -process works efficient. For temperatures higher than 3-4 GK quasi statistical-equilibrium is dominating, whereas for temperatures lower than 1 GK proton captures are slowed down due to Coulomb repulsion [43].

in general reduce the expansion velocity of matter, leading to a more effective νp -process [43]. In the case of the heavier mass progenitor, no reverse shock could be found due to the small ejection velocities that are reached in the simulation.

Within figure 4.11 we furthermore marked in grey the ideal temperature range for the νp -process. This temperature region basically arises due to the fact that for higher temperatures quasi-statistical equilibrium³ dominates, and for temperatures below 1 GK the particle capture processes freeze out because the temperature is too small for proton capture processes. In the radial plots we marked a radius of 1000 km for orientation.

With the help of the plots shown in figure 4.11, we are already able to explain the nucleosynthetic outcome of the two neutrino-driven wind scenarios available to us. The final result is given in figure 4.12, where the $10.8 M_{\odot}$ model is shown in blue and the $18.0 M_{\odot}$ model in cyan. Within this figure we show in the upper plot the final production factors of the NDW in both models. In the lower part of the figure the elemental abundance pattern is shown. The elemental abundance pattern is renormalized such that the sum of all mass fractions is unity. For the isotopic results of the $18 M_{\odot}$ model, we are able to observe that the integrated result shows a production of elements up to $A \sim 100$, before a steep decrease at $A \sim 110$ can be observed. However, for the lighter progenitor model, no production of heavy elements due to the νp -process can be observed that has influence on the star's total nucleosynthesis. The abundance pattern up to $A \sim 70$ is relatively similar but while the heavy mass star abundance pattern increases, the light progenitor model only shows a decrease.

The explanation why the νp -ejecta are predominantly produced in the heavy mass progenitor can already be found within figure 4.11. Due to the very fast expansion of matter from the PNS within the low-mass model, matter is moving rapidly to very high radii. Due to this fast expansion the reverse shock does not increase the nucleosynthesis, because matter is already too far away and too cold. This fast expansion relates to the fact that the density of the light progenitor as a function of radius decreases very fast, while for the heavy mass progenitor the density behavior is more shallow. Generally speaking will the density behavior of stars with a progenitor mass between 11 and around $14 M_{\odot}$ have very steep density profiles, progenitors with higher masses will therefore have a similar density behavior than the $18.0 M_{\odot}$ model discussed here [148]. Thus light progenitors will have in general fast expansion velocities, while more massive progenitor models will give smaller expansion velocities. Since the neutrino flux goes with r^{-2} , a fast radial expansion

² The reverse shocks can be identified within figure 4.11 due to the undershooting in temperature which recovers very soon. A reverse shock occurs, when the matter in the NDW is ejected so fast that it will collide on its expansion outwards with the shock ejecta.

³ Quasi-statistical equilibrium denotes a state in which groups of nuclei are in equilibrium. The reactions that connect these different groups are however not in equilibrium [147].

leads to a strong suppression of the neutrino rates. The second fact related to the very fast expansion is the decrease in temperature. As can be observed by the lower plot in figure 4.11, the temperature is dropping so fast that matter spends only a very short period of time in the relevant region for the νp -process.

The behavior is completely different for the high mass progenitor model. The expansion proceeds very slow in comparison to the earlier discussed model. For the light progenitor, the rapid expansion pushes matter to regions of several ten-thousands of kilometers very shortly after emission from the PNS. In the more massive model the slower ejection keeps matter almost an order of magnitude closer to the PNS surface, when the radius is measured in kilometers. The fact, that matter is expanding slower from the PNS, will keep the matter longer in a temperature range in which the νp -process can operate and the neutrino fluxes are higher. Both effects contribute to the more effective production of heavy elements due to the νp -process.

Note that, as discussed above, neutrino-nucleus scattering/capture processes have been included within the calculations, their contribution is however very small for the heavy element production in comparison to the capture process of free protons.

The elemental abundance pattern shows the same global behavior as the isotopic. The more massive progenitor produces heavier elements, while the low mass progenitor shows very little heavy element production. For comparison we added the scaled abundance pattern of the metal-poor star HD 122563 to the elemental abundance pattern of figure 4.12, where we normalized the abundance of HD 122563 to zinc ($Z=30$). The final elemental abundance of the low mass model drops off way to fast to reproduce the elemental abundance pattern of the metal-poor star. On the other hand, the heavy mass ejecta follows roughly the trend of the observation, up to charge number 44. The observed abundances of the elements with charge $Z > 44$ cannot be explained with the nucleosynthesis in this proton rich neutrino-driven wind.

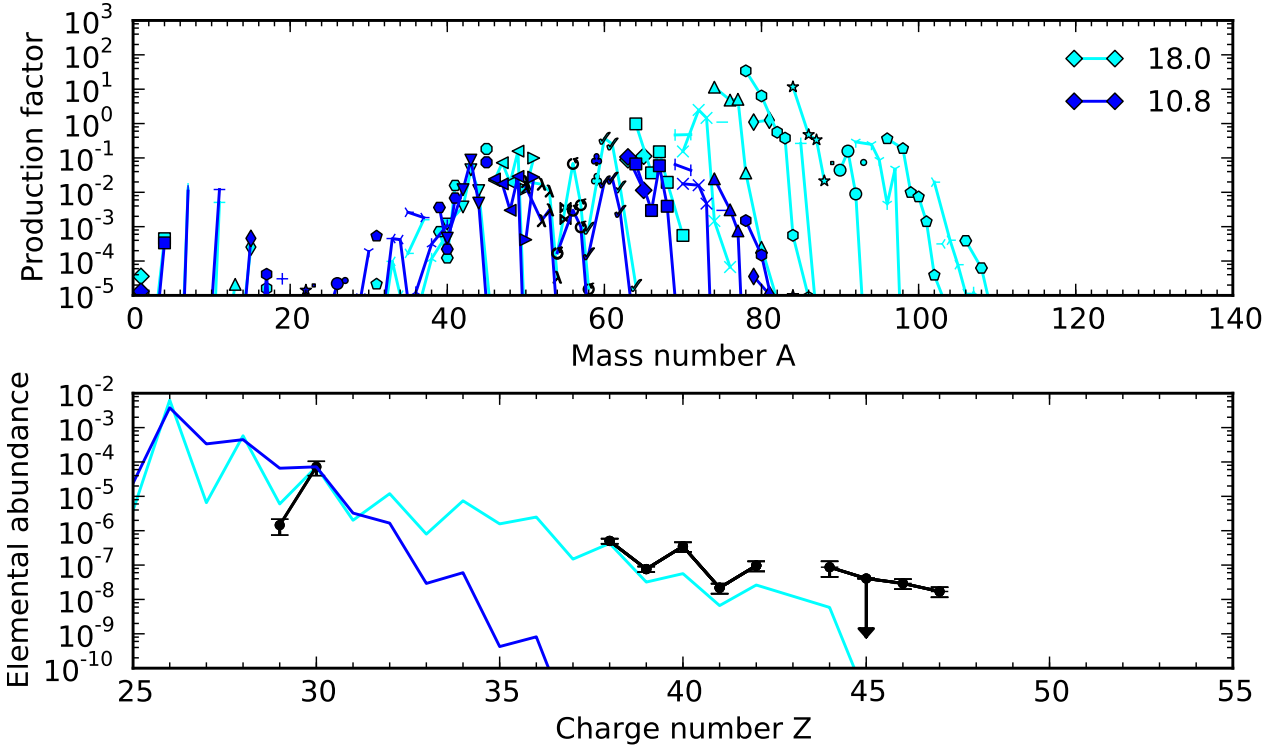


Figure 4.12.: The production factors of the complete wind for the two models studied within this work. The model with an initial progenitor mass of $18.0 M_{\odot}$ is given in cyan. In blue the results of the model with $10.8 M_{\odot}$ are presented. As we can see, the production of heavy elements is stronger pronounced in the heavier progenitor. In the lower plot we show the elemental abundance of the two models considered here. Additionally to the calculated elemental abundance, we also present the observed final abundances of the metal-poor star HD 122563 in black.

Note that by a larger neutrino flux, we are able to increase the effectivity of the νp -process to a degree in which an agreement with the metal-poor star observations could be achieved. As we saw in our previous observations the easiest way to reach this requirement for the neutrino flux is by reducing the escape velocity. This is a way how the nucleosynthesis results of the higher progenitor mass model can be met with the observations of the measured abundance pattern of HD 122563. We will however not do so, since it is not the task within this thesis to find the conditions in proton rich winds to reproduce the abundance pattern of these metal-poor stars, instead we aimed in observing what the

nucleosynthesis outcome of core-collapse supernova simulations will be, without any changes to the data, but including a full set of neutrino-nucleus rates.

Furthermore we would like to note that these studies so far only incorporate two different progenitor masses. Thus with the current set of data it would be logical to estimate that with increasing progenitor mass the heavy element production will rise, too. However, due to the aforementioned fact that for more heavy mass progenitors the density distribution will change only slightly [148], we expect that the production of heavy elements will be comparable to the $18.0 M_{\odot}$ simulation. To strengthen this statement, further simulations are required. However, this is so far only an assumption based on the density distributions of progenitor models with different mass. A realistic understanding will of course only be possible if several NDW scenarios are studied that initially had different progenitor masses. Furthermore, details of the utilized simulation have to be considered, such as neutrino luminosities, average neutrino energies and the escape velocities of the PNS which will definitely have a strong influence on the nucleosynthetic outcome of the neutrino-driven wind. Even the evolution of the progenitor will definitely be model dependent, and will vary the amount of matter already emitted before the collapse sets in, e.g. in thermal pulses. So far we are only able to conclude that the models used in the simulations of [11] tend to produce with increasing progenitor mass heavier final elemental abundances. To obtain final elemental values for this proton rich neutrino-driven wind that can be comparable with the measured elemental abundances of the metal-poor star HD 122563, the production of the νp -process has to be increased. This can be done by an increase in the reduction of the escape velocity and the increase of neutrino luminosities and average energies. We have to note again that these wind models do not consider a consistent treatment of the microphysics in the PNS.

In the next section, we would like to discuss how the inclusion of improved microphysics will change the spectra and the nucleosynthesis.

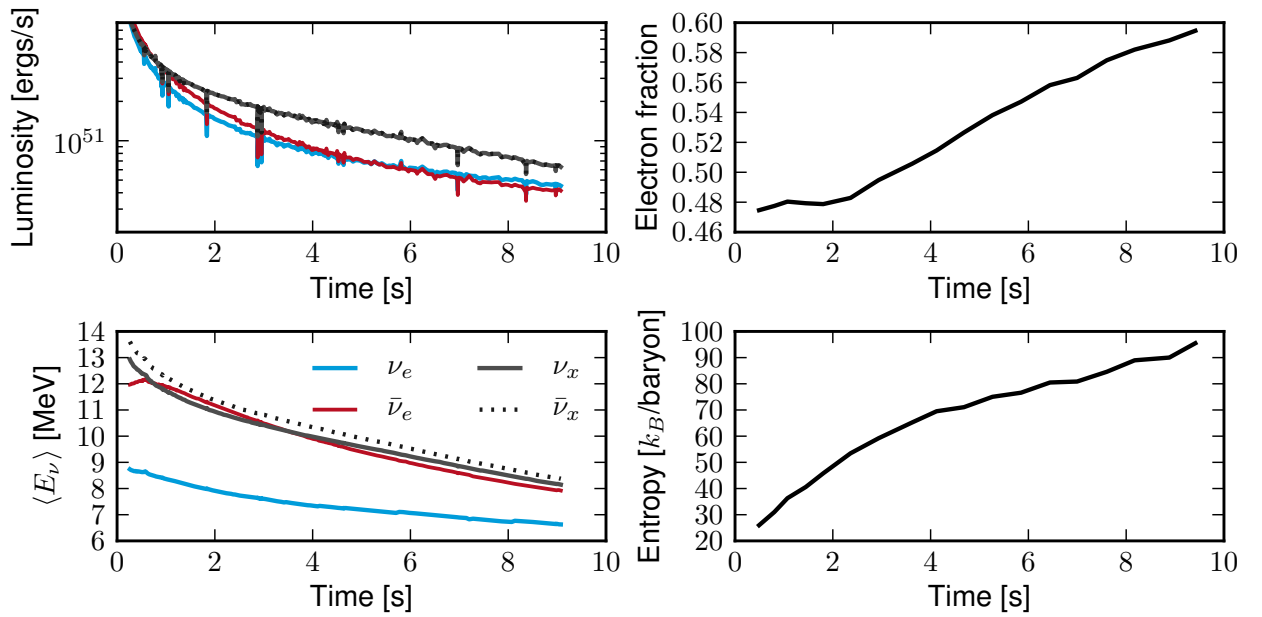


Figure 4.13.: Within these plots we show the luminosities, average energies, entropies as well as the electron fraction Y_e as a function of time for a model with an initial progenitor mass of $11.2 M_{\odot}$. The electron fraction first is neutron rich, while later ejecta will be proton rich again. With ongoing cooling, the ejected material will again become proton rich. The change in electron fraction from neutron rich to proton rich matter can be explained with the behavior of the neutrino luminosities and average energies.

Nucleosynthesis with improved microscopic nuclear input

As stated above, the production via the νp -process can only produce elements beyond germanium in proton rich ejecta, since it requires free protons to act on. The proton richness arises due to the balance of electron neutrino captures on free neutrons and electron antineutrino captures on free protons in the PNS. The interaction processes within this PNS – especially the charged-current neutrino/antineutrino reactions – shape the neutrino spectra quite sensitive. With

the continuous cooling of the PNS the neutrino-spheres⁴ will move further inwards towards higher densities. With increasing density, effects of the nuclear interaction become more important. At moderate densities within the PNS the nuclear interaction can be treated in a mean-field approach, that accounts for the proton-to-neutron distribution within the PNS. The energy-momentum relation can on the mean-field-level be described as

$$E_i(p_i) = \frac{p_i^2}{2m_i^*} + m_i^2 + U_i \quad i = n, p \quad (4.12)$$

where we assumed that protons and neutrons behave non-relativistically and (m_i^*) m_i gives the (effective) mass of the protons and neutrons. U_n and U_p are the mean-field potentials. The difference between U_n and U_p can increase up to several tens of MeV. The exact values of the potentials have to come from the equation-of-state applied within the core-collapse supernova simulation. For the description of the weak processes, we can therefore write the energy relation for the reaction $\nu_e + n \rightarrow p + e^+$ simply as

$$E_{\nu_e} = E_{e^-} - (m_n - m_p) - (U_n - U_p) \quad (4.13)$$

and

$$E_{\bar{\nu}_e} = E_{e^+} + (m_n - m_p) + (U_n - U_p) \quad (4.14)$$

in the case of antineutrino capture on free protons. We assumed for this result what is known as *zero-momentum transfer* in which nuclear recoil effects are neglected. Until now, the difference $\Delta U = (U_n - U_p)$ has been neglected in core-collapse simulations so far, although this correction will reduce the energy of the emitted electron neutrinos while the energy of the electron antineutrinos will be increased. This will raise the energy difference between electron neutrinos and anti-electron neutrinos by the value $2(U_n - U_p)$. First results with the inclusion of these mean-field potentials show that the electron fraction of the early ejecta in the neutrino-driven wind can now reach values below 0.5 [140], in which the νp -process cannot contribute to the heavy element production. Note that simulations of core-collapse supernovae in general are sensitive to the used equation-of-state due to the variety of densities, temperatures and electron fractions that can be found in different regions of the star.

Since we do include all allowed interactions between neutrinos/antineutrinos and a nucleus in the initial state, we are now able to determine the heavy element production with the improved mean-field potentials. The results from our calculations can be found in figure 4.14 for a model with an initial progenitor mass of $11.2 M_\odot$. The equation of state used in this simulation has been a generalized relativistic mean-field model, that is also reproducing the newly obtained constraints on the symmetry energy [149]. The relevant final astrophysical parameters for the nucleosynthesis are plotted within figure 4.13. As can be observed within this figure, the simulation has been carried on for over nine seconds after bounce. The most important fact for the nucleosynthesis is that the neutrino luminosities for electron neutrino and electron antineutrino have a different slope with time. At approximately three seconds post bounce, the electron fraction will move from neutron rich to proton rich matter. Two mechanisms are responsible for this behavior. The first mechanism is that the luminosities of electron neutrinos and electron antineutrinos show a different behavior with time, which goes so far that at approximately five seconds the luminosities cross. At earlier times the electron antineutrino luminosity is larger than the electron neutrino luminosity; at later times the case is inverted.

The second mechanism is the reduction of the electron neutrino mean energies. The first fact that one can observe, is the cooling rate of the PNS that leads to the reduction of the average energies of all flavors with time. This fact is well known and described by the Kevin-Helmholtz evolution of the PNS [150]. The evolution for the energy difference between mean electron neutrino energy and mean electron antineutrino energy tends to decrease with time, which leads to proton rich ejecta, as we discussed within the appendix (see 4.9.1). Both effects contribute to the increase of the electron fraction, where however the latter one is the dominant contribution.

It is interesting to note that the usual energy hierarchy in which $\langle E_{\nu_e} \rangle < \langle E_{\bar{\nu}_e} \rangle < \langle E_{\nu_\mu, \nu_\tau} \rangle < \langle E_{\bar{\nu}_\mu, \bar{\nu}_\tau} \rangle$ is at two seconds post bounce partly inverted for a time range of roughly one second. Within this time frame, the average electron antineutrino energy is higher than the average neutrino energy of μ and τ neutrinos and their corresponding antiparticles. The reason for this change is related to the corrected description of the microscopic input, which increases the average energy of $\bar{\nu}_e$ -neutrinos.

Whether this is a feature of this specific simulation or a global result needs to be evaluated in more detail.

Furthermore the μ and τ antineutrino energies have higher energies than the μ and τ neutrino energies, which is in first order surprising because processes including μ and τ neutrinos/ antineutrinos can only occur due to the neutral-current.

⁴ The neutrino-spheres define the region that separates the inner part of the PNS which is dense enough, such that the mean free path for neutrinos is very short and the outer part in which neutrinos are almost free streaming. Once the neutrinos pass the neutrino-sphere the neutrino spectra are basically fixed.

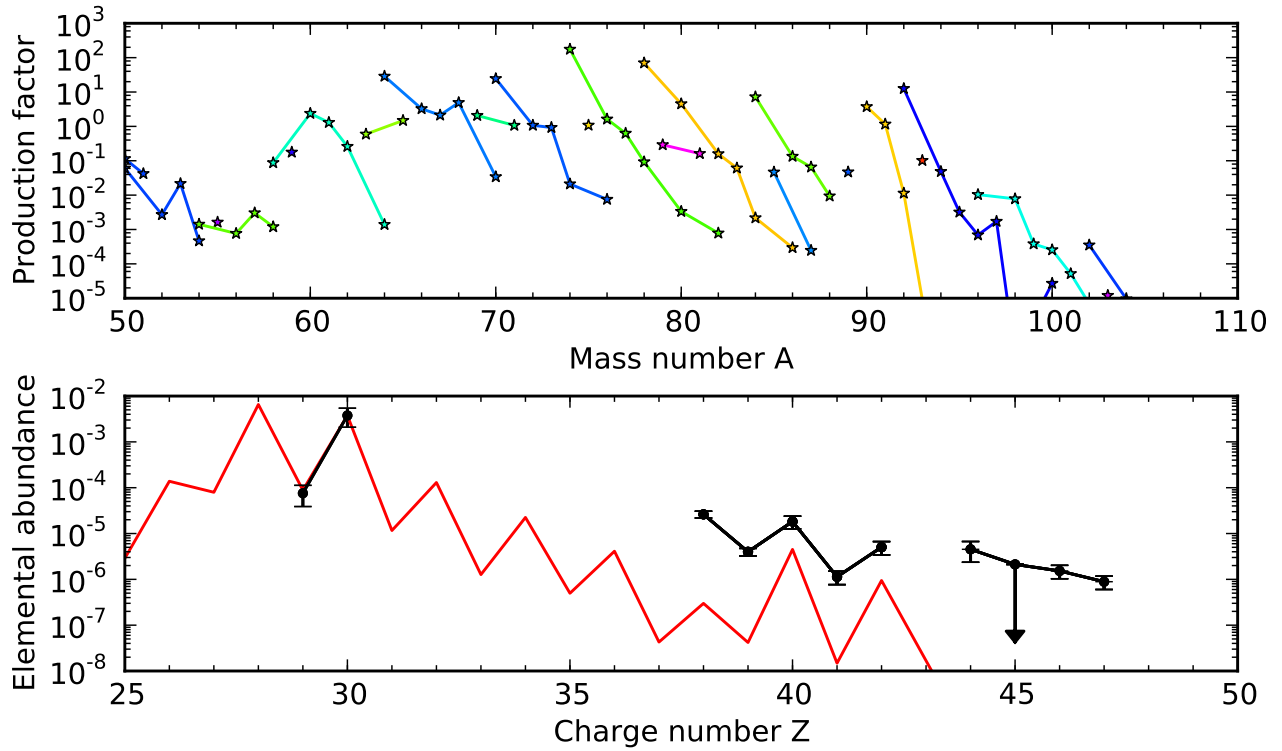


Figure 4.14.: The integrated final yield for the neutrino-driven wind of a $11.2 M_{\odot}$ model, with the improved microscopic description of charged-current rates. The used equation-of-state has been a relativistic mean-field model, known as DD2. This model shows less production of the light r-process elements in comparison to previous integrated yields ($18.0 M_{\odot}$).

The reason why the mean antineutrino energy is slightly higher than the mean neutrino energy arises due to the fact that the couplings for neutral-current scattering of μ and τ neutrinos on nucleons and electrons are different. These differing couplings result in a different cross section of neutral-current neutrino/antineutrino scattering processes on nucleons and electrons. This difference between ν_x and $\bar{\nu}_x$ is however smaller than the energy difference of ν_e and $\bar{\nu}_e$. At this point it is important to not again, that we included each neutrino flavor individually, also separating between ν_{μ} and $\bar{\nu}_{\mu}$ as well as ν_{τ} and $\bar{\nu}_{\tau}$. Thus in our nucleosynthesis studies we are able to incorporate these differences.

The integrated nucleosynthesis of the neutrino-driven wind phase with the correct mean-field potential treatment is shown in figure 4.14. Again we show for comparison of the elemental abundance pattern the abundances of the metal-poor star HD 122563. Our calculations show that the elemental abundance trend of the elements around $A = 90$ – such as Zr ($Z=40$) – can be roughly reproduced. However a contribution to heavier elements could not be observed.

The isotopic abundance pattern of the integrated yield do not show such a strong drop for each isotopic chain, than in the previous studies without the consistent potentials. What we are trying to express with that is, that for each isotopic chain within this figure, the neutron richer elements do not show such a strong decrease in abundance as in the $18 M_{\odot}$ progenitor. We found that the reason for this higher abundance of the neutron rich isotopes is not the early neutron rich ejecta, instead the dominant production of this neutron rich material arises due to νp -production, which is not as steep decreasing for less neutron deficient isotopes than the neutron rich early ejecta.

The inclusion of the mean-field potentials has for the nucleosynthesis the first order effect, that the electron fraction is reduced. With the old treatment, early ejecta were proton rich and as time continues became even more proton rich. Now initially we start of with slight neutron rich material, which will become proton rich with increasing time. With a reduced electron fraction, the νp -process cannot operate as efficient as in the case of the heavy $18 M_{\odot}$ model that we discussed above, because in the neutron rich ejecta the νp -process can not operate. This fact is also reflected in the integrated abundance pattern. For the isotopic abundance pattern we can observe that the production of heavy elements continues only up to 92, instead of up to 100 as before. In the elemental abundance pattern we are able to observe – in comparison with figure 4.11 – that the neutrino-driven wind with the inclusion of the correct microscopic description produces less material in the region above $Z = 30$. This has however two reasons that should be studied in detail with further simulations. The first reason is the already mentioned reduction in electron fraction due to the new potentials. The second fact is the dependence of the nucleosynthesis from the progenitor – especially its mass. Since

we do not have data from a simulation of the same progenitor without the new corrections, we are not able to specify the nucleosynthesis results of the neutrino-driven wind without the inclusion of the new microscopic corrections. Thus it is not possible without any further simulations to quantify how strong the change of the microphysics changes the nucleosynthesis. It would be interesting to have a set of simulations of different progenitor models with and without the mean-field potentials. This could give us a systematical insight about how the νp -process behaves with progenitor mass and how the mean-field potentials change the nucleosynthesis. However, the correct description is only given when the correct microphysics is included.

The contribution of the slightly neutron rich ejecta to the integrated nucleosynthesis is noticeable at $A = 90$ and $A = 92$, as we will show soon. Although the electron fraction of the NDW is only very shortly neutron rich (maximal three seconds), this short time is sufficient to have an imprint on the integrated abundance. The reason for this fact is related to the massflux from the PNS, which is initially higher than for late time ejecta. The massflux as a function of time is shown within figure 4.15, where we can see the strong decrease as time increases.

To study the nucleosynthesis of the neutron rich ejecta explicitly and to understand their influence in the integrated nucleosynthesis, we show in figure 4.16 the isotopic abundance pattern of neutron rich ($y_e=0.474$) and proton rich ($y_e=0.586$) ejecta. The latter one corresponds to late ejecta, that are emitted around nine seconds post bounce, while the neutron rich ejecta are emitted very early (0.3 s post bounce). The neutron rich trajectory shows a large relative abundance of the elements between $A = 60$ and 95.

Although the electron fraction is below 0.5, the dominant nuclei produced in this region are the proton rich stable nuclei which is at first sight quite surprising, but the important astrophysical parameters – especially the low entropy – do not allow the system to create the more neutron-rich nuclei. Therefore the final abundance pattern of the neutron rich trajectory in the region $60 < A < 90$ shows almost the same pattern as the nucleosynthetic results of the late ejecta. The only larger difference can be seen in the region above $A = 90$, where the production in the neutron rich environment shows a strong creation of ^{90}Zr and ^{92}Mo , which are much less produced in the proton rich case. Above these elements, very little isotopes are created in the neutron rich case, whereas the creation of matter continues a bit longer for the late ejecta. The reason for this sudden drop in abundance above Zr and Mo has its origin in the $N = 50$ shell closure, that hinders material to continue moving to higher mass number. If the electron fraction would decrease even more, the effects would be even more clear.

The production of heavy elements is thus two fold with the inclusion of the mean-field potentials. Neutron rich ejecta will have under the current entropies a hard time to overcome the $N = 50$ shell closure. The creation of heavy elements in proton rich ejecta without neutrino interactions will end at ^{64}Ge , as mentioned previously. Neutrino interactions help

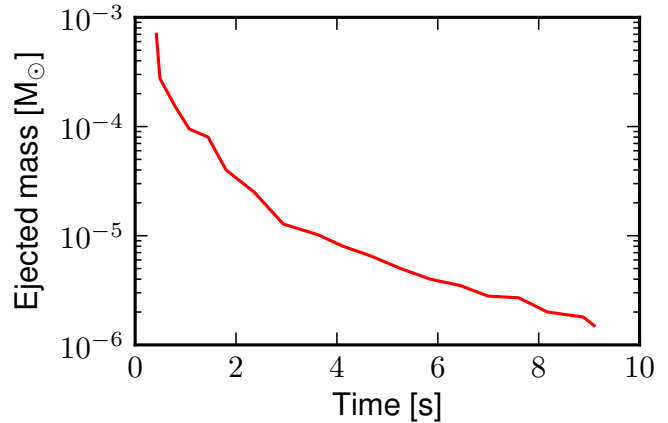


Figure 4.15.: The mass flux within the NDW of the $11.2 M_{\odot}$ model.

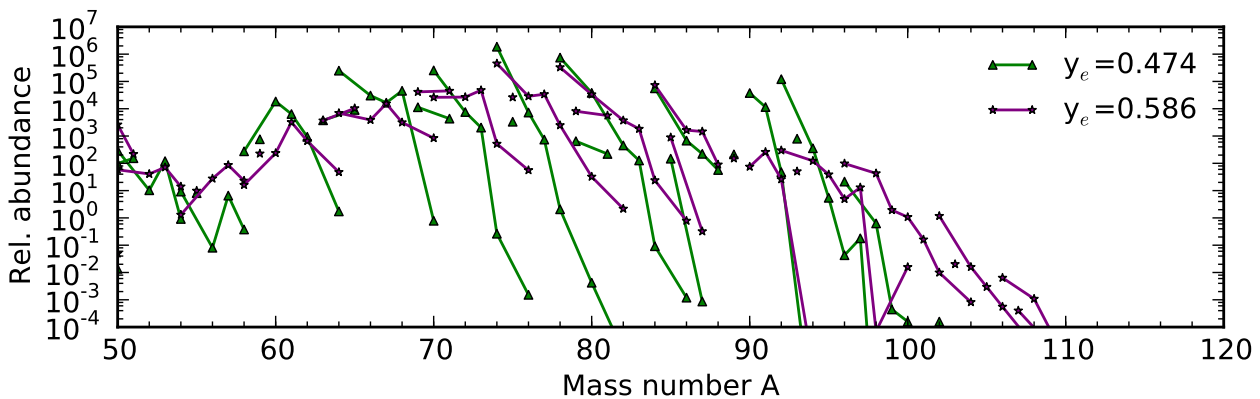


Figure 4.16.: The abundance pattern of two different trajectories in the $11.2 M_{\odot}$ model. The final abundance pattern shown in green stems from an early trajectory in the neutrino-driven wind where the matter is still neutron rich. To show the difference to proton rich ejecta we included also a trajectory that has been ejected at 7.6 s post bounce. The isotopic result of this trajectory is plotted in purple.

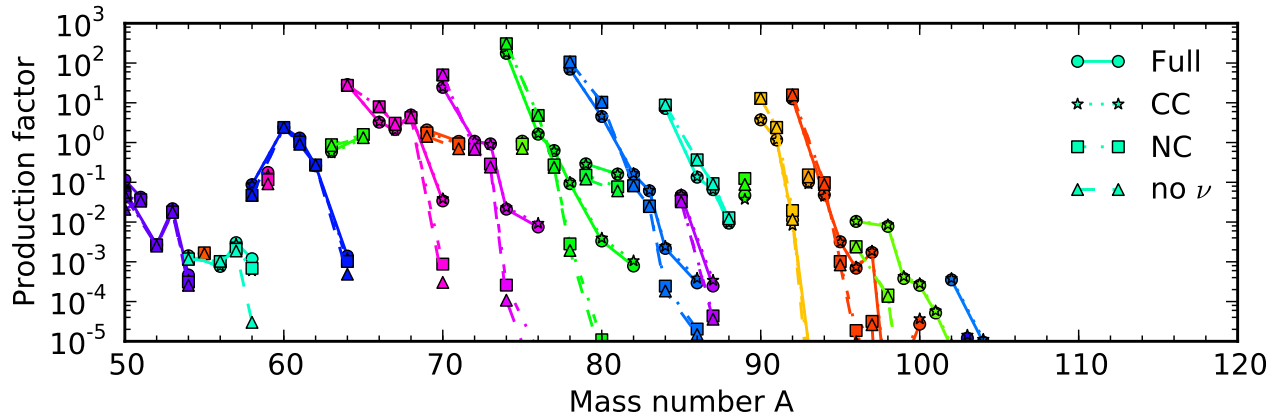


Figure 4.17.: The final integrated nucleosynthetic outcome of the one-dimensional core-collapse supernova simulation, including the improved microscopic input. The difference within the various calculations is that we suppress different neutrino processes to observe their contribution to the total nucleosynthesis. Isotopic chains are plotted with the same color. Octagons relate to a calculation where all neutrino interactions are neglected. Contrary to that, the results marked with circles include the neutrino-nucleus rates up to two-particle emission, both for neutral-current and charged-current processes. The stars (squares) are results, where only charged (neutral) current processes are considered.

creating heavier elements, mainly due the capture of antineutrinos on free protons. This is exactly what can be observed in figure 4.14.

The integrated nucleosynthesis shown so far always includes the newly calculated rates of this thesis. To observe the influence of the new included processes we apply the same procedure as before, in which we partially neglect various neutrino processes and observe their influence on the final isotopic nucleosynthesis. The results can be found in figure 4.17. The calculation with the inclusion of all rates is labeled “Full”. To study the effect of neutrino interactions, we set a baseline by calculating the same trajectory without any neutrino interactions. These calculations are labeled with “no ν ”. We additionally calculated the contribution of only charged-current processes on nuclei labeled “CC”, which denotes that we neglect the capture processes on free protons and neutrons. The same formalism is utilized for neutral-current processes; they can be found in the lower figure by the label “NC”.

The first observation that we can make is that the dominant change arises from the inclusion of antineutrino captures on free protons. However, since a lot of the total mass is emitted under neutron rich conditions or the value of the electron fraction is below 0.5, there is no contribution of the νp -process. Note that an equally strong νp -process is also not expected, since the progenitor has less mass than our $18.0 M_{\odot}$ model. The inclusion of neutral-current and charged-current processes on nuclei show only small effects, which are however noticeable. The changes are due to the

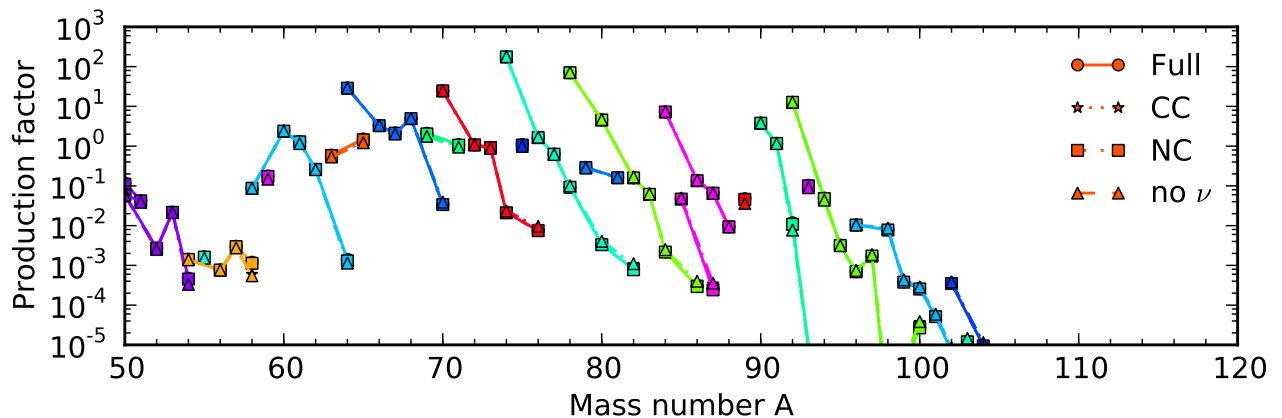


Figure 4.18.: The integrated nucleosynthetic results for the neutrino-driven wind with the new included microphysics. Contrary to figure 4.17, we always include the interaction on nucleons. Therefore the changes that can be seen in the upper figure are only due to the interactions of heavy elements.

neglect of antineutrino capture processes in the proton rich ejecta and not due to the inclusion of heavy element neutrino evaporation processes. This figure is therefore more to demonstrate the influence of the proton rich ejecta.

For each isotopic chain, the nuclei with higher neutron number seem to be more affected by neutrino processes. The main reason for this fact is that these elements have less total abundance, which will make small changes easier to observe. For example are we able to recognize that by the inclusion of only neutral-current processes the final composition of these neutron rich isotopes is changed in comparison to the case where no neutrino interactions are used. The same change is expected for the charged-current case when neutrino processes on nucleons are neglected. In comparison to the calculation where we included all neutrino interactions these changes are so marginal that they do not matter anymore, due to the fact that the νp -process has still a strong contribution on these neutron richer nuclei, since in the proton rich ejecta the total neutron flux from neutrino interactions is higher than in neutron rich ejecta.

If however the electron fraction would be smaller (≈ 0.4), such that the nucleosynthetic path within the neutron rich ejecta would proceed more on the neutron rich side, we would observe a very strong overproduction of the elements with shell closures at $N = 50$.

To show the effects from our neutrino-nucleus spallation by itself, without the effects of νp -nucleosynthesis, we made an additional calculation where we always included the capture processes on nucleons, and only turned off the currents on the heavy nuclei. The results can be found in figure 4.18, and show very little changes between the calculations. For the neutron rich isotopes a change is observable.

4.2.1 Light element production in the neutrino-driven wind

Within the last subsections we were focused on observing changes in the heavy element production due to the inclusion of our new rates. We could observe that changes in proton rich ejecta were so small that they cannot be observed on the scale shown in the figures. The dominant reaction within the NDW scenario is the creation of free neutrons over antineutrino capture of protons. The reason for this fact is that the heavy elements are much less abundant than free protons to compete with this process, although the cross section might be smaller.

The question however is if we can observe changes in the final yield of a neutrino-driven wind trajectory for light elements. For example we will have due to the α -rich freeze-out a high abundance for α -particles. Neutrino processes on these nuclei can help producing light elements.

The production of light elements under the influence of a strong neutrino flux has been already studied in neutrino nucleosynthesis [2, 134]. However within their work the authors focus has been on the outer shells of the star where the shock heats the matter shortly and initiates the expansion. In the neutrino-driven wind matter is expanded due to neutrino heating close to the PNS. Furthermore this matter does cool while expanding from the PNS, only when reaching the shock a possible short reheating is expected. The basic mechanism should however be the same: Neutrino-reactions – dominantly of neutral-current type – evaporate n,p and α -particles from the most dominant particles and help creating less abundant nuclei. In comparison to “normal” ν -nucleosynthesis are the nuclei on which the neutrino induced processes occur created while the matter is expanding from the proto-neutron star. The detailed mechanism of neutrino nucleosynthesis will be discussed later on when we present the influence of our rates in the ν -nucleosynthesis.

Within this part we will discuss a selection of the previous mentioned calculations on neutrino-driven wind nucleosynthesis, but instead on focusing on the heavy element creation we will only study the elements up to $A = 50$, which is the region that we did not show in the plots above.

What can be seen within figure 4.19 is that the inclusion of neutrino interactions do result in an increase in the abundance of the light elements Li, Be and B. The changes between the different types of calculation span several orders of magnitude and show that the inclusion of neutrino processes have an influence on the nucleosynthesis. The production factors for the inclusion of all neutrino processes show actually values that are substantially smaller than one, and therefore the neutrino-driven wind is not a suitable site for the production of these light elements. However, the changes that we could observe due to the inclusion of neutrino processes are the largest for these light elements.

For a successful production of these isotopes on this specific astrophysical site the production would have to be higher than one. This can be seen for example in the NDW ejecta of heavy elements, where relative abundance factors up to 10^3 are reached. In comparison to such large numbers, the production factors of the light element definitely do not contribute to the total nucleosynthesis. So we can conclude that the production of these light elements in the neutrino-driven wind is not relevant to the stars total nucleosynthesis. As we will see later is the main production site of these light elements the shock passage through the outer shells of the star. We will discuss that in more detail in section 4.5.

At first sight it is surprising to see that the creation of these light elements has similar contributions of both the charged- and neutral-current, because in ν -nucleosynthesis neutral-current processes should dominate [2]. The reason why within this scenario the charged-current is equally important is two-fold. The first point is, that the used neutrino spectra are taken from current simulations, while the mean energies and luminosities utilized in 4.5 are probably too high, especially for μ and τ neutrino flavor, which will reduce the folded neutral-current cross section. Second the antineutrino on free protons does create free neutrons, which in this proton rich environment can also be captured by protons to create

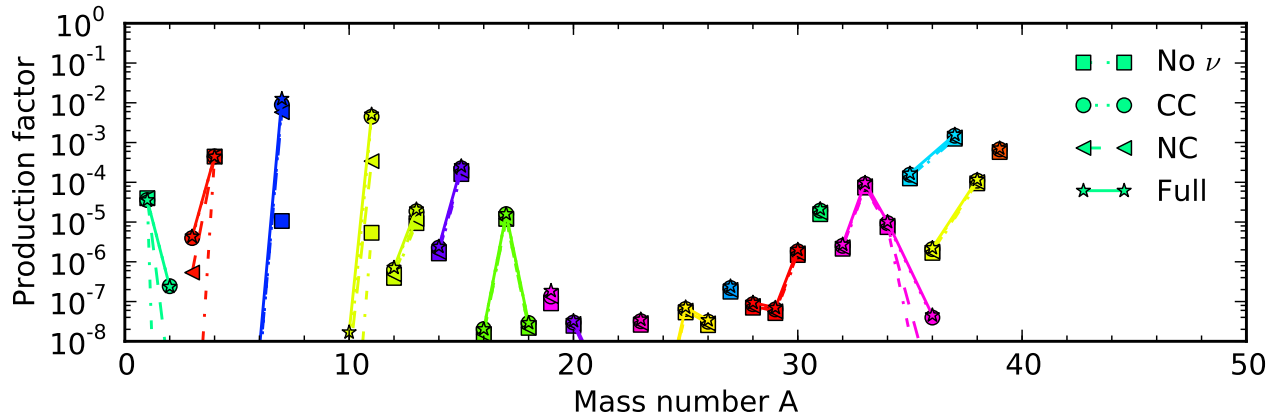


Figure 4.19: The integrated nucleosynthesis of the $18 M_{\odot}$ progenitor model. Shown are the production factors of the isotopes with mass number up to $A = 40$. The production above ^{12}C is within all different calculations almost the same. The only difference arises below carbon, where changes due to neutrino processes can be observed. However, the production factors are still substantially smaller than one, although an increase due to neutrino processes can be found for ^7Li and ^{11}B .

deuterium if the temperature is low enough. Once deuterium is created, additional neutron/proton captures will create $^3\text{H}/^3\text{He}$, which are the usual target nuclei for α -captures creating the desired nuclei ^7Li and ^{11}B . Whether ^7Li or ^{11}B is produced dominantly is sensitive to the evolution of the astrophysical parameters with time [136].

In addition to the proton rich integrated nucleosynthesis of the neutrino-driven wind with a heavy mass progenitor model, we also studied the integrated nucleosynthesis of a $11.2 M_{\odot}$ progenitor model with improved microphysics input, where initial ejecta are neutron rich. The nucleosynthesis results for the improved model are shown in figure 4.20. Within

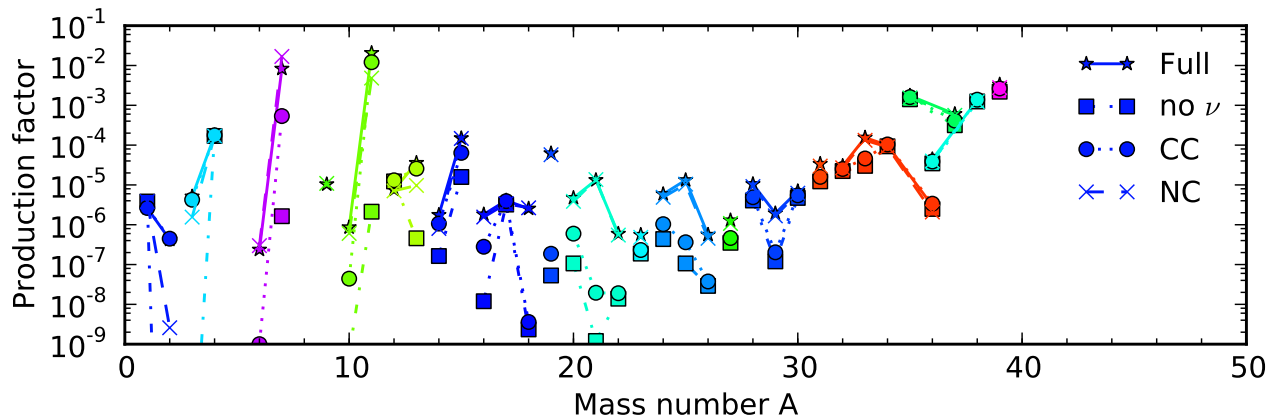


Figure 4.20: The relative abundance of the elements in the mass region up to $A = 40$. Stars correspond to the inclusion of all neutrino rates that have an influence on the nucleosynthesis. Calculations marked with a dot or cross either consider only charged-current or only neutral-current processes. The boxes are the final nucleosynthetic yields if no neutrino-processes are considered.

this figure we show the relative abundance pattern of the elements up to mass number 40. The differences between the shown calculations decrease with increasing mass number. The largest differences are obtained for Li and B as well as Be, that is actually without neutrinos produced only in negligible amounts. As in the previous model of the proton-rich wind we are able to observe that the changes have their origin in the neutral- as well as the charged-current processes.

However even by the strong increase in abundance due to the inclusion of neutrino interactions, the production of these elements is too small. Thus even so the relative changes of these light elements are very large, the total production for the star's nucleosynthesis within the wind is almost negligible. To be of relevance for the nucleosynthesis of the whole star, the production factor is required to be larger than one. The production factors shown in figures 4.19 and 4.20 exhibit that for light elements the neutrino-driven wind does not contribute to the isotopic production of this element in the star. However, the total nucleosynthesis of the star is also sensitive to the production factors of the other astrophysical sites

while the star’s explosion and not only to the wind ejecta. Therefore these light elements need to be produced somewhere else.

4.3 r-process nucleosynthesis under strong neutrino fluxes

Galactic chemical evolution models [151, 1] show hints that core-collapse supernovae are the most likely source of r-process nucleosynthesis. However, throughout this thesis we stated repeatedly that the neutrino-driven wind of a core-collapse supernova is currently not a favorable scenario for the production of heavy elements by the r-process, because the requirements of low electron fraction and high entropy cannot be simultaneously realized. This however might point to shortcomings or missing input physics in the simulations so far.

Within this thesis we would like to explore how neutrino-nucleus reactions may affect the r-process, if it occurs in an environment with large neutrino fluxes. We therefore assume an astrophysical model with high neutrino-fluxes, in which the r-process is possible. We decided to adopt the same hydrodynamical trajectories of the neutrino-driven wind given in [13] by a $15 M_{\odot}$ progenitor model and artificially increased the entropy by a factor of two, to be able to produce matter in the third r-process peak. This behavior has been adopted from [40], where the relevance of various nuclear physics inputs on the final nucleosynthesis outcome of the r-process have been studied. We will in general apply the same astrophysical parameters which lead to a final nucleosynthesis that resembles the solar r-process pattern quite well. The utilized trajectory in the previous work and in this work here is taken from [13].

Previous studies of r-process nucleosynthesis within this trajectories [40] have neglected neutrino interactions on nucleons and their influence on the nucleosynthesis, because they did not expect to see an influence. Furthermore was their focus on the nuclear Of course this is only true for the r-process network calculation. For the hydrodynamic simulation of the PNS and its expansion of matter have neutrino absorption processes on nuclei been considered to obtain the correct electron fraction. We consider all neutrino-nucleus interactions for the same trajectory and observe their influence on the nucleosynthesis. Therefore we did a calculation, where we included all neutrino interactions. This calculation is referred to as “Full” in figure 4.21. Additionally we did calculations where we used the same trajectories, however after α -rich freeze-out, where the electron fraction has already been determined, we turned off some neutrino-nucleus channels to study their influence. The cases labeled “NC” neglect charged-current processes, while neutral-current processes are considered. In cases labeled with “CC”, only charged-current processes are taken into account. Additionally we also did calculations without the inclusion of neutrino-nucleus processes in our network. These are labeled with “no ν ”.

Note that within all the different variations, the reactions on free protons and neutrons are always considered, which guarantees that the electron fraction is not altered due to the neglect of charged-current neutrino processes on free protons and neutrons that determine the electron fraction while expanding from the PNS.

The neutrino mean energies and luminosities for the electron flavor neutrinos are taken from the simulation [13]. The values are $\langle E_{\nu_e} \rangle = 16.46$ MeV and $\langle E_{\bar{\nu}_e} \rangle = 20.3$ MeV, whereas the luminosities are $L_{\nu_e} = 1.74 \times 10^{51}$ ergs/s and $L_{\bar{\nu}_e} = 2.12 \times 10^{51}$ ergs/s. The initial electron fraction has been adjusted such that, in the case of no neutrino interactions on nuclei, at α -rich freeze-out the same electron fraction value will be obtained than in previous calculations. Its value

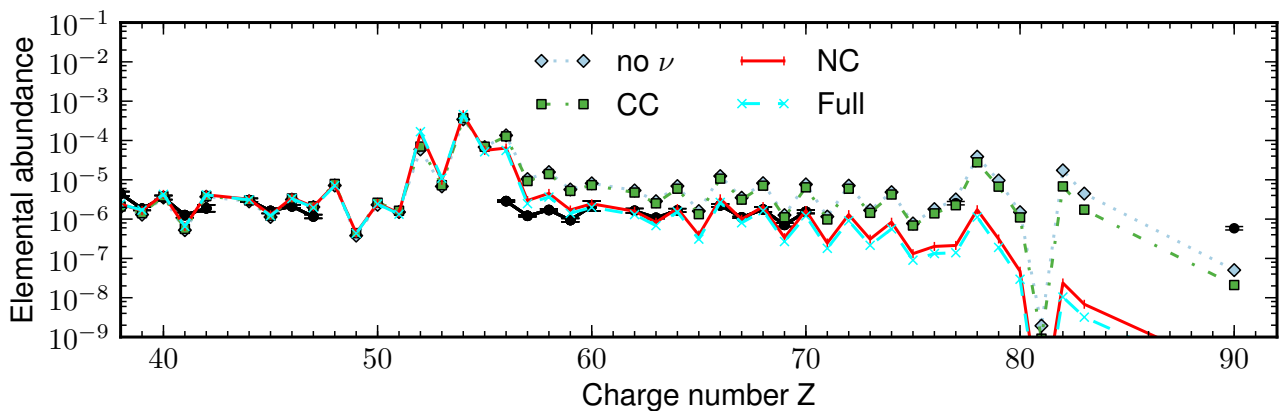


Figure 4.21.: The elemental abundance pattern of the neutrino-driven wind ejecta, where the neutrino luminosities have been adjusted such that the electron fraction at a temperature of 3×10^9 K is comparable to the values of the calculations by [40]. The black data corresponds to the r-process enriched star CS 22892-052 [152]. Grey, green, red and cyan show the nucleosynthetic results of the different calculations mentioned in the text.

is $Y_e^{\alpha\text{-rich}} = 0.469$. The only data that had to be assumed for our work are the mean energies and luminosities of the μ and τ flavor neutrinos, since no information of these neutrino flavors is given in the simulations of [13]. The neutrino luminosities of these two different flavors have a strong influence on the neutral-current processes, since neutrinos of μ and τ flavor will be 4/6 of the reactants for neutral-current spallation processes that also have higher mean energies. The luminosity of the additional flavors have been set to 3×10^{51} ergs/s, and the mean energy is set to 24 MeV⁵. These values are somewhat larger than produced in current simulations, but they allow us to explore the impact of the neutrino-induced reactions.

The results of our nucleosynthesis study can be found in figure 4.21, where we show the final r-process abundance pattern. The results without the inclusion of neutrinos agree with the final nucleosynthesis given in [40]. The strongest changes, relative to the calculation without neutrinos can be observed by the inclusion of neutral-current processes. Within figure 4.21 we can realize that neutral-current processes effectively reduce the r-process production. The reason why the r-process is reduced when neutral-current neutrino interactions are included has already been realized by Meyer in late 1995 [153] and relates to the neutrino-nucleus interaction during the α -rich freeze-out, in which the abundance of α -particles is high. Neutral-current spallation processes cannot occur on free neutrons, however on α -particles neutrino-induced spallation processes are possible. It was first believed that neutron evaporation on ${}^4\text{He}$ will lead to an improved r-process, since the amount of free neutrons will increase by the reaction ${}^4\text{He}(\nu, \nu/n){}^3\text{He}$. However the neutron evaporation off ${}^4\text{He}$ to ${}^3\text{He} + n$ is very inefficient, as neutrons are easily recaptured. On the other hand, proton evaporation on ${}^4\text{He}$ will lead to ${}^3\text{H}$, where neutron captures cannot occur, since ${}^4\text{H}$ is unbound. Thus the dominant reaction partner is another α -particle, leading to ${}^7\text{Li}$. In fact, not only one α -capture will occur, instead several α -captures will work as an additional source for creating heavy elements. The net effect for the nucleosynthesis is that the ratio of free neutrons to heavy elements – the so called *neutron-to-seed* ratio – decreases, since the amount of heavy nuclei increases. One is able to roughly estimate the created material in the r-process by (e.g. [1, 139])

$$\langle A \rangle = \frac{n}{\text{seed}} + \langle A_{\text{ini}} \rangle, \quad (4.15)$$

where $\langle A_{\text{ini}} \rangle$ is the initial average mass number and n/seed denotes the neutron-to-seed ratio. The final average mass number $\langle A \rangle$ is therefore sensitive to the neutron-to-seed ratio. As it has been shown by [153, 154] this explains why neutral-current neutrino processes decrease the efficiency of the r-process.

We are able to observe that the inclusion of charged-current processes – in comparison to the calculation without neutrinos – does change the nucleosynthesis for elements higher than $Z > 78$, where a change of a factor 2 can be observed. The reason for this change in abundance is again due to the charged-current interactions of neutrinos with α -particles. The dominant reaction, which is ${}^4\text{He}(\nu_e, e^+)$, produces the unbound ${}^4\text{H}$, that depending on its energy will dissolve into three free neutrons and one proton, or ${}^3\text{H}$ and a neutron. In the first case, the proton will be captured by a neutron due to the lack of the Coulomb barrier and the high neutron densities. Furthermore there is a high possibility to capture even another neutron, resulting, as in the latter case, to ${}^3\text{H}$ and a neutron. As we saw earlier, is ${}^3\text{H}$ a nucleus

⁵ This average neutrino energy corresponds to a neutrino temperature of 7.6 MeV, which is close to the value used in the later description of neutrino nucleosynthesis.

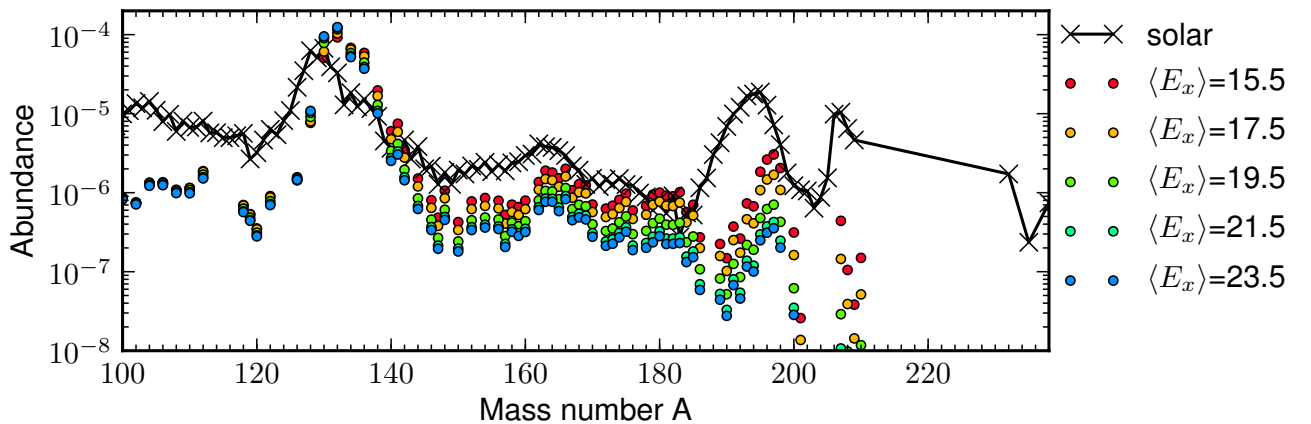


Figure 4.22.: The final isotopic yields for our r-process calculations including all neutrino interactions. To understand the sensitivity of the final nucleosynthesis from the average neutrino energy of μ and τ flavor, we changed the average energies to the values given in the legend. The energies are given in MeV. To guide the eyes we additionally added the solar r-process pattern, which has been renormalized to $A = 135$.

that can easily undergo several sequential α -particle captures which will increase the amount of heavy elements. An increase of heavy elements will again reduce the neutron-to-seed ratio, which will reduce the impact of the r-process. The inclusion of both currents – shown in figure 4.21 with the label “Full” – reduces the abundance pattern for heavy elements even more. However, this is only due to the fact that both described processes on ${}^4\text{He}$ are combined and therefore the α abundance will decrease faster. When the neutrino-spallation processes on α -nuclei are neglected, the obtained final elemental abundance pattern has a similar behavior as it is shown in figure 4.21 without neutrinos.

The statement given by [137], that the r-process abundance pattern might be changed due to charged-current neutrino reactions on heavy elements, could not be observed in our work. It was stated that charged-current neutrino processes might influence the shape of the final abundance pattern [137], since charged-current neutrino processes – including particle spallation reactions – speed up to the β -decay processes and therefore can change the abundance pattern. Since the neutrino rates are strongly sensitive on the radius, the astrophysical expansion has a strong influence on the effect that neutrino-nucleus processes have on the nucleosynthesis. Within our model the β -decay rates have changed only marginally, which relates to the fact that matter is already too far away from the PNS when the equilibrium between (n, γ) and (γ, n) reactions are interrupted and β -decay rates become important. As we will observe later is this result sensitive on the used value for the electron fraction. If we reduce the electron fraction for the same trajectory, we cannot observe a change in the final nucleosynthesis results anymore, due to the fact that the neutron-to-seed ratio is already large enough to create very heavy elements, such as ${}^{238}\text{U}$, ${}^{235}\text{U}$ and ${}^{232}\text{Th}$.

Instead of being comparable with β -decay – as in the case of charged-current neutrino processes – the neutral-current neutron spallation however effectively mimics photodissociation processes. Within our work we were able to see that these neutrino induced neutron emission processes do not dominate the nucleosynthesis, instead only small changes arise due to their inclusion.

The reason why neutral-current neutrino processes on heavier nuclei do not play a substantial role is due to the fact that these processes will occur in a region where the neutron density is still large. Furthermore, the radius at which nuclei form is large, reducing the spallation rates.

Once we understood that the dominant process reducing the efficiency of the r-process is neutral-current neutrino scattering – which is actually dominated by μ - and τ -neutrino luminosities and average energies – we decided to make a small parametric study how the isotopic abundance pattern behaves with the average energy. Therefore we modified the average neutrino energies for μ and τ neutrino flavor. The results for this calculations can be observed in figure 4.22. To guide the eye, we additionally included the solar r-process pattern [35]. The average neutrino energies start from 15.5 MeV up to 23.5 MeV, where the neutrino cross section for neutron evaporation off ${}^4\text{He}$ spans a range from $6.6 \times 10^{-44} \text{ cm}^2$ for the lowest value up to $3.9 \times 10^{-43} \text{ cm}^2$ for the highest value. Note however that some average energies used in figure 4.22 are already below the mean neutrino energies of 20.2 MeV, which would break the usually observed energy hierarchy in which μ and τ neutrinos have the highest mean energy values.

We are able to see that around mass number 180, the spread due to the average neutrino energies of μ and τ flavor is roughly one order of magnitude. With higher average energies, less material is produced for heavier elements. A further study in which we studied the influence of the neutrino luminosities for a fixed average neutrino energies of $\langle E_{\nu_x} \rangle = 24 \text{ MeV}$, where x can be μ and τ , is shown in figure 4.23.

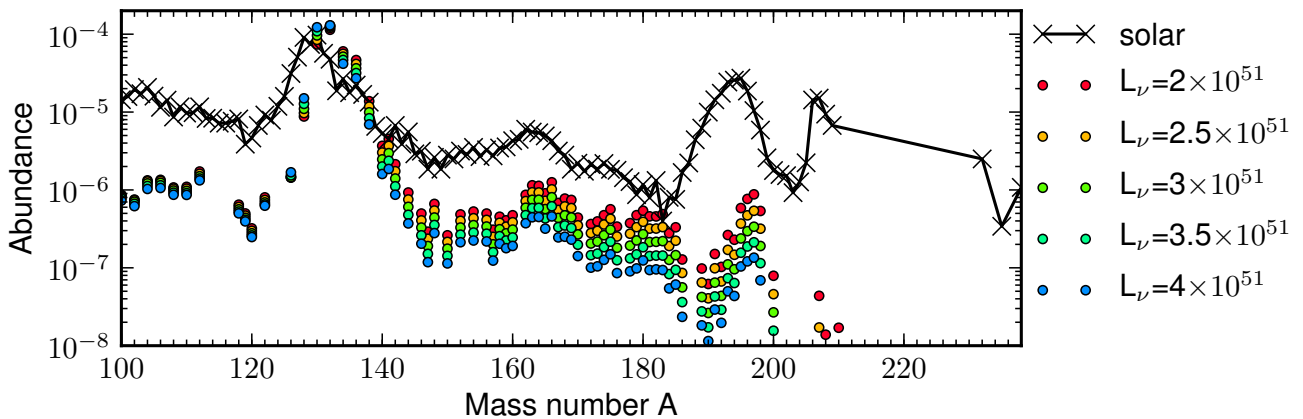


Figure 4.23.: The final isotopic yields for our r-process calculations including all neutrino interactions. To understand the sensitivity of the final nucleosynthesis from the neutrino luminosities of μ and τ flavor, we utilized an average energy of 24 MeV and the values of the luminosities given in the legend. The luminosities are given in ergs/s. Again we added the solar abundance pattern – renormalized to $A = 135$ – to guide the eye.

We are able to observe that the influence of the luminosities for μ - and τ -flavor to the final nucleosynthesis of our r-process also shows a strong dependence on the neutrino luminosity. With increasing luminosity, also the production of heavier elements is suppressed. Vice versa leads a reduction of the luminosity to a stronger heavy element production, because less free protons will be created due to neutrino-induced processes on ${}^4\text{He}$.

4.3.1 Neutrino reactions on α -particles

Within the neutrino-driven wind we discussed so far various nucleosynthesis processes that can occur in proton rich or neutron rich ejecta. So far we saw that in proton rich ejecta neutrino interactions on nuclei play a very small role for the final nucleosynthesis, while for neutron rich (r-process) ejecta the changes are clearly noticeable. Neutrino interactions on free nucleons are not considered in this statement, because neutrino reactions on nucleons close to the PNS determine whether the matter is neutron rich or proton rich. Furthermore are antineutrino-captures on free protons in proton rich ejecta very important for the nucleosynthesis. As we saw above for several cases is the most relevant rate for neutrino interactions on nuclei the neutrino reactions on ${}^4\text{He}$. The reason for this fact is that the abundance of α particles is large in the scenarios that we are studying, due to the α -rich freeze-out. In this short subsection we would like to discuss why the influence of neutrino reactions on ${}^4\text{He}$ are so strong observable in very neutron-rich ejecta, but almost no effect can be seen in proton rich ejecta.

Therefore we would like to discuss first proton rich ejecta. If neutrons are evaporated from ${}^4\text{He}$, they will be captured by heavy elements – as it is done by the converted neutrons from antineutrino capture. However, if a proton is emitted it will – as long as the temperature is high enough to overcome the Coulomb-barrier – be captured again by the free ${}^3\text{H}$, which has a smaller Coulomb barrier than the reaction ${}^3\text{H}(\alpha, \gamma){}^7\text{Li}$. If the temperature is too low and the neutrino fluxes are still relevant, the proton will not undergo any nuclear reaction.

For neutron rich ejecta the case is as follows. Neutron evaporations from ${}^4\text{He}$ will be directly recaptured, due to the high neutron abundance surrounding in the ejecta. Proton evaporations on the other hand destroy the neutron-to-seed ratio, since the created ${}^3\text{H}$ will, as we described already above, by subsequent α captures increase the amount of heavy elements. The emitted proton will however also increase the amount of heavy nuclei, while additionally reducing the neutron abundance. If the temperature is small enough the free proton will most likely be captured by a neutron, due to the lack of the Coulomb-barrier. The newly created deuteron will capture another neutron and form ${}^3\text{H}$.

This is the reason why the effects of neutrino-induced particle spallation from ${}^4\text{He}$ has stronger effects on neutron rich ejecta than on proton rich ejecta.

In the next section we would like to discuss an astrophysical scenario that is closely related to neutrino-driven winds. However, while the emission in the neutrino-driven wind is ejected from the surface of the PNS, the hot convective bubble focuses on matter that is ejected before the NDW develops. Two-dimensional simulations show that before the NDW phase neutrino emission drives matter in a convective hot bubble of nuclei and radiation. We want to study the nucleosynthesis with respect to our newly determined rates.

4.4 Nucleosynthesis in the hot convective bubble

While an explosion develops in the already collapsed iron core of the star, neutrino emissions are large enough to drive matter-emission in a hot convective bubble of radiation and nucleons outside of the PNS. This stage is the onset of what will later be the neutrino-driven wind [12]. The convective character of the hot bubble ejecta gives rise to the fact that one-dimensional simulations do not show the same characteristic behavior.

This phase is also known as *hot convective bubble* and has a rather short timespan of only up to one second, whereas the neutrino-driven wind lasts for tens of seconds. Due to the high neutrino fluxes which are initially present, the mass flux however is estimated to be of the order of 0.05 up to 0.1 M_{\odot} [47], which is much higher than in the wind, where a substantial amount of mass has already been emitted from the PNS. The material in the hot bubble originates – contrary to the neutrino-driven wind – from a region outside of the neutron star that is driven by convective neutrino heating. Due to the fact that the material does not have to escape from the deep gravitational well at the neutrino surfaces, the astrophysical conditions are rather modest and definitely less extreme than common wind conditions. Typical entropies are in the order of 20-30 k_B , with electron fractions only slightly above 0.5 [47].

We used the same trajectories within the hot convective bubble of [12] as the authors of [47], to observe how the inclusion of our neutrino rates will influence the nucleosynthesis within this astrophysical scenario. Previous studies [47, 126], that were aiming to explore the nucleosynthesis in this interesting region, observed that the hot convective bubble produces heavy elements up to $A = 70$. The dominant elements produced however are ^4He and ^{56}Ni . The authors of [126] mentioned that the inclusion of neutrino-captures on free protons and neutrons barely change the final composition, basically due to the fact that matter is further apart from the PNS and – more importantly – its electron fraction is close to 0.5, reducing the amount of free protons that can be converted by antineutrino captures.

It is therefore interesting to observe how our neutrino rates will influence the final composition of the ejecta in the hot convective bubble. Due to the fact that the electron fraction is close to 0.5, we expect that neutrino processes on free protons and neutrons do not contribute too much, because the abundance of free protons and neutrons should be rather small, as long as the entropies are small.

The hot convective bubble is an interesting scenario to study the influence of our neutrino rates, because on the one hand matter is further apart from the PNS such that the neutrino rates are smaller and the electron fraction is not dominated by neutrino processes on free protons and neutrons, on the other hand the radius is not too large that neutrino interactions will still play a role.

It has been stated by previous studies on the hot convective bubble, that due to the fact that the simulation has been carried out only approximately 1.3 s after bounce (470 ms of these 1300 ms have been calculated in a two dimensional grid, afterwards the simulation has been mapped in an one-dimensional code), the nucleosynthesis is very sensitive to the analytic expansion described in equation 4.5 and the values at the end of the simulation. Depending on the escape velocity, matter will either stay longer close to the PNS and thus be subject to stronger neutrino fluxes or undergo a rapid expansion leading to a fast decrease in the neutrino fluxes. The main focus within this study on the hot convective bubble is not governed with the possibly complicated expansion mechanism, instead we are interested in the effects that neutrino-nucleus cross sections have on the final abundances. Thus we will – as in previous calculations – assume an

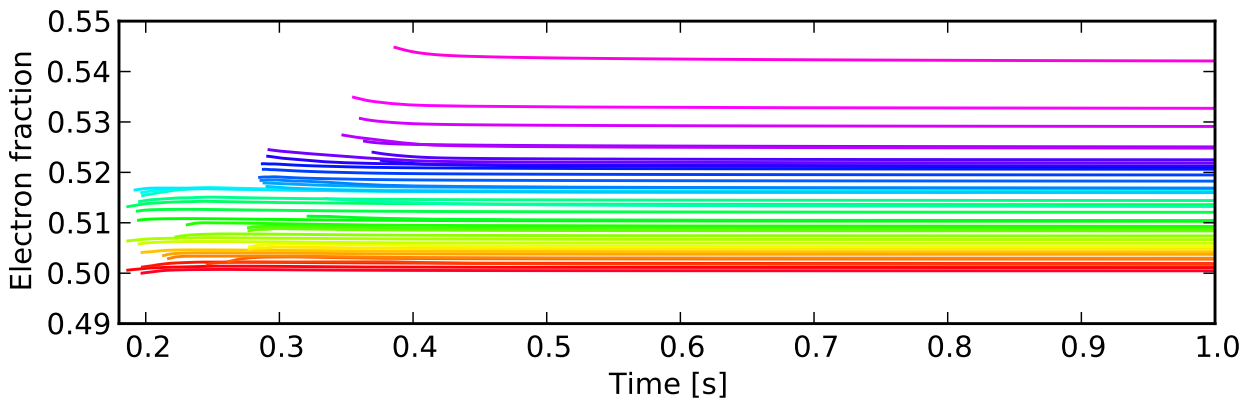


Figure 4.24.: The electron fraction values for the ejecta in the hot convective bubble. The color coding corresponds to the time the matter is ejected. Red labels early ejecta and purple labels later ejecta. We can observe that with increasing time, matter becomes more and more proton rich and the last trajectory could already mark the transition to the early wind.

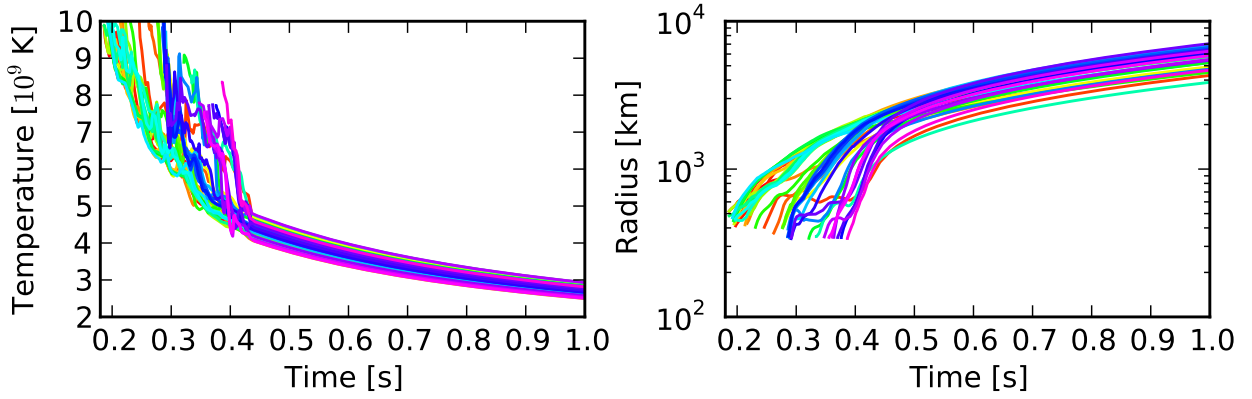


Figure 4.25.: The evolution of temperature (left) and radius (right) in the first second after core bounce. At a time of 470 ms post-bounce the evolution of the two-dimensional model is continued by a mapping to an one-dimensional model. This explains the sudden change in the evolution. The convective behavior of the first half second mixed the values with different electron fraction in a broad regime of astrophysical parameters.

adiabatic expansion where the parameter Δ is set to zero. The expansion velocity is determined by the average velocity of the last ten timesteps.

Again one of the most crucial input parameters for the nucleosynthesis is the initial value of the electron fraction. Within this work the value of Y_e has been taken directly from the publication [47], however the value given there is the final value after the nucleosynthesis, whereas we start our calculations whenever the temperature drops below 10×10^9 K with the respective values of the electron fraction given in the publication. This results to a slightly different final Y_e value than the ones given in reference [47]. To improve the determination of the electron fraction, we would require the temporal evolution of the electron fraction which is not given within the publication. Once again we would like to stress that the goal within this thesis is to understand the influence of neutrino-nucleus processes on the final nucleosynthetic yield, such that we accept this small difference within the electron fraction.

In total 40 different trajectories have been calculated with the new data set. The initial electron fraction values spread from 0.5 to 0.546 [47], which are values less proton rich than in the neutrino-driven wind.⁶ The temporal evolution of the electron fraction for all 40 trajectories can be found in figure 4.24 for the first second in which the electron fraction is still able to change. The figure also shows the transition to the proton-rich wind. Early ejecta are colored red while purple is utilized for late ejecta, the last ejected trajectory could already be accounted by the neutrino-driven wind. The almost linear behavior of the electron fraction is not met in the radial evolution of the different trajectories, instead they show a rather complicated evolution. This is illustrated in figure 4.25 for the evolution of density and radius up to one second post bounce. Instead of a linear behavior with time of the ejecta with respect to the astrophysical environment, the convection leads to an interesting mixing of different material.

As we can see within figure 4.24, the electron fraction is closer to 0.5 than in calculations of the NDW without the improved microscopic description. The relatively low electron fraction of the ejecta will decrease the effectivity of the νp -process and allows us to study processes in astrophysical regions similar to the neutrino-driven wind, but without the pure dominance of the νp -process. Electron fraction values close to 0.5 will lead to a scenario where almost no free protons or neutrons will remain after α -rich freeze-out.

As an example for the nucleosynthesis occurring in the hot convective bubble, we chose one of the 40 trajectories taken from [47] with an electron fraction of 0.5132 and show the final nucleosynthesis outcome obtained with the different sets already discussed above. The elemental result can be found in figure 4.26, which is somewhat representative to the nucleosynthesis in the hot convective bubble.

The first observation that one is able to make is that the hot convective bubble mainly creates α -particles and iron elements as stated by [47]. The production of the dominant elements is not related to any neutrino processes. By the displayed abundance pattern we are also able to realize that a heavy element production in the hot convective bubble can be excluded, since the abundance of heavy elements drops rather quick. Especially contributions to the elemental abundances of metal-poor stars, such as HD 122563, is excluded due to the fact that matter does not reach charge numbers that are high enough. The reason therefore is that very little heavy elements are created by the νp -process. A production of heavy elements by the r-process is excluded due to the electron fraction values, the too long expansion timescale and, most of all, because of the small entropies.

⁶ Note that these simulations are from late 2003, such that these models do not consider the corrections of mean-field potentials for protons and neutrons as we discussed in 4.2.

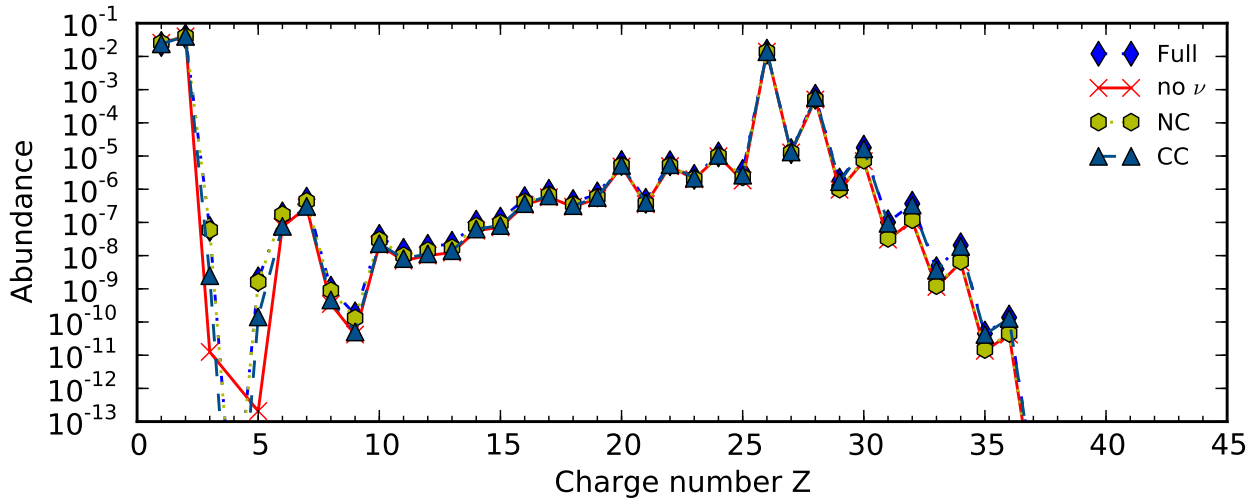


Figure 4.26.: The elemental nucleosynthetic result of a trajectory from the hot convective bubble with an initial electron fraction of 0.5132. “Full” corresponds to the inclusion of all neutrino-nucleus interactions, “no ν ” neglects all neutrino processes and “NC”/“CC” only includes neutral-/charged-current interactions.

To study changes due to the influence of neutrino reactions, we additionally calculated the possible contributions of neutrino-nucleus interactions separately to observe which process will be the dominating one, if any change is observable.

The production of elements above $Z = 26$ shows almost no change of heavy element production, only a very small increase due to νp -nucleosynthesis can be observed. By doing the ratio, we observed that the heavy elements are up to a factor of three more produced by the inclusion of charged-current processes. The ratio of the neutral-current contribution is negligible in this region.

Additionally to the changes in the higher Z region, differences arise below $Z = 10$. Contrary to the high Z changes, the nucleosynthetic yield is here substantially altered due to the inclusion of neutrino interactions. Without neutrino interactions only very little production of Li and B can be obtained, while Be is not produced at all. Neutrino interactions hereby increase the final nucleosynthetic yield such that matter within this region is produced. The relative abundances of the isotopes ${}^7\text{Li}$, ${}^{11}\text{B}$ and ${}^{15}\text{N}$ are above one and can therefore be of relevance for the total nucleosynthesis. It should be stated once more that to be of relevance for the total mass ejecta, the production factor has to compensate the additional mass of the outer shells. As a rough estimate we adjust that the total mass of the star is of the order of ten M_{\odot} and has a mass ejection of 0.1 M_{\odot} in the convective bubble. Thus the production factor should be of the order 10^2 , which can

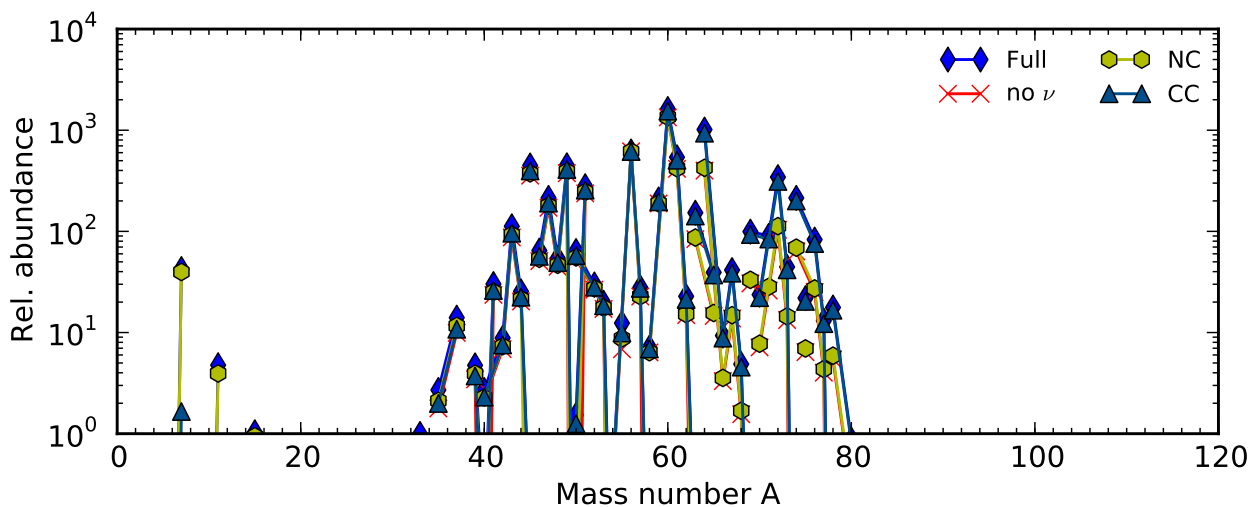


Figure 4.27.: The relative abundance pattern of one hot bubble trajectory. The labels are as in previous figures. For the light isotopes ${}^7\text{Li}$, ${}^{11}\text{B}$ and ${}^{15}\text{N}$ have a factor above one. At a relative abundance of 200, the production is strong enough to be of importance for the total nucleosynthesis of the star.

almost be reached for the light isotopes by ${}^7\text{Li}$. The relative isotopic abundance pattern is shown in figure 4.27. The process responsible for the creation of these elements originates hereby by a large fraction from neutral-current scattering of α -particles that are largely abundant. Further discussions about the creation of these light elements – especially ${}^7\text{Li}$, ${}^{10}\text{B}$ and ${}^{11}\text{B}$ – will be discussed within section 4.5.

For an integrated result of the hot convective bubble, we studied 40 trajectories within the bubble scenario of [12]. The nucleosynthesis results within each bubble trajectory does not vary too much. The only difference is that later ejecta will become more proton rich – as shown in 4.24 – which allows for a better νp -nucleosynthesis. The higher electron fraction increases the conversion of free protons to free neutrons by antineutrino captures and will lead to a slight increase of the heavy element abundance, as it could be seen in figure 4.27. The last trajectory marks already the transition to the early neutrino-driven wind phase with an initial electron fraction of 0.544. An additional parameter influencing νp -nucleosynthesis is the entropy of the ejecta, that for late ejecta in the hot bubble continuously increases.

The integrated nucleosynthesis can be found in figure 4.28. The main differences between the various calculations we made, can be observed due to the fact that the νp -nucleosynthesis is neglected when no charged-current processes are included. The dominant isotopes produced, except the dominant ${}^{60}\text{Ni}$, are ${}^{45}\text{Sc}$, ${}^{49}\text{Ti}$ and ${}^{64}\text{Zn}$. The inclusion of neutral-current processes leads to a production of the elements ${}^7\text{Li}$ and ${}^{11}\text{B}$, which however is small enough to be neglected for the star's total nucleosynthesis.

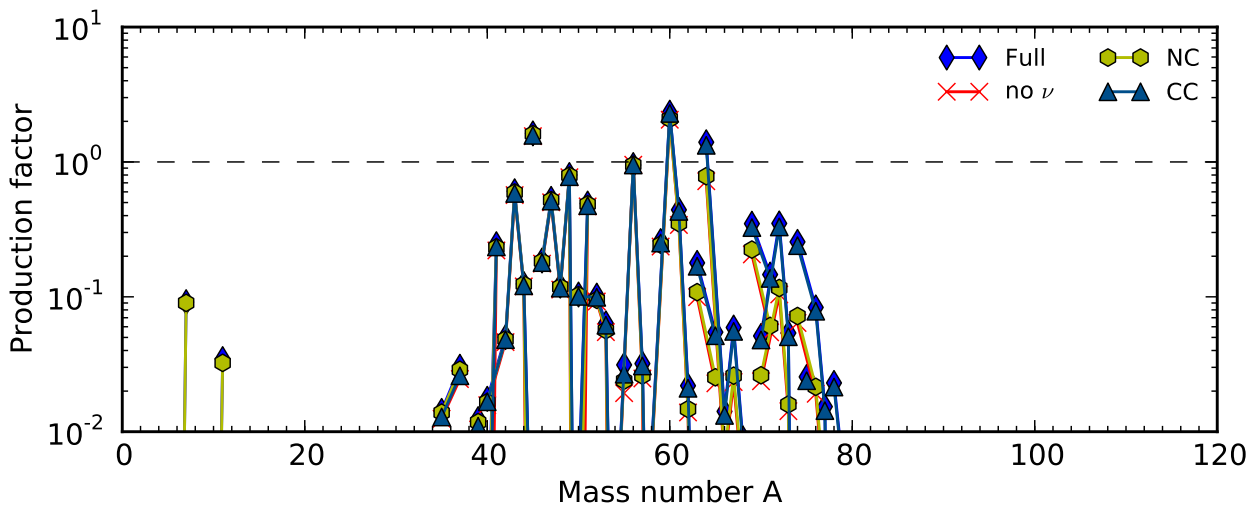


Figure 4.28.: The integrated result of the whole ejecta in the hot convective bubble. “Full” denotes both charged-current and neutral-current processes, “CC” includes all charged-current processes, “NC” includes all neutral-current processes, while “no ν ” does not include neutrino interactions at all. We can observe a strong production of the isotopes ${}^{45}\text{Sc}$, ${}^{49}\text{Ti}$, ${}^{60}\text{Ni}$ and ${}^{64}\text{Zn}$. For the heavy mass production the contribution of νp -nucleosynthesis can be seen very clearly.

In the next section we want to discuss the ν -process, that we mentioned already several times. The ν -process occurs in the outer layers of the star during a core-collapse supernova. The strong neutrino flux from the PNS cooling can lead to particle evaporation of the most dominant nuclei. In this fashion light elements such as ${}^7\text{Li}$ and ${}^9\text{B}$ are created almost exclusively in this process, while an influence on odd- Z elements is also expected. We will discuss the standard assumptions that are currently made in the ν -process and will study how the inclusion of the full set of neutrino-nucleus rates will change the composition.

4.5 Neutrino nucleosynthesis

While the core-collapse process only occurs in the iron core of the stars, the neutrinos created while cooling the PNS will however traverse through the outer layers and will interact with matter and possibly have influence on the final nucleosynthetic yield. Additionally to the neutrino fluxes passing through the matter, the final nucleosynthesis will be altered due to the passage of the shock through the star. The importance of neutrino interactions on the outer shells that will be ejected by the shock passage was first realized by Woosley *et al.* [2], and subsequently also denoted as neutrino nucleosynthesis or ν -process. With the help of a similar astrophysical setup, we would like to study how the inclusion of our calculated neutrino rates modify the final nucleosynthesis.

Within their work they utilized a $20 M_{\odot}$ progenitor model for the initial composition of the outer shells. The shock passage has been described by a phenomenological model. The time that the shock requires to reach a certain destination is approximated by using the Sedov-Taylor equation [155] as

$$t_0 \approx 0.7 \frac{r}{10^4} \left(\frac{M - M_{NS}}{E/10^{51}} \right)^{\frac{1}{2}}, \quad (4.16)$$

where the time is given in seconds. M denotes the mass contained in a sphere in units of solar masses at radius r given in kilometers, which has to be corrected by the mass of the neutron star M_{NS} . E is the total kinetic energy of the supernova in units of ergs.

Once the shock reaches the matter, the shock will increase the temperature. According to [156] the peak temperature can be approximated by assuming that matter behind the shock is isothermal and the energy is contained dominantly in the radiation field. We thus can write the total internal energy E as

$$E = \frac{4\pi r^3}{3} \times a T_{peak}^4, \quad (4.17)$$

with a being the radiation constant. By putting the according values and solving for the peak temperature, we end up with

$$T_{peak} \approx 2.4 \cdot 10^9 \text{ K} \left(\frac{E}{10^{51} \text{ ergs}} \right)^{1/4} \left(\frac{r}{10^4 \text{ km}} \right)^{-3/4}, \quad (4.18)$$

where again the total kinetic energy E is given in ergs and the radius r in kilometers. Due to the fact that the shock is rather weak, the peak density is not too different from the initial density. Thus a good first approximation is to keep the density constant while the shock is passing through the matter. For the inner radii this will underestimate the shock, but for the outer radii (He, H-shell) it is a good approximation. Once the shock has passed through the matter the density will decrease, due to the onset of hydrodynamical expansion. The decrease in density under the assumption of homologous expansion is well described by

$$\rho(t) = \begin{cases} \rho_0, & \text{if } t < t_0, \\ \rho_0 \exp\left(\frac{t-t_0}{\tau_{dyn}}\right), & \text{if } t > t_0. \end{cases} \quad (4.19)$$

The time t_0 denotes the point in time when the shock hits the matter and heats it up to the peak temperature T_{peak} . Accordingly the density ρ_0 is the matter density arising from the progenitor model. The dynamical timescale used in equation 4.19 is given by equation 1.1 or can be estimated by

$$\tau_{dyn} = \frac{446 \text{ s cm}^3}{\sqrt{\rho} \text{ g}}. \quad (4.20)$$

For an adiabatic expansion, temperature and density are tightly correlated leading also to an exponential decrease in temperature which is however three times longer.

$$T(t) = \begin{cases} T_0, & \text{if } t < t_0, \\ T_{peak} \exp\left(\frac{t-t_0}{3\tau_{dyn}}\right), & \text{if } t > t_0. \end{cases} \quad (4.21)$$

It is interesting to note that the nucleosynthesis and the explosion thermodynamics of the outer part of the star are solely depending on the progenitor structure and the explosion energy.

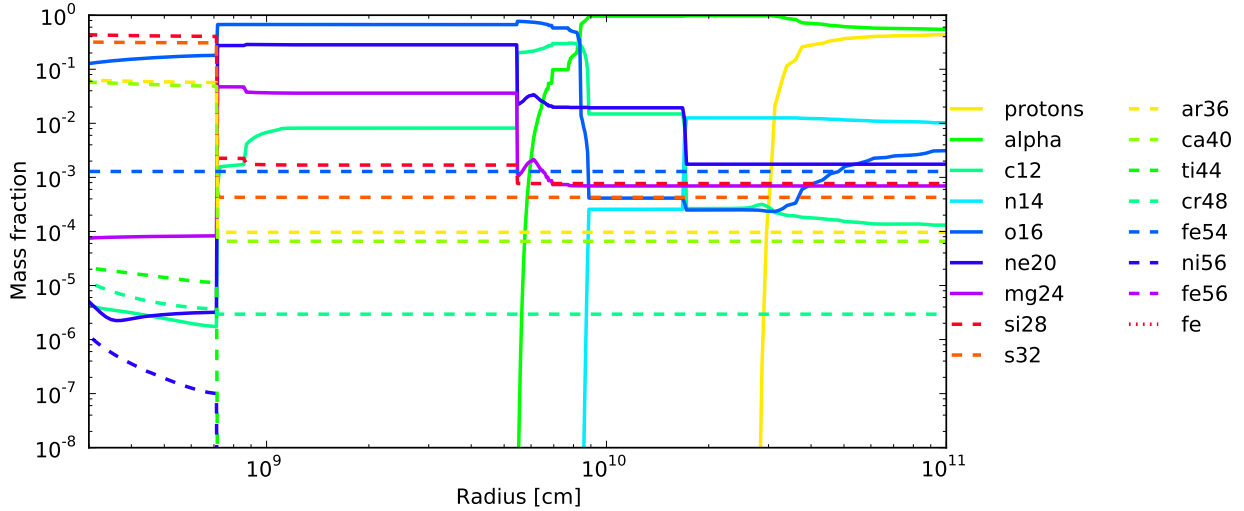


Figure 4.29.: Mass fractions of the dominant nuclei within the $20 M_{\odot}$ progenitor model with an initial metallicity that corresponds to the metallicity of our sun. The shell structure can be observed very good. The oxygen-neon and helium shells are the dominant regions within this figure. Note that we only show a small subset of the full star, at higher radii the hydrogen envelope will still be observable.

Additional to the typical astrophysical parameters such as temperature, density and initial composition, the neutrino nucleosynthesis is sensitive to the used neutrino spectra. Within their work [2] a total neutrino luminosity of 10^{53} ergs has been assumed, that is distributed equally to all neutrino flavors. We will assume the same. Contrary to our previous studies, the cooling of the PNS has to be considered explicitly and cannot be neglected as in some of the wind studies we did previously. The cooling of the PNS and its corresponding decrease in luminosity is presumed to follow an exponential decrease with a timescale of $\tau_{\nu} = 3$ s

$$L = \frac{10^{53} \text{ ergs}}{\tau_{\nu}} \exp\left(-\frac{t}{\tau_{\nu}}\right). \quad (4.22)$$

This time dependence is in rather good agreement with the long-time studies mentioned above. The neutrino temperatures of the different flavors have been assigned for our model, as well as in [2], such that ν_{μ}, ν_{τ} and their antiparticles have a neutrino temperature of 8 MeV, while electron neutrino and electron antineutrino have a neutrino temperature of 4 MeV. We utilize this rather high neutrino temperatures for an easier comparison between our model and the model of [2]. Besides the decrease in neutrino luminosity due to the cooling of the PNS, the expansion of the matter has to be included which reduces the neutrino luminosity. The key parameter for this reduction of the luminosity is of course the radial expansion. Within their work [2] the authors assumed a constant velocity of 5000 km/s for all material ejected, regardless if they were initially in the silicone shell or the outer layers of the complete star, which we will assume, too. The neutrino-nucleus rates of previous studies [2] included neutral-current one-particle spallation and charged-current capture rates of the dominant nuclei in a progenitor. These are all α -nuclei up to ^{64}Ge , and of course reactions on iron as well as on free protons and neutrons. Here we include the full set of neutrino-nucleus interactions.

Contrary to the work of Woosley and coworkers, we used in our study the initial abundances from the progenitor model [20], instead of evolving through all burning processes, although those only contained neutrons, protons, α -particles and 16 other nuclei (^3He , ^{12}C , ^{14}N , ^{16}O , ^{20}Ne , ^{24}Mg , ^{28}Si , ^{32}S , ^{36}Ar , ^{40}Ca , ^{44}Ti , ^{48}Cr , ^{52}Fe , ^{54}Fe , ^{56}Ni , ^{56}Fe). Thus we will have some discrepancies between this rather small set of nuclei and a network calculation through all burning stages⁷. The dominant nuclei will be well represented by the above nuclei. Only nuclei around these α -type elements will have an abundance that will be orders of magnitude smaller than the dominant nuclei. Note that within the work of [2] the neutrino-nucleus processes on the above nuclei have been already included. It is also noteworthy to mention that the above set of nuclei does not contain s-process nuclei, which hinders us from making statements how neutrino interactions on s-process nuclei will alter the nucleosynthesis.

All the above described parameters and variables will also be used within our calculations, but instead of the inclusion of neutrino rates for only the dominant nuclei, we include all neutrino rates that change the final nucleosynthesis. In light of recent simulations the values for the neutrino temperatures seem very high. However, we will adopt these values

⁷ Note that the stellar evolution model by itself of course evolves through the mentioned burning processes, however only with a much smaller network under the neglect of some isotopes.

for now. Furthermore we already observed in the lower right picture of figure 4.2 that the average energies – which only differ from the neutrino temperatures by a multiplicative factor – are definitely not constant as a function of time. Full hydrodynamical studies of the shock wave passing through the former star, specifically with a detailed evolution of the neutrino mean energies and luminosities as a function of time, will improve the predictive power of the neutrino nucleosynthesis. Within full hydrodynamical simulations the expansion velocities of different shells will also have no constant escape velocity, instead have a complicated structure, which however will be a very relevant parameter for neutrino nucleosynthesis, as we will see later on.

4.5.1 Nucleosynthesis effects

The initial study of neutrino nucleosynthesis [2] showed that neutrino interactions are important for explaining the solar abundance pattern of ${}^7\text{Li}$, ${}^{11}\text{B}$ and ${}^{19}\text{F}$, which are almost entirely produced due to the ν -process. Furthermore are ${}^{138}\text{La}$ and ${}^{180}\text{Ta}$ expected to be influenced by the ν -process. The production of elements in the carbon shell is for example governed by the production of ${}^{11}\text{B}$ due to particle emission off ${}^{12}\text{C}$, which is of course the dominant nucleus in carbon shells. The production of ${}^7\text{Li}$ on the other hand can be related to the helium shell, due to the processes ${}^4\text{He}(\nu, \nu'p){}^3\text{H}(\alpha, \gamma){}^7\text{Li}$ and ${}^4\text{He}(\nu, \nu'n){}^3\text{He}(\alpha, \gamma){}^7\text{Be}$, where ${}^7\text{Be}$ β -decays after 53.12 days to ${}^7\text{Li}$ [157]. Note however that lithium has several sources of production within the ν -process, and cannot be pinned down to exactly one region.

However neutrino nucleosynthesis is also believed to contribute to the solar abundance pattern of odd- Z nuclei up to the region around $Z = 28$ [2]. The main process responsible for this production is neutral-current particle evaporation off the nuclei that are most abundant. Due to the fact that the peak temperatures of the shock usually do not reach temperatures that are high enough to reach NSE, the isotopic production of elements with the ν -process is therefore strongly dependent on the initial composition, as well as the dynamical evolution. If the initial composition has a s -process contribution, a production of ${}^{138}\text{La}$ and ${}^{180}\text{Ta}$ can be observed [158, 3, 159].

The metallicity of the progenitor star has strong influence on the neutrino nucleosynthesis, because it basically increases or decreases the amount of nuclei on which particles can be evaporated. For our calculations we used the parameters and descriptions as described above. The progenitor model that we use originates from [20] and contains the abundances of the 19 isotopes used in their network, as mentioned above. The detailed structure of the progenitor can be studied in figure 4.29. The metallicity of the used model is of solar metallicity.

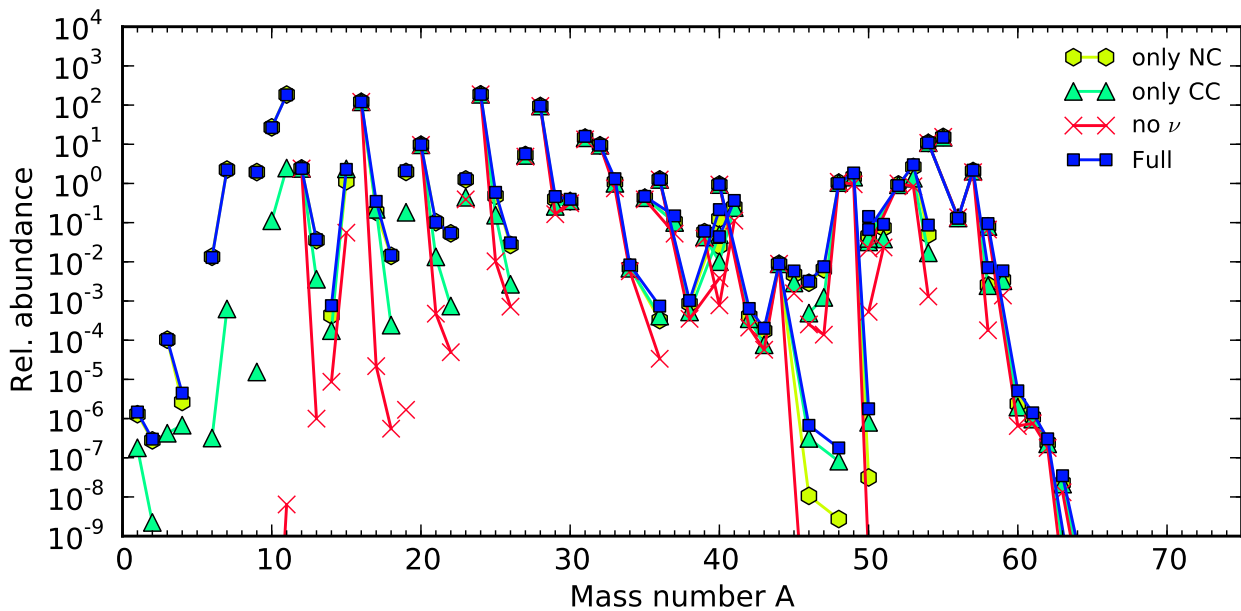


Figure 4.30.: Final relative isotopic yield for neutrino nucleosynthesis of the progenitor shown in figure 4.29, at an initial radius of 10^9 cm, which corresponds to the oxygen-neon layer of the star. Isotopic chains are connected. In red and labeled with “no ν ” is the calculation that completely neglects any neutrino interaction. It can be seen as the baseline for the effects that different neutrino processes will have on the final nucleosynthesis. The results including all neutrino interactions are marked with blue squares. Furthermore we show calculations where we only included neutral-current processes (yellow hexagon) or charged-current processes (green triangles).

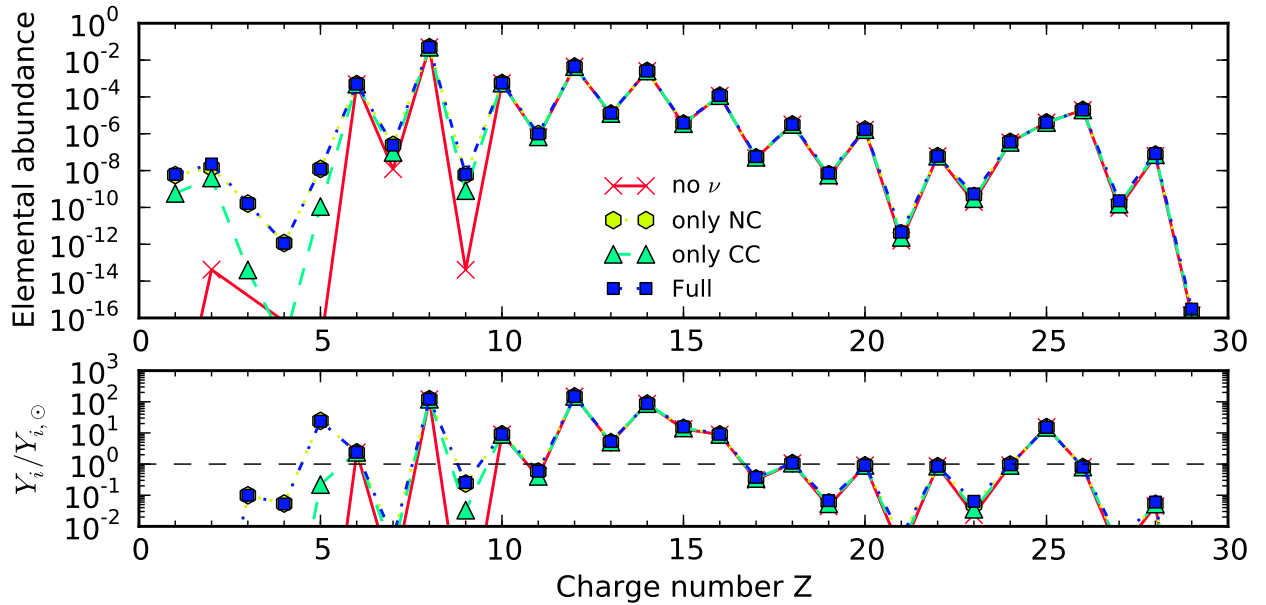


Figure 4.31.: Top: Elemental abundance pattern of the previously described trajectory for neutrino nucleosynthesis in the O-Ne-shell. The abundance pattern of the light Z elements is governed by neutrino nucleosynthesis, or to be more precise, dominantly by neutral-current neutrino processes. Additionally to the creation of the light elements, neutrino nucleosynthesis contributes to the elemental production of nitrogen and fluorine. Bottom: The same elemental abundance, yet scaled with the solar system abundance for each element.

The first results of neutrino nucleosynthesis with our full set of neutrino rates can be seen in figure 4.30. Within this figure, we studied the influence of the different neutrino processes that we considered within this work. The initial radius of the first trajectory used in this work is at a radius of 10^9 cm, which is in the O-Ne-shell of the progenitor. The explosion energy has been assumed to be 10^{51} ergs, which is a reasonable assumption for core-collapse supernovae because observations of supernova remnants give strong evidence for an explosion energy of 10^{51} ergs [155]. By using this explosion energy, we obtain a peak temperature of $T_{peak} = 2.4$ GK, where the dynamical timescale is 1.56 s. In figure 4.30 “Full” denotes the inclusion of all neutrino rates. Accordingly “only NC” includes only reactions in which the neutrino-nucleus interaction occurs over the neutral-current and that the excitation is large enough that particles are evaporated. Vice versa is the case for the data labeled with “only CC” in which only charged-current processes are allowed. To observe the production of elements without the inclusion of neutrinos, we additionally calculated the same trajectory without all neutrino-nucleus interactions. These calculations are then labeled with “no ν ”.

When looking at figure 4.30, one realizes that within this region no light elements below carbon are produced when no neutrino interactions are included. By considering neutrino interactions we are able to observe that the abundances of the dominant nuclei above neon do not change very much. However, small changes can also be observed for sodium. Below $A = 12$ a strong production of the elements ^{10}B and ^{11}B is therefore almost entirely related to the inclusion of neutrino-nucleus interactions. When comparing with the calculations where either the charged- or the neutral-current is turned off, we are able to observe that the production is dominated by neutral-current processes. This is easier to observe if we take a look at the elemental pattern of the same trajectory. It can be found in figure 4.31.

We can see that without neutrinos almost no elements up to $Z = 6$ are produced, but with the inclusion of neutrino interactions the abundance pattern of the light nuclei changes dramatically. By the inclusion of neutrino processes we furthermore observe that elements around the most dominant nucleus, which is in this case oxygen, are also strongly influenced by the ν -process. To better observe changes for the creation of heavy elements, we show in figure 4.32 the ratio of the final abundance pattern with and without neutrinos. Again, the figure shows that for the light- Z elements, the ratio can increase several orders of magnitude. For the higher charge elements the ratio is maximal three.

The production of free protons and neutrons from light nuclei can have effects on the abundances of the heavier nuclei because these nucleons can be captured by heavy elements (e.g. neutron capture on ^{44}Ti). To disentangle the influence of particle evaporation from light nuclei from the spallation on heavy nuclei, we made an additional calculation, where all neutrino reactions in nuclei with $A > 20$ were neglected. By doing the ratio

$$\frac{Y_{i,All}}{Y_{i,A < 20}}, \quad (4.23)$$

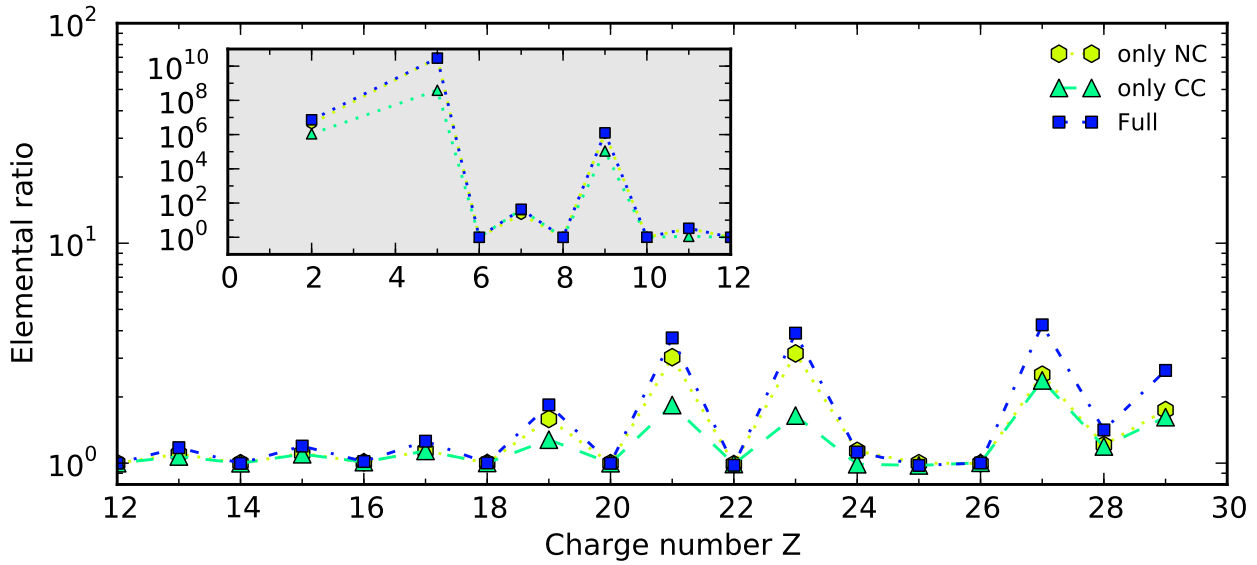


Figure 4.32.: The ratio of the different calculations that we showed in figure 4.31. The ratio is always relative to the calculation without neutrinos. What we can observe is that for the elements with $Z > 12$ the changes can be up to a factor three. Below $Z = 12$ the ratio can be several orders of magnitude.

where *All* denotes the calculation in which all neutrino reactions were included, whereas in the calculation labeled with $A < 20$ the neutrino reactions on nuclei with $A > 20$ were neglected, we were able to differentiate between both processes. The results can be found in figure 4.33, where the ratio of both abundances are shown as a function of charge number. Looking at the elemental ratio the first observation that we make is that when no neutrino processes are considered the ratio is unity, which is a necessary requirement for our model to be correct. For our other rates we are able to use this unity as a reference to better observe possible changes. The largest values can be seen in the amount of protons at the end of the simulation. Note that this change is of course not due to the fact that we changed/neglected the neutrino rate on free protons and neutrons, instead this change is due to the fact that heavy nuclei evaporate neutrons and protons. If the temperature is already low enough, the protons will not be captured by nuclei due to the Coulomb barrier.

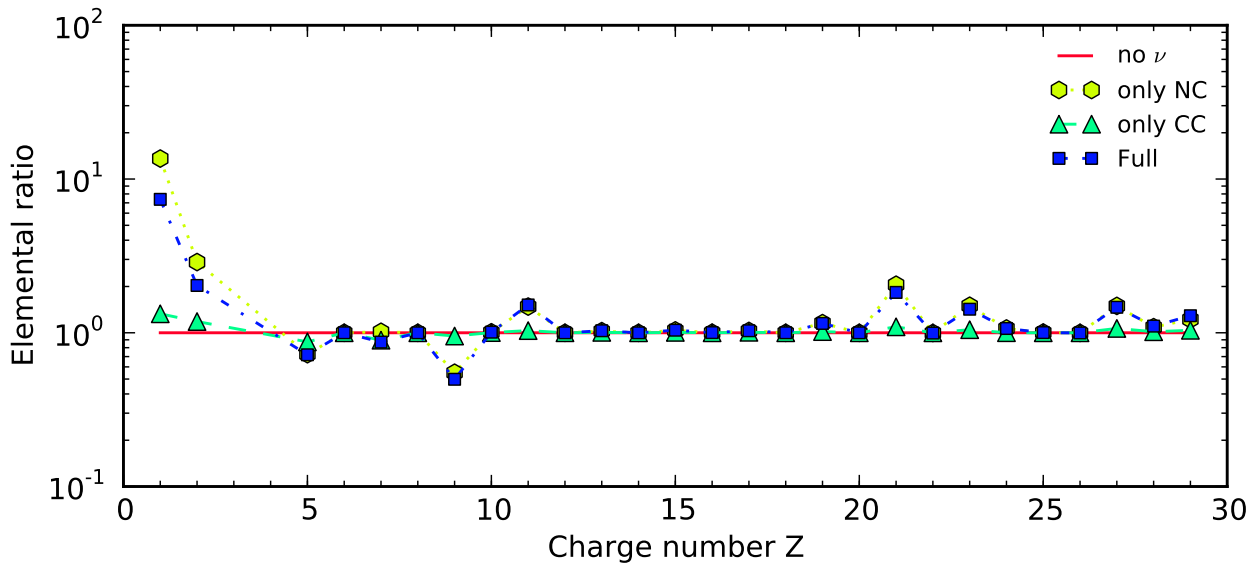


Figure 4.33.: The ratio of two different calculations that differentiate only in the treatment of neutrinos. To study the effect of heavy element neutrino scattering on the final nucleosynthesis, we did one additional calculation where we neglected all neutrino reactions above $A = 20$. The ratio of the full calculation against the reduced results is shown in this figures for all four types of calculations mentioned before.

The first real change related with the neglect of neutrino-nucleus processes for heavy elements can be seen directly at $Z = 11$ (sodium) where neutral-current neutrino processes increase the ratio by a factor of two. Charged current processes contribute only very little to the total change induced by the neutrino processes. The next changes can then be seen around charge number 20, where the elements potassium and scandium show a stronger production by the inclusion of neutrino-processes of calcium and titanium. Also vanadium and copper show a strong production due to the inclusion of neutrino nucleus processes. It is interesting to observe that when only neutral-current processes are included, the ratio of these elements is larger than when the full treatment is used. The reason for this fact is due to the used normalization and does not correspond to a real increase when using only neutral-current processes.

Coming back to figure 4.31 and keeping in mind what we learned in the last paragraphs, we can summarize that the inclusion of heavy element neutrino processes is relevant for the correct determination of neutrino nucleosynthesis. The production of elements is governed in this trajectory by the production of boron, as it can be seen in the lower plot of figure 4.31. The reason why boron is the dominant reaction partner has to do with the fact that ^{12}C is quite abundant. ^{12}C acts as a good target for neutral-current neutrino scattering processes to create then ^{11}B .

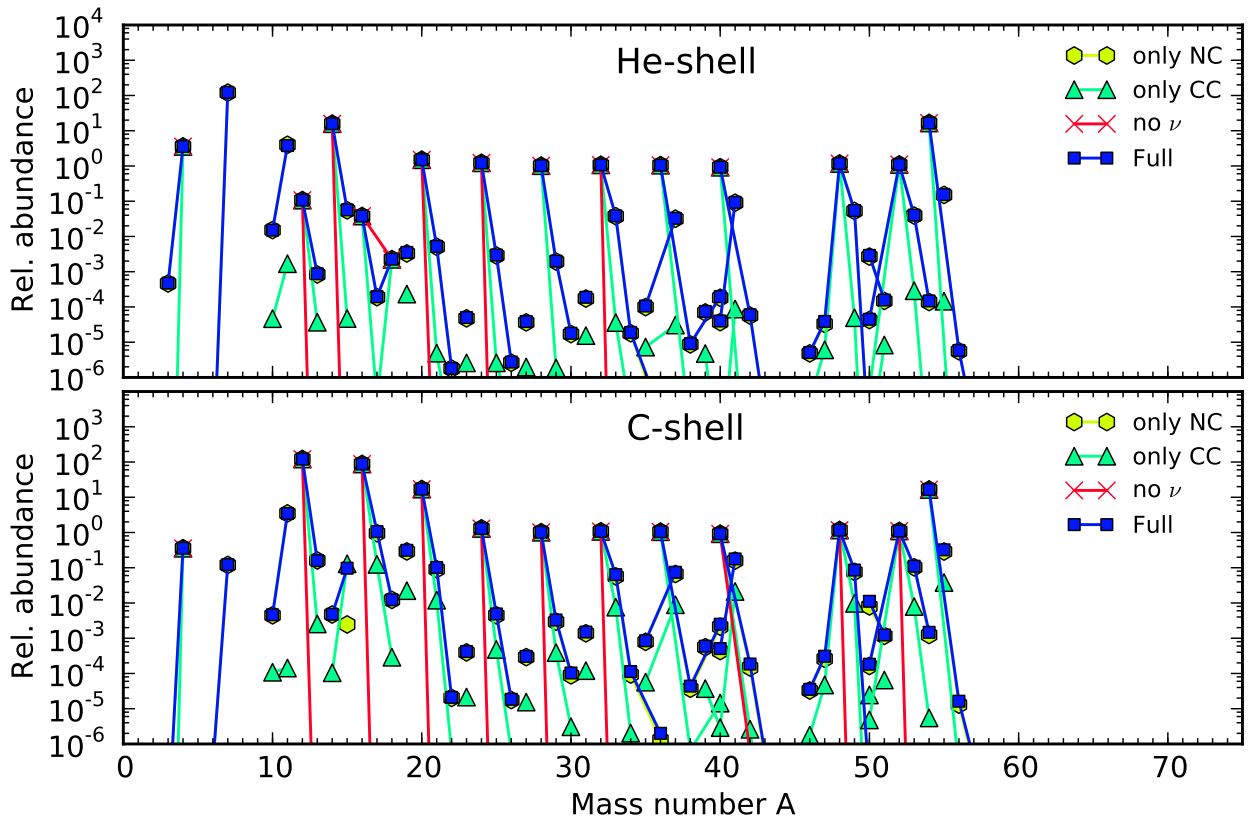


Figure 4.34.: Top: The nucleosynthetic result of a trajectory from the helium shell. Bottom: The final nucleosynthesis for a trajectory in the carbon shell. For each case the influence of the various interaction channels of neutrino interactions have been studied.

So far we only studied the nucleosynthesis effects of one trajectory that initially resided at 10^9 cm, which is in the inner part of the neon-oxygen shell. The ν -process is also important for the nucleosynthesis in the shells at larger radii. Therefore we show in figure 4.34 the production factors for the nucleosynthesis of one trajectory in the carbon as well as in the helium shell. The corresponding radii are 7×10^9 cm and 7×10^{10} cm, respectively.

The production factors show that in the helium shell ^7Li will be the nucleus that is created dominantly. The peak temperature is 0.254×10^9 K with a dynamical timescale of 108 s. The reactions governing this strong production are α -captures on ^3H and ^3He . The target nuclei itself are created from neutrino induced particle spallation. In the carbon shell the neutrino-nucleosynthesis produces dominantly ^{11}B , as we mentioned above. In this case the values for the peak temperature and dynamical timescale need to be between the two cases explained above. The temperature peaks at 0.558×10^9 K while the dynamical timescale is 17.34 s.

The nucleosynthesis results that we show in this section also illustrate that the free nucleons from neutrino induced spallation processes also have the possibility of being captured by other elements than the ones they were evaporated from. The cross section for neutron capture on heavy elements is larger than for neutron capture on light particles. For

protons the situation is different, because the Coulomb barrier will hinder captures on heavy nuclei for the temperatures that will be reached in the outer shells due to shock heating. Free neutrons on the other hand will be more likely captured by heavier elements than by the light ones. This fact can actually be observed in figure 4.34, where – in comparison to the calculations without neutrinos – the isotopic production stops at higher A. For example we are able to observe that with the inclusion of neutral-current neutrino spallation processes ^{55}Mn could be produced with a production factor of 0.89, which could not be synthesized if neutrino interactions were neglected. This production value is not very large, however, it is strongly dependent on the cooling timescale of the PNS. Thus by a longer cooling timescale the production can be increased. The production is governed by neutron captures from the stable ^{54}Fe , that is also produced without neutrinos, and a subsequent β -decay of ^{55}Fe . The neutron flux is actually high enough that also the other iron elements are produced, that have to overcome the unstable ^{55}Fe .

Before we move on, we would like to shortly discuss the previously mentioned dependence on the progenitor model. Therefore we picked three different progenitor models that differ in the metallicity content, but initially had the same mass⁸ of $20 M_{\odot}$. The first model has the same metallicity as it can be observed in the solar system, which is commonly abbreviated by Z_{\odot} . In the second model the metallicity has been reduced to $10^{-4} Z_{\odot}$. The last progenitor contains solely the metals that were created in the different burning processes; these type of stars are also called *Population III* stars [25].

For the creation of matter heavier than B, the ν -process requires heavy elements as target nuclei from which light particles will be evaporated or that act as a possible reaction partner for nucleon capture processes. The production of typical ν -process elements higher than boron is therefore sensitive to the elemental composition in the corresponding shell. With increasing abundance of heavy elements more target nuclei are available for possible neutrino evaporation reactions. Within figure 4.35 we show the relative nucleosynthesis results of the three different progenitor models at a radius of 10^{10} cm, which correspond for all models to a region in the helium shell. It shows that with decreasing metallicity the different burning spheres are further inside. Thus the chosen radius is for the Z_{\odot} model close to the inner edge of the He-shell, while for the other models this radius corresponds roughly to the center of the shell.

The fact that we utilize the same radius for our nucleosynthesis studies simplifies the comparison of the shock passage through the matter in such a way, that now parameters as the peak temperature and the time that the shock requires to get to this radius will be equal, as we assume the same neutron star mass and explosion energy. Also the neutrino fluxes will be the same until the time that matter starts to expand. The expansion itself can differ, since the expansion timescale depends on the local density at the beginning of the expansion.

For all different progenitor models the ν -process nucleosynthesis shows a strong production of the elements in the region up to $Z = 6$, especially lithium and boron. The creation of elements above carbon is very sensitive to the available amount of metals. In the model with solar metallicity the odd- Z elements are created with a relative abundance around $10^{-2} - 10^{-3}$. Even more interesting is the creation of matter with larger Z due to the inclusion of neutrino interactions, that produce the elements manganese and iron. In the model with solar system abundance we are able to observe that the relative abundance of iron is close to one, when neutrino interactions are included. When no neutrino interactions are included the relative abundance is only of the order 10^{-5} . The same holds true for manganese, where even a relative abundance larger than one can be obtained in this specific trajectory.

The creation of these elements can be explained by light particle captures on heavy elements. Of course these processes are also occurring in the case where no neutrino interactions are taken into account, however the amount of free neutrons and protons increases due to the neutrino spallation processes. Once again, the dominant neutrino processes within this context of neutrino nucleosynthesis are neutral-current processes.

While comparing the differences between the Z_{\odot} model and the $10^{-4}Z_{\odot}$ model, we are able to see that the abundance of the matter with $Z > 6$, created by the ν -process, is directly related to the abundance of the matter with the charge number increased by one. For example is the final abundance of ^{19}F directly related to the amount of neon that is in the ejecta. This leads us to the statement that the dominant reactions for the creation of matter with odd Z is neutrino induced nucleus spallation of the elements with a charge increased by one. For the latter elements it does not matter if the evaporated nucleon is a proton or a neutron, since the dominant nuclei are almost exclusively $N = Z$ nuclei, that will lead under neutron spallation to an unstable nucleus which will β^+ -decay into the same nucleus as under proton evaporation. Therefore it is logical that with decreasing heavy element abundance ($Z > 8$), the effectivity of neutrino nucleosynthesis will be reduced. The argumentation for this observation is easy. If less nuclei with charge $Z+1$ are available, less material can be converted into nuclei with charge number Z . Due to the fact that at the chosen radius the initial densities are roughly the same (150 g/cm^3 for the Z_{\odot} model against 180 g/cm^3 for the $10^{-4} Z_{\odot}$ model) the expansion timescales are also similar, while the neutrino luminosity and cooling rate are chosen to be equal by our model. Under these circumstances we are actually able to observe that the ratio of the produced nucleus to the nucleus serving as

⁸ Note however – as stated in [20] – that the mass loss during a star's life is strongly related to the metallicity of the progenitor. The less metal rich a star is, the more mass loss will occur. Thus the mass in the progenitor models before the onset of explosion will be different for each model.

a target for neutrino processes is constant between both models. The ratio of mother nucleus to the produced daughter is of the order 1000, in agreement with previous estimates [158].

One additional factor that we already mentioned previously is the creation of heavier elements by capture of free protons and neutrons. Contrary to the elements in region $8 < Z < 24$, the production is however more sensitive on the total amount of free neutrons and protons that are evaporated by spallation reactions. These neutrons will most likely be captured by heavy elements, because its cross section rises with mass number. Protons on the other hand need to overcome the Coulomb barrier and are therefore more likely not to react while the temperature stays constant. Due to neutrino spallation reactions before shock arrival, the amount of free protons will continuously rise. When the shock reaches the matter under consideration, the protons can be captured by the heavy elements, as long as the temperature is high enough to enable a sufficient production of the heavier elements. It turns out that the ideal temperature for these processes is in the region of He-shell burning, as we show in figure 4.35.

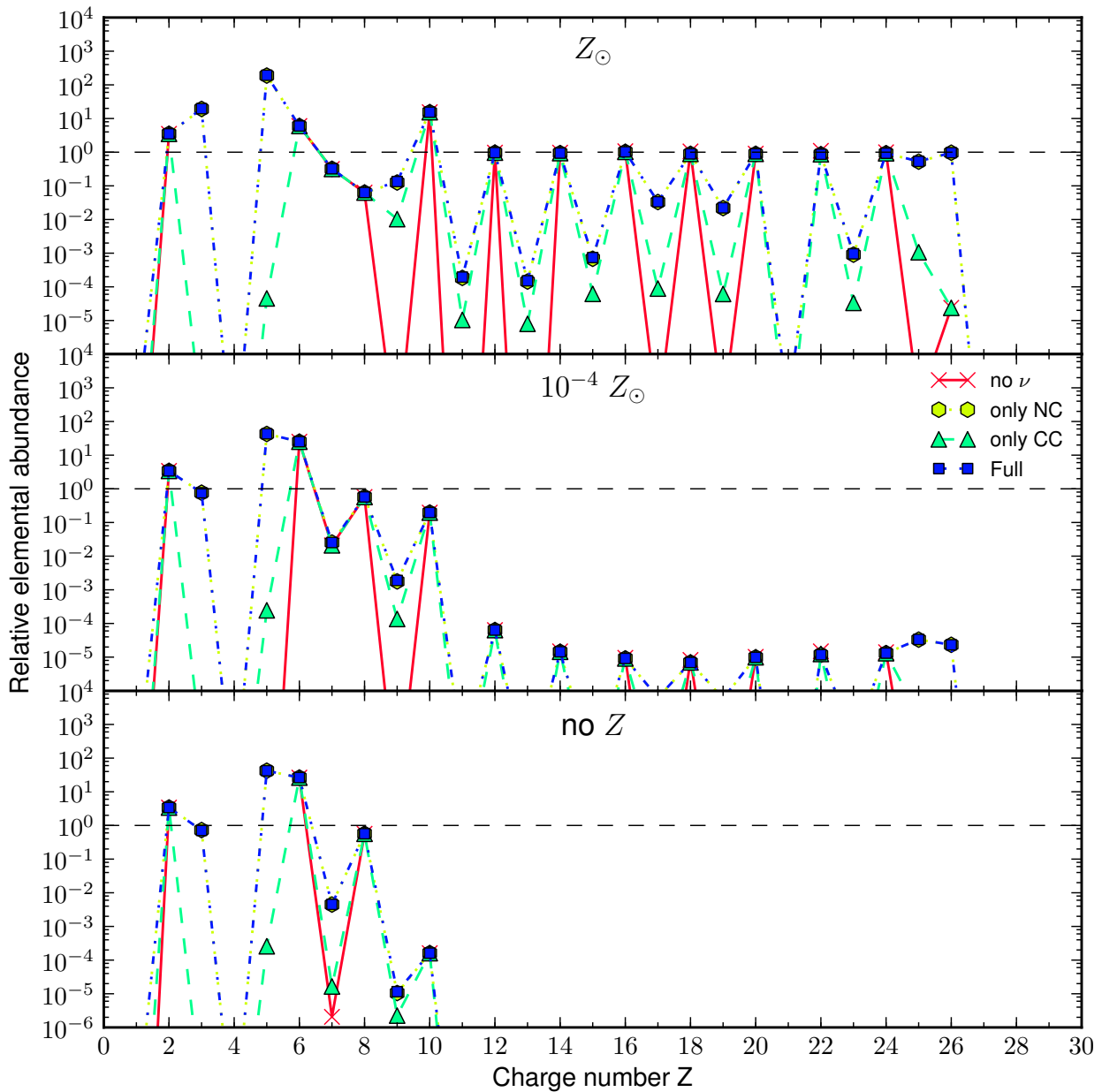


Figure 4.35: The nucleosynthesis yields of the three models used in our study. From top to bottom the models corresponds to an initial metallicity of solar metallicity (Z_{\odot}), 10^{-4} solar metallicity and no initial metallicity. The production below carbon is in all calculations very similar, because the shock temperature and the neutrino parameters are within all calculations the same. For higher charge numbers stronger differences arise, mainly due to nucleon capture on these heavy elements.

Within the last sections we saw that the production of elements by neutrino induced spallation processes is a radial dependent problem, that additionally is sensitive to the initial abundance. Depending on the radial starting point the nucleosynthesis changed substantially or only slight changes could be observed. The question of how much the ν -process contributes to the final nucleosynthesis of the stars ejecta, can therefore only be answered by an integrated nucleosynthesis. Within this thesis we calculated such an integrated nucleosynthesis of the outer ejecta of a core-collapse supernova starting from an initial radius of 1800 km, which corresponds to an enclosed mass of $1.49 M_{\odot}$. Of course these studies only have an exploratory character instead of an astrophysical accurate description. Nevertheless it will tell us how relevant neutrino-nucleus processes are within this scenario. We chose the progenitor model according to where we observed the largest effect in our fixed-radius calculations, which is of course the Z_{\odot} model. The astrophysical descriptions are used as described above.

Note once again that previous studies on ν -nucleosynthesis [2, 3] have already considered the inclusion of neutral and charged-current processes. However within their work they were limited to include these processes only on the dominant nuclei, while we consider neutrino processes on all nuclei.

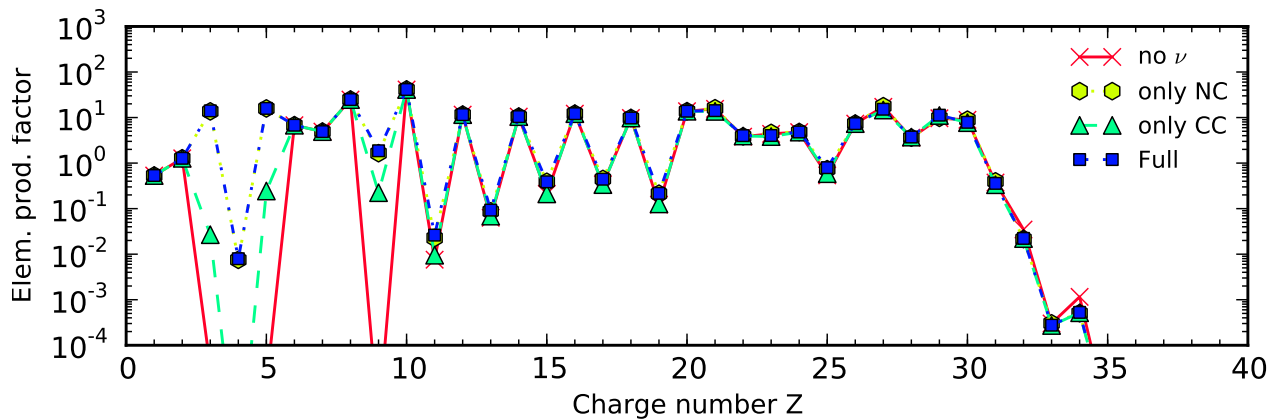


Figure 4.36.: The relative integrated nucleosynthesis of the outer ejecta of a core collapse supernova. The upper part shows the relative isotopic abundance, while the lower one shows the relative elemental abundance. In red the nucleosynthesis is shown without any neutrino interactions for the nucleosynthesis. Green and yellow correspond to the inclusion of only charged or neutral-current. The blue squares show the nucleosynthetic results for the inclusion of both charged and neutral-current processes.

In figure 4.36 we show the integrated nucleosynthesis of the matter we calculated. The shown integrated nucleosynthesis does not yield the total ejecta of the matter ejected in a core collapse supernova, since specific sites for the nucleosynthesis (e.g. the NDW or the hot convective bubble) are not incorporated. Instead the production incorporates only the elements that correspond to the matter usually connected to explosive nucleosynthesis processes. However, within this thesis, we also do not want to focus on which elements are created in the outer ejecta of a core-collapse supernova, instead we would like to study the changes that arise due to the inclusion of neutrino interactions. Therefore we are solely interested in changes between the different calculations shown in figure 4.36. The strongest changes are again observable in the light element region, where the elements ${}^7\text{Li}$, ${}^9\text{Be}$, ${}^{10}\text{B}$ and ${}^{11}\text{B}$ are produced by neutrino induced reactions.

Also for elements higher than $Z > 6$ changes can be observed that base on the inclusion of neutrino-nucleus evaporation processes. As stated by [2, 3] the changes are showing an increase only for odd- Z nuclei. The dominating reaction channel is the neutral-current channel, while the charged-current channel barely contributes above $Z = 6$. In the isotopic abundance pattern the dominant nuclei are again the neutron deficient ones. The largest changes can therefore be observed in the neutron richer elements where evaporated neutrons will be captured on.

Within this section we were able to observe that the inclusion of neutrino interactions has an impact on the outer ejecta of a core-collapse supernova. The detailed mechanisms has already been introduced in the work of [2], where already the dominant neutrino-nucleus interactions have been included. These cover mainly the reactions on $N = Z$ nuclei. On the other hand we have for the first time the possibility to include neutrino reactions on all nuclei within our network. The changes for the ν -nucleosynthesis in comparison to the results of previous studies are, if any, only marginal. However in light of further studies that could be done, changes might occur. Especially when considering an initial abundance pattern that will be enriched in s-process nuclei, the inclusion of all neutrino-nucleus rates might have an influence. For example in previous studies (see e.g. [2, 3]) a strong production of ${}^{138}\text{La}$ and ${}^{180}\text{Ta}$ has been observed, when neutral-current neutron evaporation processes on ${}^{139}\text{La}$ and ${}^{181}\text{Ta}$ are included. Within the work of [2] these processes are only approximated. Neutral-current proton evaporation processes on the other hand have been neglected.

Parent	Product	Reaction	σ [10^{-42}cm^2]	ν -temperature [MeV]
^{52}Fe	^{51}V	(ν_e, e^-n)	3	***
^{56}Ni	^{55}Mn	(ν_e, e^-p)	2	9.36
^{80}Kr	^{78}Kr	$(\nu, \nu'2n), (\nu_e, e^-2n)$	11,29	9.35, 9.69
^{86}Sr	^{84}Sr	$(\nu, \nu'2n), (\nu_e, e^-2n)$	19,50	9.78, 6.76
^{85}Rb	^{84}Sr	(ν_e, e^-n)	102	5.914
^{140}Ce	^{138}Ce	$(\nu, \nu'2n), (\nu_e, e^-2n)$	33,88	8.69, 6.9

Table 4.1.: Cross sections for the production of the showed products from the parents over the displayed reactions. The production of these isotopes will then be – according to [158, 3] – of the solar abundance. The neutrino temperatures given in the last column are the values that we require to reproduce the desired cross section in the fourth column. “***” denote that the cross section is not possible up to a neutrino temperature of 10 MeV.

Furthermore [3] showed that the charged-current electron neutrino capture on ^{138}Ba has a strong influence. Therefore with the inclusion of all the relative rates, we have a powerful tool to study possible changes of the nucleosynthesis with an initial progenitor that contains s-process material.

Furthermore in the work of [158, 3], the cross sections for the production of some heavy elements have been estimated, where the ν -process can contribute such that a production for these isotopes with the size of the solar abundance can be achieved. They estimated this by assuming that the key reactions are always neutrino-induced processes from the nearby nuclei that are very abundant. The created nuclei are nuclei in the iron region (^{51}V , ^{55}Mn) but also heavier isotopes are included. All isotopes considered by their work can be found in table 4.1. Since we have calculated the partial cross sections for the evaporation of particles in this thesis, we are now able to estimate how high the neutrino temperature for these processes will be and if they will pinpoint to one neutrino scenarios that can be met with current neutrino spectra during the core-collapse supernova. The values presented in 4.1 show that in some cases very high neutrino temperatures are required for the production of the elements. However one has to be careful, if these processes are always the most likely processes that will occur. For example can we observe that – within the helium shell – the production of ^{51}V is quite high, also by the cross section in the table the production would not be possible. The fact is, that ^{51}V is produced as ^{51}Mn by the neutral-current reaction $(\nu, \nu'p)$ of ^{52}Fe . The same holds true for the production of ^{55}Mn that is created by ^{56}Ni [3]. Note however that a production of ^{55}Mn is also possible over neutron captures on ^{52}Fe , as we showed in figure 4.34. For the creation of ^{78}Kr we did not see an additional possibility of creating the matter with other neutrino processes. We should note however that ^{78}Kr and ^{84}Sr are in the neutrino-driven wind strongly overproduced, and might therefore not have their dominant production in ν -nucleosynthesis. In some cases the heavy elements show neutrino temperatures that are low enough to occur in current core-collapse supernova environments. Therefore a further study of the ν -nucleosynthesis with our neutrino-nucleus reactions appears to be a good idea.

We saw in this section that the inclusion of neutrino processes manifests in changes in the nucleosynthesis of the outer ejecta. These processes have been well known over the last twenty years. So far the neutrino-nucleus interactions have always been limited to a small subset of nuclei. In this work we were for the first time able to study ν -nucleosynthesis including the full set of neutrino-nucleus for both charged- and neutral-current processes. Within our schematic model we were able to conclude the same results as previous studies.

The already mentioned influence on heavy element neutron captures induced by neutrino-nucleus spallation processes has become a very interesting astrophysical site for the nucleosynthesis. It was the assumption of the authors in [160] that stated that during a core-collapse the neutron density in the helium shell might be large enough to have an r-process. However this statement was disproven in 1990 [2], where similar findings could be made as we showed in figure 4.34. Only for low-metallicity and compact progenitors, an r-process nucleosynthesis could be found.

However, if one includes collective neutrino-oscillations in metal-poor stars ($10^{-4} Z_{\odot}$) it has been shown that a nucleosynthetic result can be obtained that has strong similarities to an r-process abundance [161]. Neutrino oscillations are required due to the fact that for this result the dominant neutron source is not the neutral current neutron evaporation from α -particles, instead it is the charged-current capture of an electron antineutrino with the emission of one neutron. The neutrino oscillations turn the high energetic $\bar{\mu}$ - and $\bar{\tau}$ -neutrinos into electron antineutrinos with the same energy. Thus the neutrino oscillations increase the energy spectrum, and therefore the cross section of this specific channel [161]. Note that this process only works efficiently if an inverted mass hierarchy is utilized and if these oscillations do occur.

Additional to the possibility of creating r-process material as part of neutrino nucleosynthesis, metal-poor compact progenitors and inverted hierarchy neutrino oscillations can also help in increasing the creation of the rare nucleus ^9Be [162].

4.6 Neutrino processes and neutrino fluence

After we have now discussed the two dominant astrophysical sites, where neutrinos are expected to change the nuclear composition, we would like to shortly recapitulate if, and how, the inclusion of neutrino-nucleus cross sections changed the nucleosynthesis and how that relates to the other astrophysical sites.

We would again like to start with the neutrino-driven wind, in which the neutrino interaction is actually so strong that it drives matter from the PNS surface and determines the electron fraction. Within this scenario, the initial neutrino flux is very high, however this high neutrino-flux leads to a very fast expansion of the matter from the PNS surface reducing the neutrino flux through the matter under consideration. The neutrino fluence⁹ in the NDW can be given from the beginning of the nucleosynthesis – which is at a temperature of 10^{10} K – to the end of our calculation of the order of 10^{39} cm^{-2} . For example does the neutrino-driven wind of the simulation with a progenitor model of $18 M_{\odot}$ [11] span a fluence range of 2×10^{39} cm^{-2} up to 12×10^{39} cm^{-2} . The higher fluence values have been obtained for the late ejecta trajectories that showed a rather slow expansion from the PNS, instead of the trajectories from the initial ejecta where the neutrino luminosity from the Kelvin-Helmholtz cooling of the PNS where still high. Within this whole fluence range, changes in the final nucleosynthesis could only be observed for the light elements, that will not have a strong influence on the nucleosynthesis of the total star. Also with the additional wind model of [12] – where the initial neutrino luminosities are almost an order of magnitude larger than in the model of [11] – a fluence of 4.9×10^{39} cm^{-2} could be reached, that also has no influence on the nucleosynthesis. Similar values for the fluence are obtained for the ejecta in the hot convective bubble.

We also studied the nucleosynthesis on the outer ejecta of a core-collapse supernova, where the ν -process operates. Within this scenario matter is not ejected due to neutrino-nucleus energy deposition. Instead matter will be expanded by the shock passage through the region, increasing the temperature and giving rise to explosive nucleosynthesis scenarios. However the matter will be further away from the neutrino source, which will decrease the fluence. On the other hand, the expansion is slower than in the case of the NDW ejecta. The usual values that will be reached in ν -nucleosynthesis is in the range of 3×10^{38} cm^{-2} at a starting radius of 5000 km up to 2×10^{36} cm^{-2} at a radius of 10^6 km.

Although the fluence is orders of magnitude smaller than in the case of the NDW, changes in the nucleosynthesis can be observed. This raises the question why that occurs. The reason for that is within the definition of the fluence. In this definition we do not specify a nucleus, instead we simply integrate the current neutrino fluxes. In the case of ν -nucleosynthesis the dominant nuclei are already available at the beginning of our simulation and neutrino processes can act from the beginning of neutrino emission from the PNS. The case is different for neutrino-driven wind nucleosynthesis, where the matter is created on its way outwards. Neutrino nucleus reactions require the existence of these elements to influence the composition. To put it even more drastic, the relevant issue for neutrino processes to influence the nucleosynthesis is the time window, that the neutrinos have on the target nucleus before the flux decreases. This will actually bring the fluence for a specific nucleus to the same magnitude as for the ν -process. The additional arguments made in the discussion on the neutrino-driven wind are still valid and contribute in addition to the effect, that no changes in the heavy element nucleosynthesis can be observed.

It is also important to note, that the dominant production in the ν -nucleosynthesis is neutrino spallation of the most abundant nuclei to produce the less abundant nuclei, which are the ones where we see an effect due to neutrino processes. If the ratio for the solar abundances of mother nucleus to daughter nucleus is around 10^3 , a production of the daughter nucleus over the ν -process is expected [158, 159]. Furthermore, the evaporated nucleon can be captured by another nucleus, eventually leading to a small production of heavier elements. However, in the neutrino-driven wind the idea was from the beginning, that evaporated neutrons from the most dominant heavy elements might increase the effectivity of the νp -process. Due to the fact that the neutron emission from these proton rich material is very small, the neutrino-induced spallation rates cannot contribute to the nucleosynthesis.

⁹ Note that while we are discussing the neutrino fluence within this paragraph, we are always talking about the fluence of electron neutrinos.

Part IV.

Summary & Outlook



4.7 Summary

In this thesis the influence of neutrino-induced spallation rates on the nucleosynthesis is investigated. These neutrino-induced rates are studied in various nucleosynthesis processes such as the νp -process, the r-process and the ν -process. The astrophysical site connecting all these different processes is the core-collapse supernova. Therefore our nucleosynthesis results are dependent on the information obtained by core-collapse supernova simulations and their correct input physics. The production of heavy elements in the core-collapse supernova is dominantly related to the neutrino-driven wind phase, in which matter is ejected from the proto-neutron star due to neutrino-nucleon interactions. Astrophysical parameters in the neutrino-driven wind, such as entropy and electron fraction, will determine which nucleosynthesis process occurs. The traversing shock will, when passing through the outer layers of the star, also have influence on the final nucleosynthesis. The matter in the outer layers of the star will also be subject to the neutrino fluxes from the proto-neutron star.

The question that we would like to raise in this thesis is, if neutrino-induced spallation processes have influence on the nucleosynthesis. The neutrino-induced spallation rates have been obtained in a two-step process. In a first step the excitation of the nucleus is described. The second step describes the decay of the excited nucleus. The neutrino-nucleus excitation rates have been calculated for charged-current and neutral-current processes. The nuclear excitation spectra of the target nuclei are calculated with the help of a spherical RPA based on Woods-Saxon single-particle states, adjusted to reproduce the correct separation energies. The used interaction has been of the Landau-Migdal type. The excitation-spectrum includes excitations up to $J = 4$.

For the neutrino energies in a core-collapse supernova, the excitation spectra peaks in the region of the giant resonances, which can be located above the particle threshold. Thus, it is necessary to consider not only the total cross section, but instead to consider partial cross sections for the spallation of light particles from the excited nucleus. This approach is described in a statistical model, where the usual formation cross section is replaced by the neutrino-induced nuclear excitation cross section.

The one-particle spallation probability has been calculated with the statistical code MOD-SMOKER which is based on SMOKER – a statistical reaction code with wide application in astrophysics [4, 5, 6, 7]. This code has the advantages that it has explicit knowledge of low lying experimental states, as long as they are experimentally known with its spin and parity value. Furthermore the transmission through the Coulomb potential is treated correctly by confluent hypergeometric functions. The largest disadvantage is, that it only allows for one-particle spallation and does not cover cascade reactions that might occur, if the energies of the neutrinos coming from the proto-neutron star are high enough, or the separation energies are small. Therefore, below the first two-particle emission channel opening, we change the description of the decay probabilities to a model that allows for multi-particle spallation. The code used for this description is the dynamical code ABLA07, that explicitly allows for several particle emissions. Which decay channels will be available for each nucleus is very sensitive to the energy distribution of the neutrinos. We calculated the decay probabilities up to four particle evaporation processes to determine the partial cross section. We made sure that the decay probabilities at the transition between the two models agree and give a smooth transition.

The partial cross sections – obtained as a function of incoming neutrino energy – have been folded with a respective supernova neutrino spectrum, parameterized as a Fermi-Dirac function with the parameters neutrino temperature T_ν and chemical potential μ_ν . The chemical potential is usually assumed to be zero. This distribution type has been utilized extensively in the past decades, which is the reason why we kept this description also in this work, although different descriptions are available for the neutrino spectra. Changing to one of these alternative descriptions within our model for the neutrino-spectra, such as the α -fit, can be done quite easily.

Once our neutrino induced evaporation processes were calculated, we required to implement the neutrino rates in a nuclear reaction network. The utilized nuclear reaction network has so far only been used for the calculation of r-process nucleosynthesis studies including fission cycling [8, 9]. For a better description of the weak interactions close to the proto-neutron star where high densities are available that can influence the electron capture rates, the weak interaction rates from [10] have been included.

After generating a working network that accounts for our neutrino-nucleus interactions, we could observe their influence in several nucleosynthesis studies where high neutrino fluxes are expected. These studies were related to various different nucleosynthesis processes assigned to core-collapse supernovae scenarios. These reach from the nucleosynthesis in the neutrino-driven wind to the shock passage through the outer layers of the former star.

Within our thesis we have considered different astrophysical parameters for the neutrino-driven wind nucleosynthesis, that actually are based on data from core-collapse supernova simulations. The main input parameters are the neutrino and antineutrino spectra from the cooling of the proto-neutron star, since these will determine the electron fraction. The astrophysical parameters for the neutrino-driven wind of current core simulations are such that the values of entropy and electron fraction are not extreme enough to fulfill the requirements for a successful r-process.

Before 2012 it has been shown that the ejecta from the PNS surface are proton rich ($Y_e > 0.5$) [11]. Due to νp -nucleosynthesis this proton rich matter can contribute to the heavy element nucleosynthesis [48]. Therefore we calcu-

lated the nucleosynthesis of this proton rich neutrino-driven wind with the inclusion of our newly determined spallation rates. It turned out that the nucleosynthesis is governed by the antineutrino capture processes on free protons, since the abundance of free protons is high. Furthermore we are able to see, that the partial cross section for neutron emission in neutron deficient nuclei is very small, since proton emissions are more favorable. The second argument against strong changes due to the inclusion of neutrino-nucleus spallation processes is, that the abundance of these heavy elements is substantially lower than the abundance of free protons.

Within our study we also posed the question if the observed abundance pattern of r-process poor stars – such as HD 122563 – can be explained with the nucleosynthesis in neutrino-driven wind nucleosynthesis. Therefore we calculated the integrated neutrino-driven wind nucleosynthesis of long-term core-collapse supernovae simulations with different progenitor masses. We were able to observe that with increasing mass of the progenitor, νp -nucleosynthesis acts more efficiently due to the fact that matter is expanding slower and therefore keeping matter longer in the right conditions for νp -nucleosynthesis. Thus for an 18 M_{\odot} model an agreement with the metal-poor star's abundance can be obtained between the elemental abundance pattern and the obtained nucleosynthetic result up to a mass number of roughly $Z = 44$. The newly included neutrino-spallation rates do not contribute so much that the heavy element nucleosynthesis is changed strongly. Changes can nevertheless be observed in the region of light elements. For example does the inclusion of neutrinos severely influence the creation of elements as ${}^7\text{Li}$ and ${}^{11}\text{B}$. However, the total ejected mass of these light elements is too little to contribute to the total nucleosynthesis of the star.

In mid of 2012 core-collapse supernova simulations showed that ejecta in the neutrino-driven wind with improved charged-current neutrino nucleon processes, that are treated consistently with the underlying equation of state, can reach values that are initially below 0.5 and are therefore neutron-rich [140]. Later ejecta will become proton rich again, due to the fact that during the cooling of the PNS the spectra become more and more similar. Thus late ejecta will undergo νp -nucleosynthesis, while this is not possible for the early neutron rich ejecta.

Within this work we studied the integrated neutrino-driven wind of a current core-collapse supernova model, that includes the above improved treatment, with a progenitor mass of 11.2 M_{\odot} . The electron fraction shows initially neutron rich ejecta ($Y_e = 0.474$), while later material will again become proton rich. The nucleosynthesis is hereby dominated by the initial neutron rich ejecta, since the mass flux from the PNS decreases very fast. Thus, depending on the mass flux from the proto-neutron star, this will hinder the matter production over the νp -process. However, the elements usually assigned to the νp -process – such as ${}^{92}\text{Mo}$ – are also created in the neutron-rich ejecta, that still produces dominantly neutron deficient material. The neutron rich ejecta show a minor influence on the newly included spallation rates in the nucleosynthesis. In the integrated result these influences are noticeable for the neutron rich stable elements. Large changes due to the inclusion of neutrino-nucleus processes can again be found for the lighter elements, where elements such as ${}^7\text{Li}$ and ${}^{11}\text{B}$ are produced due to the inclusion of neutral-current neutrino spallation processes. However, the production factor is too small to be considered as an astrophysical site for the production of these elements.

The elemental abundance pattern has been compared to the metal-poor star HD 122563, where it is found that matter can reproduce the abundance pattern up to $Z = 42$. Heavier elements than $Z = 42$ could not be produced, due to the neutron shell closure of $N = 50$. By comparison with the data from the metal-poor star HD 122563, we are only able to gain information on the elemental abundance pattern. As we can see from the isotopic distribution of our nucleosynthesis results in figure 4.17, we see that we overproduce the neutron deficient nuclei in comparison to the solar abundance, whereas neutron rich stable isotopes are underproduced. We are not able to say if this abundance pattern can be also observed in metal-poor stars like HD 122563, because we do not have information on the isotopic abundance. If the abundance pattern would be as it is in our solar system, it would require for another astrophysical site that can explain the creation of the neutron rich elements.

The next astrophysical process that we studied in our work was r-process nucleosynthesis in the neutrino-driven wind. Due to the fact that the astrophysical site for r-process nucleosynthesis is still not fully settled and galactic chemical evolution models favor the core-collapse supernova environment as a possible site for the r-process, we utilized a neutrino-driven wind scenario in which an electron fraction of 0.469 at a temperature of $T = 3 \times 10^9$ K was reached. To obtain an r-process that is able to reach mass numbers around $A = 195$, the entropy has been increased by a factor of 2. The luminosities and mean energies for the neutrino spectra have been taken from the original simulation [13]. Since no data has been given for μ - and τ -flavor neutrinos, a variation of these values – within a physical reasonable regime – could be used to observe the influence on neutral-current neutrino-induced particle spallation. To observe only the changes due to the inclusion of neutrino-nucleus processes, we kept for all calculations the rates of free protons and neutrons such, that the electron fraction does not change due to the neglect of these processes.

We recognized that the inclusion of charged-current neutrino processes on nuclei do not change the final r-process nucleosynthesis much, whereas neutral-current processes lead to a reduction of the heavy elements produced in this ejecta. Therefore the inclusion of all neutrino rates is dominated by neutral-current processes. The relevant process for neutral-current nucleus processes is the spallation of ${}^4\text{He}$, where proton-spallation leads to the reduction of the neutron-to-seed ratio, due to the increased production of heavy elements by subsequent α -captures, starting with the ${}^3\text{H}(\alpha, \gamma){}^7\text{Li}$

reaction. We saw that the nucleosynthesis is sensitive to the used neutrino spectra for μ - and τ -flavor, since they have the most influence on neutral-current neutrino processes, as long as the usual energy hierarchy is valid.

We should note once more that the astrophysical conditions from state-of-the-art core-collapse simulations favor the production of these light r-process elements (Sr, Y, Zr) over the νp -process or slightly neutron rich matter in their wind ejecta, as we have shown above. The question that cannot be explained in current models is, how the abundance pattern of heavy r-process elements (e.g. europium) are created, which are also observed in metal-poor stars such as HD 122563 [36].

Furthermore we studied the hot convective bubble, in which matter is ejected due to neutrino interactions [12, 47]. The matter emission does not occur directly from the proto-neutron star surface, instead it is further away in a region of a few hundred kilometers. The electron-fraction of these ejecta resides between 0.5 and 0.54, where early ejecta have values close to 0.5 and later ejecta become more proton rich. Note that these simulations do not consider the improved description of microphysics in the proto-neutron star. For these ejecta the inclusion of neutrino-nucleus processes do not change the heavy element production tremendously. The only fact that we could observe is that some production of heavy elements over the νp -process could be made, which however is also very minimal.

In a next step we focused on the nucleosynthesis in the outer shells of the exploding star, where the neutrinos, produced by the proto-neutron star, traverse through. The neutrino fluxes are of course less than in the case of the neutrino-driven wind – due to the radial decrease with $1/r^2$. As already shown in previous works [2, 3] the inclusion of neutrino interactions in this region does have influence on the odd-Z elements in the nucleosynthesis. The reason can be found in the elemental abundance ratio, where odd-Z elements show always less abundance than the even-Z nuclei. As it has been noted by [158, 159], if the ratio of the mother nucleus to the daughter nucleus is of the order 10^3 , a production over ν -nucleosynthesis might be possible. Specifically for the light elements ${}^7\text{Li}$ and ${}^{11}\text{B}$ the production in this explosive environment has shown to be an important part for the amount of these elements in our solar system. Within this work we utilized a rather phenomenological model for the shock passage and the expansion afterwards. Furthermore the neutrino luminosities have been assumed to be very high, especially for μ and τ flavor neutrinos, which are the dominating contributions for neutral-current processes.¹⁰ We used this high values to be able to compare with [2].

Due to this high values it is understandable that the dominating processes in ν -nucleosynthesis are neutral-current processes. However, charged-current processes also contribute and cannot be neglected. The main difference why in this astrophysical process neutrino-nucleus processes show prominent features, whereas in the case of the neutrino-driven wind the difference is barely noticeable, can be explained as follows. The argument is that – contrary to the neutrino-driven wind – in the ν -process the matter is already produced before the expansion starts. Thus the time window for neutrino interaction is longer, than in the neutrino-driven wind. In the neutrino-driven wind heavy elements are created by (n, p) reactions that mimic β^+ -decays, whereas in ν -nucleosynthesis the elements are created by spallation of the abundant nuclei. The abundance of the elements acting as a target for neutrino-nucleus interactions is in the outer shells substantially higher in comparison to the same elements in the neutrino-driven wind. Thus the relevant quantity of abundance times cross section will be generally higher, which allows converting more matter over spallation reactions in the ν -process.

Globally we can say that the inclusion of neutrino-nucleus processes does not have influence on the nucleosynthesis of core-collapse supernovae. For an efficient production of some elements such as ${}^7\text{Li}$, ${}^9\text{Be}$, ${}^{11}\text{B}$, but also ${}^{138}\text{La}$ and ${}^{180}\text{Ta}$, neutrino-nucleus interactions are required. However this fact has already been mentioned in [2]. For r-process calculations we can observe that the inclusion of neutrino-processes changes the final abundance. Thus, if the r-process would occur in neutrino-driven winds, at least the neutrino-nucleus interactions on ${}^4\text{He}$ need to be incorporated. However, a full treatment will be always better. Within proton-rich winds on the other hand, the effect of neutrino-nucleus interactions on heavy element nucleosynthesis is very small. However, the fact that we now have a full set of rates, allows us to explore the impact of various astrophysical sites and their nucleosynthesis processes in a more sophisticated model, which includes the possible relevant neutrino-nucleus processes in these environments.

¹⁰ However, it was also shown that even by reducing the neutrino temperature for μ and τ neutrinos to a value of 6 MeV, a successful ν -nucleosynthesis could be observed [3].

4.8 Outlook

The rates we calculated within our thesis cover already the largest part of the nuclear chart. A possible way would be to improve our model for the calculation of the nuclear excitation spectrum in a more sophisticated model. However, due to the fact that the effects for the nucleosynthesis are very small, an improved description will probably also have only minimal effects on the nucleosynthesis results. Instead it might be useful to apply the decay description of our two fold model for other weak processes that allow for additional particle emission. The weak interaction processes that might have the most influence will be β -delayed neutron emission for r-process nucleosynthesis [163]. So far, the neutron emission is determined by a theta function [164]. Once the excitation energy in the daughter nucleus is larger than the neutron separation energy, a neutron is emitted. The same holds true for more than one neutron emission processes. Following the argumentation of [163], β -delayed neutron emission will keep the neutron density higher at later times than without their inclusion, which might have an impact on the final nucleosynthesis. It would be interesting to see how the β -delayed neutron emission would change the final nucleosynthesis if our description of the decay is used. It has been shown that β -delayed neutron emission has influences on the neutron density in r-process simulations.

Once there exist more evidence where the r-process occurs and if possibly this process occurs under strong neutrino fluxes, we are in the position to study the r-process with all relevant weak interaction processes that will alter the nuclear composition.

The studies for the ν -nucleosynthesis in the outer shells of the star during a core-collapse supernova have only exploratory character. It would be interesting to study the ν -nucleosynthesis in more detail within a full detailed hydrodynamical simulation of the explosion of the star. When this star has an s-process contribution, it would be interesting to study the influence of ν -nucleosynthesis on the complete set of s-process elements, and not only for a small subset of all nuclei as it has been done in previous work [3].

With our new rates we were able to determine the neutrino mean energies (respectively neutrino temperatures) that are required to produce the solar abundance of a few heavy elements mentioned in [3]. Based on the partial cross sections we could observe neutrino temperatures that show a spread between 5.9 and 9.78 MeV. Whereas the lower values seem to agree with the model used in [3], the upper values are substantially too high. However as we mentioned already, the production of these elements might have several origins and is therefore better studied in a full nuclear network.

With respect to the nucleosynthesis in neutrino-driven winds, we are now sure that we are able to determine the final nucleosynthesis of wind ejecta with all the relevant reactions included. These reactions include the – within this thesis calculated – neutrino-nucleus processes as well as previously included fission rates [8] and neutrino reactions on free protons and neutrons [165].

One possibility for the improvement of our nuclear network would be to adjust the size of the nuclear network as a function of temperature. At high temperatures where only neutrons and protons are available, the reaction network does not require to include for example lead isotopes, because they cannot be created. When the temperature decreases, this would of course require that the size of the network automatically adjusts to the current composition and its development in the next timestep.

Part V.

Appendix



4.9 Nuclear astrophysics

4.9.1 Nuclear reaction networks

Nuclear networks are utilized for the determination of energy generation and nucleosynthesis in stellar burning processes. They are furthermore utilized to obtain the final yield distribution in nucleosynthesis scenarios. If the energy feedback from nuclear reactions is negligible, the reaction network solely requires the astrophysical state (temperature, density, ...) as a function of time and initial number densities present at the starting time. To divide changes on the number densities n_i arising from hydrodynamical expansion/compression and nuclear reactions, the nuclear abundances Y_i are defined as the ratio between the number density of species i and the total number density in the astrophysical environment ($n = \rho/m_u = \sum_i n_i A_i$ where A_i is the mass number of species i).

It is useful to furthermore define other different variables. The mass fraction X_i is then given as $X_i = A_i Y_i$. By assuming baryon number conservation we obtain $\sum_i Y_i A_i = 1$. Likewise by demanding charge conservation we obtain the electron fraction $\sum_i Y_i Z_i = Y_e = n_e/n$ that defines the number of electrons in the system by the amount of nucleons.

Before we show the set of first order differential equations that we need to solve for nuclear reaction networks, it is helpful to describe shortly the different reaction rates of interest that form one part of the input for nuclear reaction networks. Nuclear reaction networks need to include three of the four fundamental forces. These are the strong, weak and electromagnetic interactions. Although weak interactions proceed much slower than the other types of interactions, especially those reactions have a strong influence, because they can change the proton to neutron ratio (respectively the electron fraction). Under the assumption that the cross sections for our nuclear reaction network are known, either by theoretical predictions such as the statistical model mentioned in subsection 2.4.1 or by experiment, a rate is obtained by

$$r_{X,i} = \int \sigma(|\vec{v}_X - \vec{v}_i|) |\vec{v}_X - \vec{v}_i| d^3 n_X d^3 n_i. \quad (4.24)$$

\vec{v}_X, \vec{v}_i are the velocities of target X and projectile i with its responding velocity distributions n_X and n_i . The integration can be performed under the assumption that both particles obey Maxwell-Boltzmann statistics, resulting to $r = n_X n_i \langle \sigma v \rangle_{X,i}$. n_X and n_i are the number densities of particles X and i . The information for the cross section is now stored in the flux integrated cross section $\langle \sigma v \rangle$.

$$\langle \sigma v \rangle_{X,i} = \left(\frac{8}{M\pi} \right)^{1/2} (k_B T)^{-3/2} \int_0^\infty E \sigma(E) \exp(-E/k_B T) dE, \quad (4.25)$$

where M denotes the reduced mass of the system, E is the center-of-mass energy. T gives the temperature of the plasma and k_B is Boltzmann's constant.

If the projectile is a photon, n_i will be determined by the Planck distribution and the relative velocity is always c . With that we can determine the rate to

$$r_X = \frac{\int d^3 n_X}{\pi^2 (c\hbar)^3} \int_0^\infty \frac{c \sigma(E_\gamma) E_\gamma^2}{\exp(-E_\gamma/k_B T)} dE_\gamma \equiv \lambda_{X,\gamma}(T) n_X. \quad (4.26)$$

These photo-disintegration rates can be derived from the capture cross section representing the opposite direction ($Y + j \rightarrow X + \gamma$) in terms of *detailed balance*

$$\lambda_{X,\gamma}(T) = \left(\frac{G_Y G_j}{G_X} \right) \left(\frac{A_Y A_j}{A_X} \right)^{3/2} \left(\frac{M k_B T}{2\pi\hbar^2} \right)^{3/2} \langle \sigma v \rangle_{Y+j} \exp(-Q_{Y,j}/k_B T). \quad (4.27)$$

For the calculation of the reverse rate via detailed balance, we therefore require the partition functions $G_i = \sum_j (2J_j + 1) \exp(-E_j/k_B T)$ and mass numbers A_i of all involved nuclei. Additionally the inverse cross section depends strongly on the Q-value of the reaction, as well as on the temperature of the environment because the latter basically determines the photon distribution. The Q-value is defined as

$$Q = \sum_f m_f c^2 - \sum_i m_i c^2, \quad (4.28)$$

where the sum over f runs over all final elements and the corresponding sum over i runs over all initial elements in the reaction. In this specific example the Q-value reads

$$Q = m_Y c^2 + m_j c^2 - m_X c^2. \quad (4.29)$$

The rates are measured/calculated only for the bare nuclei, requiring us to modify the rates for the use within astrophysical plasmas where we have other nuclei as well as electrons present, distorting the Coulomb repulsion of charged nuclei. This is done by multiplying the rate with screening corrections

$$\langle \sigma v \rangle_{i,k}^* = f_{scr}(Z_X, Z_i, \rho, T, n_X) \langle \sigma v \rangle_{i,k}. \quad (4.30)$$

The screening corrections are sensitive to the proton numbers of projectile k and target j , as well as the density, temperature and the composition of the plasma [166].

We are now left with the fact, how to deal with weak processes in nuclear reaction networks. This is of course for key interest because this thesis deals, on the one hand with the inclusion of new weak reaction rates for nuclear reaction network calculations, on the other hand weak interactions are the only reactions that are able to change a proton into a neutron or vice versa and we already know that the electron fraction is a key parameter for nucleosynthesis studies. It appears obvious that due to the mass difference of the reacting partners in weak reactions a behavior similar to equation 4.26 is appropriate instead of equation 4.25. It is however important to note that within usual astrophysical scenarios electrons are at least partially degenerate, resulting in a non-Maxwellian distribution. This has to be considered by making the electron capture rates explicitly dependent from the electron distribution as well as the temperature, $r_X = \lambda_{j,e}(T, n_e), n_X$. The same arguments are valid for the case of positrons. Nuclear decay as it occurs here on earth, such as β -decay and α -emission is considered in the same approach as photo-dissociation $r_X = \lambda_j n_X$, where $\lambda_X = \ln 2 / \tau_{1/2}$. Whenever possible, experimental data is used. If no experimental data is available the calculations of [164] are used.

Neutrinos in nuclear reaction networks

Usually neutrino interactions with matter are neglected in nuclear reaction networks because its cross section is in general too little to change the composition. However, in scenarios with very high neutrino fluxes, such as the neutrino-driven wind phase of a core-collapse supernova, neutrinos can have a large influence on the nucleosynthesis. The neutrino distribution functions are usually assumed to have a Fermi-Dirac type with a “temperature” T_ν and a degeneracy η . With the help of $E = pc$, where p is the momentum of the neutrino, we can write:

$$\phi(E, T) = \frac{N}{F_2(\eta)(k_B T_\nu)^3} \frac{E^2}{\exp(E/k_B T_\nu - \eta) + 1}. \quad (4.31)$$

$F_2(\eta = 0)$ accounts for the proper normalization and is the relativistic Fermi integral, its value results to 0.5546. Again we would like to stress that we utilize this parametrization of the Fermi-Dirac type distribution to be comparable with previous studies.

To calculate the neutrino rates we require additional input from the hydrodynamical simulations that model the astrophysical scenario we are interested in. This additional data will be the luminosity of all neutrino flavors relevant for the nuclear network and the radius of the decoupling region, where the neutrino mean free paths will increase due to a drop in density. The rate has to be calculated as

$$\lambda_\nu = N \langle \sigma \phi(E, T_\nu) \rangle \quad (4.32)$$

which is similar to the usual rate, such as photo dissociation rates. The average cross section will be given by

$$\langle \sigma(E_\nu) \phi(E, T_\nu) \rangle = \int \sigma(E_\nu) \phi(E_\nu, T_\nu) dE_\nu, \quad (4.33)$$

where $\sigma(E_\nu)$ is the neutrino cross section as a function of incoming neutrino energy. We will shortly write the average cross section $\langle \sigma(E_\nu) \phi(E, T_\nu) \rangle$ as a function of neutrino temperature $\sigma(T_\nu)$. The amount of neutrinos that is required in equation 4.32, can easily be calculated by

$$N = \frac{L_\nu}{4\pi r^2 \langle \mu \rangle \langle E_\nu \rangle}. \quad (4.34)$$

The parameters in this equation are the neutrino luminosity L_ν , the mean neutrino energy $\langle E_\nu \rangle$ and the radius r of the mass element that is studied. The factor $\langle \mu \rangle$ is known as flux factor and denotes the angular dilution of the neutrino radiation direction to the expansion direction. The flux factor is given as

$$\langle \mu \rangle = \frac{R_{\nu_e}^2}{2\Phi \Xi r^2} \quad \Xi = 1 - \sqrt{1 - \frac{(R_{\nu_e}/r)^2}{\Phi^2}} \quad \Phi = \left(\frac{1 - (R_s/R_{\nu_e})}{1 - (r/R_{\nu_e})} \right). \quad (4.35)$$

Hereby we assumed that the neutrinos are isotropically emitted from neutrino sources located at a sphere with radius R_{ν_e} . Above reactions are valid for all electron neutrino/ electron antineutrino reactions on free nucleons as well as on nuclei. The neutral current neutrino spallation rate can be given accordingly to

$$\lambda_{ZX}^{NC} = \sum_{x=e,\mu,\tau} \left[\frac{L_{\nu_x}}{4\pi r^2 \langle \mu \rangle \langle E_{\nu_x} \rangle} \sigma_{ZX}^{\nu_x}(T_{\nu_x}) + \frac{L_{\bar{\nu}_x}}{4\pi r^2 \langle \mu \rangle \langle E_{\nu_x} \rangle} \sigma_{ZX}^{\bar{\nu}_x}(T_{\bar{\nu}_x}) \right]. \quad (4.36)$$

All the different type of rates discussed above can be described by three categories based on the number of reactants. The rate in which a specific isotopic abundance i will change can therefore be expressed as

$$\dot{Y}_i = \sum_j \mathbb{k}_j^i \lambda_j Y_j + \sum_{j,k} \mathbb{k}_{j,k}^i \left(\frac{\rho}{m_u} \right) \langle j, k \rangle Y_j Y_k + \sum_{j,k,m} \mathbb{k}_{j,k,m}^i \left(\frac{\rho}{m_u} \right)^2 \langle j, k, m \rangle Y_j Y_k Y_m, \quad (4.37)$$

differentiating between one (electron-captures, β^\pm , α -decay, neutrino reactions and photo-disintegration), two (particle-fusion reactions) and three reactants. Although from the latter three-body reactions only few exist, their influence can be very large. The most famous example is the triple- α rate in which three alpha particles fuse to a ^{12}C . The factors \mathbb{k}_x^i account for the fact that either this element is created or destroyed via this reaction. Furthermore they account for the fact that identical particles are not counted twice.

These are the sets of differential equations that we have to solve for obtaining the final yields of an arbitrary simulation. Under the assumption that the energy feedback of nuclear reactions is negligible for the hydrodynamics, one is able to evaluate the nucleosynthetic outcome after the hydrodynamic simulation. The only input the nuclear network requires are temperature and density as a function of time, as well as an initial composition. If temperature and density are high enough, the system will reach a state that is known as *nuclear statistical equilibrium* (NSE) in which all reactions, except weak interaction processes, are in equilibrium with their corresponding inverse reaction. The nuclear abundances within the range of NSE can be uniquely determined for a given set of temperature T , density ρ and electron fraction Y_e . With the above requirement of charge and baryon number conservation, we are able to chose two independent chemical potentials. We will chose the chemical potentials of protons μ_p and neutrons μ_n . We are able to relate the chemical potential of a nucleus $\mu(Z, A)$ with mass number A and charge number Z under the assumption of equilibrium with μ_p and μ_n simply by

$$\mu(Z, A) = Z\mu_p + (A - Z)\mu_n. \quad (4.38)$$

Under the assumption that nuclei obey Boltzmann statistics, we are able to formulate the chemical potential to

$$\mu = mc^2 + k_B T \eta, \quad (4.39)$$

η is known as the degeneracy parameter that can be expressed as

$$\eta_{Z,A} = \ln \left(\frac{n}{G_{Z,A}(T)} \right) + \frac{3}{2} \ln \left(\frac{2\pi\hbar^3}{m_Z A k_B T} \right). \quad (4.40)$$

$G_{Z,A}(T)$ is the partition function that measures the internal degrees of freedom of the nucleus. It is given by $G_{Z,A}(T) = \sum_i (2J_i + 1) e^{-E_i/k_B T}$. Putting this into equation 4.38, we obtain with the so called *Saha-equation*

$$Y(Z, A) = \frac{G_{Z,A}(T) A^{3/2}}{2^A} \left(\frac{\rho}{m_u} \right)^{A-1} Y_p^Z Y_n^{A-Z} \left(\frac{2\pi\hbar^3}{m_u k_B T} \right)^{3(A-1)/2} e^{B(Z,A)/k_B T}. \quad (4.41)$$

$B(Z, A)$ gives the nuclear binding energy of nucleus with mass number A and charge number Z .

With the help of this equation, we are able to determine the abundance of matter in an astrophysical scenario under the conditions that temperature and density are high enough. For very high temperatures the upper equation tells us that only free protons and neutrons will survive. In our network calculations we will always try to start from nuclear statistical equilibrium and evolve the system from there. The condition we require for nuclear statistical equilibrium is that the temperature is larger than $T = 10$ GK. If that requirement cannot be met, we start with an initial composition that has to be provided.

4.9.2 Implementation of the neutrino rates in the network

This subsection is a rather technical one, in which we describe the way how we implemented the spallation rates in the network code. Therefore it is helpful first to talk about the implementation of rates in general. The code allows up to three initial particle reactions. Of course they can be additionally subdivided into the amount of particles that are present in the outgoing channel. The currently accepted and optimal way of formatting this rate is given by what is known as the *REACLIB* format. Within this format reactions with the same amount of incoming and outgoing particles will be joined in one chapter. It allows for a very easy check if all rates conserve mass. The usual entries and their physical meaning can

Chapter	Reaction	Chapter	Reaction
1	$a \rightarrow b$	1	$a \rightarrow b$
2	$a \rightarrow b + c$	2	$a \rightarrow b + c$
3	$a \rightarrow b + c + d$	3	$a \rightarrow b + c + d$
4	$a+b \rightarrow c$	4	$a \rightarrow b + c + d + e$
5	$a+b \rightarrow c+d$	5	$a+b \rightarrow c$
6	$a+b \rightarrow c+d+e$	6	$a+b \rightarrow c+d$
7	$a+b \rightarrow c+d+e+f$	7	$a+b \rightarrow c+d+e$
8	$a+b+c \rightarrow d$	8	$a+b \rightarrow c+d+e+f$
		9	$a+b+c \rightarrow d$

Table 4.2.: Left: The old set of REACLIB chapters. Right: The updated set of REACLIB parameters.

be found in table 4.2. Several particle capture/emission processes will be written explicitly, (e.g. the triple-alpha process will be $\alpha + \alpha + \alpha \rightarrow {}^{12}\text{C}$) in chapter eight. In that format neutrino capture/scattering processes without particle spallation would have the chapter one. If we however allow for several particle emissions these entries will also change and we will have entries from chapters 1-3. However even then we could reach cases where these rates cannot be incorporated¹¹. We therefore added another entry within the *REACLIB* database that allows for one-to-four body reactions. This allows us also to include complicated combinations like an evaporation of a neutron, proton and α particle at once. So far we would be limited by the emission of maximal three particles, because the daughter nucleus also needs to be included. To overcome this problem, we combined identical particles in the outgoing channels (only for neutrino processes), resulting in a description that can always be written as the spallation of neutrons, protons and α particles plus an residual nucleus that can be always written in chapter four. We have now to account for the correct double counting coefficients, which is however a trivial thing to do.

Improvements of the used network

Within this work, several improvements have been included to the original program code. Before this work, the code required an initial abundance to start calculations from. Now the code adjusts depending on the temperature used. If the temperature is higher than 6×10^9 K, the initial abundance is calculated with the help of nuclear statistical equilibrium and the Timmes equation of state [143]. If the temperature is below 6×10^9 K the initial composition is read in from the progenitor model.

If the peak temperature of the trajectory is below the chosen 6×10^9 K, the complete trajectory is followed by the network, meaning that the starting point of the network calculations is the first point that is given from the hydrodynamical simulation. If the maximal temperature is higher than 10×10^9 K the astrophysical parameters of the trajectory are linearly interpolated to the point in time where the temperature drops below 10×10^9 K. At this temperature it is in most situations save to start with an initial composition of free protons and neutrons, that can be determined simply by

$$\begin{aligned} y_p &= y_e \\ y_n &= 1 - y_e. \end{aligned} \tag{4.42}$$

Additionally to the above described changes, we also included the possibility of replacing the weak-interaction rates within the REACLIB database. This allows us to study different theoretical models for weak processes without always creating a new reaclib file. Furthermore it simplifies also the inclusion of experimental data very easy without the problem of a possible double inclusion of weak rates. The code checks for an arbitrary weak interaction if an experimental rate is available. If that is true, any theoretical model is neglected, if not, the theoretical model is used. Additionally α -decays are included. If a nucleus has an experimental α -decay rate, possible theoretical β^- -rates, that are larger than the α -rate, are neglected, since they would distort the final nucleosynthesis. For elements heavier than $Z = 94$, which have no experimental α -rate, theoretical α -decay rates are included following the Viola-Seaborg formula [167].

¹¹ An easy example might be the four-neutron evaporation for very neutron rich nuclei.

4.10 Nuclear physics

In this section we would like to explain the basic formalism and conventions that have been used within the nuclear physics part of this work. First and foremost we applied natural units in which $c = \hbar = 1$. We define four-vectors by $A^\mu = (A^0, \vec{A})$. Whenever possible we define four-values with greek indices (μ, ν, \dots) whereas euclidean vectors will have roman indices (i, j, k, \dots). The metric is chosen to be diagonal with positive time-component, resulting to be its own inverse:

$$g_{\mu,\nu} = g^{\mu,\nu} = \begin{pmatrix} 1 & 0 & 0 & 0 & 0 \\ 0 & -1 & 0 & 0 & 0 \\ 0 & 0 & -1 & 0 & 0 \\ 0 & 0 & 0 & 0 & -1 \end{pmatrix}. \quad (4.43)$$

The inner product of two four vectors is given as $A^\mu B_\mu = A^0 B^0 - \vec{A} \cdot \vec{B}$. It is easy to prove that $A_0 = A^0$ and $A^i = -A_i$.

With the help of the Pauli matrices are we able to obtain the Dirac matrices by

$$\beta = \begin{pmatrix} 1 & 0 \\ 0 & -1 \end{pmatrix} \quad \vec{\alpha} = \begin{pmatrix} 0 & \vec{\sigma} \\ \vec{\sigma} & 0 \end{pmatrix}. \quad (4.44)$$

The gamma matrices are then simply obtained in the Dirac representation

$$\gamma^0 = \beta = \begin{pmatrix} 1 & 0 \\ 0 & -1 \end{pmatrix} \quad \vec{\gamma} = \beta \vec{\alpha} = \begin{pmatrix} 0 & \vec{\sigma} \\ -\vec{\sigma} & 0 \end{pmatrix}, \quad (4.45)$$

and

$$\gamma^5 = \gamma_5 = i\gamma^0\gamma^1\gamma^2\gamma^3 = \begin{pmatrix} 0 & 1 \\ 1 & 0 \end{pmatrix}. \quad (4.46)$$

The above defined metric is able to change the index of any gamma matrix such that

$$\gamma_\mu = g_{\mu\nu}\gamma^\nu, \quad (4.47)$$

which gives $\gamma^0 = \gamma_0$ and $\gamma^i = -\gamma_i$ for $i = 1, 2, 3$.

The 4x4 spin matrix $\vec{\Sigma}$ is defined without the factor 1/2

$$\vec{\Sigma} = \begin{pmatrix} \vec{\sigma} & 0 \\ 0 & \vec{\sigma} \end{pmatrix}, \quad (4.48)$$

giving us the opportunity of defining the helicity simply by $h = \vec{\Sigma} \cdot \vec{p}$ with the eigenvalues ± 1 .

Dirac equation

The Dirac equation is given by

$$\left(i\gamma^\mu \partial_\mu - \frac{mc}{\hbar} \right) \Psi = 0. \quad (4.49)$$

As mentioned above, within our model and also the standard Model, we assume that our neutrinos are massless, left-handed Dirac particles carrying spin of 1/2. This simplifies upper equation to

$$i\gamma^\mu \partial_\mu \Psi = 0. \quad (4.50)$$

This fact allows us to determine both the helicity ($\vec{\Sigma} \cdot \vec{p}$) and chirality (γ_5) [59, 168]. For positive energy solutions the eigenvalues of helicity and chirality are identical. If we assume a neutrino moving along the z-axis the solutions of equation 4.50 are given by

$$\Psi = N \begin{pmatrix} \chi_+ \\ \chi_+ \end{pmatrix} \exp(i\vec{p} \cdot \vec{x}). \quad (4.51)$$

The allowed solutions of the Dirac equation for a neutrino moving along the positive z-axis with negative helicity (left-handed) can in general be formulated by

$$\phi = N \begin{pmatrix} \chi_- \\ -\chi_- \end{pmatrix} \exp(i\vec{p} \cdot \vec{x}). \quad (4.52)$$

The normalization is given by $N^{-2} = 2(2\pi)^3 E_\nu$ with E_ν being the energy of the incoming neutrino, χ_\pm are the usual Pauli two-spinors as found in several textbooks [59, 168, 169]. Within our model, as in the standard model, we assume that neutrinos are only left-handed resulting to a negative helicity.

Since we already mentioned the basics on isospin coupling, we only want to shortly repeat them here. Under the assumption that protons and neutrons are the same particle, namely the nucleon, we can write neutron and proton as two different states of the nucleon as

$$|n\rangle = \begin{pmatrix} 1 \\ 0 \end{pmatrix}, \quad \text{and} \quad |p\rangle = \begin{pmatrix} 0 \\ 1 \end{pmatrix}. \quad (4.53)$$

The isospin obeys as the normal spin a $SU(2)$ symmetry, with vectors denoted by $\vec{\tau} = (\tau_1, \tau_2, \tau_3) = \frac{1}{2}\vec{\sigma}$. The τ matrices are therefore the same as the Pauli matrices and the new notation is simply to avoid confusion. For a nucleus with A nucleons we can define the total isospin as

$$\hat{\mathcal{I}} = \sum_{i=1}^A \vec{\tau}_i, \quad (4.54)$$

where the coupling is the same as for coupling of A particles with spin. The projection onto τ_3 simply adds the single τ_3 values and we obtain

$$\hat{\mathcal{I}}_3 = \frac{1}{2}(Z - N). \quad (4.55)$$

4.10.1 Angular momentum coupling and spherical harmonics

Within our work we try to keep the same conventions as given by Edmonds [60]. The Clebsch-Gordan coefficients are written with total angular momentum first, and after the separator the projections are written as

$$\langle J_1 J_2 J | J_{1z} J_{2z} J_z \rangle, \quad (4.56)$$

where J_1 and J_2 are coupled to total angular momentum J . The Wigner $3J$ symbols and the Racah W -symbols are defined as in [60]. We use a triangle notation $\Delta(J_1 J_2 J)$ that is one if J is within the range of $|J_1 - J_2|$ up to $J_1 + J_2$ and zero otherwise.

We furthermore define the square root factors of angular coupling as $[J] = \sqrt{2J+1}$. Additionally we defined χ_i as $\chi_i = (l_i - j_i)(2j_i + 1)$, where i can be either a particle or a hole index, $l_i(j_i)$ is the orbital angular momentum (total angular momentum) of i .

The vector spherical harmonics are defined by

$$\mathcal{Y}_{\mathcal{J},l,1}^{m_{\mathcal{J}}} = \sum_{\mu\lambda} \langle l1J | \mu\lambda M \rangle Y_{l\mu} \vec{e}_{\lambda}. \quad (4.57)$$

$Y_{l\mu}$ are the usual spherical harmonics with angular momentum l and projection μ . A relation that is of importance for the discussion in our theory part (see chapter 2) is obtained by the unitarity properties of the Clebsch-Gordan coefficients and it states

$$Y_{l\mu} \vec{e}_{\lambda} = \sum_{JM} \langle l, 1, J | \mu\lambda M \rangle \mathcal{Y}_{\mathcal{J},l,1}^{m_{\mathcal{J}}}. \quad (4.58)$$

The multipole expansion that we applied is given in the appendix of Walecka (1975) [55]. We can start by introducing a new orthonormal basis \vec{e}_0, \vec{e}_{\pm} , where

$$\vec{e}_0 = \vec{e}_z = \vec{\kappa} / |\kappa| \quad \text{and} \quad \vec{e}_{\pm} = \mp \frac{1}{\sqrt{2}}(\vec{e}_x \pm i\vec{e}_y). \quad (4.59)$$

The components of this new orthonormal spherical basis vectors obey the following identities

$$(\vec{e}_\nu)^\dagger = (-)^\nu \vec{e}_{-\nu}, \quad (\vec{e}_\nu)^\dagger \cdot \vec{e}_{\nu'} = \delta_{\nu,\nu'}. \quad (4.60)$$

From basic quantum mechanics we know that the partial wave expansion of the plane wave can be given by

$$\exp(i\vec{k} \cdot \vec{x}) = \sum_{J=0}^{\infty} \sqrt{4\pi} [J] i^J j_J(\kappa x) Y_{J,0}(\Omega_x). \quad (4.61)$$

$j_J(\kappa x)$ is the spherical Bessel function of order J and $Y_{J,M}(\Omega_x)$ is the spherical harmonic of order J with projection M . Furthermore we applied $|\vec{\kappa}| = \kappa$, $\vec{\kappa} = \kappa$. The product of the partial wave expansion and the spherical basis vectors as defined above are

$$\vec{e}_0 \exp(i\vec{k} \cdot \vec{x}) = -\frac{i}{\kappa} \sum_{J=0}^{\infty} \sqrt{4\pi[J]} i^J \nabla \left(j_J(\kappa x) Y_{J,0}(\Omega_x) \right) \quad (4.62)$$

and

$$\vec{e}_\lambda \exp(i\vec{k} \cdot \vec{x}) = -\sum_{J=1}^{\infty} \sqrt{2\pi[J]} i^J \left[\lambda j_J(\kappa x) \mathcal{Y}_{J,J,1}^\lambda + \frac{1}{\kappa} \nabla \wedge \left(j_J(\kappa x) \mathcal{Y}_{J,J,1}^\lambda \right) \right], \quad (4.63)$$

for $\lambda = \pm 1$. Again $\mathcal{Y}_{J,L,1}^M$ are the spherical vector harmonics representing the coupling of spherical harmonics $Y_{L,m}$ and the spherical basis vectors, which have intrinsic angular momentum $(1, \lambda)$ to total angular momentum (J, M) . For the conjugate expression, the plane wave is expressed simply by

$$\exp(-i\vec{k} \cdot \vec{x}) = \sum_{J=0}^{\infty} \sqrt{4\pi[J]} (-i)^J j_J(\kappa x) Y_{J,0}(\Omega_x). \quad (4.64)$$

For the product of the spherical basis vectors with the plane wave above we obtain

$$\vec{e}_0 \exp(-i\vec{k} \cdot \vec{x}) = \frac{i}{\kappa} \sum_{J=0}^{\infty} \sqrt{4\pi[J]} (-i)^J \nabla \left(j_J(\kappa x) Y_{J,0}(\Omega_x) \right) \quad (4.65)$$

and

$$\vec{e}_{-\lambda} \exp(-i\vec{k} \cdot \vec{x}) = -\sum_{J=1}^{\infty} \sqrt{2\pi[J]} (-i)^J \left[\lambda j_J(\kappa x) \mathcal{Y}_{J,J,1}^\lambda + \frac{1}{\kappa} \nabla \wedge \left(j_J(\kappa x) \mathcal{Y}_{J,J,1}^\lambda \right) \right], \quad (4.66)$$

for $\lambda = \pm 1$. Equation 4.60 has been already applied for above equation. We furthermore utilized the equality

$$\left(\mathcal{Y}_{J,l,1}^M \right)^\dagger = (-1)^{l+1-J+M} \mathcal{Y}_{J,l,1}^{-M} \quad (4.67)$$

and the expressions

$$\begin{aligned} \nabla_\rho \left(j_J(\rho) Y_{J,M}(\Omega_\rho) \right) &= \sqrt{\frac{J+1}{2J+1}} j_{J+1}(\rho) \mathcal{Y}_{J,J+1,1}^M + \sqrt{\frac{J}{2J+1}} j_{J-1}(\rho) \mathcal{Y}_{J,J-1,1}^M \\ \frac{1}{\kappa} \nabla \wedge \left(j_J(\kappa x) \mathcal{Y}_{J,J,1}^M \right) &= -i \sqrt{\frac{J}{2J+1}} j_{J+1}(\rho) \mathcal{Y}_{J,J+1,1}^M + i \sqrt{\frac{J+1}{2J+1}} j_{J-1}(\rho) \mathcal{Y}_{J,J-1,1}^M. \end{aligned} \quad (4.68)$$

Vector currents

Due to the fact that we applied CVC, we only have three independent vector currents. Let us start with the Coulomb vector current that simplifies to

$$\langle (l_i \ 1/2) j_i | \mathcal{M}_J^V(q) | (l_\alpha \ 1/2) j_\alpha \rangle = (-1)^{j_\alpha + J - 1/2} \frac{[j_\alpha][j_i][J]}{\sqrt{4\pi}} \begin{pmatrix} j_i & j_\alpha & J \\ 1/2 & -1/2 & 0 \end{pmatrix} \times \int dr r^2 j_J(qr) f_i^*(r) f_\alpha(r), \quad (4.69)$$

where we applied $[x] \equiv \sqrt{2x+1}$. $f(r)$ are the radial single particle wave functions. By calculating the Coulomb part we already have the longitudinal part of the vector current [55]

$$\langle (l_i \ 1/2) j_i | \mathcal{L}_J^V(q) | (l_\alpha \ 1/2) j_\alpha \rangle = \frac{\omega}{q} \langle (l_i \ 1/2) j_i | \mathcal{M}_J^V(q) | (l_\alpha \ 1/2) j_\alpha \rangle. \quad (4.70)$$

Here ω gives the energy transfer. The transverse current has two parts, an electric and a magnetic one. They can be given via

$$\begin{aligned}
\langle (l_i \ 1/2) j_i || \mathcal{F}_{el,J}^V(q) || (l_\alpha \ 1/2) j_\alpha \rangle = & \\
(-1)^{j_\alpha+J-1/2} \frac{1}{2M} \frac{[j_\alpha][j_i][J]}{\sqrt{4\pi}} \begin{pmatrix} j_i & j_\alpha & J \\ 1/2 & -1/2 & 0 \end{pmatrix} & \\
\times \frac{1}{q} \int dr r^2 j_J(qr) f_i^*(r) f_\alpha(r) \left\{ \sqrt{J(J+1)} \frac{f_i^*(r) f_\alpha'(r) - f_i'^*(r) f_\alpha(r)}{r} \right. & \\
+ \frac{l_i(l_i+1) - l_\alpha(l_\alpha+1)}{\sqrt{J(J+1)}} (f_i^*(r) f_\alpha(r))' \left. \right\} & \quad (4.71) \\
+ (-1)^{l_i} \frac{q}{2M} \frac{[j_\alpha][j_i][J]}{\sqrt{4\pi}} \begin{pmatrix} j_i & j_\alpha & J \\ 1/2 & 1/2 & -1 \end{pmatrix} \times \int dr r^2 j_J(qr) f_i^*(r) f_\alpha(r), &
\end{aligned}$$

and

$$\begin{aligned}
\langle (l_i \ 1/2) j_i || \mathcal{F}_{mag,J}^V(q) || (l_\alpha \ 1/2) j_\alpha \rangle = & \\
(-1)^{j_\alpha+J-1/2} \frac{1}{i \cdot 2M} \frac{[j_\alpha][j_i][J]}{\sqrt{4\pi}} \begin{pmatrix} j_i & j_\alpha & J \\ 1/2 & -1/2 & 0 \end{pmatrix} & \\
\times \int dr r^2 j_J(qr) \frac{f_\alpha^*(r) f_i(r)}{r} \left[\frac{(\chi_i + \chi_\alpha)(\chi_i + \chi_\alpha + 1) - J(J+1)}{\sqrt{J(J+1)}} \right] & \quad (4.72) \\
+ (-1)^{j_\alpha+J-1/2} \frac{1}{i \cdot 2M} \begin{pmatrix} j_i & j_\alpha & J \\ 1/2 & -1/2 & 0 \end{pmatrix} & \\
\times \int dr r^2 j_J(qr) \left\{ \frac{\sqrt{J(J+1)}}{r} + \frac{\chi_\alpha + \chi_i}{\sqrt{J(J+1)}} \left(\frac{d}{dr} + \frac{1}{r} \right) \right\} f_i^*(r) f_\alpha(r). &
\end{aligned}$$

Axial vector currents

For the axial vector current no conserved vector current hypothesis exists due to the mass of the pion. The axial vector current is conserved in the limit of zero pion mass. By the ratio of the pion to nucleon mass we are able to determine the breaking of this symmetry to a factor smaller than 15%. Based on this “small” symmetry breaking one therefore applies the term *partially conserved axial current* (PCAC) [59]. The Coulomb axial vector looks like

$$\begin{aligned}
\langle (l_i \ 1/2) j_i || \mathcal{M}_J^A(q) || (l_\alpha \ 1/2) j_\alpha \rangle = & \\
(-1)^{j_\alpha+J+1/2} \frac{1}{i \cdot 2M} \frac{[j_\alpha][j_i][J]}{\sqrt{4\pi}} \begin{pmatrix} j_i & j_\alpha & J \\ 1/2 & -1/2 & 0 \end{pmatrix} & \quad (4.73) \\
\times \int dr r^2 j_J(qr) \left\{ f_i^*(r) f_\alpha'(r) - f_i'^*(r) f_\alpha(r) + (\chi_\alpha - \chi_i) \frac{f_i^*(r) f_\alpha(r)}{r} \right\}, &
\end{aligned}$$

while the longitudinal part now has the form

$$\begin{aligned}
\langle (l_i \ 1/2) j_i || \mathcal{L}_J^A(q) || (l_\alpha \ 1/2) j_\alpha \rangle = & \\
(-1)^{j_\alpha+J-1/2} \frac{i}{q} \frac{[j_\alpha][j_i][J]}{\sqrt{4\pi}} \begin{pmatrix} j_i & j_\alpha & J \\ 1/2 & -1/2 & 0 \end{pmatrix} & \quad (4.74) \\
\times \int dr r^2 j_J(qr) \left\{ (\chi_\alpha + \chi_i) \frac{f_i^*(r) f_\alpha(r)}{r} + \left(\frac{d}{dr} + \frac{1}{r} \right) f_i^*(r) f_\alpha(r) \right\}. &
\end{aligned}$$

Transverse electric and magnetic axial vector currents are given by

$$\begin{aligned}
\langle (l_i \ 1/2) j_i || \mathcal{F}_J^{elA}(q) || (l_\alpha \ 1/2) j_\alpha \rangle = & \\
(-1)^{j_\alpha+J-1/2} \frac{1}{iq} \frac{[j_\alpha][j_i][J]}{\sqrt{4\pi}} \begin{pmatrix} j_i & j_\alpha & J \\ 1/2 & -1/2 & 0 \end{pmatrix} & \quad (4.75) \\
\times \int dr r^2 j_J(qr) \left\{ \frac{\sqrt{J(J+1)}}{r} + \frac{(\chi_\alpha + \chi_i)}{\sqrt{J(J+1)}} \left(\frac{d}{dr} + \frac{1}{r} \right) \right\} f_i^*(r) f_\alpha(r) &
\end{aligned}$$

and

$$\langle (l_i \ 1/2) j_i || \hat{\mathcal{T}}_J^{mag,A}(q) || (l_a \ 1/2) j_a \rangle = (-1)^{l_i} \frac{[j_a][j_i][J]}{\sqrt{4\pi}} \begin{pmatrix} j_i & j_a & J \\ 1/2 & -1/2 & 0 \end{pmatrix} \times \int dr r^2 j_J(qr) f_i^*(r) f_a(r). \quad (4.76)$$



Bibliography

- [1] Y.-Z. Qian and G. Wasserburg. Where, oh where has the r-process gone? *Physics Reports*, 442(1-6):237–268, April 2007.
- [2] S. E. Woosley, D.H. Hartmann, R. D. Hoffman, and W.C. Haxton. The ν -process. *The Astrophysical Journal*, 356:272–301, 1990.
- [3] A. Heger, E. Kolbe, W.C. Haxton, et al. Neutrino nucleosynthesis. *Physics Letters B*, 606(3-4):258–264, January 2005.
- [4] T. Rauscher, F.-K. Thielemann, and K.-L. Kratz. Applicability of the Hauser-Feshbach approach for the determination of astrophysical reaction rates. *Nuclear Physics A*, 621(1-2):331–334, August 1997.
- [5] T. Rauscher, F.-K. Thielemann, J. Görres, and M. Wiescher. Capture of α particles by isospin-symmetric nuclei. *Nuclear Physics A*, 675:695–721, 2000.
- [6] H.P. Loens, K. Langanke, G. Martínez-Pinedo, T. Rauscher, and F.-K. Thielemann. Complete inclusion of parity-dependent level densities in the statistical description of astrophysical reaction rates. *Physics Letters B*, 666(4):395–399, September 2008.
- [7] T. Rauscher. Origin of the p-Nuclei in Explosive Nucleosynthesis. *Proceedings of Science*, NIC(XI), 2010.
- [8] G. Martínez-Pinedo, D. Mocerlj, N.T. Zinner, et al. The role of fission in the r-process. *Progress in Particle and Nuclear Physics*, 59(1):199–205, July 2007.
- [9] Ilka Petermann. *Influence of fission processes on nucleosynthesis in R-Process network calculations*. PhD thesis, 03 2011.
- [10] K. Langanke and G. Martínez-Pinedo. Shell-model calculations of stellar weak interaction rates: Weak rate for nuclei in the mass-range $A=45-65$ in supernovae environments. *Nuclear Physics A*, 673:481–508, 2000.
- [11] T. Fischer, S. C. Whitehouse, A. Mezzacappa, F. Thielemann, and M. Liebendörfer. Protoneutron star evolution and the neutrino-driven wind in general relativistic neutrino radiation hydrodynamics simulations. *Astronomy & Astrophysics*, 517(A80), 2010.
- [12] H.-T. Janka, R. Buras, and M. Rampp. The mechanism elements of core-collapse supernovae and the ejection of heavy elements. *Nuclear Physics A*, 718:269–276c, 2003.
- [13] A. Arcones, H.-T. Janka, and L. Scheck. Nucleosynthesis-relevant conditions in neutrino-driven supernova outflows. I. Spherically symmetric hydrodynamic simulations. *Astronomy & Astrophysics*, 467(3):1227–1248, 2007.
- [14] H.A. Bethe and C.L. Critchfield. The formation of deuterons by proton combination. *Physical Review*, 54(4):248–254, 1939.
- [15] K. Lodders. Solar system abundances and condensation of the elements. *The Astrophysical Journal*, 591:1220–1247, 2003.
- [16] M.E. Burbidge, G.R. Burbidge, W.A. Fowler, and F. Hoyle. Synthesis of the Elements in Stars. *Reviews of modern Physics*, 29(4):547–655, 1957.
- [17] A.G.W. Cameron. On the origin of the heavy elements. *The Astronomical Journal*, 62:9–10, 1957.
- [18] H.A. Bethe. Energy production in stars. *Science (New York, N.Y.)*, 161(3841):541–7, August 1938.
- [19] C.E. Rolfs and W.S. Rodney. *Cauldrons in the Cosmos: Nuclear Astrophysics*. Theoretical Astrophysics. University of Chicago Press, 1988.
- [20] S. E. Woosley, A. Heger, and T. A. Weaver. The evolution and explosion of massive stars. *Reviews of modern Physics*, 74(October):1015–1072, 2002.

-
- [21] H.-T. Janka, K. Langanke, A. Marek, G. Martínez-Pinedo, and B. Müller. Theory of core-collapse supernovae. *Physics Reports*, 442(1-6):38–74, April 2007.
- [22] Y.-Z. Qian and S. E. Woosley. Nucleosynthesis in neutrino-driven winds I: The physical conditions. *The Astrophysical Journal*, 471(1):331–351, November 1996.
- [23] R. C. Duncan, S. L. Shapiro, and I. Wasserman. Neutrino-driven winds from young, hot neutron stars. *The Astrophysical Journal*, 309:141–161, 1986.
- [24] A. Burrows. Neutrinos from supernova explosions. *Annual Review of Nuclear and Particle Science*, 40(4):181–212, 1990.
- [25] R. Klippenhahn, A. Weigert, and A. Weiss. *Stellar structure and evolution*. Springer, 2nd edition, 2012.
- [26] A Maeder. *Physics, Formation and Evolution of Rotating Stars*. Astronomy and Astrophysics Library. Springer, Berlin, Heidelberg, 2009.
- [27] M. Arnould and S. Goriely. The p-process of stellar nucleosynthesis: astrophysics and nuclear physics status. *Physics Reports*, 384(1-2):1–84, September 2003.
- [28] F. Käppeler and A. Mengoni. Nuclear input for the s process: progress with experiments and theory. *Nuclear Physics A*, 777:291–310, October 2006.
- [29] F. Käppeler, R. Gallino, S. Bisterzo, and W. Aoki. The s process: Nuclear physics, stellar models, and observations. *Reviews of Modern Physics*, 83(1):157–193, April 2011.
- [30] C. Freiburghaus, S Rosswog, and F.-K. Thielemann. r-Process in neutron star mergers. *The Astrophysical Journal*, 525(10):L121–L124, 1999.
- [31] Yong-Zhong Qian. Astrophysical models of r-process nucleosynthesis: An update. In S. Kubono, T. Hayakawa, T. Kajino, et al., editors, *AIP Conference Proceedings*, pages 201–208. American Institute of Physics Conference Series, 2012.
- [32] D. L. Burris, C. A. Pilachowski, T. E. Armandroff, et al. Neutron-capture elements in the early galaxy: Insights from a large sample of metal-poor giants. *The Astrophysical Journal*, 544:302–319, 2000.
- [33] a. Burrows, L. Dessart, E. Livne, C. D. Ott, and J. Murphy. Simulations of Magnetically Driven Supernova and Hypernova Explosions in the Context of Rapid Rotation. *The Astrophysical Journal*, 664(1):416–434, July 2007.
- [34] C. Winteler, R. Käppeli, A. Perego, et al. Magnetorotationally driven Supernovae as the origin of early galaxy r-process elements? *The Astrophysical Journal*, 750(1):L22, May 2012.
- [35] C. Sneden, J. J. Cowan, and R. Gallino. Neutron-Capture Elements in the Early Galaxy. *Annual Review of Astronomy and Astrophysics*, 46(1):241–288, September 2008.
- [36] S. Honda, W. Aoki, Y. Ishimaru, S. Wanajo, and S.G. Ryan. Neutron-capture elements in the very metal poor star HD 122563. *The Astrophysical Journal*, 643:1180, 2006.
- [37] C. Sneden, J.J. Cowan, J.E. Lawler, et al. The American Astronomical Society. All rights reserved. Printed in U.S.A. *The Astrophysical Journal*, 591:936–953, 2003.
- [38] C. Travaglio, R. Gallino, E. Arnone, et al. Galactic Evolution of Sr, Y, and Zr: A Multiplicity of Nucleosynthetic Processes. *The Astrophysical Journal*, 601(2):864–884, February 2004.
- [39] F. Montes, T. C. Beers, J. Cowan, et al. Nucleosynthesis in the Early Galaxy. *The Astrophysical Journal*, 671(2):1685–1695, December 2007.
- [40] A. Arcones and F. Montes. Production of Light-Element Primary Process Nuclei in Neutrino-Driven Winds. *The Astrophysical Journal*, 731(1):5, April 2011.
- [41] C. J. Hansen, F. Primas, H. Hartman, et al. Silver and palladium help unveil the nature of a second r-process. *Astronomy & Astrophysics*, 545:A31, September 2012.
- [42] L. Dessart, C. D. Ott, a. Burrows, S. Rosswog, and E. Livne. Neutrino Signatures and the Neutrino-Driven Wind in Binary Neutron Star Mergers. *The Astrophysical Journal*, 690(2):1681–1705, January 2009.

- [43] S. Wanajo, H.-T. Janka, and S. Kubono. Uncertainties in the νp -process: Supernova dynamics versus nuclear physics. *The Astrophysical Journal*, 729(1):46, March 2011.
- [44] Y.-Z. Qian. The Origin of the Heavy Elements : Recent Progress in the Understanding of the r-Process Introduction. *Progress in Particle and Nuclear Physics*, 50:153–199, 2003.
- [45] G. M. Fuller and B. S. Meyer. Neutrino capture and supernova nucleosynthesis. *The Astrophysical Journal*, 453:792–809, 1995.
- [46] G. Martínez-Pinedo. Selected topics in nuclear astrophysics. *The European Physical Journal Special Topics*, 156(1):123–149, April 2008.
- [47] J. Pruet, S.E. Woosley, R. Buras, H.-T. Janka, and R.D. Hofman. Nucleosynthesis in the hot convective bubble in core-collapse supernovae. *The Astrophysical Journal*, 400:325–336, 2005.
- [48] C. Fröhlich, G. Martínez-Pinedo, M. Liebendörfer, et al. Neutrino-Induced Nucleosynthesis of $A > 64$ Nuclei: The νp -process. *Physical Review Letters*, 96(14):1–4, April 2006.
- [49] W. Greiner and B. Müller. *Gauge Theory of Weak Interactions Fourth Edition*. Springer, 2009.
- [50] V.F. Weisskopf and D.H. Ewing. On the yield of nuclear reactions with heavy elements. *Physical Review*, 4(1937):472–485, 1939.
- [51] T.D. Lee and C.N. Yang. Parity Nonconservation and a Two-Component Theory of the Neutrino. *Physical Review*, 105(5):1671–1675, 1957.
- [52] J. Beringer, J. F. Arguin, R. M. Barnett, et al. Review of Particle Physics. *Physical Review D*, 86(1):010001, July 2012.
- [53] T.W. Donnelly and R.D. Peccei. Neutral current effects in nuclei. *Physics Reports*, 50(1):1–85, January 1979.
- [54] R.P. Feynman and M. Gell-Mann. Theory of the fermi interaction. *Physical Review*, 109:193–198, 1958.
- [55] J.D. Walecka. Semileptonic weak interactions in nuclei. In *Muon Physics, Volume II: Weak Interactions*, volume 1, page 114, 1975.
- [56] L. Marcucci, R. Schiavilla, M. Viviani, et al. Weak proton capture on ^3He . *Physical Review C*, 63(1):015801, December 2000.
- [57] S. Weinberg. Charge symmetry of weak interactions. *Physical Review*, 112(1958):1375–1379, 1958.
- [58] M.L. Goldberger and S.B. Treiman. Decay of the Pi meson. *Phy*, 110:1178–1184, 1958.
- [59] C. Giunti and C.W. Kim. *Fundamentals of neutrino physics and astrophysics*, volume 54. Oxford University Press, USA, 2007.
- [60] A.R. Edmonds. *Angular Momentum in Quantum Mechanics*. Investigations in physics. Princeton University Press, 1968.
- [61] J.D. Walecka. *Theoretical Nuclear And Subnuclear Physics*. World Scientific Pub Co Inc, 2nd edition, 2004.
- [62] DJ Griffiths. *Introduction to quantum mechanics*. Pearson Prentice Hall, 2005, 1 edition, 1995.
- [63] K. Langanke and E. Kolbe. Neutrino-induced charged-current reaction rates for r-process nuclei. *Atomic Data and Nuclear Data Tables*, 79(2):293–315, November 2001.
- [64] P. Ring and P. Schuck. *The nuclear many-body problem*. Springer, 2000.
- [65] G. Baumgärtner and P. Schuck. *Kernmodelle*. B.I.-Hochschultaschenbücher. Bibliograph. Inst., Hochschultaschenbücher-Verlag, 1968.
- [66] H. D. Vries, C. W. D. Jager, and C. D. Vries. Nuclear charge-density-distribution parameters from elastic electron scattering. *Atomic Data and Nuclear Data Tables*, 36(3):495–536, 1987.
- [67] A. Bohr and B. R. Mottelson. *Nuclear Structure Volume 1*. W. A. Benjmain, Inc., 1969.

-
- [68] M. G. Mayer. On closed shells in nuclei. II. *Physical Review*, 75, 1949.
- [69] O. Haxel, J.H.D. Jensen, and H.E. Suess. On the "magic numbers" in nuclear structure. *Physical Review*, 75:766, 1949.
- [70] W. Hornyak. *Nuclear Structure*. Elsevier Science, 1975.
- [71] J. Rinker and J. Speth. Nuclear polarization in muonic 204, 206, 207, 208Pb in the random-phase approximation. *Nuclear Physics A*, 306(3):360–396, 1978.
- [72] N.T. Zinner. *Nuclear Reactions for Nuclear Astrophysics*. PhD thesis, University of Aarhus, 2007.
- [73] N.T. Zinner, K. Langanke, K. Riisager, and E. Kolbe. Muon capture on nickel and tin isotopes. *The European Physical Journal A - Hadrons and Nuclei*, 17(4):625–631, August 2003.
- [74] A.H. Wapstra, G. Audi, and C. Thibault. The Ame2003 atomic mass evaluation. *Nuclear Physics A*, 729(1):129–336, December 2003.
- [75] P. Möller, J.R. Nix, W. D. Myers, and W. J. Swiatecki. Nuclear ground-state masses and deformations. *Atomic Data and Nuclear Data Tables*, 59:185–381, 1995.
- [76] LD Landau. The theory of a fermi liquid. *Sov. Phys. JETP*, 3(6):920–925, 1957.
- [77] A. B. Migdal. *Theory of finite Fermi systems and applications to atomic nuclei*. Internat. Sci. Mono. Texts Phys. Astron. Interscience, New York, NY, 1967.
- [78] V.N. Guman and B.L. BirBrain. Fermi liquid theory and spectrum of excitations of the Pb208 nucleus. *Nuclear Physics*, 70:545–552, 1965.
- [79] M. R. Plumley, J. W. Watson, B. D. Anderson, et al. Spin observables for the Pb(p,n)208 Bi reaction at 135 MeV. *Physical Review C*, 56(1):263–269, 1997.
- [80] E. Kolbe, K. Langanke, and P Vogel. Weak reactions on 12C within the continuum random phase approximation with partial occupancies. *Nuclear Physics A*, 652(1):91–100, May 1999.
- [81] M. Goldhaber and E. Teller. On nuclear dipole vibrations. *Physical Review*, 74(9):1046–1049, 1948.
- [82] T. Wakasa, H. Sakai, H. Okamura, et al. Gamow-Teller strength of Nb in the continuum studied via multipole decomposition analysis of the 90Zr(p,n) reaction at 295 MeV. *Physical Review C*, 55(6):2909–2922, 1997.
- [83] T. Wakasa, H. Sakai, H. Okamura, et al. Strength observed in Gamow-Teller resonance plus continuum in the reaction at 295 MeV. *Physics Letters B*, 426(3-4):257–262, May 1998.
- [84] G.F. Bertsch and H. Esbensen. The (p,n) reaction and the nucleon-nucleon force. *Rep. Prog. Phys*, 607(50):607–654, 1987.
- [85] E. Caurier, G. Martínez-Pinedo, F. Nowacki, A. Poves, and A.P Zucker. The shell model as a unified view of nuclear structure. *Reviews of modern Physics*, 77(April):427–488, 2005.
- [86] A. Richter. Probing the nuclear magnetic dipole response with electrons, photons and hadrons. *Progress in Particle and Nuclear Physics*, 34(261):261–284, January 1995.
- [87] M. Rho. Quenching of axial-vector coupling constant in beta-decay and pion-nucleus optical potential. *Nuclear Physics A*, 231:493–503, 1974.
- [88] M. Ichimura, H. Sakai, and T. Wakasa. Spin-isospin responses via (p,n)(p,n) and (n,p)(n,p) reactions. *Progress in Particle and Nuclear Physics*, 56(2):446–531, April 2006.
- [89] I.S. Towner. Quenching of spin matrix elements in nuclei. *Physics Reports*, 155(5):263–377, November 1987.
- [90] N. D. Dang, A. Arima, T. Suzuki, and S. Yamaji. Study of the Gamow-Teller resonance in 9° Nb and 208Bi. *Nuclear Physics A*, 621:719–735, 1997.

-
- [91] E. Caurier, K. Langanke, G. Martínez-Pinedo, and E. Nowacki. Shell-model calculations of stellar weak interaction rates. I. Gamow-Teller distributions and spectra of nuclei in the mass range $A = 45 - 65$. *Nuclear Physics A*, 653:439–452, 1999.
- [92] N. Bohr. Neutron capture and nuclear constitution. *Nature*, 137:344, 1936.
- [93] W. Hauser and H. Feshbach. The inelastic scattering of neutrons. *Physical Review*, 87(2):366–373, 1952.
- [94] J.-P. Jeukenne, A. Lejeune, and C. Mahaux. Optical-model potential in finite nuclei from Reid’s hard core interaction. *Physical Review C*, 16(1):80–96, 1977.
- [95] C. Mahaux. Nonlocality corrections to the mean free path of a nucleon. *Physical Review C*, 28(4):15–16, 1983.
- [96] S. Fantoni, B. L. Friman, and V. R. Pandharipande. The imaginary part of the nucleon optical potential in nuclear matter. *Physics Letters*, 104(2):89–91, 1981.
- [97] L. McFadden and G.R. Satchler. Optical-model analysis of the scattering of 24.7 MeV alpha particles. *Nuclear Physics*, 84:177–200, 1966.
- [98] J.M. Blatt and V.F. Weisskopf. *Theoretical nuclear physics*. Wiley, 1952.
- [99] J.A. Holmes, S.E. Woosley, W. A. Fowler, and B. A. Zimmerman. Tables of thermonuclear-reaction-rate data for neutron-induced reactions on heavy nuclei. *Atomic Data and Nuclear Data Tables*, 18(4):305–412, October 1976.
- [100] E. Lipparini and S. Stringari. Sum rules and giant resonances in nuclei. *Physics Reports*, 4(September 1988):103–261, 1989.
- [101] W. D. Myers, W. J. Swiatecki, T. Kodama, L.J. El-Jaick, and E.R. Hilf. Droplet model of the giant dipole resonance. *Physical Review C*, 15(6):2032–2043, 1977.
- [102] M. Danos. On the long-range correlation model of the photonuclear effect. *Nuclear Physics*, 5:23–32, 1958.
- [103] R. Capote, M. Herman, P. Obložinský, et al. RIPL – Reference Input Parameter Library for Calculation of Nuclear Reactions and Nuclear Data Evaluations. *Nuclear Data Sheets*, 110(12):3107–3214, December 2009.
- [104] T. Ericson. The statistical model and nuclear level densities. *Advances in Physics*, 9(36):425–511, October 1960.
- [105] K. Langanke, D. J. Dean, P. B. Radha, Y. Alhassid, and S. E. Koonin. Shell-model Monte Carlo studies of fp-shell nuclei. *Physical Review C*, 52(2):718–725, 1995.
- [106] S. Hilaire and S. Goriely. Global microscopic nuclear level densities within the HFB plus combinatorial method for practical applications. *Nuclear Physics A*, 779:63–81, November 2006.
- [107] J. J. Cowan, F.-K. Thielemann, and J. W. Truran. The r-process and nucleochronology. *Physics Reports*, 5:267–394, 1991.
- [108] A. Gilbert and A. G. W. Cameron. A composite nuclear-level density formula with shell corrections. *Canadian Journal of Physics*, 43:1446, 1965.
- [109] D. Mocerlj, T. Rauscher, G. Martínez-Pinedo, et al. Large-scale prediction of the parity distribution in the nuclear level density and application to astrophysical reaction rates. *Physical Review C*, 75(4):045805, April 2007.
- [110] S. Siem, M. Guttormsen, K. Ingeberg, et al. Level densities and γ -strength functions in 148,149Sm. *Physical Review C*, 65(4):1–10, March 2002.
- [111] L.V. Wormer, J. Görres, C. Iliadis, and M. Wiescher. Reaction rates and reaction sequences in the rp-process. *The Astrophysical Journal*, 432:326–350, 1994.
- [112] T. Kawano, P. Talou, M.B. Chadwick, and T. Watanabe. Monte Carlo Simulation for Particle and γ -Ray Emissions in Statistical Hauser-Feshbach Model. *Journal of Nuclear Science and Technology*, 47(5):462–469, 2010.
- [113] F.-K. Thielemann, M. Arnould, and J. W. Truran. Thermonuclear reactions at high temperatures and densities. In *Advances in Nuclear Astrophysics*, pages 91–101, 1987.

-
- [114] A. Kelić, M. V. Ricciardi, and K.-H. Schmidt. ABLA07 - towards a complete description of the decay channels of a nuclear system from spontaneous fission to multifragmentation. Technical report, GSI Helmholtzzentrum für Schwerionenforschung GmbH, Darmstadt, 2010.
- [115] P.E. Hodgson. Compound nucleus reactions. *Rep. Prog. Phys.*, 50:1171–1228, 1987.
- [116] R. Bass. Fusion reactions: successes and limitations of a one-dimensional description. In W. von Oertzen, editor, *Deep-Inelastic and Fusion Reactions with Heavy Ions*, pages 281–293. Springer Berlin Heidelberg, Berlin, 1979.
- [117] F.S. Dietrich. Simple Derivation of the Hauser-Feshbach and Weisskopf-Ewing Formulae , with Application to Surrogate Reactions. Technical report, Lawrence Livermore National Laboratory, 2004.
- [118] M. Kildir, G. L. Rana, R. Moro, et al. Ingoing-wave boundary condition versus optical model transmission coefficients: A systematic comparison with particle emission data. *Physical Review C*, 51(4):1873–1881, 1995.
- [119] Y. Avishai. Fusion cross section at sub-Coulomb energies. *Zeitschrift für Physik A*, 286:285–290, 1978.
- [120] M. Matsumoto and T. Nishimura. Mersenne Twister : A 623-dimensionally equidistributed uniform Pseudo-Random Number Generator. *ACM Transactions on Modelling and Computer Simulation (TOMACS)*, 8(1):3–30, 1998.
- [121] R. Becker. *Theorie der Wärme*. Berlin, 1955.
- [122] P. Fröbrich and R. Lipperheide. *Theory of Nuclear Reactions*. Oxford science publications. Clarendon Press, 1996.
- [123] K.-H. Schmidt. Deexcitation mechanisms in compound nucleus reactions. Technical Report March, Universidad de Santiago de Compostela, Santiago de Compostela, 2009.
- [124] A.S. Goldhaber. Volume versus surface sampling of Maxwellian distributions in nuclear reactions. *Physical Review C*, 17:2243–2244, 1978.
- [125] P. Axel. Electric dipole ground-state transitions width strength function and 7-MeV photon interaction. *Physical Review*, 126(2):671–683, 1962.
- [126] J. Pruet, R. D. Hoffman, S. E. Woosley, H.-T. Janka, and R. Buras. Nucleosynthesis in Early Supernova Winds. II. The Role of Neutrinos. *The Astrophysical Journal*, 644(2):1028–1039, June 2006.
- [127] E. Kolbe, K. Langanke, S. Krewald, and F.-K. Thielemann. Inelastic neutrino scattering on ^{12}C and ^{160}Gd above the particle emission threshold. *Nuclear Physics A*, 540:599–620, 1992.
- [128] E. Kolbe, K. Langanke, and S. Krewald. Neutrino-induced reactions on ^{12}C within the continuum random phase approximation. *Physical Review C*, 49(2):1122–1126, 1994.
- [129] E. Kolbe and K. Langanke. Role of ν -induced reactions on lead and iron in neutrino detectors. *Physical Review C*, 63(2):1–11, January 2001.
- [130] E. Kolbe, K. Langanke, P. Vogel, and G. Martinez-Pinedo. Neutrino–nucleus reactions and nuclear structure. *Journal of Physics G Nuclear and Particle Physics*, 29:2569–2596, 2003.
- [131] J.P. Elliott and T.H.R. Skyrme. Centre-of-mass effects in the nuclear shell-model. *Proceedings of the Royal Society of London, Series A, Mathematical and Physical sciences*, 232(1191):561–566, 1955.
- [132] E. Kolbe. *Investigation of inelastic Neutrino scattering off nuclei and applications to Nuclear Physics and Astrophysics*. PhD thesis, Westfälische Wilhelms-Universität Münster, 1992.
- [133] K. Langanke and E. Kolbe. Neutrino-induced neutral-current reaction cross-sections for r-process nuclei. *Atomic Data and Nuclear Data Tables*, 82(2):191–209, November 2002.
- [134] T. Suzuki, S. Chiba, T. Yoshida, T. Kajino, and T. Otsuka. Neutrino-nucleus reactions based on new shell model Hamiltonians. *Physical Review C*, 034307:1–9, 2006.
- [135] D. Gazit and N. Barnea. Neutrino neutral reaction on ^4He : Effects of final state interaction and realistic NN force. *Physical Review C*, 70(4):048801, October 2004.

-
- [136] T. Suzuki and T. Kajino. Element synthesis in the supernova environment and neutrino oscillations. *Journal of Physics G: Nuclear and Particle Physics*, 40(8):083101, August 2013.
- [137] Y.-Z. Qian, W.C. Haxton, K. Langanke, and P. Vogel. Neutrino-induced neutron spallation and supernova r-process nucleosynthesis. *Physical Review C*, 55(3):1532–1544, March 1997.
- [138] A. Hektor, E. Kolbe, K. Langanke, and J. Toivanen. Neutrino-induced reaction rates for r-process nuclei. *Physical Review C*, 61:1–10, 2000.
- [139] K. Langanke and G. Martinez-Pinedo. Nuclear weak-interaction processes in stars. *Reviews of modern Physics*, 75:2003, 2008.
- [140] G. Martínez-Pinedo, T. Fischer, A. Lohs, and L. Huther. Charged-Current Weak Interaction Processes in Hot and Dense Matter and its Impact on the Spectra of Neutrinos Emitted from Protoneutron Star Cooling. *Physical Review Letters*, 109(25):251104, December 2012.
- [141] S. W. Bruenn. Stellar core collapse: Numerical model and infall epoch. *The Astrophysical Journal Supplement Series*, 58:771–841, 1985.
- [142] Bradley Meyer. r-Process Nucleosynthesis without Excess Neutrons. *Physical Review Letters*, 89(23):231101, November 2002.
- [143] F. X. Timmes and F. D. Swesty. The accuracy, consistency, and speed of an electron-positron equation of state based on table interpolation of the helmholtz free energy. *The Astrophysical Journal Supplement Series*, 2(1):501–516, 2000.
- [144] T. Fischer. private communication.
- [145] B. S. Meyer. Entropy and nucleosynthesis. *Physics Reports*, 227(1-5):257–267, May 1993.
- [146] L. F. Roberts, S. E. Woosley, and R. D. Hoffman. Integrated Nucleosynthesis in Neutrino-Driven Winds. *The Astrophysical Journal*, 722(1):954–967, October 2010.
- [147] B. S. Meyer, T. D. Krishnan, and D. D. Clayton. Theory of quasi-equilibrium nucleosynthesis and applications to matter expanding from high temperature and density. *The Astrophysical Journal*, 498:808–830, 1998.
- [148] Adam Burrows. Colloquium: Perspectives on core-collapse supernova theory. *Reviews of Modern Physics*, 85(1):245–261, February 2013.
- [149] M. Hempel, J. Schaffner-Bielich, S. Typel, and G. Röpke. Light clusters in nuclear matter: Excluded volume versus quantum many-body approaches. *Physical Review C*, 84(5):055804, November 2011.
- [150] A. Burrows and J. M. Lattimer. The birth of neutron stars. *The Astrophysical Journal*, 307:178–196, 1986.
- [151] S. Wanajo and Y. Ishimaru. r-Process calculations and Galactic chemical evolution. *Nuclear Physics A*, 777:676–699, October 2006.
- [152] C. Sneden, J. J. Cowan, I. I. Ivans, et al. Evidence of multiple r-process sites in the early galaxy: new observations of CS 22892-052. *The Astrophysical Journal*, 533:L139–L142, 2000.
- [153] B. S. Meyer. Neutrino reactions on 4He and the r-process. *The Astrophysical Journal*, 449:L55–L58, 1995.
- [154] B.S. Meyer, G.C. Mclaughlin, and G.M. Fuller. Neutrino capture and r -process nucleosynthesis. *Physical Review C*, 58(6):3696–3710, 1998.
- [155] C.F. McKee and J.K. Truelove. Explosions in the interstellar medium. *Physics Reports*, 256(1-3):157–172, May 1995.
- [156] T. A. Weaver and S. E. Woosley. Evolution and Explosion of Massive Stars. *Annals of the New York Academy of Sciences*, 336(1 Ninth Texas S):335–357, February 1980.
- [157] A. Ray, P. Das, S. K. Saha, et al. Observation of large change of 7Be decay rate in Au and Al 2 O 3 and its implications. *Physics Letters B*, 455(May):69–76, 1999.

-
- [158] A. Heger, S.E. Woosley, K. Langanke, et al. Nucleosynthesis of heavy elements in massive stars. *Nuclear Physics A*, 718:159c–166c, 2003.
- [159] S Woosley and a Heger. Nucleosynthesis and remnants in massive stars of solar metallicity. *Physics Reports*, 442(1-6):269–283, April 2007.
- [160] R. I. Epstein, S. A. Colgate, and W. C. Haxton. Neutrino-induced r-process nucleosynthesis. *Physical Review Letters*, 61(18):2038–2041, 1988.
- [161] Projjwal Banerjee, W. C. Haxton, and Yong-Zhong Qian. Long, Cold, Early r Process? Neutrino-Induced Nucleosynthesis in He Shells Revisited. *Physical Review Letters*, 106(20):201104, May 2011.
- [162] P. Banerjee, Y.-Z. Qian, W. C. Haxton, and A. Heger. New Primary Mechanisms for the Synthesis of Rare ^9Be in Early Supernovae. *Physical Review Letters*, 110(14):141101, April 2013.
- [163] F.-K. Thielemann, J. Metzinger, and H.V. Klapdor. Beta-delayed fission and neutron emission: Consequences for the astrophysical r-Process and the age of the galaxy. *Zeitschrift für Physik A*, 309:301–317, 1983.
- [164] P. Möller. New calculations of gross β -decay properties for astrophysical applications: Speeding-up the classical r process. *Physical Review C*, 67(5):055802, May 2003.
- [165] A. Burrows. Neutrino-matter interactions in the context of core-collapse supernovae. *Progress in Particle and Nuclear Physics*, 46:59–71, 2001.
- [166] W. R. Hix and B. S. Meyer. Thermonuclear kinetics in astrophysics. *Nuclear Physics A*, 777:188–207, October 2006.
- [167] T. Dong and Z. Ren. New calculations of α -decay half-lives by the Viola-Seaborg formula. *The European Physical Journal A*, 26(1):69–72, September 2005.
- [168] A.L. Fetter and J.D. Walecka. *Quantum theory of many-particle systems*. McGraw-Hill, 1971.
- [169] F. Schwabl. *Quantenmechanik für Fortgeschrittene (QM II)*. Springer-Lehrbuch. Springer, 2008.